JP0450249

JAERI-Research
2003-028

STUDY OF NON-INDUCTIVE CURRENT DRIVE USING HIGH ENERGY NEUTRAL BEAM INJECTION ON JT-60U

January 2004

Toshihiro OIKAWA

日本原子力研究所
Japan Atomic Energy Research Institute

本レポートは、日本原子力研究所が不定期に公刊している研究報告書です。
入手の問合わせは、日本原子力研究所研究情報部研究情報課（〒319-1195 茨城県那珂郡東海村）あて、お申し越し下さい。なお、このほかに財団法人原子力弘済会資料センター（〒319-1195 茨城県那珂郡東海村日本原子力研究所内）で複写による実費頒布を行っております。

This report is issued irregularly.
Inquiries about availability of the reports should be addressed to Research Information Division, Department of Intellectual Resources, Japan Atomic Energy Research Institute, Tokai-mura, Naka-gun, Ibaraki-ken 〒319-1195, Japan.

© Japan Atomic Energy Research Institute, 2004

編集兼発行　日本原子力研究所

JAERI－Research 2003－028

Study of Non-inductive Current Drive Using High Energy Neutral Beam Injection on JT-60U

Toshihiro OIKAWA

Department of Fusion Plasma Research
Naka Fusion Research Establishment
Japan Atomic Energy Research Institute
Naka-machi, Naka-gun, Ibaraki-ken

(Received October 23, 2003)

The negative ion based neutral beam (N-NB) current drive was experimentally studied. The N-NB driven current density was determined over a wide range of electron temperatures by using the motional Stark effect spectroscopy. Theoretical prediction of the NB current drive increasing with beam energy and electron temperature was validated. A record value of NB current drive efficiency 1.55×10^{19} $Am^{-2}W^{-1}$ was achieved simultaneously with high confinement and high beta at a plasma current of 1.5 MA under a fully non-inductively current driven condition. The experimental validation of NB current drive theory for MHD quiescent plasmas gives greater confidence in predicting the NB current drive in future reactors.

However, it was also found that MHD instabilities caused a degradation of NB current drive. A beam-driven instability expelled N-NB fast ions carrying non-inductive current from the central region. The lost N-NB driven current was estimated to be 7 % of the total N-NB driven current. For the neoclassical tearing mode (NTM), comparisons of the measured neutron yield and fast ion pressure profile with transport code calculations revealed that the loss of fast ions increases with the NTM activity and that fast ions at higher energies suffer larger transport than at lower energies.

Keywords : Negative Ion Based Neutral Beam, NB Driven Current, Motional Stark Effect, Current Drive Efficiency, MHD Instability, Beam-driven Instability, Neoclassical Tearing Mode

---

This paper includes the doctral thesis accepted in Department of Physics, Graduate School of Science, University of Tokyo in November 2003.

JAERI－Research　2003－028

JT-60Uにおける高エネルギー中性粒子ビーム入射による非誘導電流駆動の研究

日本原子力研究所那珂研究所炉心プラズマ研究部
及川　聡洋

（２００３年１０月２３日受理）

負イオン中性粒子ビーム(N-NB)による電流駆動の研究を行った。動的Stark効果偏光計を用い、N-NB駆動電流を広範囲な電子温度領域に渡って計測した。NB電流駆動はビームエネルギーと電子温度と共に増加するという理論予測を検証した。プラズマ電流1.5 MAにおいて高閉じ込め、高ベータ、完全電流駆動、NBの電流駆動効率の最高値1.55×10^{19} $Am^{-2}W^{-1}$を同時達成した。これらの結果は将来の核融合炉におけるNB電流駆動性能の予測性に更なる信頼を与えた。

一方、MHD不安定性によりNB電流駆動が減少することも明らかにした。ビーム駆動型不安定性によりN-NB高速イオンが輸送され駆動電流が7%減少した。新古典テアリングモードについては、中性子発生率と高速イオン圧力の計測値と理論値の比較から、磁場揺動の増加と共に高速イオン損失が増大すること、粒子のエネルギーが高い程より大きな輸送をうけることを明らかにした。

那珂研究所：〒311-0193　茨城県那珂郡那珂町向山801-1
東京大学大学院理学系研究科により博士論文として2003年11月受理された内容を含む。

Contents

1 Introduction 1
1.1 Fusion Reaction 1
1.2 Tokamak 2
1.3 Non-inductive Current Drive 3
1.4 Neutral Beam Injection 6
1.4.1 Neutral Beam Production and Negative Ion Based Neutral Beam 7
1.4.2 Ionization 9
1.4.3 NB Current Drive 12
1.4.4 NB Heating 13
1.4.5 Fast Ion Distribution Function 15
1.5 Neoclassical Transport Theory 18
1.5.1 Particle Orbit in Tokamak 18
1.5.2 Transport 20
1.5.3 Bootstrap Current 21
1.5.4 Neoclassical Conductivity 22
1.6 Plasma Confinement Modes 23
1.7 Instabilities in Tokamak Plasmas 23
1.7.1 Neoclassical Tearing Mode 23
1.8 Motional Stark Effect Spectroscopy 26
1.9 Objective of This Thesis 26

2 Experimental Devices 28
2.1 JT-60U 28
2.1.1 JT-60U Device 28
2.1.2 Diagnostic System 29
2.1.3 Heating and Current Drive Systems 32
2.2 Motional Stark Effect Spectroscopy 34
2.2.1 Principle of Diagnostics 34
2.2.2 Diagnostic System 34
2.2.3 Calibration 41
2.2.4 Derivation of the MSE Polarization Angle 42

3 Analysis Methods 46
3.1 Plasma Equilibrium 46
3.1.1 Grad-Shafranov Equation 46
3.1.2 Definitions of the Important Equilibrium Quantities 47
3.1.3 Equilibrium Reconstruction in JT-60U 49
3.2 Determination of Non-inductively-driven Current Profile 55
3.3 Computational Codes for Tokamak Plasma Simulation 57
3.3.1 ACCOME 57
3.3.2 OFMC 59
3.3.3 TOPICS 60

4 Characteristics of Current Drive by High Energy Neutral Beam 62
4.1 N-NB Current Drive Experiment 62
4.1.1 Effect of N-NB Injection on Plasma 62
4.1.2 Determination of the Non-inductively-driven Current Profile 66
4.2 Current Drive at High Electron Temperature 68
4.2.1 Measurement of the N-NB Current Drive in EC Heated Plasmas 69
4.2.2 Verification of N-NB Current Drive Capability at High Electron Temperature Regime 76
4.3 Integration of N-NB Current Drive and High Beta High Confinement Plasma 79
4.3.1 Full Current Drive in ELMy H Mode Plasma 79
4.3.2 Summary of the N-NB Current Drive Capability 88

5 Influence of MHD Instabilities on Neutral Beam Current Drive 91
5.1 Beam-driven Instability 91
5.2 Neoclassical Tearing Instability in High Beta Plasmas 94
5.2.1 Behavior of the Magnetic Island 95
5.2.2 Experimental Observation of Influence on Neutral Beam Fast Ions 98
5.2.3 Experimental Evaluation of Fast Ion Profile Modification 106

6 Discussion 117
6.1 High Energy Neutral Beam Current Drive 117
6.2 Influence of MHD Instabilities on Current Drive 118
6.2.1 Beam-driven Instability 118
6.2.2 Neoclassical Tearing Instability 119

7 Conclusions 124

8 Prospect and Research Issues toward ITER Burning Plasmas 126

Acknowledgment 128

Bibliography 129

Appendix Glossary 134

目　次

1. 導　入 …… 1
1.1 核融合反応 …… 1
1.2 トカマク …… 2
1.3 非誘導電流駆動 …… 3
1.4 中性粒子ビーム入射 …… 6
1.4.1 中性粒子ビーム生成と負イオン源中性粒子ビーム (N-NB) …… 7
1.4.2 電離過程 …… 9
1.4.3 中性粒子ビーム電流駆動 …… 12
1.4.4 中性粒子ビーム加熱 …… 13
1.4.5 高速イオン分布関数 …… 15
1.5 新古典輸送理論 …… 18
1.5.1 トカマクにおける粒子軌道 …… 18
1.5.2 輸送 …… 20
1.5.3 自発電流 …… 21
1.5.4 新古典導電率 …… 22
1.6 プラズマ閉じ込めモード …… 23
1.7 トカマクプラズマにおける不安定性 …… 23
1.7.1 新古典テアリングモード …… 23
1.8 Motional Stark Effect (動的シュタルク効果) 偏光計 …… 26
1.9 本論文の目的 …… 26
2. 実験装置 …… 28
2.1 JT-60U …… 28
2.1.1 JT-60U装置 …… 28
2.1.2 計測システム …… 29
2.1.3 加熱電流駆動機器 …… 32
2.2 Motional Stark Effect (動的シュタルク効果) 偏光計 …… 34
2.2.1 計測原理 …… 34
2.2.2 計測システム …… 34
2.2.3 較正 …… 41
2.2.4 MSE偏光角表式の導出 …… 42
3. 解析手法 …… 46
3.1 プラズマ平衡 …… 46
3.1.1 Grad-Shafranov方程式 …… 46
3.1.2 主要平衡量の定義 …… 47

3.1.3 JT-60Uにおける平衡再構築 …… 49
3.2 非誘導電流駆動分布の同定 …… 55
3.3 トカマクプラズマシミュレーションコード …… 57
3.3.1 ACCOME …… 57
3.3.2 OFMC …… 59
3.3.3 TOPICS …… 60
4. 高エネルギー中性粒子ビームの電流駆動特性 …… 62
4.1 N-NB電流駆動実験 …… 62
4.1.1 N-NB入射によるプラズマへの影響 …… 62
4.1.2 非誘導駆動電流分布の同定 …… 66
4.2 高電子温度領域における電流駆動 …… 68
4.2.1 電子サイクロトロン波加熱プラズマでのN-NB電流駆動計測 …… 69
4.2.2 高電子温度領域におけるN-NB電流駆動特性の検証 …… 76
4.3 N-NB電流駆動と高ベータ高閉じ込めプラズマの両立 …… 79
4.3.1 ELMy Hモードプラズマにおける完全非誘導電流駆動 …… 79
4.3.2 N-NB電流駆動性能のまとめ …… 88
5. 中性粒子ビーム電流駆動への電磁流体力学的不安定性の影響 …… 91
5.1 ビーム駆動不安定性 …… 91
5.2 高ベータプラズマにおける新古典テアリングモ …… 94
5.2.1 磁気島の振る舞い …… 95
5.2.2 中性粒子ビーム高速イオンへの影響の実験的観測 …… 98
5.2.3 高速イオン分布への影響の実験的評価 …… 106
6. 考　察 …… 117
6.1 高エネルギー中性粒子ビーム電流駆動 …… 117
6.2 電流駆動への電磁流体力学的不安定性の影響 …… 118
6.2.1 ビーム駆動不安定性 …… 118
6.2.2 新古典テアリングモード …… 119
7. 結　論 …… 124
8. ITERにおける核燃焼プラズマに向けた展望と研究課題 …… 126
謝　辞 …… 128
参考文献 …… 129
付録A　用語集 …… 134

1. Introduction

The goal of the development of magnetic confinement fusion is to identify the attractive magnetic geometries for fusion reactors. In addition to technological problems, a number of challenging physics problems need to be solved. The physics problems are categorized into three basic areas: equilibrium and stability, heating and current drive, and transport (confinement). The most obvious common feature of presently explored magnetic fusion concepts is that they have the topology of a torus rather than a linear system with open-ends. The tokamak configuration [1] has been most successful, and is the most promising candidate for a fusion reactor among a variety of magnetic confinement concepts. The first burning experimental device ITER (International Thermonuclear Experimental Reactor) [2] is based on the tokamak concept.

1.1 Fusion Reaction

By far the most promising fusion reaction is that in which the nuclei of deuterium and tritium fuse to produce an alpha particle with the release of a neutron, that is

$$\mathrm{D}^2 + \mathrm{T}^3 \rightarrow \mathrm{He}^4(3.52\mathrm{MeV}) + \mathrm{n}^1(14.06\mathrm{MeV})$$

The reason the D-T reaction is preferred to other reactions is clear from Fig. 1.1 where the cross-sections [3] for

$$\begin{aligned}
\mathrm{D}^2 + \mathrm{D}^2 &\rightarrow \mathrm{He}^3(0.82\mathrm{MeV}) + \mathrm{n}^1(2.45\mathrm{MeV}) \\
\mathrm{D}^2 + \mathrm{D}^2 &\rightarrow \mathrm{T}^3(1.01\mathrm{MeV}) + \mathrm{H}^1(3.03\mathrm{MeV}) \\
\mathrm{D}^2 + \mathrm{He}^3 &\rightarrow \mathrm{He}^4(3.67\mathrm{MeV}) + \mathrm{H}^1(14.67\mathrm{MeV})
\end{aligned}$$

are also shown. It is seen that these cross-sections are considerably less than that for D-T except at impractically high energies. The two branches of the D-D reaction occur with nearly equal probability, and the sum of their cross-sections is plotted in the figure.

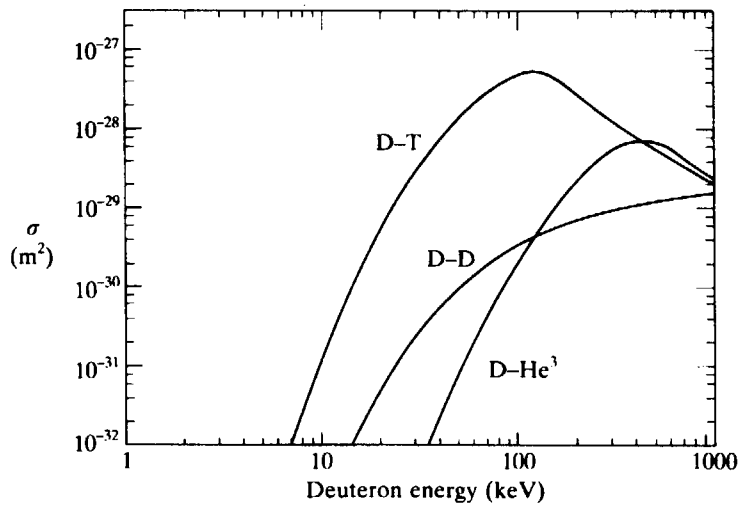

Figure 1.1: Cross-sections for the reactions D-T, D-D and D-He^3. The two D-D reactions have similar cross-sections, the graph gives their sum (from Ref. [4]).

1.2 Tokamak

The tokamak [4] is a toroidal plasma confinement system [Fig. 1.2 (a)]. The principal magnetic field $\boldsymbol{B}$ is the toroidal field. In the presence of a purely toroidal magnetic field, however, charged particles suffer the toroidal drift due to the curvature of the magnetic field line and the gradient of the magnetic field (the toroidal magnetic field is non-uniform in a toroidal configuration as described below). The drift directions for electrons and ions are opposite to each other in the vertical direction [z-direction in Fig. 1.2 (b)]. Thus, the electric field $\boldsymbol{E}$ induced by the resultant charge separation causes outward drift for both electrons and ions by $\boldsymbol{E} \times \boldsymbol{B}/B^2$ drift. Consequently, a simple toroidal field cannot confine a plasma unless separated charges are short-circuited by an appropriate method. If magnetic field lines connect the upper and lower regions by introducing a poloidal magnetic field, the separated charges can be short-circuited, as charged particles can move freely along the field lines. In the tokamak, the poloidal magnetic field is produced mainly by the current in the plasma itself (I_{p}) which flows in the toroidal direction [Fig. 1.2 (a)]. The combination of the toroidal magnetic field B_{T} and the poloidal magnetic field B_{p} gives rise to magnetic field lines which have a helical trajectory around the torus as illustrated in Fig. 1.2 (c).

The toroidal magnetic field is produced by currents in toroidal field coils which encircle the plasma ring in the poloidal direction as shown in Fig. 1.3 (a). Thus, the toroidal magnetic field is inversely proportional to the major radius R. The plasma current is driven principally by a toroidal electric field induced by transformer action in which the flux change through the torus is generated by the primary coil (ohmic coil) as shown in Fig. 1.3 (a). The plasma current also contributes to plasma heating by Joule dissipation (ohmic heating). A vertical magnetic field is required to balance the hoop force of the plasma ring. This field is produced by currents in external coils (vertical field coils) wound in the toroidal

direction as shown in Fig. 1.3 (b). The poloidal magnetic field is typically an order of magnitude smaller than the toroidal field.

The plasma pressure which can be confined increases with the toroidal magnetic field and the toroidal plasma current. The magnitude of the toroidal field is limited by technological factors, i.e., cooling and magnetic forces in normal conducting coils, or critical magnetic field and magnetic forces in superconducting coils. The magnitude of the toroidal plasma current is limited by a disruptive MHD (Magnetohydrodynamic) instability. There are advantages for confinement and achievable pressure in vertically elongated plasmas in which the plasma current can be higher than in circular cross-section plasmas. In addition, a triangular plasma shape gives better stability against a variety of MHD instabilities, increasing the achievable pressure. Therefore, poloidal field coils other than the vertical field coils are placed at appropriate locations to control the plasma shape and position. In many tokamaks with auxiliary heating such as neutral beam injection or radiofrequency (RF) wave, a "divertor" configuration is created to avoid impurity influx generated through interaction between the plasma and the vacuum vessel wall [Fig. 1.3 (c)]. Impurity ions in the plasma, including partially stripped ions, molecules or atoms of non-fuel, cause radiation loss and dilution of the fuel ions. The heat and particle fluxes from the plasma core region through diffusive or convective processes are removed along the open magnetic fields connected to the divertor plates. The tokamak equilibrium is described in detail in Sec. 3.1. The tokamak coordinate system is shown in Fig. 1.2 (a), where the plasma major radius R_0 and the minor radius a are defined. For plasmas with non-circular cross section, there are four definitions of the minor radius based upon area, volume, poloidal magnetic flux and toroidal magnetic flux that are contained inside each flux surface. Unless otherwise specified, the minor radius defined by the plasma volume within each closed flux surface is used in this thesis.

1.3 Non-inductive Current Drive

A tokamak reactor with current generated by an inductive electric field is a pulsed device, and so it has substantial drawbacks such as a low duty factor, intermittent power output and high fatigue stress produced by the thermal cycling. These are not compatible with cost competitiveness or steady generation of electric power. Non-inductive current drive enables steady state operation and remove problems associated with the pulsed operation. In addition, the non-inductive current drive system could be used to control the radial profile of plasma current density to improve confinement and avoid MHD instabilities. The non-inductive current drive can be realized by neutral beam injection [5] and the RF wave injection [6]. There are several methods of RF current drive, including the use of the electron cyclotron wave, the lower hybrid wave and the fast wave. There is another important method of non-inductive current, the self-generated bootstrap current [7, 8], which is spontaneously driven in the plasma by the pressure gradient. This current results from particles trapped in the low field region along the magnetic field line (sec. 1.5.3). Therefore, the total current density j is the sum of the ohmic (inductive) portion j_{OH} and

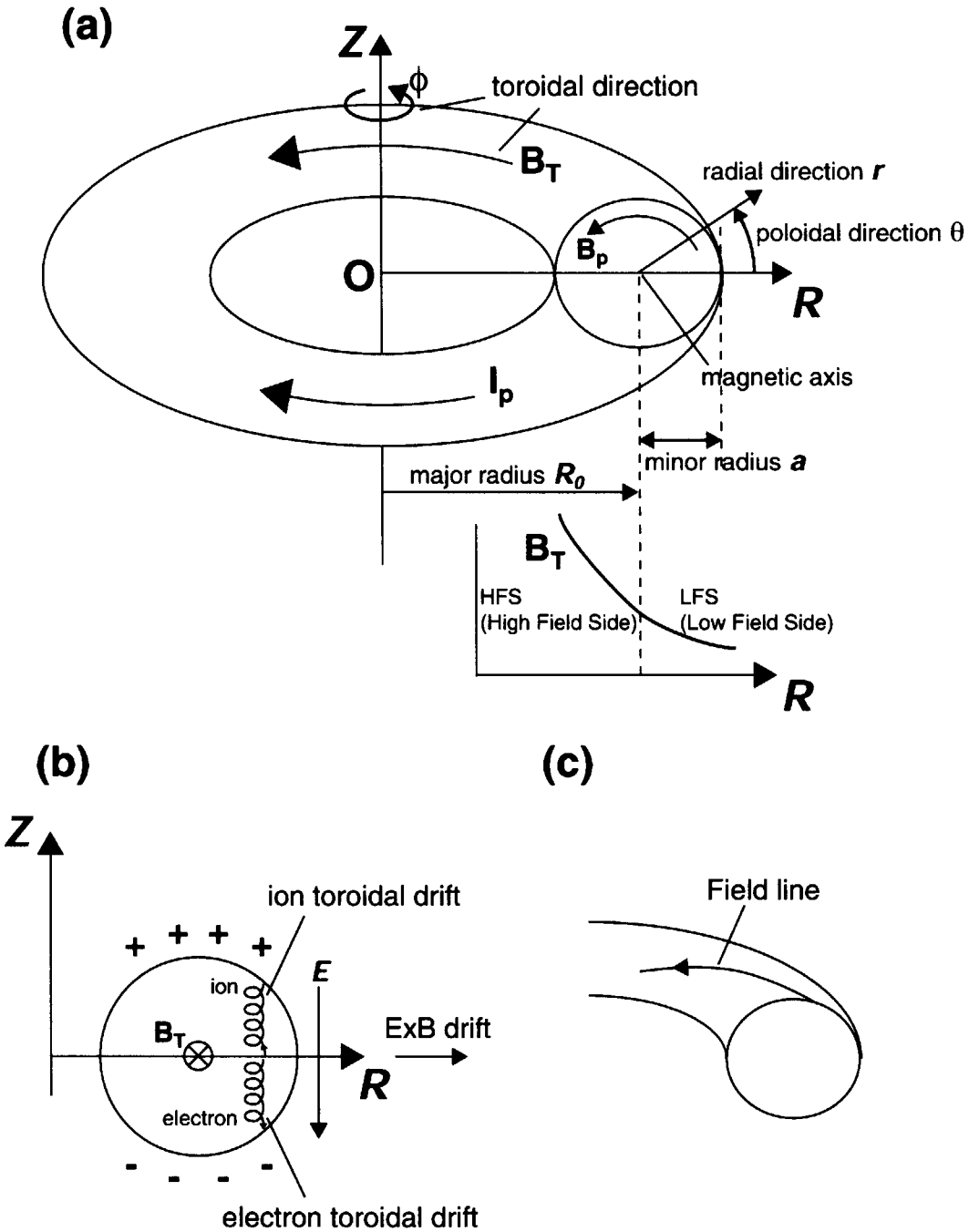

Figure 1.2: (a) Toroidal magnetic field configuration. The magnetic field line is formed by a combination of the toroidal field B_T and the poloidal field B_p. The toroidal current in the plasma I_p produces B_p. The external coil current produces B_T (see Fig. 1.3). (b) The toroidal and $\boldsymbol{E} \times \boldsymbol{B}$ drifts are shown in the poloidal cross section (R-Z plane). (c) Combination of B_T and B_p causes field lines to twist around the plasma.

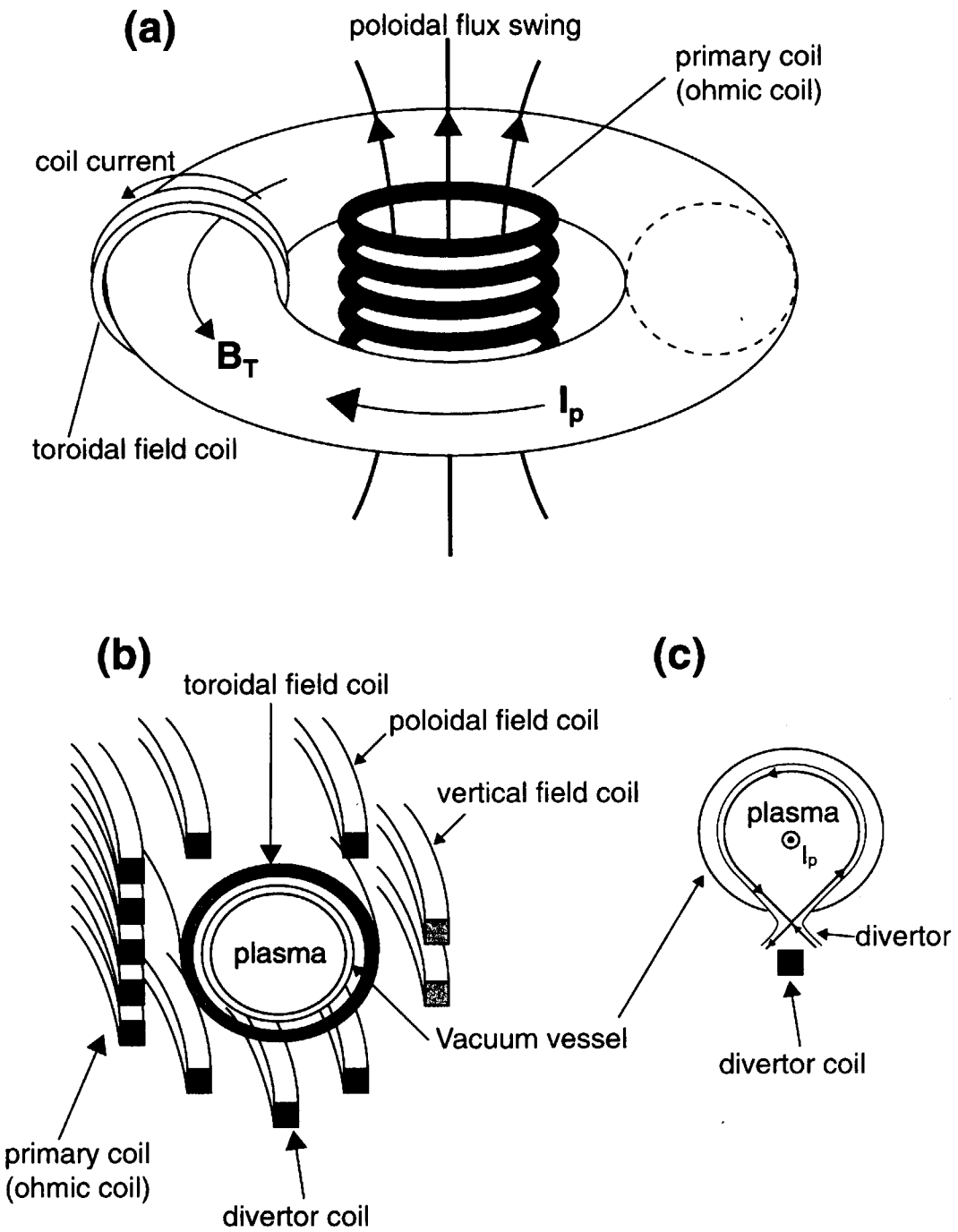

Figure 1.3: (a) Toroidal magnetic field is produced by the current in external toroidal field coils. The plasma current is induced by the magnetic flux swing produced by the primary coil (ohmic coil). (b) The poloidal field coils (position and shape control coils) balance the hoop force and determine the plasma shape. (c) Divertor configuration is formed by the "divertor" coil, one of the poloidal field coils.

non-inductive one j_{NIND},

$$j = j_{\mathrm{OH}} + j_{\mathrm{NIND}}, \quad j_{\mathrm{NIND}} = j_{\mathrm{NB}} + j_{\mathrm{BS}} + j_{\mathrm{RF}} ,$$

where j_{NIND} is composed of the components driven by neutral beam (sec. 1.4.3), bootstrap current (sec. 1.5.3) and RF, j_{NB}, j_{BS} and j_{RF}, respectively.

Here, the current drive efficiency is introduced as a figure of merit for current drive capability by the external current drive methods such as neutral beam and RF. The non-inductive driven current by the power injection from the external generally decreases with plasma density. The charged particles produced by the non-inductive current drive methods give rise to a larger driven current in a toroidal device with a smaller major radius at the same energy, because they can circulate around the torus more frequently in a smaller device. Thus, the current drive efficiency η_{CD} is defined by

$$\eta_{\mathrm{CD}} \equiv \frac{\bar{n}_{\mathrm{e}} R_{\mathrm{p}} I_{\mathrm{CD}}}{P_{\mathrm{abs.}}} ,$$

where $\bar{n}_{\mathrm{e}}$ is the averaged electron density, R_{p} is the plasma major radius, I_{CD} is the total driven current in a plasma, and $P_{\mathrm{abs.}}$ is the power absorbed in the plasma.

In the next section 1.4, the neutral beam current drive is described. The bootstrap current is described in 1.5.

1.4 Neutral Beam Injection

Neutral beam (NB) was first employed for plasma heating. Neutral atoms injected into a plasma travel in straight lines, being unaffected by the magnetic field. The atoms become ionized through collisions with the plasma particles and the resulting ions and electrons are then held by the magnetic field. Since the ions and electrons have the same velocity, the energy is carried almost entirely by the more massive ions. Once ionized, the ions have orbits in the magnetic field determined by their energy, angle of injection and point of deposition. The energy of the injected ions is gradually transferred to the plasma electrons and ions through Coulomb collisions. Thus, the injected ions are initially slowed and then thermalized.

The tangential neutral beam injection [Fig. 1.4] produces a circulating current of fast ions which can be used to aid or oppose the plasma current. Ohkawa first suggested the use of fast ions for current drive [5]. Since the NB current drive was demonstrated experimentally in the DITE tokamak for the first time [9], the NB current drive and the current profile control using NB have been studied in many tokamaks. Higher beam energies are favorable to produce higher fast ion currents.

It is desirable that as much of the NB deposition as possible should take place in the plasma central region. This is because the plasma core has higher temperature and density than the edge region, and heat and particle fluxes are directed outward and lost through radiation or across the last closed flux surface. The NB current drive in the plasma central region also needs the beam penetration to the core as well as the NB heating. The beam deposition depends on the beam energy and the plasma density. In the

experiments up to present, a beam energy of several tens keV $\sim$ 100 keV has been employed, which can penetrate to the plasma core at the operational plasma density. However, in a reactor where has a larger plasma radius and higher electron density around $10^{20}\mathrm{m}^{-3}$, a 100 keV NB is deposited in the plasma peripheral region. In ITER, the plasma performance and discharge operation scenario are prospected at the electron density $\sim 1 \times 10^{20}\mathrm{m}^{-3}$ by using the 1 MeV neutral beam. To obtain a MeV neutral beam of several tens MW, the negative ion based method should be established as described in 1.4.2. In 1996, the world's first negative ion based NB (500 keV) started to operate in JT-60U to study plasma physics associated with high energy NB injection and to develop such system technologically through a routine operation in the experimental device [10, 11].

In 1.4.1, the neutral beam production based on the negative ions is introduced. The beam ionization in the plasma, NB current drive and heating are described in 1.4.2, 1.4.3 and 1.4.4, respectively. Temporal behavior of the fast ion distribution function is presented in 1.4.5.

1.4.1 Neutral beam production and negative ion based neutral beam

The conventional method of producing neutral beam is based on positive ions. For a deuterium beam, D^+ ions produced in an ion source are extracted and accelerated to the required energy through the voltage applied electrodes. The resulting ion beam is neutralized by passing through D_2 gas in which charge exchange occurs [Fig. 1.5], and injected into the plasma. The neutralizer gas, however, also produces re-ionization of the neutralized particles. This unwanted charged fraction of the beam leaving the neutralizer has a power of the same order as that of the neutral beam injected into the plasma. The charged particles are therefore deflected by a magnet and dumped before entering the influence of the tokamak magnetic fields where they would otherwise be deflected on to the walls of injection port.

There are difficulties in producing NB with MeV beam energy by using conventional method, the positive ion based NB (P-NB), because the neutralization efficiency for the positive ions rapidly decreases with the beam energy higher than $\sim$100 keV. At 1 MeV, positive ions are hardly neutralized. The proposed solution is to use negative ion based neutral beam (N-NB). The negative ions are produced in an ion source as follows. In deuterium case, D^0 and D^+ are produced in an arc discharge in an ion

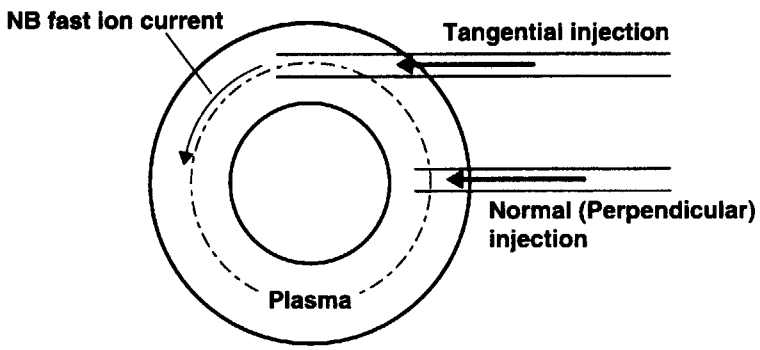

Figure 1.4: Tangential and perpendicular NB injections are illustrated in a top view of torus.

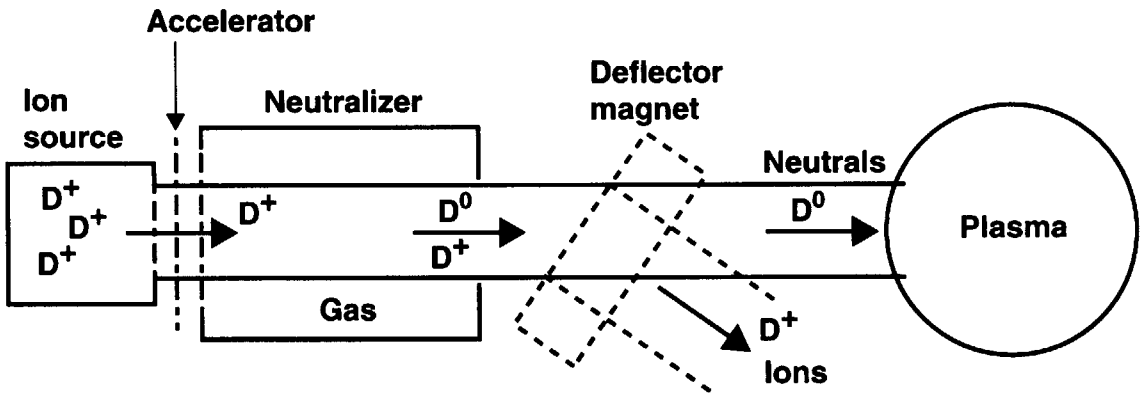

Figure 1.5: Layout of a neutral injection system. D^+ ion based beam is illustrated.

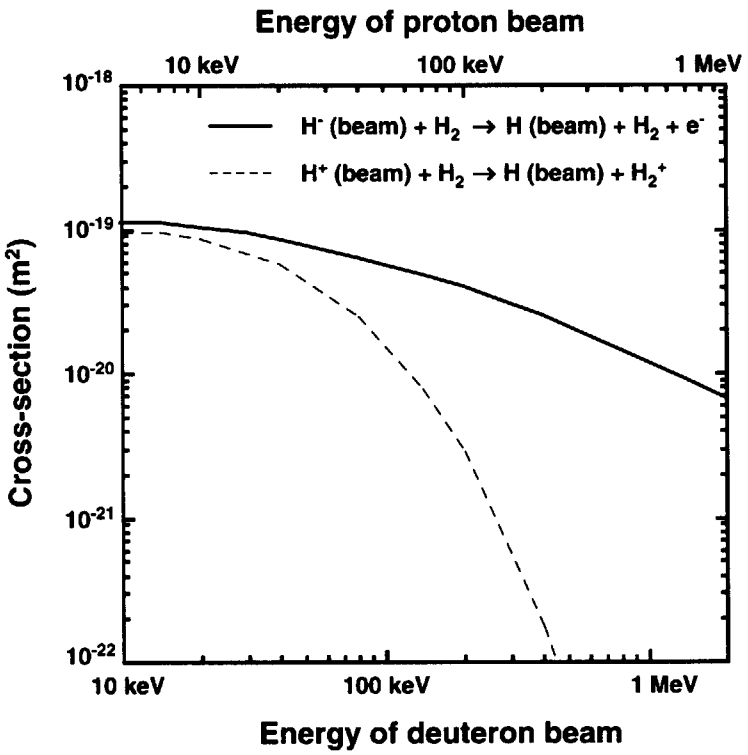

Figure 1.6: Energy dependence of the cross-sections for electron detachment of negative ions (H^-, D^-) and electron capture by positive ions (H^+, D^+). Numerical data are taken from Ref. [12].

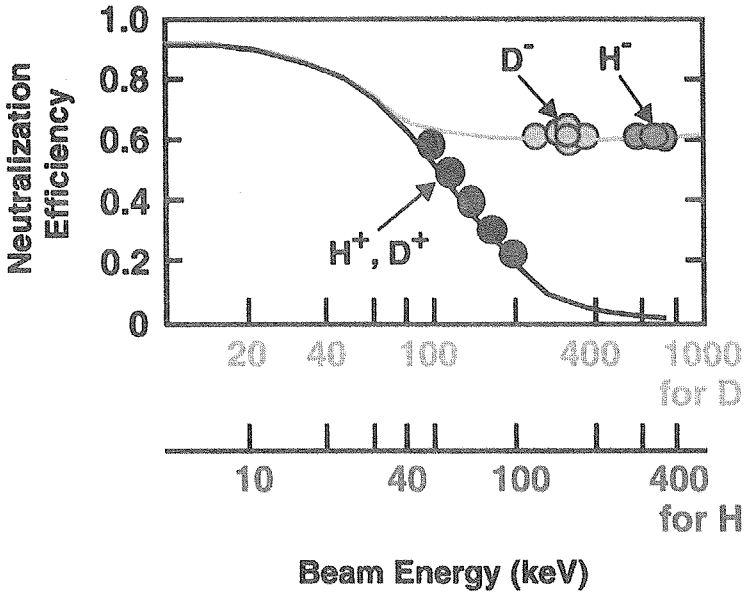

Figure 1.7: Energy dependence of the neutralization efficiency of positive and negative ion beams. Measurements (circles) and theoretical curves are shown (from Ref. [13]).

source through the process $D_2 + e^- \rightarrow D^0 + D^+ + 2e^-$. They become negative ions D^- by obtaining electrons from the cesium coated surface with a low work function. The produced negative ions are extracted and accelerated through the voltage applied electrodes. The negative ions can be efficiently neutralized at substantially higher energies. The cross-sections for electron detachment of negative ions (H^-, D^-) and electron capture by positive ions (H^+, D^+) are shown in Fig. 1.6. The cross-section of electron capture by positive ions rapidly decreases when beam energy exceeds ~100 keV for deuteron beam. Figure 1.7 shows the energy dependence of the neutralization efficiency for positive and negative ions, where the line-integrated density of neutral gas in the neutralizer are optimized at each beam energy. Theory predicts that the neutralization efficiency of D^- at 1 MeV is ~60 % which is nearly same as that for D^+ at 80 keV. The measured neutralization efficiencies (circles in the figure) show good agreements with the theoretical curves [13].

The 1 MeV neutral beam in ITER is designed as N-NB as well as the 500 keV system in JT-60U.

1.4.2 Ionization

There are three basic atomic processes leading to neutral beam ionization: charge exchange, ionization by ions, and ionization by electrons. These processes are listed below using the symbol H to represent the species and the subscripts b and p for beam and plasma, respectively.

Charge exchange	$H_b + H_p^+$	$\rightarrow$	$H_b^+ + H_p$
Ionization by ions	$H_b + H_p^+$	$\rightarrow$	$H_b^+ + H_p^+ + e$
Ionization by electrons	$H_b + e$	$\rightarrow$	$H_b^+ + 2e$

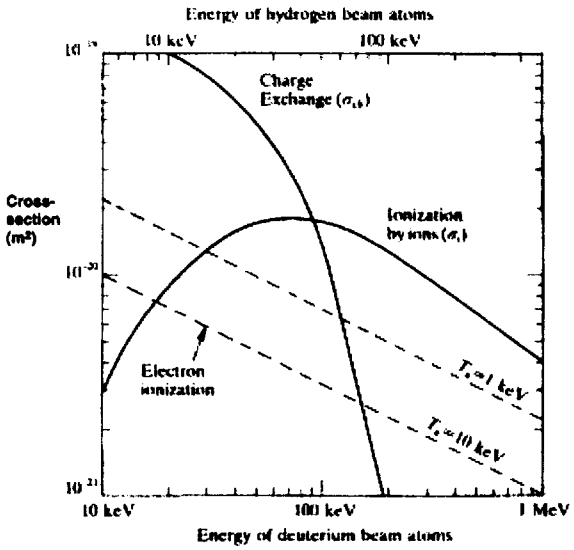

Figure 1.8: Cross-sections for charge exchange and ionization by plasma ions and the effective cross-section for ionization by electrons, as functions of the neutral beam energy.

If the intensity of the beam along the beam injection path (x coordinate) is

$$I(x) = N_{\mathrm{b}}(x) v_{\mathrm{b}}$$

where N_{b} is the number of beam particles per unit length and v_{b} is their velocity, its decay is governed by the equation

$$\frac{\mathrm{d}I}{\mathrm{d}x} = -n\left(\sigma_{\mathrm{ch}} + \sigma_{\mathrm{i}} + \frac{\langle \sigma_{\mathrm{e}} v_{\mathrm{e}} \rangle}{v_{\mathrm{b}}}\right) I$$

where $n(x)$ is the electron (and ion) density, σ_{ch} and σ_{i} are the cross-sections for charge exchange and ionization by ions, respectively, and $\langle \sigma_{\mathrm{e}} v_{\mathrm{e}} \rangle$ is the electron ionization rate coefficient. The different form of the electron ionization term is due to the fact that the electrons will generally have velocities greater than the particles in the beam while the plasma ion velocities are less.

The cross-sections for the various processes are shown in Fig. 1.8, the electron ionization being represented by the effective cross-section $\langle \sigma_{\mathrm{e}} v_{\mathrm{e}} \rangle / v_{\mathrm{b}}$. Below 90 keV, charge exchange is the most effective process for a deuterium beam. Above this energy, ionization by ions becomes dominant.

There are two theoretical models for beam ionization. The single step ionization model considers only ionization by the first impact mentioned above. On the other hand, multistep ionization model [14] considers not only single step ionization process but also excitation process and the subsequent ionization. The multistep ionization can be important in neutral beams with energies of several hundreds keV or higher. The cross-section for electron loss (ionization and charge exchange) can be enhanced through multistep processes, and it is predicted theoretically that the enhancement factor is increased by increasing the beam energy E_{B} and the electron density n_{e}. This is because the excited neutral atoms at higher energies experience more frequent collisions with background species at higher density before they decay to the ground state. From a calculation of the multistep model, the enhancement factor can

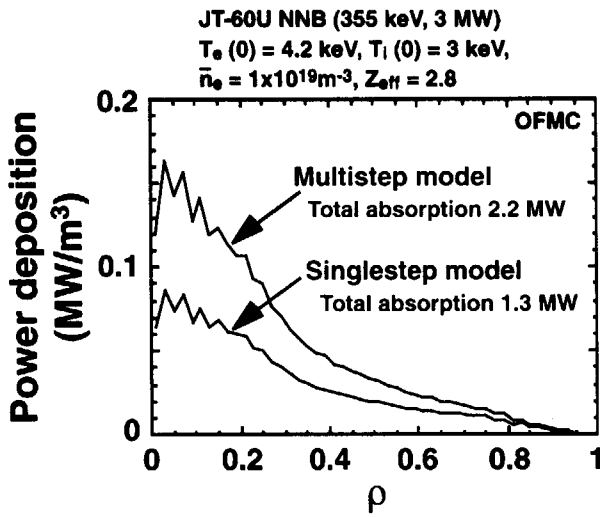

Figure 1.9: The N-NB power deposition profiles with the single step and multistep ionization models calculated by the OFMC code. $E_b = 355$ keV, $P_{NNB} = 3$ MW, $\bar{n}_e = 1 \times 10^{19}$ m^{-3}, $T_e(0) = 4.2$ keV, $T_i(0) = 3$ keV, and $Z_{eff} = 2.8$.

be as large as 20% when $E_B = 500$ keV and $n_e = 1 \times 10^{19}$ m^{-3} in hydrogen plasma. Figure 1.9 shows N-NB ($E_b = 355$ keV, $P_{NNB} = 3$ MW) power deposition profiles calculated by the Orbit Following Monte Carlo (OFMC) code [15] using the single step and multistep models. The plasma parameters are the line-averaged electron density $\bar{n}_e = 1 \times 10^{19}$ m^{-3}, the central electron temperature $T_e(0) = 4.2$ keV, the central ion temperature $T_i(0) = 3$ keV and the effective plasma ion charge $Z_{eff} = 2.8$. Here, the effective plasma ion charge Z_{eff} is defined by

$$Z_{eff} \equiv \sum_i n_i Z_i^2 / \sum_i n_i Z_i \ ,$$

where the summation is taken over all ion species in plasma and the i-th species has a density n_i and an ion charge Z_i. The deposition profiles are different even at relatively low density. The total absorbed powers with the two models are 1.3 and 2.2MW, respectively. Thus, the beam-stopping cross-section has a large impact on the estimation of beam deposition. However, the experimental data obtained before was up to 140 keV [16], at which the difference between the two models, is not large and it is difficult to confirm the multistep model experimentally.

The ionization process of an N-NB has been studied experimentally in JT-60U from shine-through measurements [17, 18]. The shine-through is estimated from the temperature rise of the armor tiles facing the N-NB lines. Figure 1.10 shows the dependence of the measured shine-through of the 350 keV N-NB on n_eL, where n_eL is the integrated electron density along the beam path in the plasma. Two theoretical predictions, for single step and multistep ionization processes, are also shown. The experimental results agree with multistep processes over a wide range of n_eL. Thus, it has been confirmed that the multistep ionization processes are essential for high energy neutral beams.

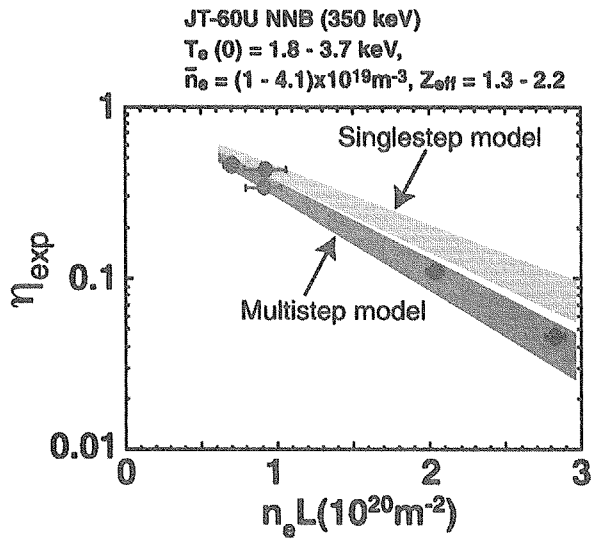

Figure 1.10: $n_e L$ dependence of the shine-through η. The predictions of single step and multistep models are also shown. The shaded areas correspond to a 20 % error in $Z_{\rm eff}$. $E_{\rm b} = 350$ keV, $\bar{n}_{\rm e} = (1-4.1)\times 10^{19}$ m^{-3}, $T_{\rm e}(0) = 1.8-3.7$ keV, and $Z_{\rm eff} = 1.3-2.2$. Hydrogen plasma and beam (from Ref. [17]).

1.4.3 NB current drive

The neutral beam injection produces a current of fast ions circulating around the torus. The fast ion current stacks up during the beam injection period as the fast ions circulate repeatedly around the torus. A steady state is reached when the build up rate of current due to stacking is balanced by the loss rate due to slowing down through collisions with the plasma electrons and bulk ions, or to charge exchange of the fast ions with neutral atoms. The parallel current density produced by NB with a nuclear charge of $Z_{\rm b}$ is (neglecting toroidal orbit effects)

$$\begin{aligned} j_{\rm fast} &= n_{\rm b}\left\langle v_{//}\right\rangle eZ_{\rm b} \\ &= eZ_{\rm b}\int_0^\infty v^3 dv \int_{-1}^{1} f(v,\lambda)\lambda d\lambda\,, \end{aligned} \tag{1.1}$$

where $n_{\rm b}$ is the beam fast ion density, $v_{//}$ is the velocity parallel to the magnetic field line, v is the velocity, λ is a pitch in velocity space defined by $\lambda \equiv v_{//}/v$, and f is the beam fast ion velocity distribution function in a steady state.

The slowing down of these fast ions by collisions with electrons causes the electrons to drift toroidally in the same direction as the fast ions. Thus, there is some cancellation between these two components [19, 20]. This tendency is opposed by electron collisions with the background ions. The degree of cancellation depends on $Z_{\rm b}$, $Z_{\rm eff}$, and the number of trapped electrons. Motion of trapped particles are described in 1.5. In the regime where the electron thermal velocity well exceeds the fast ion velocity, the net beam driven current density in the classical description, i.e., when trapped electron orbits are not

considered, is

$$\langle j_{\text{classical}} \rangle = \langle j_{\text{fast}} \rangle \left(1 - Z_{\text{b}}/Z_{\text{eff}}\right), \quad (< \ldots > : \text{flux surface average}). \tag{1.2}$$

Thus, the collisional electron current will cancel the fast ion current if $Z_{\text{b}} = Z_{\text{eff}}$. Equation 1.2 is modified by the trapped electron orbit correction to [20]

$$\langle j_{\text{NB}} \rangle = \langle j_{\text{fast}} \rangle \left\{ 1 - \frac{Z_{\text{b}}}{Z_{\text{eff}}} \left[1 - G(Z_{\text{eff}}, \epsilon)\right] \right\}, \tag{1.3}$$

where the trapped electron correction, $G(Z_{\text{eff}}, \epsilon)$, depends on the inverse aspect ratio, $\epsilon = r/R$, and on Z_{eff}. The trapped electron fraction is a function of ϵ (approximately $\propto \sqrt{\epsilon}$).

In this thesis, two computational codes, ACCOME [21] and OFMC, are used for the theoretical predictions of the NB current drive. They calculate the fast ion distribution function in different manners. The OFMC code employs an orbit following Monte-Carlo technique. The ACCOME code solves a Fokker-Planck equation in the 2-dimensional velocity space. The trapped electron correction $G(Z_{\text{eff}}, \epsilon)$ is evaluated by the formula given in ref. [20].

1.4.4 NB heating

Once the neutral beam particles entering the plasma have become ionized, the resulting fast ions are slowed down by Coulomb collisions. As the slowing down occurs, energy is passed to the particles of the plasma, causing heating of both electrons and ions. At a high injection velocity, the electron heating is initially dominant. Then, as the beam ions slow down, the ion heating becomes a dominant channel of the beam energy loss.

The electron and ion heating powers per beam ion with energy E_{b} are

$$\begin{aligned} P_{\text{e}} &= \frac{e^4 m_{\text{e}}^{1/2} n \ln \Lambda E_{\text{b}}}{3\pi (2\pi)^{1/2} \epsilon_0^2 m_{\text{b}} T_{\text{e}}^{3/2}} \\ P_{\text{i}} &= \frac{e^4 m_{\text{b}}^{1/2} n \ln \Lambda}{2^{5/2} \pi \epsilon_0^2 m_{\text{i}} E_{\text{b}}^{1/2}}, \end{aligned}$$

where m_{e}, m_{i} and m_{b} are the masses of electron, bulk ion and beam ion, respectively, n is the density, and $\ln \Lambda$ is called the Coulomb logarithm, typically $\sim$17 in tokamak plasmas. Thus, the total direct heating per beam ion, $P = P_{\text{e}} + P_{\text{i}}$, is

$$\begin{aligned} P &= \frac{n e^4 \ln \Lambda}{2\pi \epsilon_0^2 m_{\text{b}}} \left(\frac{2 m_{\text{e}}^{1/2} E_{\text{b}}}{3(2\pi)^{1/2} T_{\text{e}}^{3/2}} + \frac{m_{\text{b}}^{3/2}}{2^{3/2} m_{\text{i}} E_{\text{b}}^{1/2}} \right) \\ &= \frac{e^4 m_{\text{e}}^{1/2} n \ln \Lambda}{3\pi (2\pi)^{1/2} \epsilon_0^2 m_{\text{b}} T_{\text{e}}^{3/2}} E_{\text{b}} \left(1 + \left(\frac{E_{\text{c}}}{E_{\text{b}}} \right)^{3/2} \right), \end{aligned} \tag{1.4}$$

where the critical energy E_{c} is

$$E_{\text{c}} = \left(\frac{3\sqrt{\pi}}{4} \right)^{2/3} \left(\frac{m_{\text{i}}}{m_{\text{e}}} \right)^{1/3} \frac{m_{\text{b}}}{m_{\text{i}}} T_{\text{e}}.$$

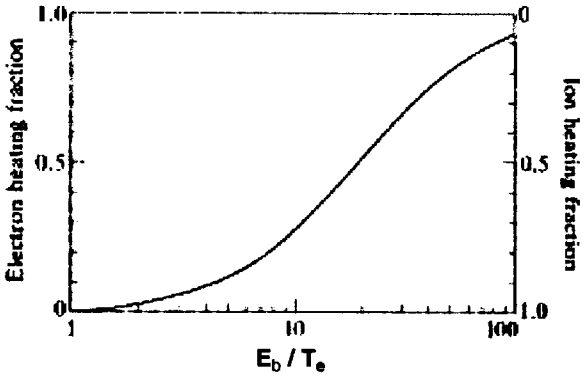

Figure 1.11: Electron and ion heating by deuterium beam ions with energy E_b as fractions of the total heating plotted against E_b/T_e for a deuterium plasma.

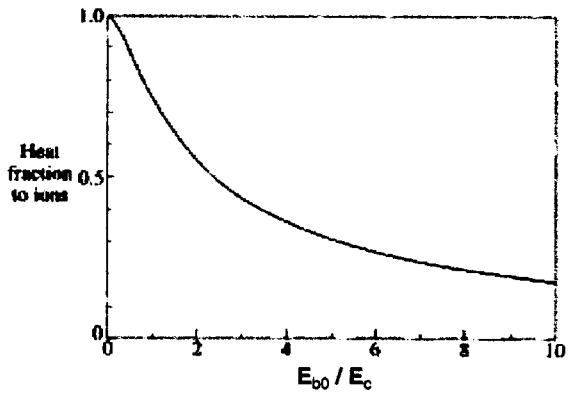

Figure 1.12: Fraction of the initial beam energy which is directly transferred to the plasma ions as a function of the ratio E_{b0}/E_c.

At the critical beam energy, $E_b = E_c$, the electron and ion heating rates are equal. For deuteron background plasma and beam ($A_b = A_i = 2$), the critical energy is $19T_e$. Figure 1.11 shows the fraction of the direct heating by a beam ion going to electrons and ions as a function of E_b/T_e for $A_b = A_i = 2$.

Figure 1.11 gives the fraction of the heating going to ions and electrons for a beam ion of a given energy. In Fig. 1.12, the overall ion heating fraction allowing for the time dependent energy of the beam ions is plotted as a function of the ratio of the initial beam energy (E_{b0}) to the critical energy.

As the beam ions lose their energy, their velocities are increasingly scattered in the perpendicular direction, so-called pitch angle scattering. The slowing and scattering ultimately lead to a thermalization of the beam at the plasma temperature. The scattering is predominantly caused by collisions with the ions. Thus, it is small for $E_b \gg E_c$ and increases as E_b falls. Figure 1.13 schematically illustrates a time development of the velocity distribution of a set of ions injected at a given time. The slowing down

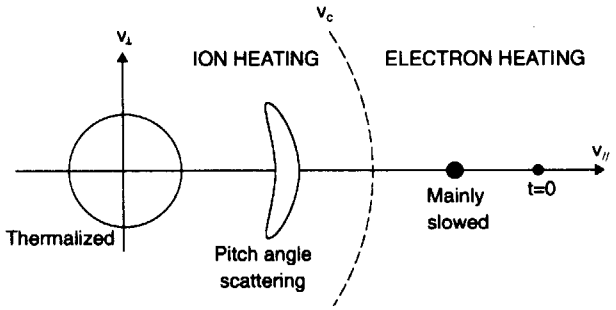

Figure 1.13: Sketch of the time development of the velocity distribution of beam ions injected at $t = 0$, showing the change in behavior when the ions are slowed below the critical velocity $v_c = (2E_c/m_b)^{1/2}$. "//" and "⊥" denote the directions parallel and perpendicular to the initial direction of a set of beam ions, respectively.

time τ_s^b and deflection time $\tau_\perp^b$ are defined by

$$\tau_s^b \equiv -\int_0^{E_{b0}} \frac{dE_b}{dE_b/dt} = \frac{(2\pi)^{1/2} 2\pi\epsilon_0^2 m_b m_e^{-1/2} T_e^{3/2}}{Z_b^2 e^4 n_e \ln\Gamma} \ln\left\{1 + \left(\frac{E_{b0}}{E_c}\right)^{3/2}\right\},$$

$$\tau_\perp^b \equiv \frac{v^2}{\langle dv_\perp^2/dt\rangle} = \frac{2\pi\epsilon_0^2 m_b v_b^3}{e^4 Z_b^2 \sum_j \ln\Lambda Z_j^2 n_j \Phi(b_j v_b)},$$

$$b_j \equiv \left(\frac{m_j}{2T_j}\right)^{1/2}, \quad \Phi(x) \equiv \frac{2}{\pi^{1/2}} \int_0^x \exp\left(-\xi^2\right) d\xi$$

where n_e is the electron density, v_b is the beam velocity, j denotes the j-th species, and dE_b/dt is given in Eq. 1.4. In a plasma with $T_e = T_i = 4$ keV and $n_e = 1 \times 10^{19}\mathrm{m}^{-3}$, τ_s^b is 1.06 s and $\tau_\perp^b$ is 8.13 s for 360 keV deuterons, while τ_s^b is 0.58 s and $\tau_\perp^b$ is 0.68 s for 85 keV deuterons. The NB ions at 360 keV has a longer time constant for 90 degree deflection (pitch angle scattering) than for slowing down because electron collisions are dominant until the beam ions slow down to $\sim$ 80 keV. On the other hand, the slowing down and deflection times are almost same for the NB ions at 85 keV which collide with bulk ions dominantly from their birth to thermalization.

1.4.5 Fast ion distribution function

Temporal behaviors of distribution function of the NB ions are given in this section. The OFMC code calculates a time evolution of fast ion distribution function in the energy and pitch angle space. Figure 1.14 shows the fast ion population at $\rho = 0.1625$ for the N-NB injection (360 keV, 3.7 MW) in the pulse E32460 whose waveforms and profiles of temperature and density are given in section 4.1. Both NBs and background bulk ions are deuterons. Figure 1.15 shows the case of the P-NB injection (85 keV, ctr.-tang.: 1.8 MW, perp.: 0.9 MW). The fast ion population at $\rho = 0.1625$ is the number of fast ion contained in the shell between the $\rho = 0.15$ and $\rho = 0.175$ flux surfaces. In the figures, τ denotes the time after NB injection, and the pitch angle ($\equiv v_{//}/v$) has a range of $(-1, 1)$ by its definition ("//" denotes the component parallel to the local magnetic field line). The positive and negative values of the

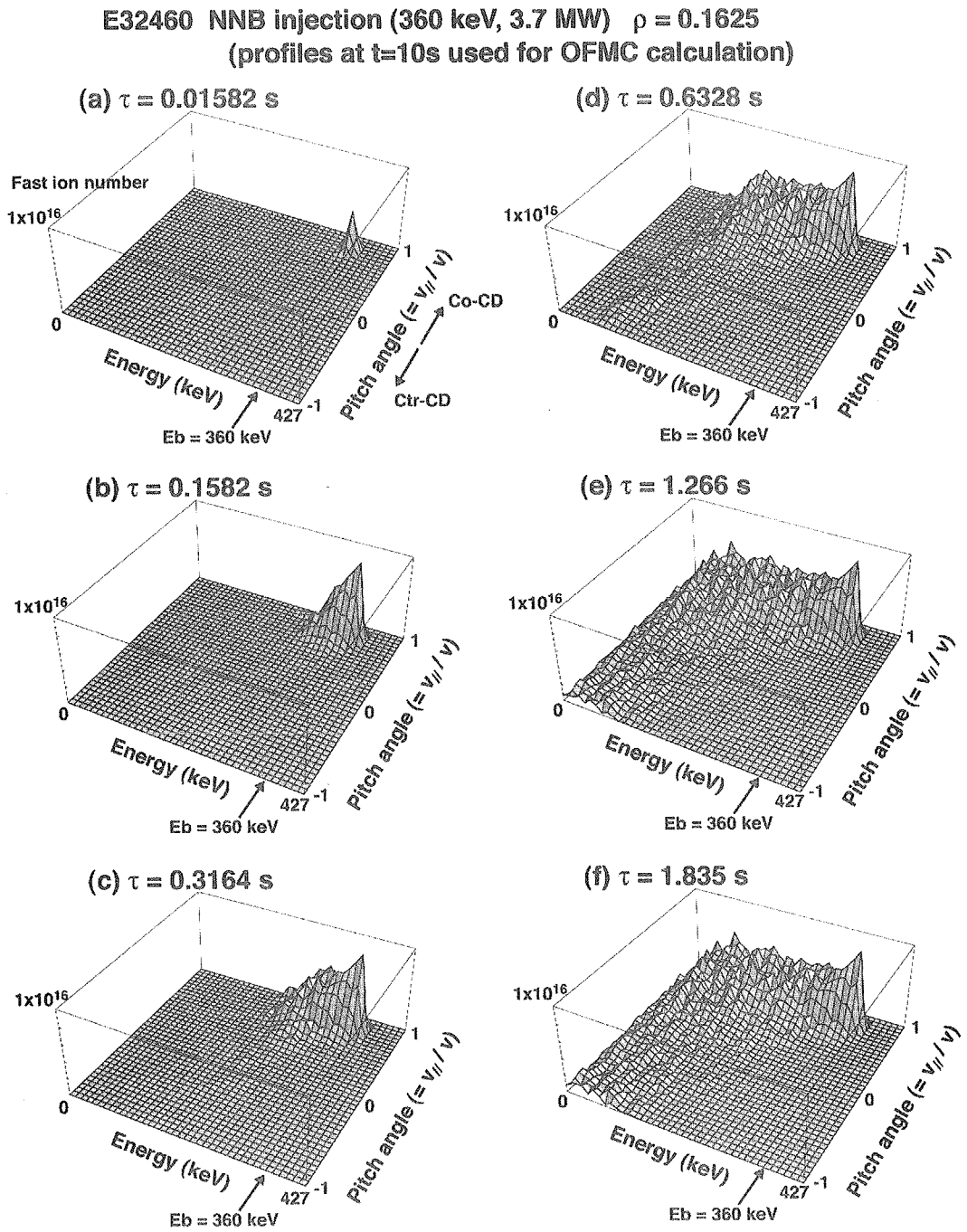

Figure 1.14: Time evolution of fast ion distribution in the energy and pitch angle ($\equiv v_{//}/v$) space for the N-NB injection (360 keV, 3.7 MW) in the pulse E32460. The pulse E32460 is discussed in section 4.1.

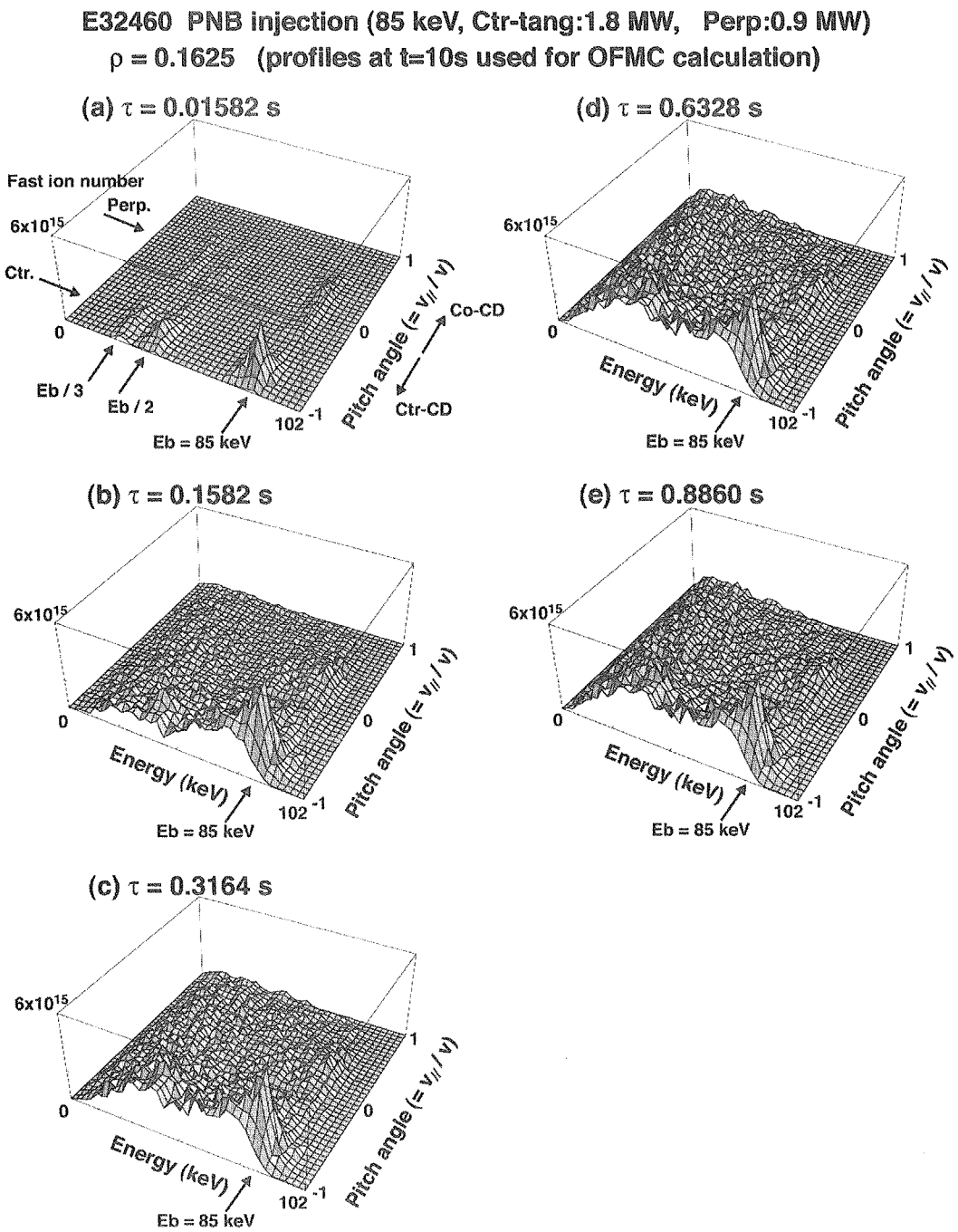

Figure 1.15: Time evolution of fast ion distribution in the energy and pitch angle ($\equiv v_{//}/v$) space for the P-NB injection (85 keV, ctr.-tang.: 1.8 MW, perp.: 0.9 MW) in the pulse E32460. The pulse E32460 is discussed in section 4.1.

pitch angle correspond to the co- and counter current drives, respectively. As shown in Fig. 1.14 (a), the N-NB fast ions are born at 360 keV and the pitch angle $\sim$ 0.78. Pitch angle scattering is small during slow down to $\sim$ 100 keV (Fig. 1.14 (a)-(d)). This is because collisions with electrons are dominant as mentioned in the previous section. Below $\sim$ 100 keV, pitch angle scattering occurs in a shorter time scale than at higher energies due to collisions with background ions. In the P-NB case, the initial profile has three peaks in the energy axis and two peaks in the pitch angle axis (Fig. 1.15 (a)). Three peaks in the energy axis correspond to the primary beam energy ($E_b = 85$ keV), the half energy ($E_b/2$) and the one third energy ($E_b/3$), because in the P-NB system D_2^+ and D_3^+ are produced in an ion source and become D_2 and D_3 in a neutralization cell. Two peaks at ~ -0.78 and 0.2 in the pitch angle axis correspond to the counter tangential P-NB (1.8MW) and perpendicular P-NB (0.9MW), respectively. As shown in the figure, pitch angle scattering proceeds in a time constant similar to that for slow down.

Figure 1.16 shows the one dimensional ($v_{//}$) fast ion distribution function for the N-NB injection. The distribution function is calculated by integrating the fast ion populations in Fig. 1.14 along the $v_\perp$ axis and dividing them by the shell volume. The profile extends to the negative $v_{//}$ side in the steady state ($\tau = 1.835$ s). For comparison, shown is the Maxwellian distribution function for the background thermal ions with $T_i = 2.7$ keV and $n_D = 5.5 \times 10^{18}$ m^{-3} at $\rho = 0.1625$. This is shifted to the negative $v_{//}$ side by the toroidal rotation velocity (-1×10^5 m/s), which is nearly equal to the parallel velocity. Here, the toroidal rotation velocity was measured for carbon ions as explained in section 2.1.1, and the rotation velocity of the bulk ions is assumed to be equal to that. Figure 1.16 shows the P-NB injection case.

To see the contribution of the fast ions at $v_{//}$ to the NB driven current density, the integrand of the NB fast ion current density $j_{\rm fast}$ (Eq. 1.1), $ef(v_{//})v_{//}$, is shown in Fig. 1.17 (a) and (b) for the N-NB and P-NB injections, respectively. The profile for the N-NB injection has a peak at higher $v_{//}$ than that for the P-NB injection. In the steady state, the fast ions at $v_{//}$ larger than 60 % of the initial parallel velocity (4.5×10^6 m/s) carry 80 % of the total $j_{//}$ at $\rho = 0.1625$. The total fast ion current densities $j_{\rm fast}$ at $\rho = 0.1625$ for the N-NB and P-NB injections evolve as shown in Fig. 1.18. For the N-NB injection, it takes 0.95 s for $j_{\rm fast}$ to build up to 95 % of the steady-state value ,while $j_{\rm fast}$ for the P-NB injection reaches 95 % at $\tau = 0.31$ s.

1.5 Neoclassical Transport Theory

1.5.1 Particle orbit in tokamak

In a uniform magnetic field a charged particle gyrates around a magnetic field line and the guiding center of the particle's orbit moves with constant velocity along the magnetic field. In a tokamak, the non-uniformity of the magnetic field leads to drifts of the guiding center. In the absence of collisions, these drifts give rise to two types of guiding center orbit.

Particles with a sufficiently large velocity parallel to the magnetic field circulate continually round the torus. These are called passing particles (or transit particles). The remaining particles are 'trapped'

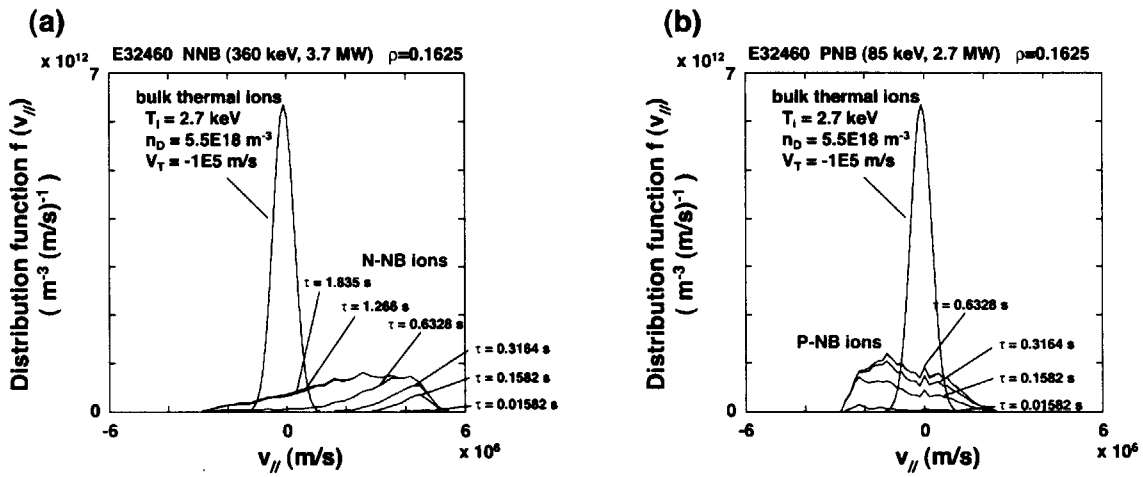

Figure 1.16: The one dimensional ($v_{//}$) fast ion distribution functions for the (a) N-NB and (b) P-NB injections in E32460. The Maxwellian distribution function for the background thermal ions with $T_{\rm i} = 2.7$ keV and $n_{\rm D} = 5.5 \times 10^{18}$ m^{-3} at $\rho = 0.1625$ is also shown.

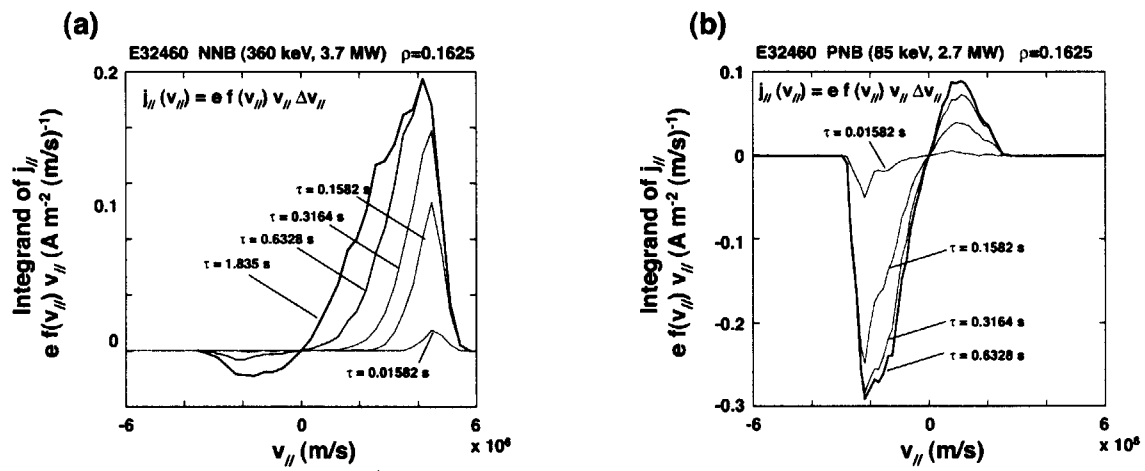

Figure 1.17: Profile evolution of the contribution to the NB fast ion current density, $ef(v_{//})v_{//}$, is shown for the (a) N-NB and (b) P-NB injections in E32460.

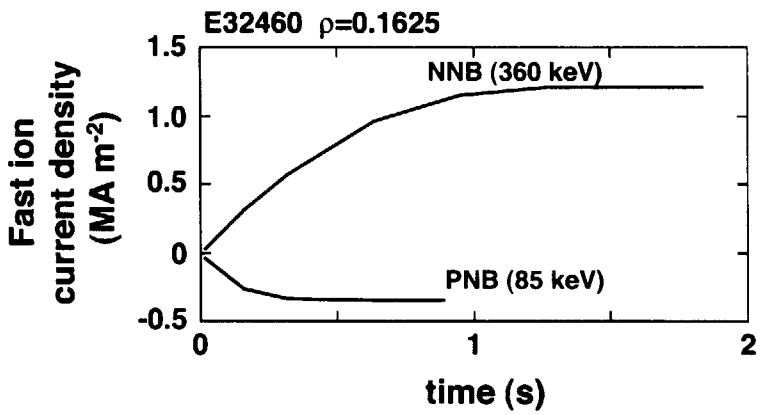

Figure 1.18: Time evolution of the NB fast ion current density at $\rho = 0.1625$ for the N-NB and P-NB injections in E32460.

particles, being trapped on the outer side of the torus by the magnetic mirrors formed as a result of the poloidal variation of the magnetic field as shown in Fig. 1.19 (a). Both types of orbit lie on toroidally symmetric drift surfaces. The poloidal cross-sections of such surfaces are illustrated in Fig. 1.19 (b) with the projections of particle orbits.

The drift surface on which the trapped particle orbit lies has the shape of a banana, as illustrated in Fig. 1.19 (b), and the orbits are called banana orbits. The half width, $\Delta_{\rm b}$, of the orbit for particles with a charge e_j and a mass m_jt is

$$\Delta_{\rm b} = \frac{v_{//0}}{\omega_{c\theta}} ,$$

where $v_{//0}$ is the initial parallel velocity of the trapped particle, and $\omega_{c\theta} = e_j B_\theta / m_j$. Thus, Δr is equal to the Larmor radius calculated for a particle of velocity $v_{//0}$ using the poloidal magnetic field B_θ.

1.5.2 Transport

In absence of collisions, the trapped particles execute banana orbits. When a small collisionality is allowed for, it is these trapped particles which dominate the transport. When the collisionality is sufficiently low that particles complete at least one bounce orbit before suffering a collision, the plasma is said to be in the banana regime. Collisions cause scattering out of the region of velocity space where particles are trapped.

The collisions which scatter the electrons out of their trapped orbits displace the particles across the flux surface by a distance $\sim \Delta_{\rm be}$ the electron banana width. This provides the step length for the diffusion process. Since $\Delta_{\rm be} \sim (q/\epsilon^{1/2})\rho_{\rm e}$, this step length is larger than the Larmor radius step length $\rho_{\rm e}$ associated with classical diffusion Using the banana width step length, diffusion coefficient is estimated to be

$$D \sim \frac{q^2}{\epsilon^{3/2}} \nu_{\rm e} \rho_{\rm e}^2 ,$$

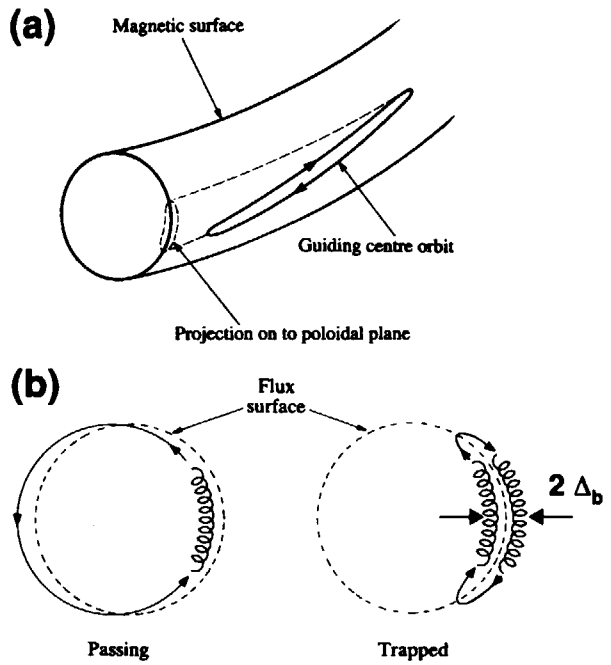

Figure 1.19: (a) Showing the banana orbit of a trapped particle with its projection onto a poloidal plane. (b) Diagram illustrating drift surfaces for the orbit of a passing particle and the (banana) orbit of a trapped particle.

where ν_e is the electron collision frequency and q is the safety factor (sec. 3.1.2). This exceeds the classical diffusion coefficient by the large factor $q^2/\epsilon^{3/2}$.

The electron and ion thermal diffusivities are

$$\begin{aligned} \chi_e &\sim D \sim \frac{q^2}{\epsilon^{3/2}}\nu_e\rho_e^2 \\ \chi_i &\sim \frac{q^2}{\epsilon^{3/2}}\nu_i\rho_i^2 = \left(\frac{m_i}{m_e}\right)^{1/2}\chi_e. \end{aligned}$$

The transport enhanced by the trapped particles is called neoclassical transport [22, 23]

1.5.3 Bootstrap current

The trapped particle in a tokamak has a larger radial excursion than that for the untrapped particle. This difference produces a distortion of the velocity distribution function in an inhomogeneous plasma. As illustrated in Fig. 1.20, radial inhomogeneity of both temperature and density produces a distortion of the trapped-electron part of the velocity distribution function since the trapped-electron population with $v_{//} < 0$ (comes from the inner high density and temperature region) is larger than with $v_{//} > 0$ (comes from the low density and temperature region). The asymmetry in the trapped-electron population from both side produces the parallel current. This trapped-electron current is fairly small. However, the collisional diffusion (mainly through pitch-angle scattering) across the trapped-untrapped boundary

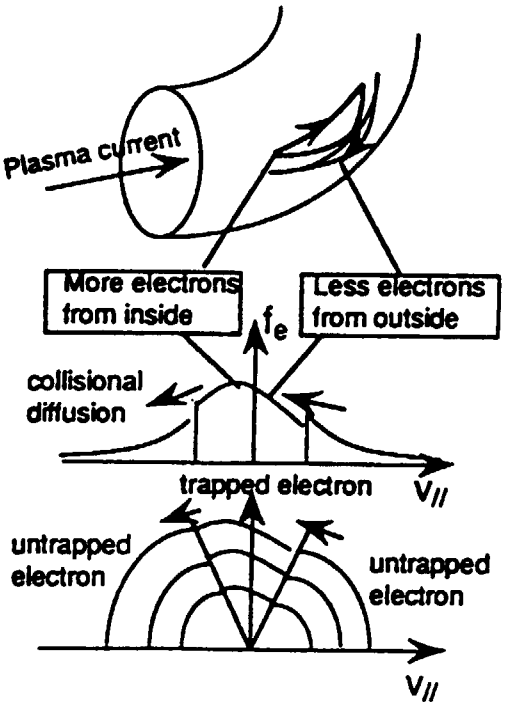

Figure 1.20: Trapped-electron orbits and schematics of the velocity distribution function in a collisionless tokamak plasma.

in the velocity space extends this asymmetry to the untrapped-electron region. The force supplied for this velocity-space diffusion is the $v_r \times B_\theta$ force on the trapped electron during the radial excursion. The parallel momentum transfer to the untrapped electron is associated with the net radial motion of the trapped particles. The ion velocity distribution function is also distorted similarly to that of the electron although the direction of the deformation is opposite to that for the electron. This deformation of the velocity distribution function produces a net parallel plasma current, the 'bootstrap current' [8].

1.5.4 Neoclassical conductivity

In a cylindrical plasma composed of electron and single ion species, the plasma conductivity along the magnetic field is given by its Spitzer value

$$\sigma_{//}^{\mathrm{SP}} = 1.96 \frac{3\epsilon_0^2 (2\pi T_e)^{3/2}}{m_e^{1/2} e^2 \ln \Lambda}.$$

For the plasma composed of several ion species, the conductivity is given by

$$\sigma_{//}^{\mathrm{classical}} = \sigma_{//}^{\mathrm{SP}} / Z_{\mathrm{eff}}.$$

In a tokamak, however, the trapped electrons are unable to move freely along the magnetic field in response to an applied electric field. The current is thus reduced by the presence of trapped particles. An

analytic expression for the electrical conductivity in a tokamak is given by [8, 24]

$$\sigma_{//}^{\mathrm{NC}} = \sigma_{//}^{\mathrm{classical}} \left(1 - \frac{f_{\mathrm{t}}}{1+\xi\nu_{\mathrm{e}}^{*}}\right)\left(1 - C_{\mathrm{R}}(Z_{\mathrm{eff}})\frac{f_{\mathrm{t}}}{1+\xi\nu_{\mathrm{e}}^{*}}\right),$$

where f_{t}, ν_{e}^{*}, C_{R} and ξ are the trapped-particle fraction, electron-collisionality and functions of Z_{eff}, respectively. The physical meaning is rather simple, namely that, in a collisionless limit $\nu_{\mathrm{e}}^{*} \to 0$, only the untrapped electron can contribute to the electrical conductivity.

1.6 Plasma Confinement Modes

Experimental observation indicates that transport in tokamak does not obey the predictions of neoclassical transport theory. The energy confinement is found to be much shorter than the neoclassical value. The underlying cause is not understood well, and so a specific state of confinement and transport, which is obtained experimentally, are referred as a "confinement mode". The confinement behavior can be conveniently put into four categories. The first covers ohmically heated plasmas and the other three relate to plasmas with additional heating. The two basic modes of additionally heated plasma are the so-called L (for low) and H (for high) confinement regimes. The third category covers a variety of plasmas for which operational procedures producing enhanced confinement have been found. The ohmic heating contributes to initial heating of plasmas. However, the ohmic heating decreases with plasma temperature, and it is limited to low temperature ($T_{\mathrm{e}} \sim 2$ keV) because plasma resistivity is proportional to $T_{\mathrm{e}}^{-3/2}$. Thus, the additional heating such as neutral beams or RF waves are necessary to increase plasma temperature. However, the initial result of auxiliary heating experiments was that the confinement degraded as heating power was increased (L-mode : Low confinement mode). In 1982, the improved confinement, the H-mode (High confinement mode), was discovered on the ADEX tokamak[25]. When sufficient power was applied, the plasma made an abrupt transition to the state with the improved confinement, which was attributed to the reduction of transport in the edge region. Other improved confinement regimes have been discovered such as IOC (Improved Ohmic Confinement) [26], high β_{p} mode [27, 28, 29, 30], VH-mode [31], RS (Reversed shear) mode [32, 33, 34, 35] and their hybrid. These modes are produced by the operational procedure and their characteristic parameters. The internal transport barrier (ITB) was first found in high β_{p} mode in JT-60U [27]. Similarly to the H-mode, the steep gradient in the temperature and density are formed in plasmas. The high β_{p} mode and RS mode have the ITB structure. The hybrid operations of the ITB and H modes, the high β_{p} H-mode and the H-mode edge RS mode, are employed in research of the steady state high performance discharge in JT-60U.

1.7 Instabilities in Tokamak Plasmas

1.7.1 Neoclassical tearing mode

When MHD (Magnetohydrodynamic) instabilities occur in a plasma, they usually bring about a change in the magnetic topology. This occurs at resonant surfaces which have rational values of $q = m/n$ (the safety factor in sec. 3.1.2, m and n are integers). At these surfaces, the magnetic field lines break

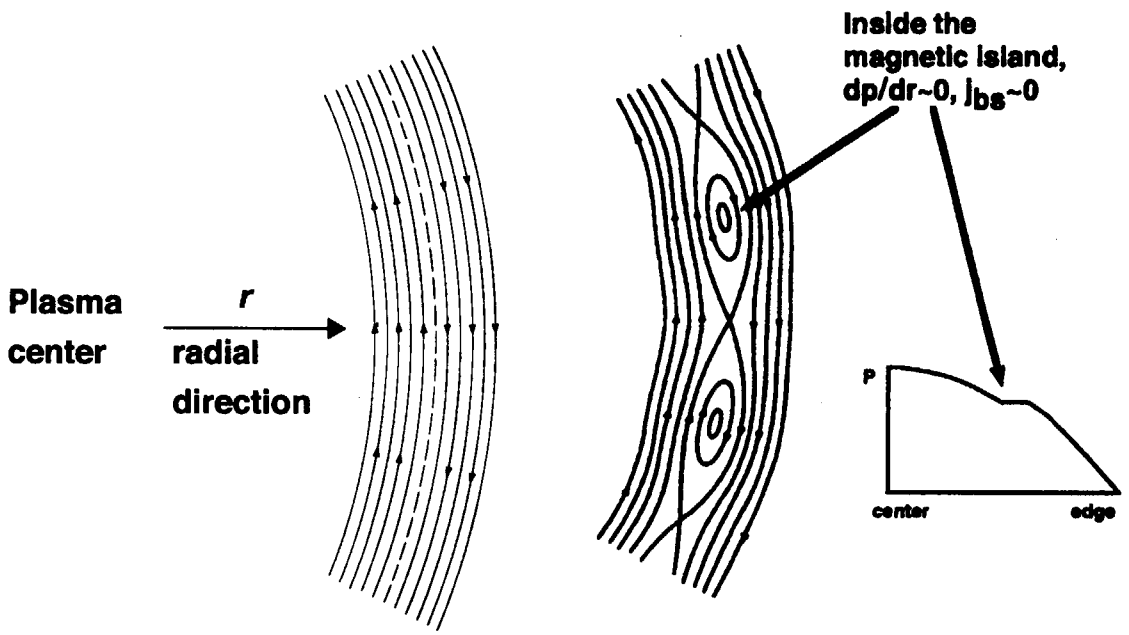

Figure 1.21: Reconnection of magnetic field producing magnetic islands. The bootstrap current density becomes nearly zero inside magnetic islands because the pressure profile is flattened inside islands.

and reconnect to form magnetic islands as illustrated in Fig. 1.21. The formation of magnetic islands is generally associated with resistive instabilities and particularly tearing modes.

Here, considering the equilibrium configuration around a resonant surface, s, having $q = q_s = m/n$, the magnetic field lines on this surface define a helix. A perturbation resonant with this surface has the form $\exp im\chi$ where

$$\chi = \theta - \frac{n}{m}\phi \quad (\theta, \phi : \text{poloidal and toroidal angles})$$

is an angular coordinate orthogonal to the helix. The equilibrium field in this orthogonal direction is

$$B_* = B_\theta \left(1 - \frac{n}{m} q(r)\right)$$

and close to the magnetic surface this may be written

$$B_* = -\left(B_\theta \frac{q'}{q}\right)_s z \tag{1.5}$$

where $z = r - r_s$.

The geometry of the change in the magnetic topology arising from the resonant perturbation is illustrated in Fig. 1.22. It can be calculated by determining the trajectory of a magnetic field line from the equation

$$\frac{\mathrm{d}r}{r_s \mathrm{d}\chi} = \frac{B_r}{B_*}. \tag{1.6}$$

The radial field perturbation may be taken to have the form

$$B_r = \hat{B}_r(r) \sin m\chi \tag{1.7}$$

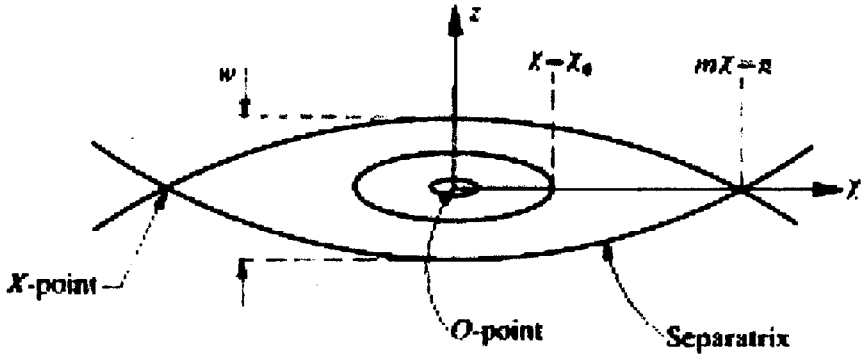

Figure 1.22: Geometry of magnetic field lines of a magnetic island in the (z, χ) plane.

so that, substituting eqns (1.5) and (1.7) into Eq. (1.6), the differential equation for the field line is

$$-\left(B_\theta \frac{q'}{q}\right)_s z\,\mathrm{d}r = r_s \hat{B}_r \sin m\chi\,\mathrm{d}\chi. \tag{1.8}$$

Taking $\hat{B}_r$ to be essentially constant over the radial extent of the island, integration of Eq. (1.8) gives the equation of the field line

$$z^2 = \frac{w^2}{8}(\cos m\chi - \cos m\chi_0)$$

where

$$w = 4\left(\frac{rq\hat{B}_r}{mq'B_\theta}\right)_s^{1/2} \tag{1.9}$$

is the width of the magnetic island and χ_0 is the value of χ for which the field line under consideration has $z = 0$.

The magnetic field lines within the magnetic island lie on a set of helical magnetic surfaces with their own magnetic axis. This is labelled the *O*-point in Fig. 1.22. The island is bounded by the separatrix, the two parts of which meet at the *X*-points. The distance between the *X*-points is one full wavelength.

The tearing instability in a tokamak is driven by the radial gradient of the equilibrium toroidal current density. The name derives from the tearing and rejoining of magnetic field lines which occur during the instability as a consequence of finite resistivity. In tokamak plasmas tearing modes take the form of magnetic islands. The growth of the magnetic island is governed by the equation

$$\tau_R \frac{\mathrm{d}}{\mathrm{d}t}\frac{w}{r_s} = \Delta'(w) r_s, \tag{1.10}$$

where $\tau_R = \mu_0 r_s^2 \sigma_{NC}/1.22$ is the magnetic diffusion time, and the discontinuity, Δ', in Ψ'/Ψ across $r = r_s$ is defined by

$$\Delta' \equiv \left.\frac{\Psi'}{\Psi}\right|_{r=r_s-\epsilon}^{r=r_s+\epsilon} \quad (\epsilon \to 0).$$

The tearing instability described above is based on the resistive MHD model which assumes a sufficiently large collision frequency. In the recent experiments, due to improvement of the plasma performance, a mean free path of electron becomes longer and the plasma goes into the collisionless regime. Therefore, the resistive MHD equation set has been extended to be applicable to the banana regime in the neoclassical transport theory [36]. In this 'neoclassical' MHD equation, the bootstrap current has the most important effect.

When the magnetic islands grow, the plasma pressure profile is flattened inside the islands, and hence, the bootstrap current, which is driven by the pressure gradient, disappears inside the islands. The difference in current density between inside and outside islands destabilizes the tearing mode and widens the magnetic island width. Thus, neoclassical tearing modes (NTMs) are induced by lack of the bootstrap current inside the magnetic island (Fig. 1.21). Time evolution of the magnetic island width is governed by the modified Rutherford equation [37, 38, 39, 40] which is extended from the equation for the 'classical' tearing mode (1.10).

1.8 Motional Stark Effect Spectroscopy

An injected beam of neutral hydrogen or deuterium atoms with velocity $\boldsymbol{v}$ experiences the Lorentz electric field $\boldsymbol{E}_{\mathrm{L}} = \boldsymbol{v} \times \boldsymbol{B}$ in its own frame. This electric field gives rise to Stark splitting of emission lines. Since hydrogen and its isotopes exhibit a linear, and thus very strong Stark effect, the line spectrum of hydrogen is dominated by the motional Stark effect. The H_α or D_α line is split into π and σ components which are polarized in the parallel and perpendicular directions to the electric field, respectively. With knowledge of the beam velocity $\boldsymbol{v}$, a measurement of polarization direction gives information about the local magnetic field in the plasma. The MSE (Motional Stark Effect) spectroscopy is based on this principle [41].

Before the MSE spectroscopy was established, plasma equilibria were reconstructed from only external magnetic measurements, i.e., magnetic flux loops and magnetic field pick-up coils. However, the reconstructed internal profiles of the current density, safety factor, pressure and poloidal flux does not have enough accuracy. The MSE diagnostic has enabled accurate measurements of the plasma current density profile and the one-turn loop voltage profile, which are essential for current drive study, as discussed in 3.2. The MSE diagnostic used in the JT-60U [42] tokamak is described in 2.2. Methods of plasma equilibrium reconstruction and the one-turn loop voltage profile analysis are described in 3.1 and 3.2, respectively.

1.9 Objective of This Thesis

The non-inductive current drive is required for the steady state operation of tokamak reactor. High energy neutral beam is a principal method of heating and current drive in the future tokamak reactors such as ITER. Neutral beam designs for the future reactors, such as beam energy, injection power and geometry (injection angle), are based on theory of the NB heating and current drive, which predicts

improvement of the NB current drive capability with increasing beam energy and electron temperature. Therefore, the NB current drive should be experimentally investigated in the regime closer to the ITER condition which has a beam energy of 1 MeV and electron temperature of 20 - 30 keV.

The non-inductive current drive methods have been studied both experimentally and theoretically over twenty years, since the idea of NB current drive was suggested in 1970 [5] and the RF current drive was proposed in 1978 [6]. However, the experimental study was discussed based only on the behaviors of macroscopic parameters such as the internal inductance or the loop voltage at the plasma surface because a reliable current profile reconstruction was difficult due to the lack of measurement of the internal magnetic field. It is only in the steady state (i.e., when a spatially uniform loop voltage profile is realized) that the non-inductively driven current can be evaluated from the surface loop voltage. Therefore, although the NB current drive was demonstrated in a small size device at low temperature [9], even the total NB driven current, which could be evaluated from assumption of a spatially uniform loop voltage profile, was not so accurate in large devices at relatively high electron temperature because a current diffusion time was longer than the pulse duration. It should be noted that without knowledge on the current density profile the non-inductive current density profile can not be determined even when the steady state is reached. The internal inductance is not more than a measure of peakedness of the current density profile. Even when a simulation code is employed with the measured macroscopic measurements and its calculation reconstructs a time evolution of the measured internal inductance, it is not straightforward to determine the radial profile of the non-inductively driven current density and conclude the validity of the NB current drive theory because different current profiles with the same value of the internal inductance can exist.

The world's first N-NB with the designed values of 500 keV and 10 MW was installed in JT-60U to study high energy neutral beam current drive. The MSE spectroscopy was also introduced to measure the internal magnetic field, which enables not only the accurate equilibrium reconstruction including the current density profile but also separation of the inductive and non-inductive components of the current density profile using the analysis method described in Sec. 3.2. In this thesis, a comprehensive experimental study of N-NB current drive is given. The current drive characteristics of N-NB such as the driven current density profile and dependence on plasma and beam parameters (electron temperature and beam energy) are measured over a wide range of plasma parameters, and the NB current drive theory should examined. Simultaneous achievements of a high current drive capability of N-NB, high plasma pressure and high confinement should be demonstrated. In addition to these fundamentals of the NB current drive, the influence of MHD instabilities on the NB current drive is important issue because such theory has not been established and there has been reported only an experimental result on a low energy NB (P-NB) during tearing instability. Two MHD instabilities are investigated in this thesis. One is a beam driven instability which appears intermittently in a burst-like behavior, and the other is the neoclassical tearing mode. Study on a beam driven instability contributes to the understanding of influence of the fast ion induced instabilities which will be driven by alpha particles (3.5 MeV He^4) produced through the D-T fusion reaction in the burning plasma such as in ITER. The neoclassical tearing mode appears in long-sustained high beta plasmas, and so it is one of principal instabilities to be considered in ITER.

2. Experimental Devices

An overview of the JT-60U tokamak and the MSE spectroscopy are presented in this chapter.

2.1 JT-60U

2.1.1 JT-60U device

A perspective view of JT-60U is illustrated in Fig. 2.1. JT-60U [43, 44] is one of the world's three large tokamaks, together with JET of EU and TFTR of the U.S. Experimental research using large size high temperature plasmas has been conducted since 1985. JT-60U is a noncircular tokamak device with a vacuum vessel of 3.4 m in major radius and 1.1 m (horizontal) / 1.4 m (vertical) in minor radius. Maximum plasma volume is 100 m^3. Toroidal magnetic field can be produced up to 4.2 T by 18 toroidal coils. Maximum plasma current is 3 MA in the present W-shaped divertor structure. Carbon tiles are used as the first wall. Deuterium or hydrogen is used as a fuel gas. Pulse duration of discharge is 15 seconds, and the flattop time length of the plasma current is typically 10 seconds.

Plasma current is initiated, increased and terminated by the ohmic coil called F coil [45]. Horizontal position of plasma is controlled by the vertical magnetic field produced by VR coil. Vertical position is controlled by the horizontal magnetic field produced by H coil. D coil controls the X-point height in the divertor configuration (Sec. 1.2). The triangularity of the plasma cross-section shape can be varied up to 0.6 at plasma current of 1 MA by VT coil. These poloidal magnetic field coils (F, VR, H, D and VT coils) are wound around the torus. Their locations in the poloidal cross section are shown in Fig. 2.2.

Waveforms of plasma current, position and shape are preprogrammed as a discharge operation condition [46, 47]. Toroidal magnetic field is also chosen as a operation condition. Plasma shape and position are detected in real-time and controlled according to the preprogrammed waveforms by feedback control of poloidal coil currents. Real-time feedback controls [48] of plasma parameters such as the line averaged density, neutron emission rate [49], plasma stored energy [50] and electron temperature [51] are available by using actuators such as gas-puff and neutral beam injection.

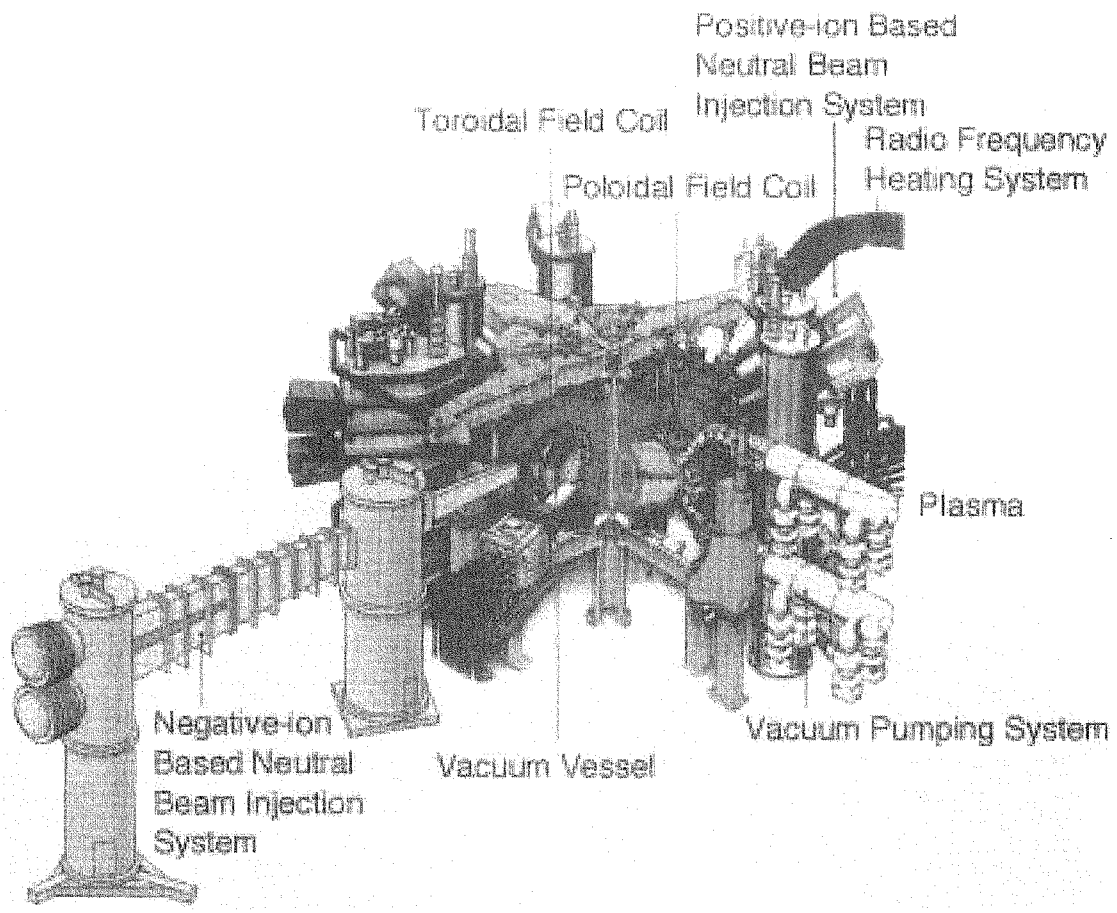

Figure 2.1: A perspective view of JT-60U.

2.1.2 Diagnostic system

The diagnostic system of JT-60U are composed of (1) devices for machine protection and operation, and (2) devices for plasma parameter measurements for improvement of plasma performance and physical understanding.

Diagnostics for machine protection and operation

Fundamental measurements for machine protection and plasma operation are the total plasma current and the shape and position of plasma. The plasma current is measured in real-time by rogowski coils wound around the poloidal cross section and controlled to trace the preprogrammed waveform by adjusting the applied one-turn loop voltage using F coil. Using the poloidal coil currents and the signals of magnetic pick-up coils and flux loops installed around the wall, plasma boundary is detected in real-time and controlled using the poloidal coils. When the difference between the measured signal and the preprogrammed value exceeds a certain threshold, the plasma control system judges that the plasma is out of control due to some causes such as disruption and jumps to the "soft-landing" procedure (decreasing the plasma current by applying negative loop voltage). Diamagnetic flux measurement (toroidal flux change

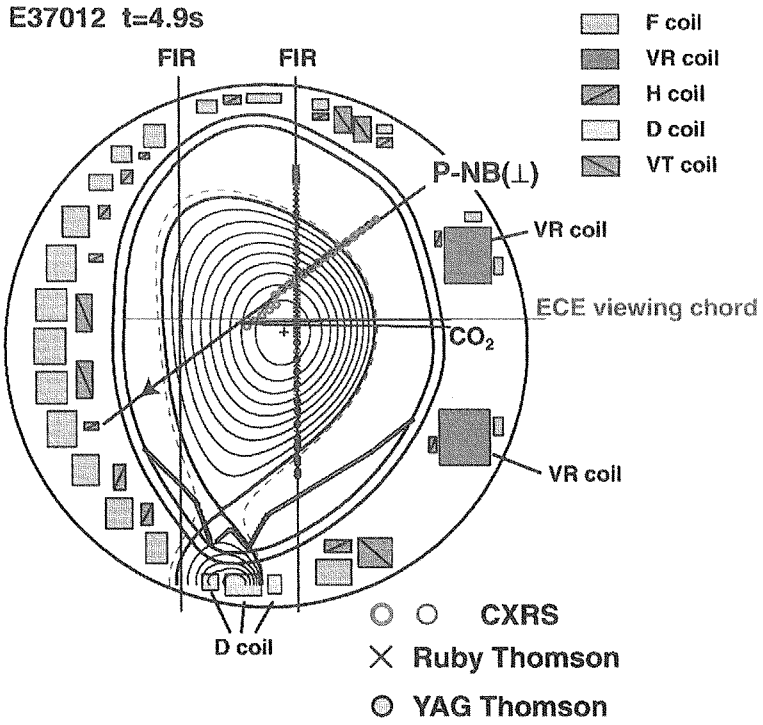

Figure 2.2: Poloidal coils (F, VR, H, D and VT) and principal diagnostics are shown in the poloidal cross section. Spatial points of two CXRS systems, Ruby and YAG thomson scattering are shown. Viewing chords of FIR interferometer, CO_2 interferometer and the ECE diagnostic are also shown.

due to the poloidal current flowing in plasma) enables a real-time detection of the plasma stored energy, which is used for the real-time control of the stored energy using NB as an actuator [50].

The emission rate of the 2.45 MeV neutron produced by the D-D fusion reaction is measured with ^{235}U and ^{238}U fission chambers installed outside the vacuum vessel. The neutron yield value and the integrated amounts for a discharge, a day, a week and three months are monitored. If any of them exceeds the upper limit approved by the government, the plasma control system immediately stops the additional heating (NB and RF) and shifts to the soft-landing procedure. The real-time signal of the neutron yield is used also for the real-time control using NB as an actuator.

Penning gauge monitors the neutral particle pressure and can detects air leak of the vacuum vessel. It also helps to optimize the filling pressure of fueling gas at the plasma initiation. The visible TV system enables a visible check inside vacuum vessel. Rarely, carbon tiles (the first wall) are broken during discharge, and their broken pieces enter plasma. Carbon spectral lines emitted from them are found through the visible TV. The infrared TV views the divertor plate where the heat and particle exhausted from the main plasma are concentrated. Although the carbon fiber composite (CFC) material with high thermal conductivity and high thermal shock resistance are used for divertor tiles, its limitation is possible to be exceeded during long-pulse discharges with high heating power.

Plasma parameter measurements for physics study

The radial profile measurements of plasma parameters such as temperatures, density, plasma current density have been continuously improved because the understanding of the internal structure of plasmas leads to advance in plasma physics and improvement of plasma performance such as confinement and plasma beta. Principal diagnostics [52] are shown in Fig. 2.2.

Thomson scattering is a standard tool in fusion plasma research for measuring simultaneously the electron temperature and electron density at the same spatial points. In JT-60U, two Thomson scattering systems using the ruby laser and YAG laser are in operation. The ruby laser Thomson scattering system [53] has two lasers and measures 60 spatial points. Each laser operates at 0.25 Hz. The YAG laser Thomson scattering system [54] has 15 spatial points and operates at 50 Hz. Fine spatial resolution of the ruby laser system has contributed to understanding of the edge pedestal structure in temperature and density characterizing H mode. Fine time resolution of the YAG laser system revealed the formation and evolution of the transport barrier structure in electron system [32, 55].

The electron temperature is measured also by ECE (Electron Cyclotron Emission) diagnostic. There are three diagnostic systems for ECE measurement, a Fourier transform spectroscopy (FTS) [56], a grating polychromater spectrometer (GPS) [57, 58] and a heterodyne radiometer spectroscopy (HRS) [59]. In the FTS system, a frequency spectrum of the ECE signal (proportional to electron temperature) is obtained using a Fourier transform technique. As the ECE frequency depends on the local magnetic field and the principal magnetic field B_{T} has $1/R$ dependence in toroidal systems, a frequency spectrum of the ECE signal is equal to a spatial profile (in R direction). The FTS system has a time resolution of 25 ms and a frequency resolution of 3.66 GHz corresponding to a spatial resolution of 5.6 cm at $B_{\mathrm{T}} = 4$ T. In the GPS system, input ECE signal is frequency-resolved by using the cross Czerny-Turner spectrometer. The time and frequency resolutions are 20 μs and 1.3 GHz (2 cm at $B_{\mathrm{T}} = 4$ T), respectively. Profiles of electron temperature and its fluctuation are measured by the GPS system. Its advantage is that the measurement range can be arbitrarily changed. The HRS system has a time resolution of 20 μs and a fine frequency resolution of 0.5-1 GHz corresponding to 1-2 cm at B_{T}=4 T. The HRS system is used especially for the measurement of structure of MHD instability such as the neoclassical tearing mode. The viewing chord of the ECE measurement is 0.2 m above the midplane of the vacuum vessel as shown in Fig. 2.2.

The CO_2 laser interferometer and FIR (Far Infrared) laser interferometer measure the line integrated electron density. The CO_2 laser interferometer views the plasma tangentially, while two FIR viewing chords are vertical (Fig. 2.2). The real-time control of the plasma density is based on the CO_2 and FIR laser interferometer measurements with an actuator of gas-puff.

The ion temperature and plasma rotation velocity are measured by a charge exchange recombination spectroscopy (CXRS) [60] based on CXR spectra of fully stripped carbon ions CVI (n=8-7) induced by neutral beam injection, $\mathrm{D}^0 + \mathrm{C}^{6+} \rightarrow \mathrm{D}^+ + \mathrm{C}^{5+}(\mathrm{n} = 8)^* \rightarrow \mathrm{D}^+ + \mathrm{C}^{5+}(\mathrm{n} = 7)$. There are two CXRS systems. One views toroidally (tangentially) and measure 23 points profile of the ion temperature and

toroidal rotation velocity. Other system views poloidally and provides fine profiles (36 points in maximum). The toroidal and poloidal systems are used for the core and edge measurements, respectively. Transport barrier structure was discovered by the toroidal CXRS system [27]. The poloidal CXR system can measure a fine structure of edge pedestal structure in H mode plasma. The CXRS measurement also gives the carbon density profile, which is used to determine the $Z_{\rm eff}$ profile.

The $Z_{\rm eff}$ profile is determined also from the bremsstrahlung measurement using electron temperature and density. Measurement of spectral lines of impurity species contributes to a study of impurity transport and determination of $Z_{\rm eff}$. Radiation profiles are measured by a soft X-ray pulse height analyzer, a hard X-ray pulse height analyzer and a bolometer system.

The motional Stark effect (MSE) spectroscopy [61, 62] gives information on the local magnetic field, which drastically improves equilibrium reconstruction. The MSE spectroscopy is described in detail in Sec. 2.2.

2.1.3 Heating and current drive systems

The neutral beam (NB) and radio-frequency (RF) injection systems are installed in JT-60U for heating and current drive. There are two different NB systems, i.e., the positive ion-based neutral beam (P-NB) and the negative ion-based NB (N-NB). Three kinds of RF systems, ECRF (Electron Cyclotron Range of Frequency), LHRF (Lower Hybrid Range of Frequency) and ICRF (Ion Cyclotron Range of Frequency), are available.

The P-NB system [63] consists of upper perpendicular NBs for on-axis heating, lower perpendicular NBs for off-axis heating, co- and counter-tangential NBs for heating and current drive, where 'co-' means the same toroidal direction as the plasma current flows and 'counter-' is opposite to the plasma current direction. The total P-NB power is $\sim$ 25 MW with 2-2.5 MW per unit at the beam energy of 80-90 keV. The N-NB [64] with design values of 10 MW at 500 keV has been developed for central heating and current drive. Normally, it is operated at 360-400 keV and 2-6 MW. Neutral beams are installed in JT-60U as illustrated in Fig. 2.3. Figure 2.4 shows the sideview of the N-NB beamline. The NB trajectories are projected on the poloidal cross-section (Fig. 2.5).

The LHRF system [65] has 2 multijunction launchers at 1.74-2.23 GHz with $N_{||}^{\rm peak} = 1.3 - 2.3$ and injection power of $\sim$ 3.5 MW. The 112 MHz ICRF system [66] for second harmonic hydrogen minority heating consists of 2 antennas and has the function of the real-time impedance matching by frequency feedback control. The 110 GHz ECRF system [67, 68, 69] is composed of four 1 MW-level gyrotrons. The launching system has one focusing mirror and one steering mirror, which enables control of the power deposition profile.

These heating and current drive systems have greatly contributed to the achievements of high performance plasmas and physics studies. Especially, NB system with many kind of heating, current drive and momentum deposition profiles enables the profile control study.

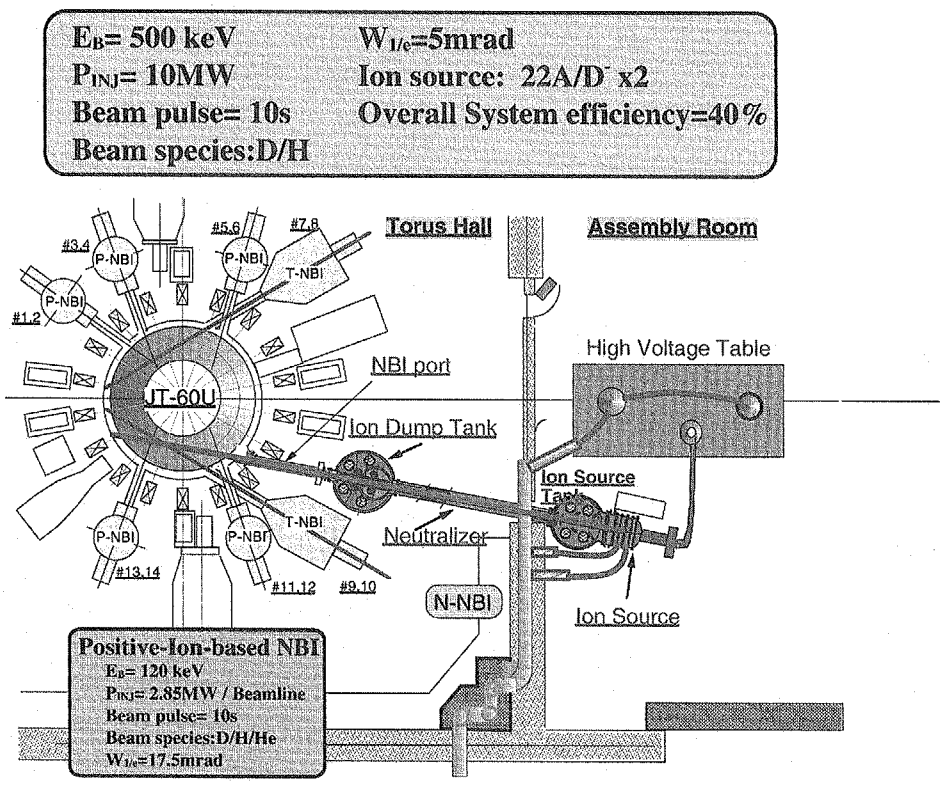

Figure 2.3: Topview of JT-60U. P-NB and N-NB are shown.

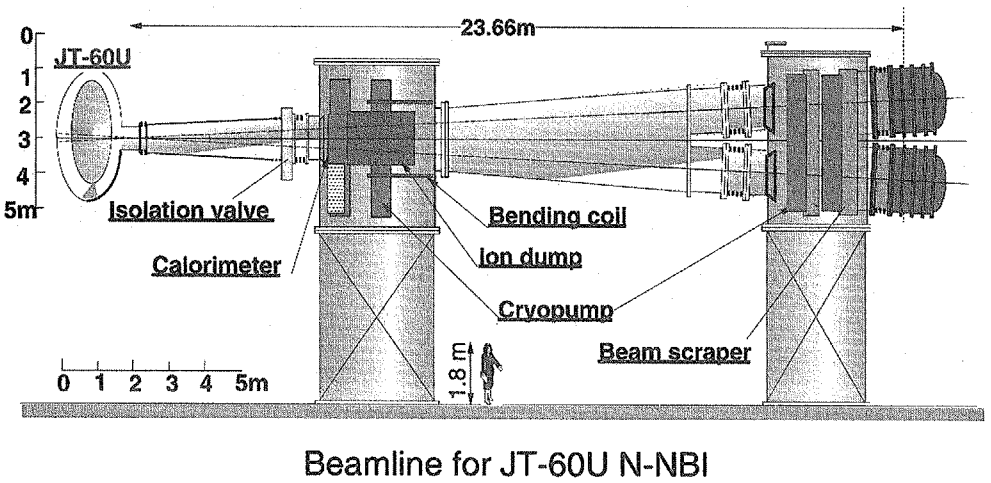

Figure 2.4: Sideview of the beamline for N-NB.

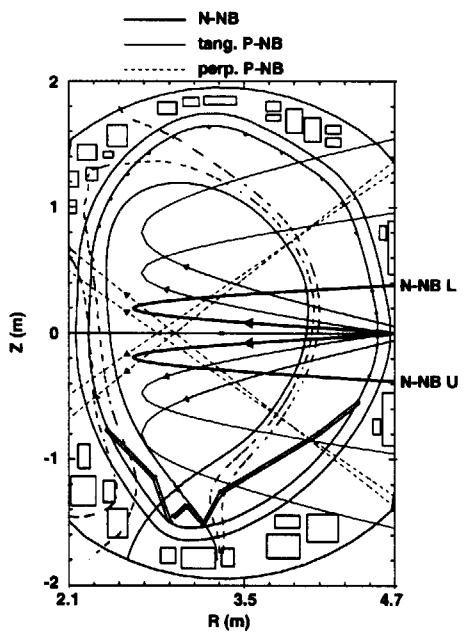

Figure 2.5: NB trajectories projected on the poloidal cross section.

2.2 Motional Stark Effect Spectroscopy

2.2.1 Principle of diagnostics

The motional Stark effect (MSE) spectroscopy is based on principle of the Stark effect [41]. An injected beam of neutral hydrogen or deuterium atoms with velocity $\boldsymbol{v}$ experiences the Lorentz electric field $\boldsymbol{E}_{\mathrm{L}} = \boldsymbol{v} \times \boldsymbol{B}$ in its own frame. This electric field gives rise to Stark splitting of emission lines. Since hydrogen and its isotopes exhibit a linear, and thus very strong Stark effect, the line spectrum of hydrogen is dominated by the motional Stark effect. The H_α or D_α line emitted by beam atoms is split into π and σ components which are polarized in the parallel and perpendicular directions to the electric field, respectively, as schematically shown in Fig. 2.6. The MSE spectroscopy measures the direction of polarization, i.e., the direction of the Lorentz electric field $\boldsymbol{E}_{\mathrm{L}}$. Thus, the direction of the local magnetic field can be determined with knowledge of the beam velocity $\boldsymbol{v}$.

As the velocities of beam neutral atoms are normally far greater than the thermal velocity of the bulk ions, the polarized D_α lines are separated from the background D_α line due to the Doppler shift. This is important for measurement of the polarized light because polarized background light is possible to be generated from unpolarized light due to the reflectivity characteristics of the mirror in the diagnostic system.

2.2.2 Diagnostic system

First MSE measurement was conducted in the PBX-M tokamak [41]. Afterwards, the MSE spectroscopy was introduced in the middle to large scale tokamak such as DIII-D [70, 71], TFTR [72], JT-60U [61] and JET [73, 74]. In JT-60U, after investigating possibility of the MSE measurement by

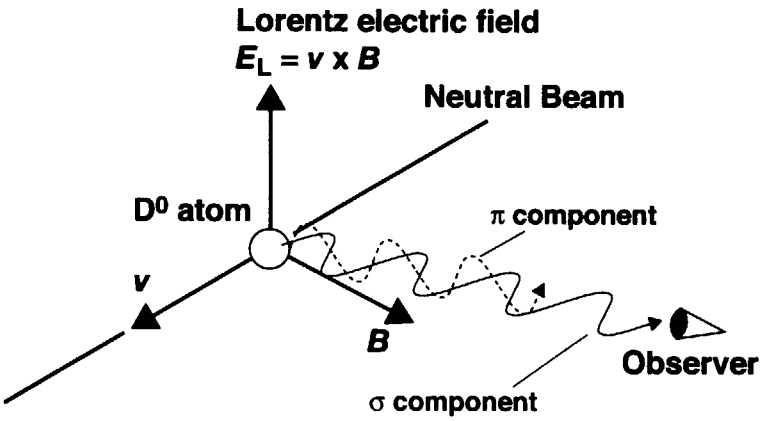

Figure 2.6: Principle of the motional Stark effect (MSE) spectroscopy. The D_α line emitted by deuterium neutral beam atoms is split into π and σ components.

one spatial point system, a multi-point MSE system became operational in 1994. A schematic view of the JT-60U tokamak and the present MSE polarimeters is shown in Fig. 2.7. Three MSE systems, called P17, P13 and P3 systems, named after the installed ports on the vacuum vessel, are used. The P13 system was a first MSE system installed in JT-60U. While only the P13 system worked, it had five spatial points (presently, 4 points) covering the central region of plasma, and hence gave the current density profile in the plasma core. In 1996, the P17 system, which had 15 spatial points and covered the whole plasma region, was installed to determine the current density profile accurately in wider region. The P17 system was upgraded to 17 spatial points measurement in 2000. The P3 system became operational in 2000. This system is motivated principally for measurement of the radial electric field profile. The radial electric field originated from the electrostatic potential in plasmas can be reconstructed by using two MSE systems having different geometries [62]. This is described in the next section. In addition to more accuracy due to the increased number of total spatial points, another important merit of introducing the P3 system is an application to the NB current drive experiment because the P3 system views the opposite directional tangential NB to P17 and P13 systems. The polarimeters of the P17 and P13 systems observe the σ component of the D_α or H_α line from one of the injected NBs (#7B) through a double fused-silica vacuum window. The P3 system observe the σ component from one of the co-tangential NBs (#9B). The diameter of the neutral beam is about 38 cm. The image on the beamline is typically 6 cm wide and 8 cm high. Figure 2.8 shows observation points for each MSE system, beam paths of #7B and #9B and a typical plasma equilibrium in the poloidal cross section. The P17 polarimeter has 17 viewing points which cover the range R = 3.276-4.374 m. The P13 and P3 systems have 4 and 9 viewing points, respectively, which cover R=3.123-3.429 m and R=3.310-4.090 m. For the equilibrium configuration shown in Fig. 2.8, the measurement covers the region from r/a=0.1 to the plasma surface. The radial extent of the measurement volume is determined by the beam diameter, the image size and the geometry. The P17

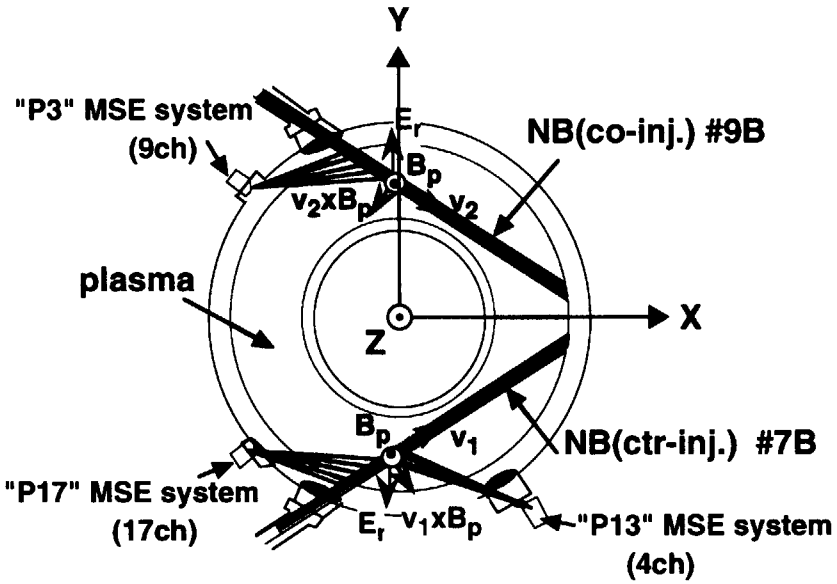

Figure 2.7: Three MSE systems, "P17", "P13" and "P3", are illustrated as viewed from the top of JT-60U. "P17", "P13" and "P3" systems are named after the ports of the vacuum vessel on which each system is installed, and have 17, 4 and 9 spatial channels, respectively.

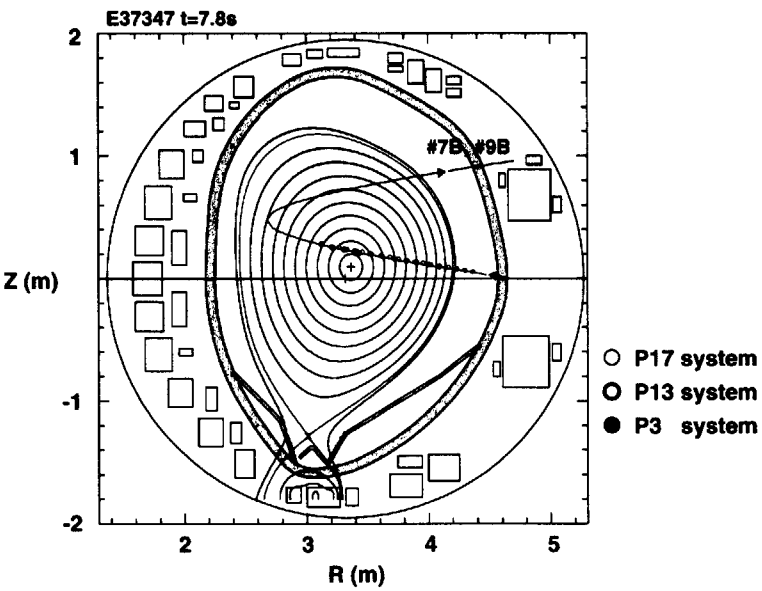

Figure 2.8: The MSE observation points (red circles for P17, green for P13, and blue for P3) are shown in the poloidal cross-section, with a typical plasma equilibrium.

system, whose lines of sight are nearly tangential, has the best spatial resolution of ΔR =6 to 10 cm.

Figure 2.9 shows the spectrum around the D_α line observed by the P13 system when a 94 keV

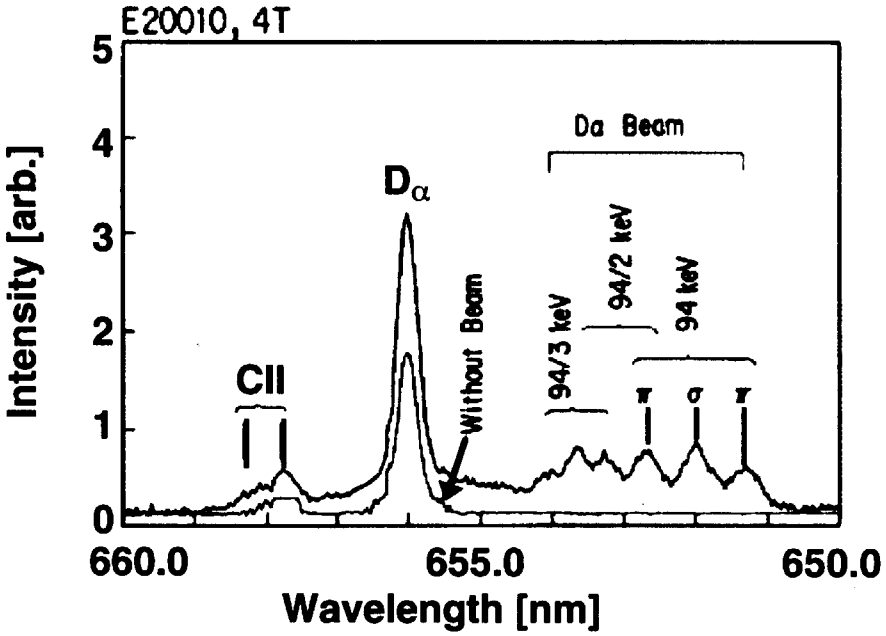

Figure 2.9: The spectrum around the D_α line with and without NB injection, seen from the blue Doppler shifted side. The spectrum is observed from by the "P13" MSE system (Fig. 2.7).

deuterium NB was injected into a deuterium plasma. The observed spectrum without NB injection is also plotted for comparison. The D neutral beam consists of D, D_2 and D_3 components because D^+, D_2^+ and D_3^+ are produced in ion sources. The fraction of D, D_2 and D_3 in the P-NB in JT-60U is 78%, 15% and 7%. The D_α line from NB with a velocity v_b ($= 3 \times 10^6$ m/s at 94 keV for D) deviates from 656.1 nm (D_α wavelength in the stationary frame) due to the Doppler shift. A series of D_α lines corresponding to E_b=94 keV, $E_b/2$ and $E_b/3$ are observed in blue Doppler shift side by 2 - 5 nm from 656.1 nm. Three components of E_b=94 keV, $E_b/2$ and $E_b/3$ are emitted from D, D_2 and D_3 excited by collisions with electrons and ions. These Doppler-shifted lines are not observed in the spectrum without NB injection. The σ and π components corresponding to the three beam energy components of NB appeared at wavelength Doppler-shifted from 656.1 nm. Stark effect splits the Doppler-shifted line into σ and π polarizing components. The σ line appears at the Doppler-shifted wavelength, while the π lines appear in both shorter and longer wavelength sides around the σ line. The Stark split wavelength of the π component is proportional to the experienced electric field for hydrogen and its isotopes. The motional electric field is nearly proportional to the toroidal magnetic field. Therefore, σ component is convenient to observe for the experiments at various toroidal magnetic field which is chosen according to the experimental objectives, because the central wavelengths of the bandpath filters are not necessary to be adjusted for the toroidal magnetic field.

The components of the MSE diagnostics are shown in Fig. 2.10. The collection optics consists of

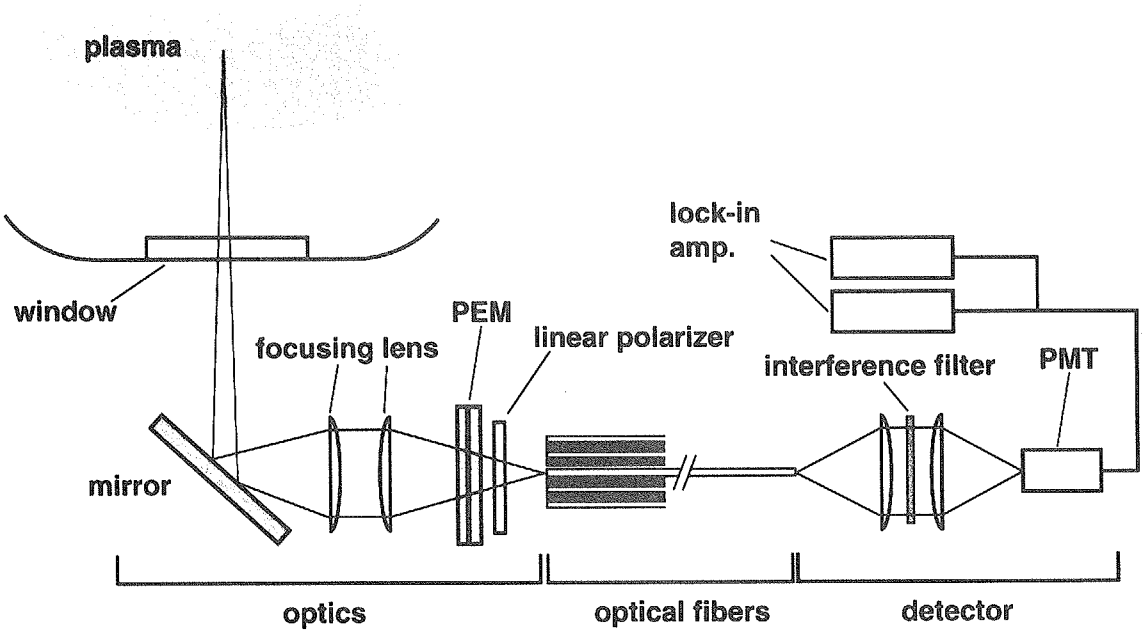

Figure 2.10: Components of the MSE system.

one or two mirrors, lenses, a pair of photoelastic modulators (PEMs), and a linear polarizer. The vacuum windows (fused silica) are located in front of the mirror, and hence, the mirrors are in the air. The lens in the collection optics is made of Schott SFL6 glass to minimize birefringence in the lens, thus, minimize Faraday rotation of the polarized light emitted from plasma.The collected light is transmitted through optical fibers of ~120 m length to a diagnostic room, where the optical fibers are connected to detectors. The diameter of the fiber core is 0.4 mm, and typically 20 fibers are used for one spatial channel. At the detector, the σ component of the D_α or H_α line of the full-energy (~85 keV) beam is spectrally resolved by interference filters with 0.3 nm bandpass and is converted to an electronic signal by a photomultiplier (PMT) with a Ga-As photocathode. The filter wavelength is tuned by changing its temperature. The output of the photomultiplier is fed into two lock-in-amplifiers for demodulation at the second harmonic of the reference frequencies of the PEMs.

A pair of PEMs are used to modulate the polarized component of incident light. Figure 2.11 shows a principle of PEM. The fused silica crystal is oscillated by a piezo actuator at a specified frequency. A refractive index in the oscillating direction (x-axis in Fig. 2.11) becomes smaller when the fused silica crystal is compressed, and becomes larger when expanded. Therefore, when the fused silica crystal is compressed (expanded), the phase velocity of the light polarized in the x-axis is larger (lower) than that in the y axis. Thus, the phase difference between the x- and y- polarized components, which is called "retardation", is modulated at the oscillation frequency of the piezo actuator. Figure 2.12 shows an arrangement of two PEMs and a linear polarizer. For an incident linear polarized light with the electric field $\boldsymbol{E}_0 = E_0(\cos\gamma\hat{\boldsymbol{x}} + \sin\gamma\hat{\boldsymbol{y}})e^{-i\omega t}$, the Stokes parameters, Q and U, are written by

$$Q = E_0^2\cos(2\gamma), \tag{2.1}$$

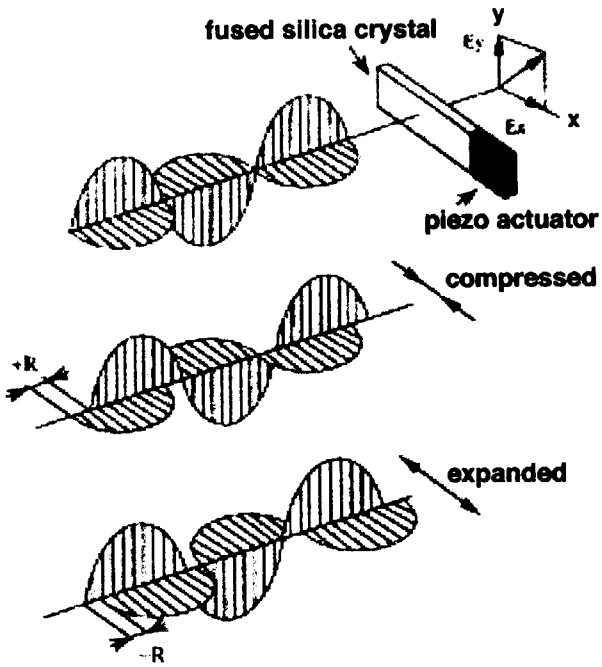

Figure 2.11: A principle of PEM.

$$U = E_0^2 \sin(2\gamma), \tag{2.2}$$

where γ is the polarization angle of incident light, $\omega_1 = 2\pi f_1$, $\omega_2 = 2\pi f_2$, and f_1 and f_2 are the oscillation frequencies of the PEM 1 and PEM 2, respectively. The intensity of the electric field $\boldsymbol{E}_{\mathrm{PEM}}$ of the polarized light after passing a linear polarizer is written by

$$\begin{aligned}\left|\boldsymbol{E}_{\mathrm{PEM}}^2\right| &= \frac{E_0^2}{2}\left[1+\frac{J_0(A_1)}{2\sqrt{2}}\cos(2\gamma)+\frac{J_0(A_2)}{2\sqrt{2}}\sin(2\gamma)\right] \\ &\quad -\frac{J_2(A_1)}{\sqrt{2}}E_0^2\cos(2\gamma)\cos(2\omega_1 t)+\frac{J_2(A_2)}{\sqrt{2}}E_0^2\sin(2\gamma)\cos(2\omega_2 t)+\cdots,\end{aligned}$$

where J_n is the Bessel function of the 1st kind, "$\cdots$" denotes higher harmonic terms such as $\cos(4\omega_1)$, $\cos(6\omega_1)$, ..., $\cos(4\omega_2)$, $\cos(6\omega_2)$, ..., and A_1 and A_2 are the retardations of the PEM 1 and PEM 2, respectively. Retardations are normally set to π radian. Two lock-in amplifiers demodulate the detected signal, which is proportional to $\left|\boldsymbol{E}_{\mathrm{PEM}}^2\right|$, at $2\omega_1$ and $2\omega_2$. The outputs of two lock-in amplifiers, $V(2\omega_1)$ and $V(2\omega_2)$ are written by

$$\begin{aligned}V(2\omega_1) &= -\frac{J_2(A_1)}{\sqrt{2}}E_0^2\cos(2\gamma), \\ V(2\omega_2) &= \frac{J_2(A_2)}{\sqrt{2}}E_0^2\sin(2\gamma).\end{aligned}$$

Thus, the polarization angle is determined by

$$\gamma = \frac{1}{2}\tan^{-1}\left(\frac{V(2\omega_2)}{V(2\omega_1)}\right).$$

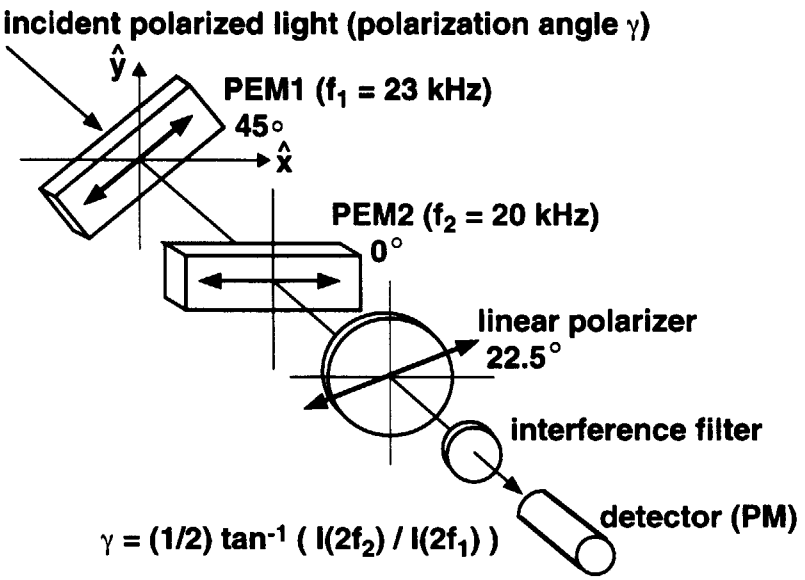

Figure 2.12: An arrangement of two PEMs (Photo-Elastic Modulator) and the linear polarizer.

Originally, aluminum-coated mirrors were used in the collection optics, but substantial amount of polarized background light was observed, which appears to be caused by the spurious generation of polarized light from unpolarized light due to the difference in mirror reflectivity for s- and p-polarization. A "two-wavelength detector", which measures light with two different wavelengths by splitting the light with a half-mirror, was installed to monitor the background light. Assuming that the shape of wavelength spectrum of the background light does not change in time, the signals measured at the wavelength corresponding to the σ component of the split D_α lines were corrected by subtracting the background portion measured at the other wavelength at which any other spectral line does not exist, where the ratio of the back ground light intensities at two wavelengths was determined when the diagnostic NB was not injected. Afterwards, dielectric multilayer mirrors, which were designed to minimize the difference in reflectivity for s- and p-polarization at the proper wavelengths and incident angles, were installed. Then, the amount of polarized background light was reduced significantly, and the measurements became possible without the correction by the two-wavelength detector. The polarization angle is changed at the dielectric multilayer mirrors due to the difference in phase for s- and p-polarization. The change was calibrated with a light source and a polarizer put in the vacuum vessel during the maintenance period. During the experiments the vacuum vessel of JT-60U is heated up to 280 °C, and the mirrors in the P17 and P3 systems are also warmed up to 50 to 80°C. It was found that this caused a significant change in the polarization properties of the dielectric multilayer mirrors. To resolve this problem, a heater was equipped at the back of the mirror, which enabled us to calibrate the mirrors when heated up to the same temperatures as during the experiments.

2.2.3 Calibration

To obtain a polarization angle of an incident light from plasma, two kinds of calibration are necessary. One is for correction of reflection at mirror. A polarization state (Stokes parameters) changes when a light reflects at mirror. The correction coefficients are determined by the following calibration method conducted during the maintenance period (so, persons can work in the vacuum vessel of JT-60U). Setting a light source and a polarizer on the viewing chord of each MSE channel, a polarized light is input to the MSE optics and detector system. By rotating the direction of polarizer from 0 to π, a data set of $V(2\omega_1)$, $V(2\omega_2)$ and the polarization angle γ_2 is obtained. The polarization angle of the input polarized light γ_2 can be written by

$$\gamma_2 = \gamma_2^0 + \sum_{n=1} \left(a_n \cos(2n\gamma_0) + b_n \sin(2n\gamma_0)\right),$$
$$\gamma_2^0 = \frac{1}{2}\tan^{-1}\left(\frac{V(2\omega_2)}{V(2\omega_1)}\cos\delta\right),$$

The coefficients of the Fourier series (a_n and b_n) up to the second order and δ (the difference in the phase change at reflection for s- and p-polarization components) are determined from a obtained calibration data. It should be noted that this calibration is conducted without toroidal magnetic field and so its data does not suffer the Faraday rotation mentioned below.

Second calibration is conducted to correct the effect of birefringence, i.e., the Faraday rotation, in the window and the collection optics due to toroidal magnetic field. The Faraday rotation effect is calibrated by monitoring the beam injection into a gas-filled torus. A "polarizer shutter" is located in front of the window for the P17 and P3 systems. By inserting this polarizer in the optical axis (by closing the shutter), a fixed polarization angle to calibrate the effect of birefringence can be obtained. By scanning the applied toroidal magnetic field, the correction coefficient for the Faraday rotation C_{Bt} is determined. The correction coefficient C_{BT} for the P17 MSE system is shown in Fig. 2.13. The coefficient C_{BT} has a tendency to decrease with channel (decreasing R). This is because the amount of the Faraday rotation has a cosine dependence on the angle between the viewing chord and toroidal magnetic field. Coefficients for higher order correction of mirror reflection is also determined from this "gas-filled torus" calibration, using a linear approximation. This higher order correction compensates the deviation of the mirror reflection characteristics from that calibrated by the in-vacuum-vessel work described above. The cause of this deviation is considered to be that the temperature of mirror at the actual experiment (a "gas-filled torus") is different from the one set up by a heater at the in-vacuum-vessel calibration work. Figure 2.14 (a) shows the waveforms of the outputs from two lock-in amplifiers demodulating at the second harmonic frequencies of the PEMs (f_1 =23 kHz and f_2 =20 kHz) for the 9th channel of the P17 MSE system. The corrected polarization angles at two stages of correction, γ_2 and γ_1, are also shown in Fig. 2.14 (b). The polarization angle corrected for the mirror reflection is γ_2 mentioned above. The polarization angle γ_1 is corrected for the Faraday rotation and the mirror reflection including higher order effect. It is γ_1 that is the polarization angle of the polarized light emitted by the beam neutral atoms in the plasma and that is used in the equilibrium reconstruction code. Spikes around t=5.7 s are due to a

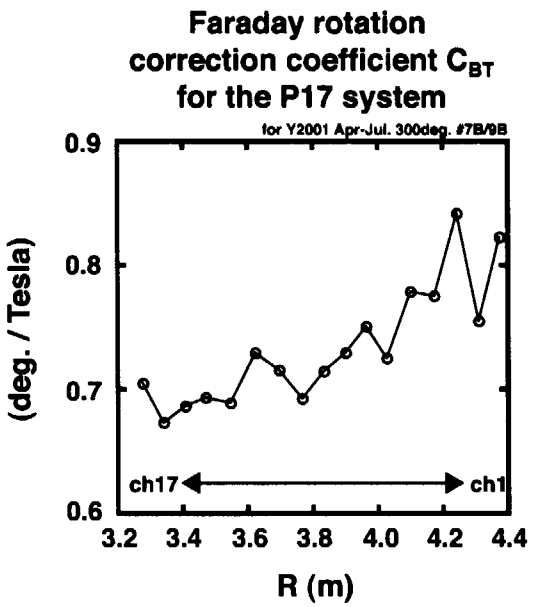

Figure 2.13: The correction coefficient of Faraday rotation C_{BT} for the P17 MSE system is plotted against the R coordinate of each channel.

short period breakdown of the diagnostic NB (#7). As two more NB units are injected during t=7-7.8 s, the plasma density increases. Thus, the intensity of the polarized light increases, and so the outputs of the lock-in amplifiers, V(46) and V(40), also increase. Naturally, the polarization angles do not show the change corresponding to this increase because the current density profile does not change so much.

A calibration using a tokamak discharge is also employed to check possible drifts in calibration and / or when the gas-filled torus calibration is unavailable. The sawtooth inversion radius determined by the ECE measurement used to retrieve the location of the $q = 1$ surface ("sawtooth" is an MHD instability with $m/n = 1/1$), in combination with a slow sweep of plasma major radius with a steady state current profile and a rapid sweep of plasma major radius ('jog') for the calibration.

Typical errors of the calibration are 0.2 degree in the polarization angles while the typical statistical errors in the measurement are less than 0.1 degree with a time resolution of 20 ms.

2.2.4 Derivation of the MSE polarization angle

The MSE polarization angle is formulated by using local magnetic and electric fields [62]. Neutral beam atoms experience not only the Lorentz electric field but also the electric field originated from the electrostatic potential in plasmas. The radial electric field is produced by pressure gradient and plasma rotation. Therefore, it can not be neglected when the steep pressure gradient and / or large plasma rotation exist, while the toroidal and poloidal components of electric field are negligibly small.

The response of the MSE polarization angle to the magnetic and radial electric fields is derived in this section. In the following discussion, the (X, Y, Z) coordinate system is used, where −X corresponds to the major radial direction at the port 1 of JT-60U. In Fig. 2.15 (a) and (b), let "P" be a point on the beam

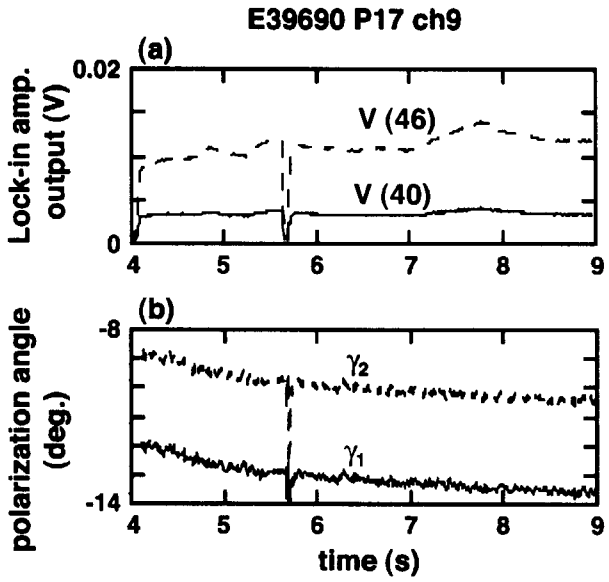

Figure 2.14: (a) Waveforms of the outputs from two lock-in amplifiers demodulating at the second harmonic frequencies of the PEMs for the 9th channel of the P17 MSE system. V(46) and V(40) correspond to the PEM frequencies f_1 =23 kHz and f_2 =20 kHz, respectively. (b) waveforms of the corrected polarization angles, γ_2 and γ_1 determined from V(46) and V(40). γ_2 is corrected for only the mirror reflection. γ_1 is corrected for the Faraday rotation and the mirror reflection (incl. higher order effect).

line and "Q" be the point corresponding to the observer. The azimuthal angle and angle of elevation of the beam line are denoted by θ and α, respectively. The azimuthal angle of point P is $\phi_{\rm P}$. The azimuthal angle and angle of elevation of vector PQ are $\phi_{\rm PQ}$ and $\alpha_{\rm PQ}$. Their domains are $-180° \leq \phi_{\rm P}, \phi_{\rm PQ} \leq 180°$ and $-90° \leq \alpha, \alpha_{\rm PQ} \leq 90°$. The unit vector parallel to the beam line is $\mathbf{UB}$. In Fig. 2.15 (c), the (H, V) coordinates are defined on a plane K perpendicular to the line PQ. The V-axis is a normal projection of the z-axis to plane K. Vector $\mathbf{UV}$ is the unit vector parallel to the V-axis. The H-axis is perpendicular to the V-axis. Vector $\mathbf{UH}$ is the unit vector parallel to the H-axis which is perpendicular to $\mathbf{UV}$ and on plane K. $\mathbf{UB}$, $\mathbf{UH}$ and $\mathbf{UV}$ can be expressed as

$$\mathbf{UB} = \begin{pmatrix} \cos\theta\cos\alpha \\ \sin\theta\cos\alpha \\ \sin\alpha \end{pmatrix}, \mathbf{UH} = \begin{pmatrix} -\sin\phi_{\rm PQ} \\ \cos\phi_{\rm PQ} \\ 0 \end{pmatrix} \quad \text{and} \quad \mathbf{UV} = \begin{pmatrix} -\cos\phi_{\rm PQ}\sin\alpha_{\rm PQ} \\ -\sin\phi_{\rm PQ}\sin\alpha_{\rm PQ} \\ \cos\alpha_{\rm PQ} \end{pmatrix}.$$

The motional electric field is

$$\boldsymbol{E}_{\rm m} = \boldsymbol{v} \times \boldsymbol{B}, \qquad \boldsymbol{B} = \begin{pmatrix} B_{\rm R}\cos\phi_{\rm P} - B_\phi \sin\phi_{\rm P} \\ B_{\rm R}\sin\phi_{\rm P} + B_\phi\cos\phi_{\rm P} \\ B_{\rm Z} \end{pmatrix}, \tag{2.3}$$

where B_ϕ is negative for the normal direction (CW) in JT-60U. The horizontal (H) and vertical (V) components of $\boldsymbol{E}_{\rm m}$ (see Fig. 2.15 (d)) are

$$E_{\rm H} = (\boldsymbol{v} \times \boldsymbol{B}) \cdot \mathbf{UH} = v_{\rm b}\mathbf{UB} \cdot (\boldsymbol{B} \times \mathbf{UH}) = v_{\rm b}\left(A_4^0 B_{\rm Z} + A_3^0 B_{\rm R} + A_2^0 B_\phi\right), \tag{2.4}$$

$$E_{\rm V} = v_{\rm b}\mathbf{UB} \cdot (\boldsymbol{B} \times \mathbf{UV}) = v_{\rm b}\left(A_1^0 B_{\rm Z} + A_5^0 B_{\rm R} + A_6^0 B_\phi\right) \tag{2.5}$$

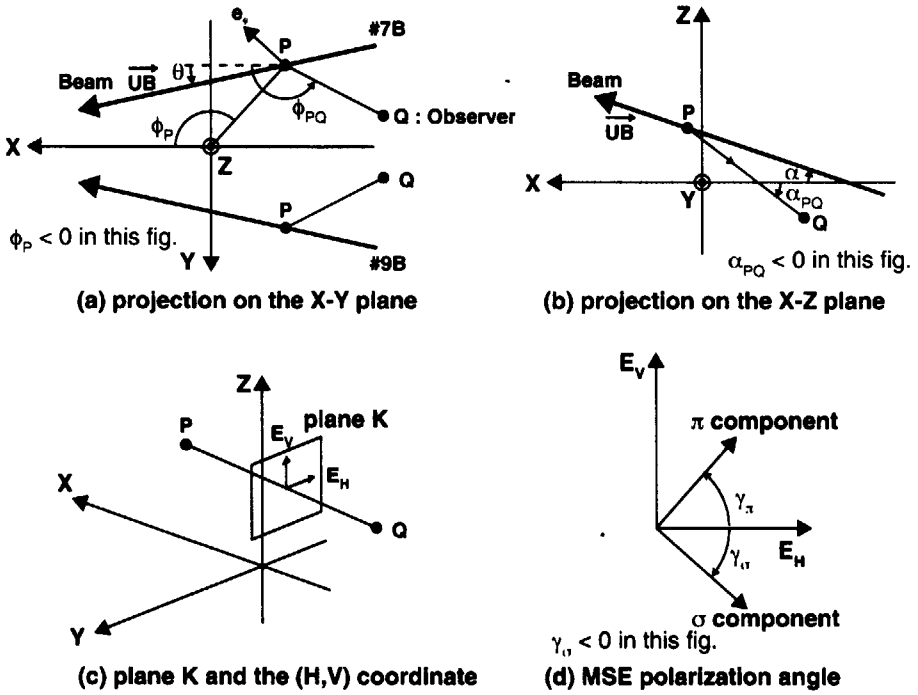

Figure 2.15: Schematic views of the coordinate system, beam trajectory and the observer (MSE polarimeter).

, where v_b is a beam velocity. Thus, the tangent of the MSE polarization angle (π component) γ_π can be written as

$$\tan\gamma_\pi = \frac{E_V}{E_H} = \frac{A_1^0 B_Z + A_5^0 B_R + A_6^0 B_\phi}{A_4^0 B_Z + A_3^0 B_R + A_2^0 B_\phi}\ , \tag{2.6}$$

where
$$\begin{aligned}
A_1^0 &= \mathrm{UVX}\cdot\mathrm{UBY} - \mathrm{UVY}\cdot\mathrm{UBX}, \qquad A_4^0 = \mathrm{UHX}\cdot\mathrm{UBY} - \mathrm{UHY}\cdot\mathrm{UBX},\\
A_5^0 &= \mathrm{UBZ}\,(-\mathrm{UVX}\sin\phi_P + \mathrm{UVY}\cos\phi_P) + \mathrm{UVZ}\,(\mathrm{UBX}\sin\phi_P - \mathrm{UBY}\cos\phi_P),\\
A_6^0 &= -\mathrm{UBZ}\,(\mathrm{UVX}\cos\phi_P + \mathrm{UVY}\sin\phi_P) + \mathrm{UVZ}\,(\mathrm{UBX}\cos\phi_P + \mathrm{UBY}\sin\phi_P),\\
A_3^0 &= \mathrm{UBZ}\,(-\mathrm{UHX}\sin\phi_P + \mathrm{UHY}\cos\phi_P) + \mathrm{UHZ}\,(\mathrm{UBX}\sin\phi_P - \mathrm{UBY}\cos\phi_P),\\
A_2^0 &= -\mathrm{UBZ}\,(\mathrm{UHX}\cos\phi_P + \mathrm{UHY}\sin\phi_P) + \mathrm{UHZ}\,(\mathrm{UBX}\cos\phi_P + \mathrm{UBY}\sin\phi_P).
\end{aligned}$$

It should be noted that the MSE polarization angle for the σ component (γ_σ) itself is used in JT-60U ($\gamma_\sigma = \gamma_\pi - 90°$).

Next, we consider the effect of the radial electric field on the MSE polarization angle. The radial electric field can be written as,

$$\boldsymbol{E}_r = -\nabla\Phi = -\omega\nabla\Psi = -\omega R B_Z \mathbf{e_R} + \omega R B_R \mathbf{e_Z} = \omega R \mathbf{e}_\phi \times \boldsymbol{B}, \tag{2.7}$$

where Φ and Ψ are the electrostatic potential and the poloidal flux per radian in ϕ (toroidal angle: positive for CCW), and $\mathbf{e_R}$, $\mathbf{e_Z}$ and $\mathbf{e}_\phi$ are the unit vectors in the R, Z and ϕ directions in the cylindrical coordinate

system, and $\omega \equiv \partial\Phi/\partial\Psi$ (rad/s), $RB_{\rm Z} = \partial\Psi/\partial R$ and $RB_{\rm R} = -\partial\Psi/\partial Z$. The total electric field is given as

$$\boldsymbol{E}_{\rm total} = \boldsymbol{v}_{\rm b} \times \boldsymbol{B} + \omega R \mathbf{e}_{\mathbf{R}} \times \boldsymbol{B} = (\boldsymbol{v}_{\rm b} + \omega R \mathbf{e}_{\mathbf{R}}) \times \boldsymbol{B}. \tag{2.8}$$

Thus, replacing $\boldsymbol{v}_{\rm b}$ with $\boldsymbol{v}_{\rm b} + \omega R \mathbf{e}_{\mathbf{R}}$ in eq.(2.6), the response function for the MSE polarization angle can be expressed by the following equation.

$$\tan\gamma_\pi = \frac{E_{\rm V}}{E_{\rm H}} = \frac{A_1 B_{\rm Z} + A_5 B_{\rm R} + A_6 B_\phi + E_1 E_{\rm R} - E_4 E_{\rm Z}}{A_4 B_{\rm Z} + A_3 B_{\rm R} + A_2 B_\phi + E_2 E_{\rm R} - E_3 E_{\rm Z}}, \tag{2.9}$$

where

$$\begin{aligned}
E_{\rm R} &= -\omega R B_{\rm Z}, \quad E_{\rm Z} = \omega R B_{\rm R}, \\
A_1 &= A_1^0 + (\mathrm{UVX}\cos\phi_{\rm P} + \mathrm{UVY}\sin\phi_{\rm P})\,(\omega R/v_{\rm b}), \quad A_5 = A_5^0 - \mathrm{UVZ}\,(\omega R/v_{\rm b}), \\
A_6 &= A_6^0, \\
A_4 &= A_4^0 + (\mathrm{UHX}\cos\phi_{\rm P} + \mathrm{UHY}\sin\phi_{\rm P})\,(\omega R/v_{\rm b}), \quad A_3 = A_3^0, \quad A_2 = A_2^0, \\
E_1 &= -\frac{\mathrm{UVX}\,\cos\phi_{\rm p} + \mathrm{UVY}\sin\phi_{\rm p}}{v_{\rm b}} = \frac{\cos(\phi_{\rm PQ} - \phi_{\rm P})\sin\alpha_{\rm PQ}}{v_{\rm b}}, \\
E_4 &= \frac{\mathrm{UVZ}}{v_{\rm b}} = \frac{\cos\alpha_{\rm PQ}}{v_{\rm b}}, \\
E_2 &= -\frac{\mathrm{UHX}\,\cos\phi_{\rm p} + \mathrm{UHY}\sin\phi_{\rm p}}{v_{\rm b}} = \frac{\sin(\phi_{\rm PQ} - \phi_{\rm P})}{v_{\rm b}}, \quad E_3 = 0.
\end{aligned}$$

The coefficients A_i and E_i vary depending on the viewing geometry and the beam velocity. Since Φ, not E_r, is considered to be constant on a flux surface, the plasma equilibrium code reconstructs the gradient of the electrostatic potential Φ.

3. Analysis Methods

The analysis methods of the plasma equilibrium and the non-inductively driven current density profile are described in this chapter.

3.1 Plasma Equilibrium

In this section, first, the equilibrium equation is derived, and an example of the equilibrium reconstruction of the JT-60U plasma using the MSE measurement is presented.

3.1.1 Grad-Shafranov equation

For axisymmetric equilibria, that is equilibria which are independent of the toroidal angle ϕ, the magnetic field lines lie in nested toroidal magnetic surfaces as illustrated in Fig. 3.1. The magnetic axis is defined as the center of the nested flux surfaces (Fig. 3.1). Here, we derive the equilibrium equation for an axisymmetric magnetic configuration including tokamak. The equilibrium equation is a two-dimensional nonlinear, elliptic partial differential equation, usually called the Grad-Shafranov equation [4].

The equilibrium condition requires that the magnetic force balances the force due to the plasma pressure, that is,

$$\boldsymbol{j} \times \boldsymbol{B} = \nabla p. \tag{3.1}$$

This equation gives $\boldsymbol{B} \cdot \nabla p = 0$ and $\boldsymbol{j} \cdot \nabla p = 0$. Thus, there is no pressure gradient along the magnetic field lines and the magnetic surfaces are surfaces of constant pressure, and the current lines also lie in the magnetic surfaces as shown in Fig. 3.1. The poloidal magnetic flux function Ψ, which is determined by the poloidal flux lying within each magnetic surface and is therefore a constant on that surface, satisfies

$$\boldsymbol{B} \cdot \nabla \Psi = 0$$

In the toroidal coordinate system (Fig. 3.1), the poloidal magnetic field is related to Ψ (the poloidal flux per radian in ϕ) by

$$B_R = -\frac{1}{R}\frac{\partial \Psi}{\partial Z}, \quad B_Z = \frac{1}{R}\frac{\partial \Psi}{\partial R} \tag{3.2}$$

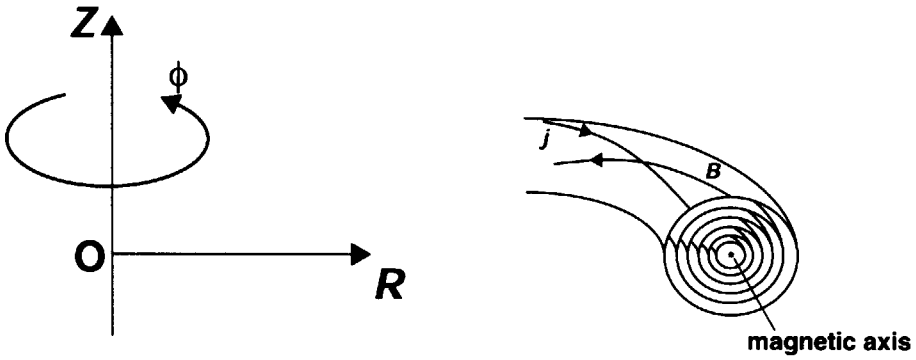

Figure 3.1: Magnetic flux surfaces forming a set of nested toroids. Magnetic field lines and current lines lie in magnetic surfaces.

This conforms to the requirement $\nabla \cdot \boldsymbol{B} = 0$.

Similarly, the poloidal current density is related to the function $F \equiv RB_\phi$ by

$$j_R = -\frac{1}{\mu_0 R}\frac{\partial F}{\partial Z}, \quad j_Z = \frac{1}{\mu_0 R}\frac{\partial F}{\partial R}, \tag{3.3}$$

where B_ϕ is the toroidal magnetic field. The function F is a function of Ψ as well as the pressure p.

The equation (3.1) is written as

$$\boldsymbol{j}_\mathrm{p} \times \boldsymbol{B}_\phi + \boldsymbol{j}_\phi \times \boldsymbol{B}_\mathrm{p} = \nabla \boldsymbol{p}, \tag{3.4}$$

where $\boldsymbol{j}_\phi$ and $\boldsymbol{j}_\mathrm{p}$ are the toroidal and poloidal components of the current density, and $\boldsymbol{B}_\mathrm{p}$ is the poloidal magnetic field. Substituting Eqs. (3.2) and (3.3) into Eq. (3.4),

$$j_\phi = Rp' + \frac{1}{\mu_0 R}FF' \tag{3.5}$$

Substitution of Eq. (3.2) into the toroidal component of Ampère's equation gives

$$-\mu_0 R j_\phi = R\frac{\partial}{\partial R}\frac{1}{R}\frac{\partial \Psi}{\partial R} + \frac{\partial^2 \Psi}{\partial Z^2} \tag{3.6}$$

and using Eq. (3.6) to substitute for j_ϕ in Eq. (3.5) gives the Grad-Shafranov equation,

$$R\frac{\partial}{\partial R}\frac{1}{R}\frac{\partial \Psi}{\partial R} + \frac{\partial^2 \Psi}{\partial Z^2} = -\mu_0 R^2 p'(\Psi) - F(\Psi)F'(\Psi). \tag{3.7}$$

3.1.2 Definitions of the important equilibrium quantities

Several quantities associated with equilibrium are explained in this section.

Safety factor

The safety factor, q, is so called because of the role it plays in determining stability. In general terms, higher values of q lead to greater stability. It also appears as an important factor in transport theory.

In an axisymmetric equilibrium each magnetic field line has a value of q. The field line follows a

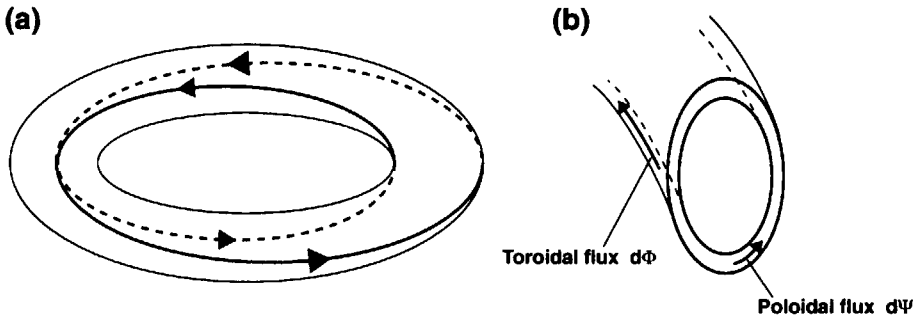

Figure 3.2: (a) Field line on $q = 2$ surface. (b) Flux annulus containing toroidal flux $\mathrm{d}\Phi$ and poloidal flux $\mathrm{d}\Psi$

helical path as it goes round the torus on its associated magnetic surface. If at some toroidal angle, ϕ, the field line has a certain position in the poloidal plane, it will return to that position in the poloidal plane after change of toroidal angle $\Delta\phi$. The q-value of this field line is defined by

$$q = \frac{\Delta\phi}{2\pi}$$

Thus if a magnetic field line returns to its starting position after exactly one rotation round the torus, then $q = 1$. If it moves more slowly in the poloidal direction it has a higher value of q. Rational values of q play an important role in stability. If $q = m/n$, where m and n are integers, the field line joins up on itself after m toroidal and n poloidal rotations round the torus. A $q = 2$ line is illustrated in Fig. 3.2 (a).

The safety factor q is expressed as the rate of change of toroidal flux Φ with poloidal flux Ψ. Considering toroidal and poloidal fluxes, $\mathrm{d}\Phi$ and $\mathrm{d}\Psi$ within an infinitesimal annulus between two magnetic surfaces as illustrated in Fig. 3.2 (b),

$$q = \frac{\mathrm{d}\Phi}{\mathrm{d}\Psi}.$$

Plasma beta and internal inductance

The plasma β is a parameter that measures the efficiency of plasma confinement by the magnetic field. It is defined as the ratio of the averaged plasma energy to the magnetic energy.

$$\beta \equiv \frac{\langle p \rangle}{B^2/2\mu_0}$$

where $\langle ... \rangle$ means the volume averaged value. Instead of the total magnetic field B (toroidal and poloidal magnetic fields), the definition by the vacuum toroidal magnetic field at the geometric center of the plasma B_{T0} is often used because it is more proper as an economical measure from the technological viewpoint.

$$\beta \equiv \frac{\langle p \rangle}{B_{\mathrm{T0}}^2/2\mu_0}$$

Similarly, the poloidal beta β_{p} is defined by

$$\beta_{\mathrm{p}} \equiv \frac{\int p\,\mathrm{d}S / \int \mathrm{d}S}{B_a^2/2\mu_0}$$

where the integrals are surface integrals over the poloidal cross-section and

$$B_a = \frac{\mu_0 I_{\mathrm{p}}}{l}$$

where I_{p} is the plasma current and l is the length of the poloidal perimeter of the plasma.

The normalized beta β_{N} is used as a measure of efficiency of magnetic confinement of plasma pressure to compare among the plasmas with various plasma size, toroidal magnetic field and plasma current which the plasma beta depends on [75].

$$\beta_{\mathrm{N}} \equiv \frac{aB_{\mathrm{T}}}{I_{\mathrm{p}}}\beta(\%)$$

where a is a horizontal minor radius and I_{p} is in unit of MA.

The normalized internal inductance per unit length associated with the toroidal current flowing in the plasma,

$$\ell_{\mathrm{i}} \equiv \frac{\overline{B_{\mathrm{p}}^2}}{\overline{B_{\mathrm{p}a}}^2} = \frac{1}{V_{\mathrm{p}}}\frac{\int B_{\mathrm{p}}^2\,\mathrm{d}V}{\overline{B_{\mathrm{p}a}}^2}$$

Here, V_{p} is the plasma volume, $\int dV$ is the volume integral, and $\overline{B_{\mathrm{p}a}}$ is the averaged poloidal magnetic field along the plasma surface. The internal inductance ℓ_{i} is a measure of the peakedness of the current density profile.

3.1.3 Equilibrium reconstruction in JT-60U

Solution of the Grad-Shafranov equation

The Grad-Shafranov equation (3.7) is numerically solved for the JT-60U plasma equilibrium by the SELENE code with the free boundary condition. The total plasma current, the vacuum toroidal magnetic field, the poloidal coil currents, 17 poloidal magnetic field signals measured by the magnetic pick-up coils and 15 poloidal magnetic flux signals measured by the flux loops located along the vessel wall, and the MSE spectroscopy are used.

Tokamak equilibria can be treated as axisymmetric, and so they should satisfy the Grad-Shafranov equation (3.7). Two flux surface functions in the toroidal current density expression Eq. (3.5), $p(\Psi)$ and $F(\Psi)$, are arbitrary functions in Ψ. Solution of Eq. 3.5 should satisfy the following conditions on the plasma boundary Γ_{p}.

$$\Psi^{\mathrm{p}}|_{\Gamma_{\mathrm{p}}} = \Psi^{\mathrm{v}}|_{\Gamma_{\mathrm{p}}}, \quad \left.\frac{\partial\Psi^{\mathrm{p}}}{\partial \mathrm{n}}\right|_{\Gamma_{\mathrm{p}}} = \left.\frac{\partial\Psi^{\mathrm{v}}}{\partial \mathrm{n}}\right|_{\Gamma_{\mathrm{p}}},$$

where the labels "p" and "v" denote the plasma and vacuum sides, respectively. Generally, the plasma boundary Γ_{p} is unknown (free boundary problem).

As constraints imposed by the external magnetic measurements, the following conditions should be satisfied at the locations of flux loops $(R_{\rm k}, Z_{\rm k})$ and pick-up coils $(R_{\rm i}, Z_{\rm i})$,

$$\Psi^{\rm v}(R_{\rm k}, Z_{\rm k}) = \Psi_{\rm k},$$
$$\frac{\partial \Psi^{\rm v}(R_{\rm i}, Z_{\rm i})}{\partial {\rm Z}} = -RB^{\rm i}_R,$$
$$\frac{\partial \Psi^{\rm v}(R_{\rm i}, Z_{\rm i})}{\partial {\rm R}} = RB^{\rm i}_Z,$$

where $\Psi_{\rm k}$ the k th flux loop signal, and $B^{\rm i}_R$ and $B^{\rm i}_Z$ are the R and Z components of poloidal magnetic field measured by the i th pick-up coil. The plasma current should be equal to the measurement $I_{\rm p}^{\rm meas.}$

$$\int j_\phi dS = I_{\rm p}^{\rm meas.}.$$

The current density profile j_ϕ is unknown and can be determined only when the complete information on the geometric shapes of the flux surfaces within plasma is given [76]. Thus, only with the external magnetic measurements, there exists a limitation in a full equilibrium reconstruction, and so it is necessary to assume proper functional forms for $p(\Psi)$ and $F(\Psi)$.

In the equilibrium reconstruction code SELENE for the JT-60U plasmas, the following expression for j_ϕ (Eq. 3.5) is used assuming p' and FF' to have a same functional form.

$$j_\phi = j_0 \left\{ \beta^*_{\rm p} R/R_{\rm p} + (1-\beta^*_{\rm p}) R_{\rm p}/R \right\} g(\hat{\Psi}), \tag{3.8}$$
$$\hat{\Psi} \equiv \frac{\Psi - \Psi_{\rm axis}}{\Psi_{\rm surface} - \Psi_{\rm axis}}, \tag{3.9}$$

where j_0 is the normalization factor, $\beta^*_{\rm p}$ is approximately a poloidal beta, $R_{\rm p}$ is the plasma major radius, and $\hat{\Psi}$ is the normalized poloidal flux taking the values of 0 and 1 at the magnetic axis and the plasma surface, respectively. As the arbitrary function $g(\hat{\Psi})$, a polynomial function or a power function is generally adopted.

$$g(\hat{\Psi}) = (1-\hat{\Psi}^3) + C_1\left(\hat{\Psi} - \hat{\Psi}^3\right) + C_2\left(\hat{\Psi}^2 - \hat{\Psi}^3\right), \tag{3.10}$$
$$g(\hat{\Psi}) = \left(1 - \hat{\Psi}^\alpha\right)^\gamma, \tag{3.11}$$

Thus, there are 4 unknown parameters to determine the current density profile, $(j_0, \beta^*_{\rm p}, C_1, C_2)$ or $(j_0, \beta^*_{\rm p}, \alpha, \gamma)$. In a polynomial representation, j_0, $\beta^*_{\rm p}$, C_1 and C_2 are used to adjust the central safety factor $q_{\rm axis}$, $\beta_{\rm p}$, $\ell_{\rm i}$ and $I_{\rm p}$, respectively. In a power functional form, j_0, $\beta^*_{\rm p}$, α and γ are used to adjust $I_{\rm p}$, $\beta_{\rm p}$, $q_{\rm axis}$, $\ell_{\rm i}$ and $I_{\rm p}$, respectively. As $I_{\rm p}$ is measured, the SELENE code searches a solution in $(q_{\rm axis}, \beta_{\rm p}, \ell_{\rm i})$ space by using the least squares method. A chi-square statistic for the external magnetic measurements is

$$\chi^2_{\rm mag.} = \sum_{\rm i} w_{\rm i} \left(\hat{b}_{\rm i} - b_{\rm i}\right)^2,$$

where $w_{\rm i}$ is the weight for the i th magnetic signal, and $\hat{b}_{\rm i}$ and $b_{\rm i}$ are the calculated and measured signals at the i th magnetic sensor, respectively. When the MSE data are available, the SELENE code also

minimizes a chi-square statistic for the MSE polarization angles, $\chi^2_{\rm MSE}$.

$$\chi^2_{\rm MSE} = \sum_{\rm j} w_{\rm j} \left(\hat{\gamma}_{\rm j} - \gamma_{\rm j}\right)^2 ,$$

where $w_{\rm j}$ is the weight for the j th MSE data, and $\hat{\gamma}_{\rm j}$ and $\gamma_{\rm j}$ are the calculated and measured MSE polarization angle for the j th viewing point, respectively.

The Grad-Shafranov equation is solved within the computational box with $R = 2.1 - 4.7$ m and $Z = -1.8 - 1.8$ m. The number of grid is 129×129.

Equilibrium reconstruction using the external magnetic measurements

Examples of equilibrium reconstruction using only the external magnetic measurements are presented below. Results are taken from Ref. [77]. A test equilibrium is numerically calculated using $q_{\rm axis} = 1.0$, $\beta_{\rm p} = 0.5$, $\ell_{\rm i} = 1.50$ and a power function in Eq. (3.11). Figure 3.3 shows the equilibrium profiles. From the simulated signals of the magnetic measurements for the test equilibrium, the equilibrium is reconstructed and compared to the original equilibrium quantities. Here, giving the true value of $q_{\rm axis}$(=1.0), the SELENE code searched a optimal set of $(\beta_{\rm p}, \ell_{\rm i})$ having a minimum $\chi^2_{\rm mag.}$. Figure 3.4 shows the $\chi^2_{\rm mag.}$ contour plot in the $(\beta_{\rm p}, \ell_{\rm i})$ plane. To check an uncertainty in equilibrium reconstruction due to the errors in magnetic measurements, 10 reconstruction results for the simulated magnetic signals including random 1 % errors are also plotted as open circles in Fig. 3.4. The internal inductance $\ell_{\rm i}$ ranges from 1.2 to 1.55, and $\beta_{\rm p}$ varies from 0.5 to 0.65, where the true values of $\ell_{\rm i}$ and $\beta_{\rm p}$ are 1.50 and 0.5, respectively. Figure 3.5 shows the reconstructed current density profiles corresponding to the points of both ends on the $\chi^2_{\rm mag.} = 0.001$ contour curve. Their resultant $(\beta_{\rm p}, \ell_{\rm i})$ are $(0.675, 1.15)$ and $(0.305, 1.849)$, respectively. Thus, even with the convergence condition of $\chi^2_{\rm mag.} = 0.001$ and the measurement error of 1 %, the current density profile can not be reconstructed accurately only from the external magnetic measurements.

Another reconstruction test was conducted. A test equilibrium is produced with $q_{\rm axis} = 1.1$, $\beta_{\rm p} = 0.2$, $\ell_{\rm i} = 1.048$ and $F(\hat{\Psi}) = 1 - \hat{\Psi}^{0.7}$. Using the simulated magnetic signals (without adding artificial error), the SELENE code searched a solution having a minimum $\chi^2_{\rm mag.}$ in the $(q_{\rm axis}, \beta_{\rm p}, \ell_{\rm i})$ space. Scanning $q_{\rm axis}$, an optimal set of $\beta_{\rm p}$ and $\ell_{\rm i}$ was determined for each $q_{\rm axis}$ as shown in Fig. 3.6. There is no

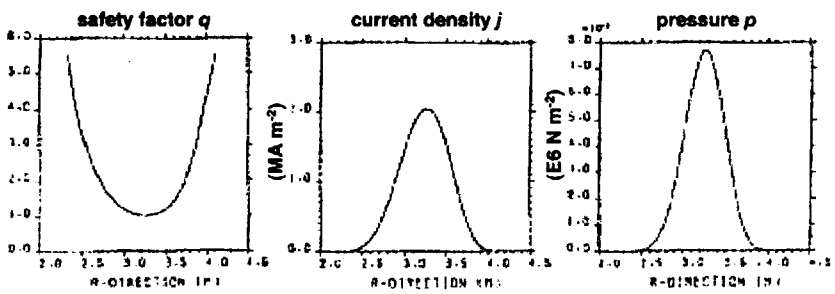

Figure 3.3: Profiles of the safety factor, current density and pressure for the test equilibrium.

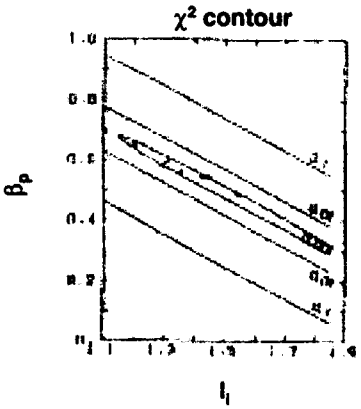

Figure 3.4: $\chi^2_{\mathrm{mag.}}$ contour plot in the $(\beta_{\mathrm{p}}, \ell_{\mathrm{i}})$ plane. Open circles are the reconstruction results for the simulated magnetic signals including 1 % errors.

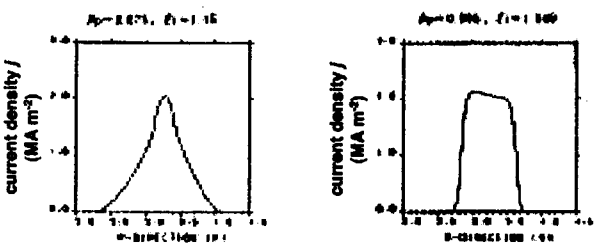

Figure 3.5: The current density profiles in two reconstruction results satisfying the convergence condition of $\chi^2_{\mathrm{mag.}} = 0.001$.

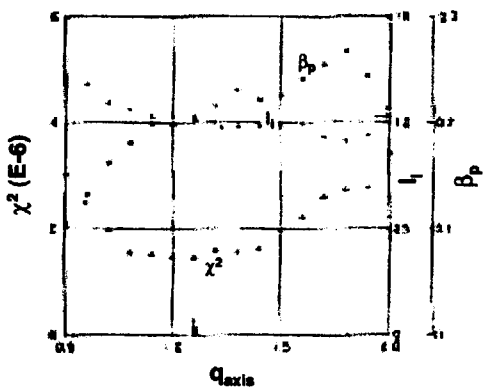

Figure 3.6: The result of finding a solution in $(q_{\mathrm{axis}}, \beta_{\mathrm{p}}, \ell_{\mathrm{i}})$ space. The optimal $(\beta_{\mathrm{p}}, \ell_{\mathrm{i}})$ having a minimum $\chi^2_{\mathrm{mag.}}$ are plotted at each q_{axis}. $\chi^2_{\mathrm{mag.}}$ is also shown.

significance change in $\chi^2_{\mathrm{mag.}}$ around the minimum value for $q_{\mathrm{axis}} = 0.8 - 1.4$. This means that there is ~ 50 % uncertainty in the reconstructed q_{axis} which correspond to 50 % uncertainty in the central current density. Thus, it is concluded again that it is difficult to obtain a satisfactory reconstruction of the current density profile from only the external magnetic measurements.

Equilibrium reconstruction using the MSE spectroscopy

The MSE spectroscopy gives information on the internal magnetic field. The radial profile of the internal magnetic field sets a strong constraint on a possible current density profile. Figure 3.7 shows a example of the reconstructed equilibrium for the JT-60U plasma. The equilibrium magnetic flux surface and profiles of the toroidal current density and plasma pressure on $Z = Z_{\mathrm{axis}}$ are shown. The current density profile is adjusted so as to fit the MSE polarization angles calculated from the equilibrium to the

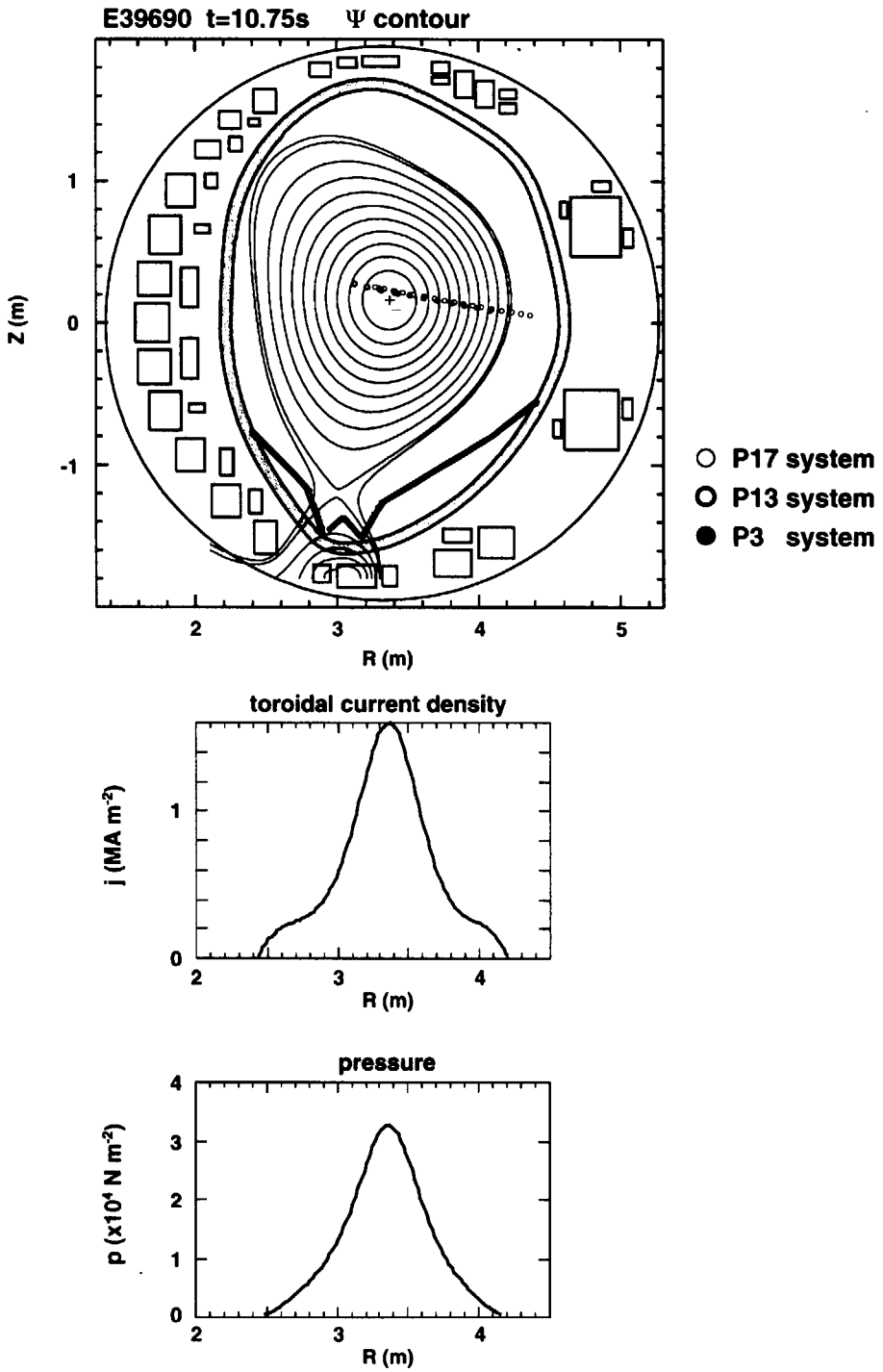

Figure 3.7: The reconstructed equilibrium for E39690 t = 10.75 s. The MSE viewing points are indicated by circles. The current density and pressure profiles on $Z = Z_{\mathrm{axis}}$ are also shown, where Z_{axis} is the Z coordinate of the magnetic axis.

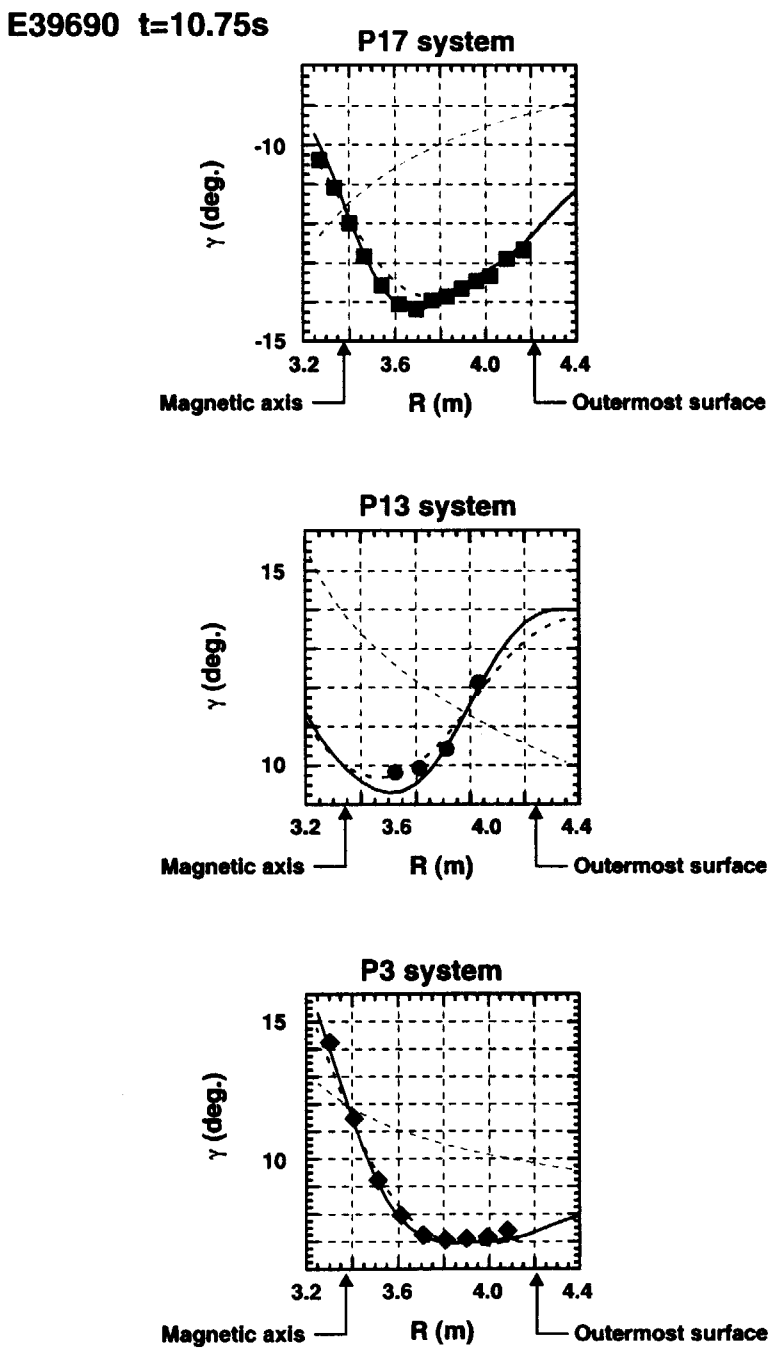

Figure 3.8: The MSE polarization angles for P17, P13 and P3 MSE systems are plotted versus a major radius R. Solid lines are the calculated MSE polarization angle profiles for each MSE systems. The short dashed lines are the calculated angle profiles for the vacuum magnetic field (without the poloidal magnetic field). The long dashed lines correspond to the equilibrium solution under constraint of $q_{\text{axis}} = 1.5$.

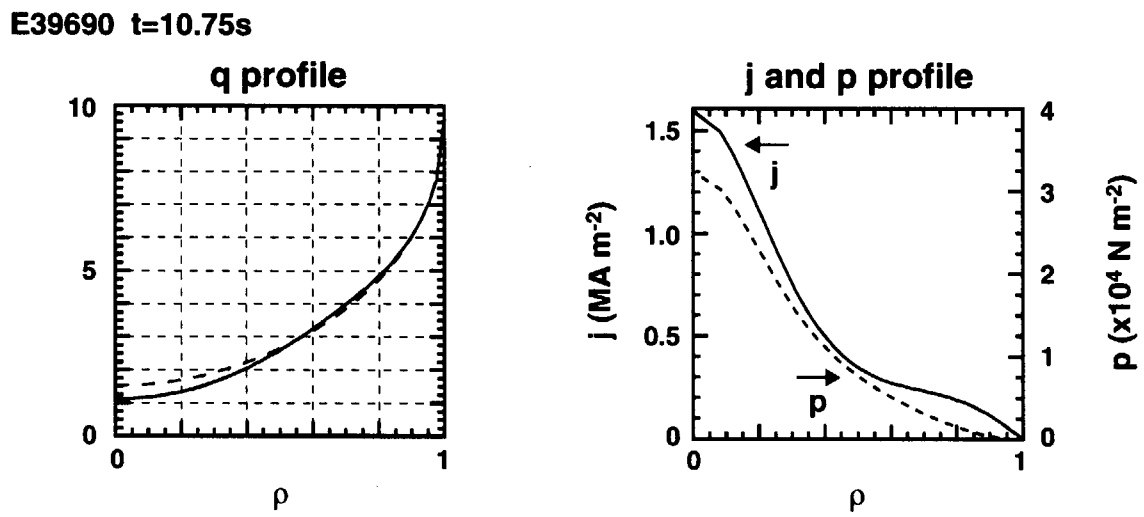

Figure 3.9: The safety factor (q), toroidal current density (j) and pressure (p) profiles are plotted versus the normalized minor radius ρ. The long dashed line in q profile corresponds to the equilibrium solution under constraint of $q_{\rm axis} = 1.5$.

measured ones by P17, P13 and P3 MSE systems. This is shown in Fig. 3.8. The calculated angles (solid lines) agree well with the measured angles by three MSE systems. The short dashed lines in Fig. 3.8 are the calculated angle profiles for only the vacuum toroidal magnetic field. The difference between the solid and dashed lines is approximately proportional to the local poloidal magnetic field, which is in turn proportional to the toroidal current contained within each flux surface. Figure 3.9 shows the safety factor (q), toroidal current density (j) and pressure (p) profiles plotted against the normalized minor radius (ρ). As the current density is not a surface quantity (a quantity constant on a magnetic flux surface), the averaged value on the flux surface is used.

The equilibrium solution under constraint of $q_{\rm axis} = 1.5$ is also shown by the long dashed lines in Figs. 3.8 and 3.9 (q profile). Although the difference between $\chi^2_{\rm mag.}$ values for two equilibria is ~ 5 %, $\chi^2_{\rm MSE}$ for the best solution with $q_{\rm axis} = 1.12$ (solid lines) is nearly half of that for the $q_{\rm axis} = 1.5$ solution indicated by the long dashed lines ($\chi^2_{\rm MSE} = 1.10$ and 2.02, respectively). Thus, the MSE spectroscopy substantially improves accuracy in reconstructing the current density profile which is impossible with only the external magnetic measurements.

3.2 Determination of non-inductively-driven current profile

The analysis method of non-inductive current density profile was first introduced by C.B. Forest [78]. The generalized Ohm's law is written as

$$\boldsymbol{E} + \boldsymbol{v} \times \boldsymbol{B} = \eta(\boldsymbol{j} - \boldsymbol{j}_{\rm NIND}). \tag{3.12}$$

where η is the plasma resistivity and $\boldsymbol{j}_{\mathrm{NIND}}$ is the non-inductive portion of the current density $\boldsymbol{j}$. Taking the dot product of Eq. (3.12) with $\boldsymbol{B}$,

$$\frac{B_{\mathrm{p}}}{B}E_{\mathrm{p}} + \frac{B_{\phi}}{B}E_{\phi} = \eta_{//}\left(j_{//} - j_{\mathrm{NIND},//}\right) \tag{3.13}$$

is obtained. Here, B_{ϕ} and B_{p} are the toroidal and poloidal components of the magnetic field $\boldsymbol{B}$, and E_{ϕ} and E_{p} are the toroidal and poloidal components of the electric field $\boldsymbol{E}$. Subscript $//$ denotes the component parallel to the magnetic field line. In steady state, the toroidal component of Faraday's law $\nabla \times \boldsymbol{E} = -\partial \boldsymbol{B}/\partial t$ is written as

$$\oint E_{\mathrm{p}}\, \mathrm{d}s = 0 \tag{3.14}$$

where $\mathrm{d}s$ is a poloidal line element along the magnetic surface, and the line integral is taken round a flux surface in the poloidal plane. Substituting Eq. (3.13) into Eq. (3.14),

$$\begin{aligned}
\left\langle j_{//}B\right\rangle - \left\langle j_{\mathrm{NIND},//}B\right\rangle &= \sigma_{//}\left\langle B_{\phi}E_{\phi}\right\rangle \\
&= \sigma_{//}\left\langle B_{\phi}\frac{V_{\phi}}{2\pi R}\right\rangle = \frac{\sigma_{//}V_{\phi}}{2\pi F}\left\langle B_{\phi}^{2}\right\rangle \\
&= \sigma_{//}\frac{\left\langle B_{\phi}^{2}\right\rangle}{F}\frac{\partial\Psi}{\partial t}
\end{aligned} \tag{3.15}$$

is derived. Here, the conductivity $\sigma_{//}$ $(= 1/\eta_{//})$, the one-turn loop voltage in the toroidal direction V_{ϕ} and $F = RB_{\phi}$ are constant on each flux surface (i.e., surface quantities), and Ψ is the poloidal flux function $(= \Psi_{\mathrm{p}}/2\pi)$. it should be noted that V_{ϕ} is equal to the time derivative of the poloidal flux $\Psi_{\mathrm{p}}(= 2\pi\Psi)$. $\langle ... \rangle$ is the flux surface average as defined by

$$\langle X\rangle \equiv \oint (X/B_{\mathrm{p}})\ dl/\oint (dl/B_{\mathrm{p}})\,.$$

Multiplying Eq. (3.15) with B_{T}/B^{2} and taking a flux surface average again,

$$\left\langle j_{//}B\right\rangle\left\langle\frac{B_{\mathrm{T}}}{B^{2}}\right\rangle - \left\langle j_{\mathrm{NIND},//}B\right\rangle\left\langle\frac{B_{\mathrm{T}}}{B^{2}}\right\rangle = \sigma_{//}\frac{\left\langle B_{\phi}^{2}\right\rangle}{\langle RB^{2}\rangle}\frac{\partial\Psi}{\partial t}$$

thus,

$$\left\langle j_{//}B\right\rangle\frac{F}{\langle RB^{2}\rangle} - \left\langle j_{\mathrm{NIND},//}B\right\rangle\frac{F}{\langle RB^{2}\rangle} = \sigma_{//}\frac{\left\langle B_{\phi}^{2}\right\rangle}{\langle RB^{2}\rangle}\frac{\partial\Psi}{\partial t} \tag{3.16}$$

is obtained.

Defining the toroidal components of the total current density and noninductive current density by the first and second terms in the left side of Eq. (3.16), respectively, the expression for the toroidal noninductive current density at minor radius ρ is obtained as

$$\begin{gathered}
j_{\mathrm{NIND},\phi}(\rho) = j_{\phi}(\rho) - \sigma_{//}\frac{\left\langle B_{\phi}^{2}\right\rangle}{\langle RB^{2}\rangle}\frac{\partial\Psi}{\partial t}, \\
j_{\mathrm{NIND},\phi}(\rho) \equiv \left\langle j_{\mathrm{NIND},//}B\right\rangle\frac{F}{\langle RB^{2}\rangle}, \quad j_{\phi}(\rho) \equiv \left\langle j_{//}B\right\rangle\frac{F}{\langle RB^{2}\rangle}
\end{gathered} \tag{3.17}$$

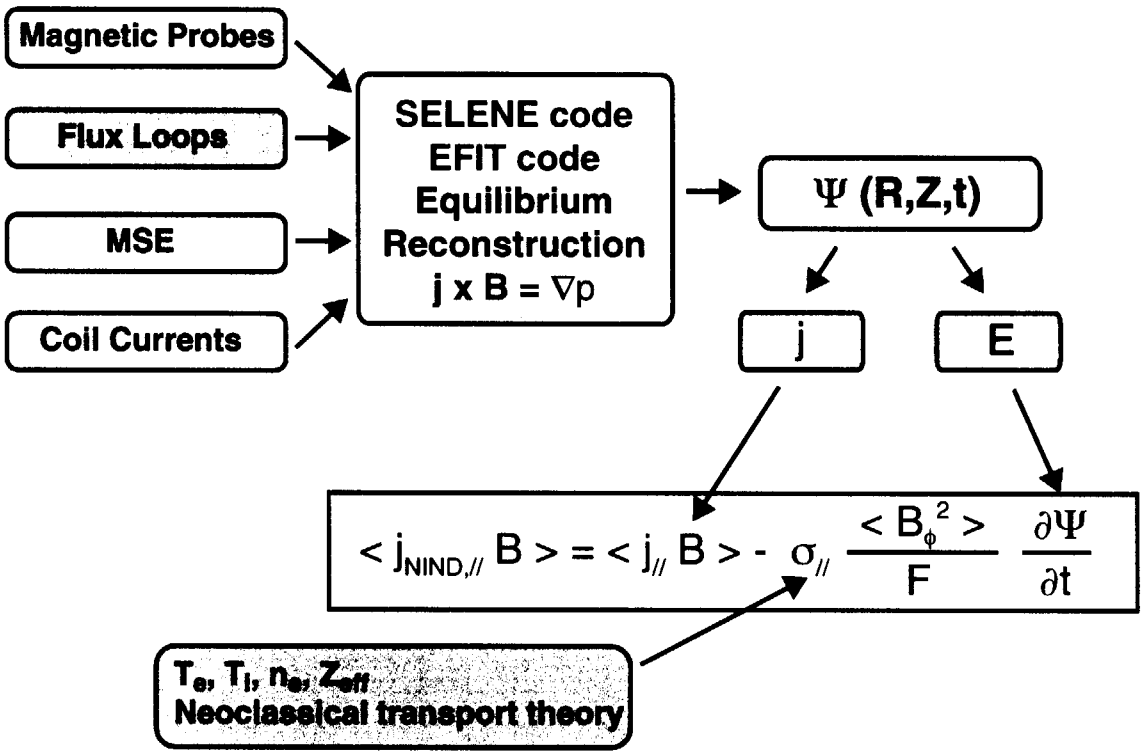

Figure 3.10: Flow of determination of the noninductive current density profile from equilibrium reconstruction and profile measurement. SELENE and EFIT [79] are equilibrium reconstruction codes.

where all flux surface averages, $\sigma_{//}$ and $\partial\Psi/\partial t$ are evaluated at minor radius ρ. The conductivity $\sigma_{//}$ is calculated from the neoclassical transport theory and the measured profiles of the ion and electron temperatures, electron density and effective charge. Time derivative of the poloidal flux is calculated from a time-series of reconstructed equilibria. The period for time derivative should be chosen so that the toroidal electric field does not change much (or time evolution of the poloidal flux can be approximated to be linear) but the poloidal flux change can be evaluated in enough accuracy. All other quantities averaged on the flux surface can be evaluated from the equilibrium. Thus, the toroidal noninductive current density profile is determined from a time-series of equilibria. Flow of this analysis is illustrated in Fig. 3.10.

3.3 Computational Codes for Tokamak Plasma Simulation

In this thesis, three computational codes for tokamak plasma simulation, ACCOME [21], OFMC [15], TOPICS [80], are used to compare the experimentally measured profile of the NB driven current density with theoretical prediction.

3.3.1 ACCOME

The ACCOME (**A**nalyzer for **C**urrent drive **CO**nsistent with **M**HD **E**quilibrium) [21] code has been developed for the investigation of steady state NB-driven, ohmic, and bootstrap currents which are consistent with MHD equilibrium. The NB driven current is derived by numerically solving the eigenfunc-

tions of the bounce-averaged Fokker-Planck equation (bounce is a cycle of particle's motion in a toroidal configuration). Effects of particle trapping, energy diffusion, and bounce motion of fast ions on the NB driven current are taken into consideration. Variables of the distribution function f in Eq. (1.1) is separated as

$$f(v,\lambda,\Psi) = s(\Psi)\tau_s(\Psi)\sum_n a_n(v,\Psi)c_n(\lambda,\Psi). \tag{3.18}$$

The volume source of the NB fast ions $s(\Psi)$ is calculated from the NB geometries, profiles of temperatures, density and $Z_{\rm eff}$, and the ionization model. The gaussian beam profile with a finite beam width is taken into consideration. The slowing down time τ_s is evaluated from temperature and density. The energy diffusion term a_n is given by

$$\begin{aligned} a_n(v,\Psi) &= \frac{1}{v^3+v_c^3}\left[\frac{v^3}{v_b^3}\frac{v_b^3+v_c^3}{v^3+v_b^3}\right]^{\gamma_n Z_2/6} \quad (v<v_b), \\ &= \frac{1}{v_b^3+v_c^3}\exp\left[-\frac{2(1+v_c^3/v_b^3)}{T_e/E_b+(T_i/E_b)(v_c^3/v_b^3)}\frac{v-v_b}{v_b}\right] \quad (v>v_b), \end{aligned}$$

where $v_b=\sqrt{2E_b/m_b}$, $v_c(\Psi)=\sqrt{2E_C/m_b}$ is the local critical velocity;

$$Z_2 = \left(\sum_i \ln\Lambda_i n_i Z_i^2/m_b\right) / \left(\sum_i \ln\Lambda_i n_i Z_i^2/m_i\right),$$

$\ln\Lambda_i$ denotes the Coulomb logarithm for the i th bulk ion species, and γ_n the n th eigenvalue. The bounce-averaged differential equation for eigenfunction c_n can be written as [81]

$$\frac{1}{R(\lambda,\lambda_t)}\frac{d}{d\lambda}\left[(1-\lambda^2)Q(\lambda,\lambda_t)\frac{dc_n}{d\lambda}\right]+\gamma_n c_n = 0,$$
$$R(\lambda,\lambda_t)=\frac{2}{\pi}K\left[\left(\frac{\lambda_t}{\lambda}\right)^2\right],\ Q(\lambda,\lambda_t)=\frac{2}{\pi}E\left[\left(\frac{\lambda_t}{\lambda}\right)^2\right],$$

where λ_t is the pitch of the barely-trapped particles, and K and E are the complete elliptic integrals of the first and the second kinds, respectively. The effect of bounce motion of fast ions as well as the effect of particle trapping are taken into consideration in this equation. These eigenfunctions $c_n(\Psi)$ and eigen values γ_n are numerically derived.

The bootstrap current is evaluated for multi-species ions including impurity and fast ions on the basis of the Hirshman-Sigmar moment approach [23, 8]. The bootstrap current density averaged over each flux surface, is calculated as

$$\left\langle j_{//}^{\rm BS}\cdot B\right\rangle - R_t B_T p_e \sum_a \frac{T_a}{|Z_a|T_a}\left(L_{31}^a\frac{\partial}{\partial\Psi}\ln p_a + L_{32}^a\frac{\partial}{\partial\Psi}\ln T_a\right),$$

where R_t is the geometric major radius, p_a is the pressure of the particle species denoted by "a", the effective temperature T_b for the NB fast ions is defined by $T_b \equiv p_b/m_b$, and the bootstrap coefficients L_{31}^a and L_{32}^a are evaluated by solving the neoclassical transport equation.

The flux surface averaged Faraday's law in a steady state tokamak can be written as

$$\left\langle j_{//}^{\rm OH}B\right\rangle = \sigma_{//}V_\phi F\left\langle R^{-2}\right\rangle,$$

where the toroidal one-turn loop voltage V_ϕ is spatially uniform.

All the types of plasma current described above depend on the geometry of MHD equilibrium. On the other hand, the MHD equilibrium directly depends on those current profile. Therefore, an iterative procedure is employed to obtain an MHD equilibrium solution which is consistent with computed plasma currents. The NB driven, bootstrap and ohmic current density profiles at the i th iteration step are calculated based on the $(i-1)$ th MHD equilibrium. As the NB driven and bootstrap currents and the plasma conductivity are determined from the equilibrium and given input information (NB geometries and profiles of temperatures, density and $Z_{\rm eff}$), the ohmic current is adjusted to match the total plasma current $I_{\rm p}$ with the input value by regulating a spatially uniform value of the toroidal one-turn loop voltage V_ϕ. Then, ACCOME solves the i th MHD equilibrium having the profiles of the current density (sum of the NB driven, bootstrap and ohmic current densities) and pressure (sum of the thermal and fast ion fractions) under the fixed boundary condition. These calculation of plasma current and MHD equilibrium are executed iteratively until the value of $\left\langle j_{//}B\right\rangle$ at each radial mesh point is converged well; that is,

$$\left|\left(\left\langle j_{//}B\right\rangle_i - \left\langle j_{//}B\right\rangle_{(i-1)}\right) / \left\langle j_{//}B\right\rangle_i\right| < \epsilon,$$

where ϵ is usually set at $\lesssim 10^{-2}$.

The input and output quantities in the experimental analysis mode are summarized below. The inputs are the measured profiles of temperatures, density and $Z_{\rm eff}$, information on NBs (beam energies, injection powers and geometries), plasma boundary, total plasma current, vacuum toroidal magnetic field and currents of the poloidal field coils. The outputs are the MHD equilibrium including the total current density profile, the noninductive (NB and bootstrap) and ohmic current density profiles, the toroidal one-turn loop voltage V_ϕ, power deposition profiles for bulk species and the shinethrough power. The shinethrough power is carried by particles not ionized in plasma and goes to the counter-facing first wall. Before the MSE spectroscopy and the analysis method of noninductive current have been established, only the macroscopic quantities such as the internal inductance, neutron yield, fast ion stored energy, surface loop voltage and shinethrough power could be compared to measurements. In this thesis, the ACCOME prediction of the NB driven current density profile is validated from comparison with the measured one.

3.3.2 OFMC

The OFMC (**O**rbit **F**ollowing **M**onte **C**arlo) code solves the fast ion distribution function in a manner different from that in ACCOME. OFMC follows test particles' trajectories in the background plasma with ionization, collision and charge-exchange processes considered.

First, the fast ion birth profile is determined for the specified NB injections. Trajectories of the produced fast ions are followed by numerical integration of the guiding center equations of motion. The guiding center equations in the toroidal coordinate $\boldsymbol{r} = (R, Z, \phi)$ are

$$\frac{d\boldsymbol{r}}{dt} = \frac{1}{eZ_{\rm b}}\left(\mu_{\rm m} + \frac{m_{\rm b}}{B}v_{\rm g,//}^2\right)\frac{\boldsymbol{B}}{B}\times\frac{\nabla B}{B} + \frac{\boldsymbol{B}}{B}v_{\rm g,//},$$

$$\frac{dv_{g,//}}{dt} = -\frac{\mu_m}{m_b}\frac{\partial B}{\partial \ell},$$

where $\mu_m = m_b v_{g,\perp}^2/2B$ the magnetic moment, $v_{g,//}$ and $v_{g,\perp}$ are the guiding center velocities parallel and perpendicular to the magnetic field line, and ℓ the length along the field line.

The collisional process of fast ions are simulated by a technique of Monte-Carlo. The mean values and mean square deviations of the longitudinal and transverse components of the velocity change due to Coulomb collision with field particles, Δv_l and Δv_t, respectively, are given by analytical formulas using temperatures, density and masses and charge numbers of field particles and fast ions when field particles have Maxwellian velocity distributions. In the Monte-Carlo simulation, Δv_l and Δv_t are computed at every time step by generating normal random numbers with the mean values and the mean square deviations given by these analytical formulas. The charge-exchange process of fast ions is also simulated by a Monte-Carlo technique using the charge-exchange reaction rate $\langle \sigma v \rangle_{CX}$.

OFMC follows test particles' trajectories until all the injected particles are lost or thermalized. The loss processes are classified as the ripple, orbit and charge-exchange losses according to their physical mechanisms. The ripple loss is caused from the toroidal field ripple structure, i.e., the asymmetric magnetic field in toroidal direction originating from the finite number of toroidal coils. Thus, the effect of ripple is important near the toroidal field coils at outboard. The particles trapped in the toroidal field ripple (between adjacent toroidal coils) experience the ripple-enhanced banana drift and the orbit change due to collisions, and some particles hit the first wall before they are thermalized. Orbit loss occurs when particles have drift orbits leading to the first wall. In collisionless case, some particles are "born" to suffer orbit loss, depending on the birth coordinates in the phase space. In collisional case, particles initially running on the "orbit loss" trajectories are possible to change their orbits so as not to suffer orbit loss due to collisions, and vice versa.

The inputs for the OFMC code are the measured profiles of temperatures, density and Z_{eff}, information on NBs and the plasma MHD equilibrium. The outputs are the fast ion distribution function, heat and momentum transfer profiles for bulk plasma species, lost power fractions due to the shinethrough and the ripple, orbit and charge-exchange processes, and the NB driven current density profile. The quantities which can be compared to the measurements are the NB driven current density profile and the shinethrough power. The OFMC calculation is compared to the measured NB driven current density profile in this thesis. The iterative analysis of self-consistent MHD equilibrium employed in ACCOME is not implemented in OFMC because Monte-Carlo calculation requires a very long CPU time.

3.3.3 TOPICS

The TOPICS (**TO**kamak **P**rediction and **I**nterpretation **C**ode **S**ystem) has been developed to solve transport and simulate a tokamak plasma evolution. It can treat both time-dependent and steady state solutions. In a full simulation study, TOPICS solves a time evolution of plasma discharge based on given transport models for heat, particle, momentum and current density, starting from the given initial plasma state. In the experimental analysis of this thesis, time series of profiles of temperatures, density and Z_{eff}

are given as inputs, and so the transports of heat and particle are not solved (instead, diffusion coefficients for heat and particle transports are obtained as outputs).

In a time-dependent analysis mode, TOPICS solves the diffusion equations of ohmic current density, heat and particle based on the specified transport models. Generally, ohmic current diffusion obeys the neoclassical transport theory, while the anomalous term is needed in heat and particle transport to reproduce the experimental profiles of temperatures and density. The NB fast ion distribution function is calculated by solving the Fokker-Planck equation in the similar way as in ACCOME. The noninductive current densities by NB, RF and bootstrap current are calculated at each time step. Plasma equilibrium is solved at each time step so as to have profiles of the total current density (sum of the ohmic and noninductive current densities mentioned above) and pressure (sum of the thermal and fast ion fractions).

In section 4.3.1 of this thesis, a time-dependent analysis is executed. Time evolutions of the total current density and pressure profiles are compared with the measured ones, and the theoretical models adopted in TOPICS are validated. In section 5.2.3, the fast ion pressure profile calculated using TOPICS is compared with the measurement in order to evaluate the effect of MHD instability on fast ion transport which is not implemented in TOPICS.

4. Characteristics of Current Drive by High Energy Neutral Beam

4.1 N-NB current drive experiment

Current drive characteristics of N-NB have been investigated experimentally and the theory of neutral beam current drive has been tested [82]. In 4.1.1, the response of plasma parameters to N-NB injection is described. The spatial profile of the N-NB driven current density and the dependence of the current drive efficiency on plasma and beam parameters, such as the beam energy E_B and the electron temperature T_e, are discussed and compared with theoretical prediction.

4.1.1 Effect of N-NB injection on plasma

In the N-NB current drive experiments discussed in this thesis, the plasma configuration (Fig. 4.1) was chosen so that the diagnostics essential for current drive analysis, i.e., MSE spectroscopy for internal magnetic field profile and Thomson scattering for electron temperature and density profiles, cover the whole plasma cross section from the magnetic axis to the plasma surface for equilibrium reconstruction and derivation of plasma conductivity profile with sufficient accuracy. The ion temperature and toroidal rotation velocity measurement (CXRS : Charge eXchange Recombination Spectroscopy) also covers the region from the normalized minor radius of ~ 0.2 to the surface. The lower unit of N-NB passes through the magnetic axis in this configuration. The P17 and P13 MSE systems view the counter-directional tangential P-NB (#7B). CXRS views an upper perpendicular P-NB. Plasma discharge (E32460) has a plasma current of $I_P = 1$ MA, a toroidal magnetic field of $B_T = 3.5$ T and a line-averaged electron density of $\bar{n}_e = 0.9 \times 10^{19}$ m^{-3}. Figure 4.2 shows discharge waveforms of injection powers of N-NB (P_{NNB}) and P-NB (P_{PNB}), surface one-turn voltage V_{surf}, plasma stored energy W_{dia}, neutron emission rate S_n, line-average electron density $\bar{n}_e$, central electron and ion temperatures $T_e(0)$, $T_i(0)$ and toroidal rotation velocity near the magnetic axis V_T. The resistive decay of the plasma current is compensated by the inductive plasma current driven by the toroidal voltage induced by the ohmic coil under constant I_P control. Thus, V_{surf} can be a simple measure of the inductive current fraction, although the change in plasma resistivity by plasma heating and the loop voltage profile should be considered to evaluate the

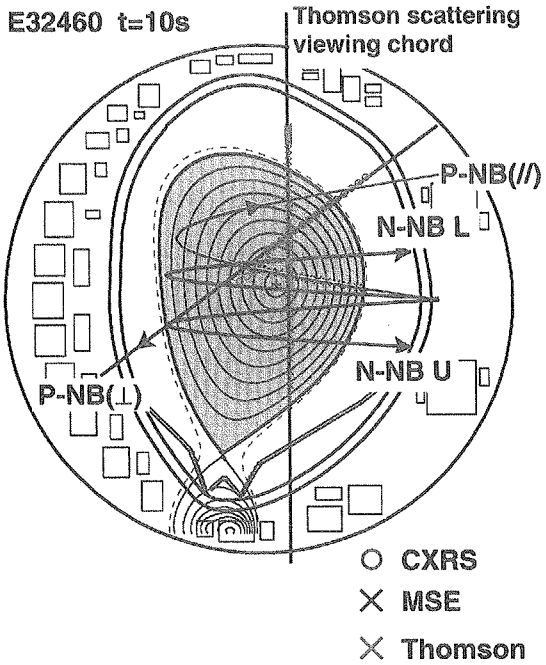

Figure 4.1: Plasma configuration (poloidal cross-section) of pulse E32460. Trajectories of N-NB (Upper and Lower units), tangential P-NB injected for MSE spectroscopy and upper perpendicular P-NB injected for CXRS are projected. The measured spatial points of MSE (blue crosses), CXRS (red open circles) and Thomson scattering (green crosses) are also shown. The viewing chord of Thomson scattering lies vertically crossing the plasma near the magnetic axis.

inductive fraction more precisely, as described in 4.1.2. The plasma stored energy consists of thermal energies of bulk ions (deuterium), electrons and impurity (dominantly, carbon) ions, and the energy of fast ions produced by NB injection. The plasma stored energy determined from the diamagnetic toroidal flux measurement, $W_{\rm dia}$, is used in JT-60U. The D-D fusion reaction produces 2.45 MeV neutrons. The measured $S_{\rm n}$ consists of neutrons produced by the D-D fusion reactions among thermal ions, beam and thermal ions, and beam ions. Increasing the deuterium temperature and density and the injected beam power increases $S_{\rm n}$. The beam energy $E_{\rm B}$ is 360 keV and $P_{\rm NNB}$ is 3.7 MW. The pulse length ($>$ 2 s) is sufficiently longer than the slowing-down time of N-NB fast ions, which is 0.5-0.65 s within the inner half minor radius where 60 % of the N-NB injected power is absorbed. P-NBs of 3 MW at $E_{\rm B} = 83$ keV are also injected for measuring the current density profile by MSE and the ion temperature profile by CXRS. The plasma stored energy and the neutron emission rate increase during N-NB injection (t = 8-10.2 s). The increase in $W_{\rm dia}$ comes mainly from the buildup of fast ions. The large increase in $S_{\rm n}$ is mostly due to the beam-thermal and beam(N-NB)-beam(P-NB) reactions. Due to the low $T_{\rm i}$ and low density in E32460, the beam-beam reaction dominates $S_{\rm n}$ (about 84 %), and the beam-thermal reaction contributes 16 %. The thermal-thermal reaction is negligibly small. The central electron temperature $T_{\rm e}(0)$ increases during N-NB injection, while increase in $T_{\rm i}(0)$ is small (Fig. 4.2). The $T_{\rm e}$ profiles just before N-NB injection (t = 8 s) and at the end of the N-NB pulse (t = 10 s) and $T_{\rm i}$ profiles during the very

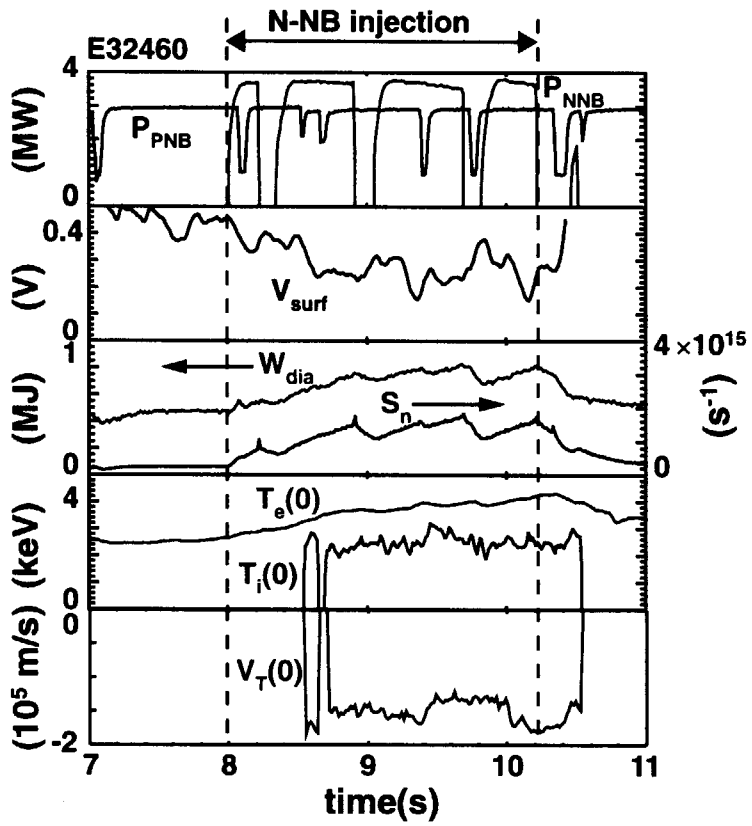

Figure 4.2: Discharge waveforms of pulse E32460. Shown are time evolutions of the NB injection powers (P_{NNB} , P_{PNB}), the surface one-turn voltage(V_{surf}), the plasma stored energy W_{dia} , the neutron emission rate S_{n} , the line-average electron density $\bar{n}_{\mathrm{e}}$, the central electron and ion temperatures $T_{\mathrm{e}}(0)$, $T_{\mathrm{i}}(0)$ and the toroidal rotation velocity near the magnetic axis V_{T}.

early phase of N-NB injection (t = 8.55 s) and t = 10 s are shown in Fig. 4.3. The electron temperature increases mostly within the inner half minor radius, while the T_{i} profile does not change much. These results indicate the dominance of electron heating by N-NB with central deposition ($T_{\mathrm{e}}(0) \sim 4$ keV, $T_{\mathrm{i}}(0) \sim 2.7$ keV). According to the Orbit Following Monte Carlo (OFMC) code calculation, the powers absorbed by electrons and ions during the slowing-down process of N-NB injected fast ions are 61 % and 14 % of the injected power, respectively, while 26 % and 35 % of the injected P-NB power go to electrons and ions, respectively. Shine-through losses are 21 % for N-NB and 19 % for P-NB and other losses due to toroidal field ripple, banana drift orbit and charge exchange are 4 % for N-NB and 20 % for P-NB. As shown in Fig. 4.4 (a), the electron density stays nearly unchanged because of the low particle fueling by N-NB. The change in toroidal rotation velocity due to N-NB injection is not significant [Fig. 4.4 (b)]. The plasma toroidal rotation velocity ($-1 \sim -2 \times 10^5$ m/s at the plasma center) is negligible compared to the velocity of N-NB fast ions carrying the non-inductive current (4.5×10^6 m/s for the N-NB ions). A gradual decrease in the surface voltage V_{surf} from 0.45 V to less than 0.3 V occurs for two reasons. One is the gradual T_{e} increase because the plasma conductivity is proportional to $T_{\mathrm{e}}^{3/2}$. The other is relaxation of the electric field (the loop voltage profile relaxes towards a flat profile). The loop

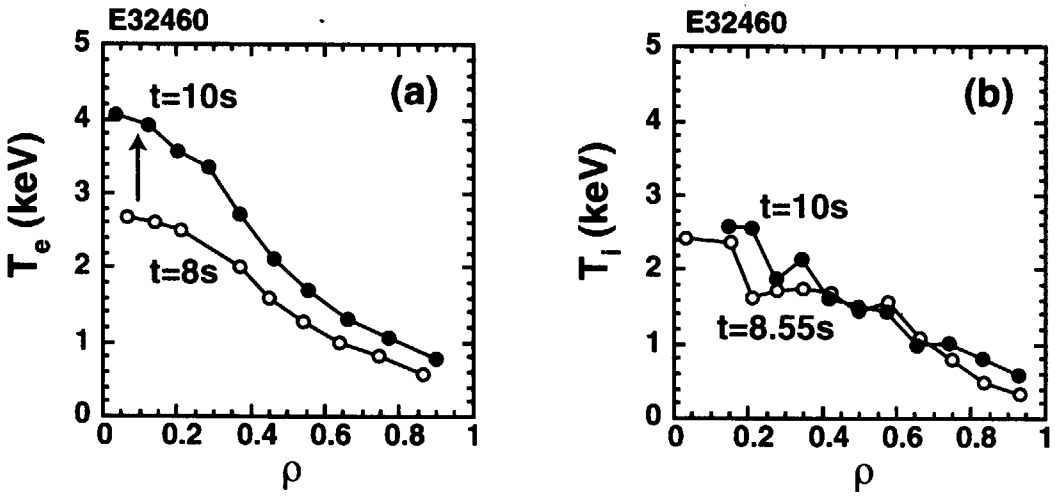

Figure 4.3: Profiles of (a) electron temperature T_e at t = 8 s and 10 s and (b) ion temperature T_i at t = 8.55 s and 10 s.

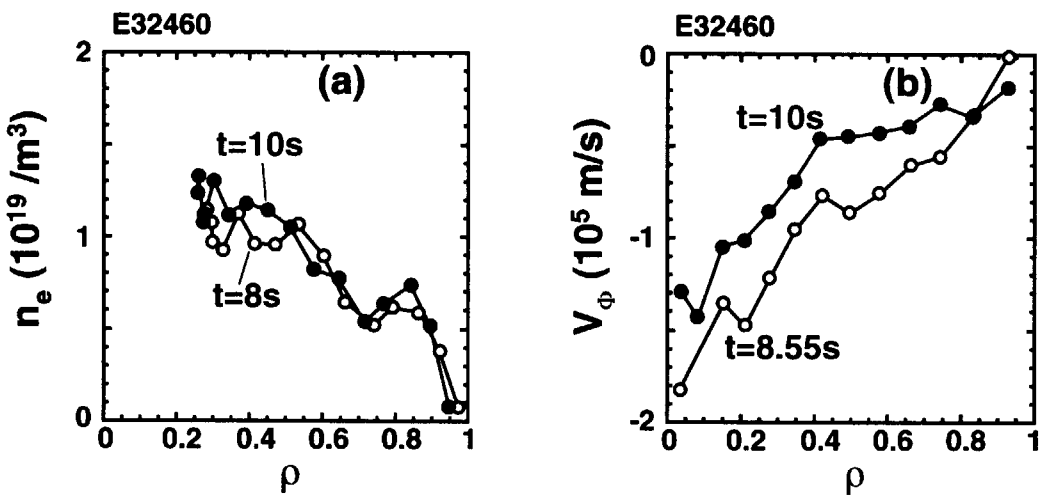

Figure 4.4: Profiles of (a) electron density n_e at t = 8 s and 10 s and (b) toroidal rotation velocity V_T at t = 8.55 s and 10 s.

voltage is applied at the plasma surface by a flux swing of the ohmic coil, and penetrates towards the inside by diffusion.

4.1.2 Determination of the non-inductively-driven current profile

The plasma current density profile $j(\rho)$ and the one-turn loop voltage profile $V_{\rm loop}(\rho)$ must be determined in order to evaluate the N-NB driven current profile $j_{\rm NNB}(\rho)$ [78, 83]. As described in chap. 3, $j(\rho)$ is obtained as a result of plasma equilibrium reconstruction and $V_{\rm loop}(\rho)$ is determined from the time-series of reconstructed plasma equilibria. In a cylindrical or toroidal plasma, the plasma current penetrates towards the magnetic axis, and the current density profile peaks up with time, and becomes stationary when the loop voltage profile becomes spatially uniform. Normally, the $q = 1$ rational surface appears during the discharge evolution as the current profile peaks up. Here, q is the safety factor introduced in 3.1. The sawtooth instability occurs when the $q = 1$ surface exists in tokamak plasmas. Such an instability should be avoided for current drive analysis.

The non-inductively-driven current profile was analyzed during the time interval t = 8.5-9 s in E32460 described in 4.1.1. Figure 4.5 shows the safety factor profile $q(\rho)$ at t = 9 s. The central safety factor (the minimum value in a normal magnetic shear configuration) $q(0)$ is 1.15 and there is no $q = 1$ surface. No sawtooth activity was observed experimentally. Thus, this discharge is suitable for loop voltage analysis. The loop voltage profiles for E32460 and a similar discharge without N-NB injection are shown in Fig. 4.6. A large decrease of $V_{\rm loop}$ is observed in the central region. This is due to both reduction of the inductive current density (N-NB current drive effect) and increase in the conductivity through electron temperature increase (N-NB heating effect). The loop voltage in the peripheral region away from the N-NB deposition region also decreases, because the heat flux caused by diffusion from inside to outside increased the electron temperature. The plasma conductivity profile $\sigma(\rho)$ was calculated from the measured profiles of $T_{\rm e}$, $n_{\rm e}$ and $Z_{\rm eff}$ using the neoclassical plasma transport theory (Fig. 4.7). The inductive current density profile $j_{\rm OH}(\rho)$ was calculated from $V_{\rm loop}(\rho)$ and $\sigma(\rho)$ as shown in Fig. 4.8. The total current density (equilibrium current density) j and non-inductive current density ($j_{\rm NIND} \equiv j - j_{\rm OH}$) are also shown in Fig. 4.8. The analysis method used here gives the total non-inductive current density and can not separate the bootstrap current and the NB driven currents by each NB unit. Thus, in the present case (E32460), the N-NB driven current density profile $j_{\rm NNB}(\rho)$ is determined by subtracting the calculated bootstrap current density and the P-NB driven current density from the measured $j_{\rm NIND}$. Validity of the neoclassical transport theory in determining the bootstrap current has been confirmed in JT-60U [7]. Although the argument was limited to the total bootstrap current in ref. [7], the bootstrap current profile measured subsequently in a bootstrap current dominated discharge agreed well with theoretical prediction [84]. Figure 4.9 shows the profiles of bootstrap current and P-NB driven current (counter current drive) calculated by the current-drive code ACCOME, which solves the inductive and non-inductive current density profiles which are consistent with plasma equilibrium. The N-NB driven current profile determined from measured $j_{\rm NIND}$ is compared with the result of ACCOME calculation in Fig. 4.10. ACCOME calculation was performed using two models of ionization cross-section for the injected N-

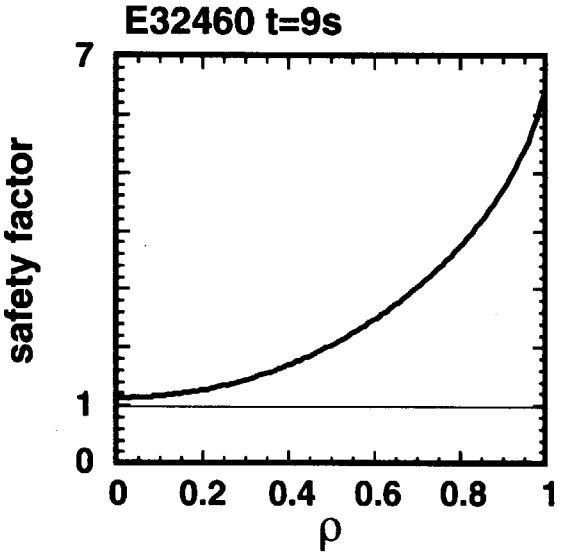

Figure 4.5: Experimentally determined safety factor profile $q(\rho)$ at t = 9 s of E32460. There is no $q = 1$ rational surface.

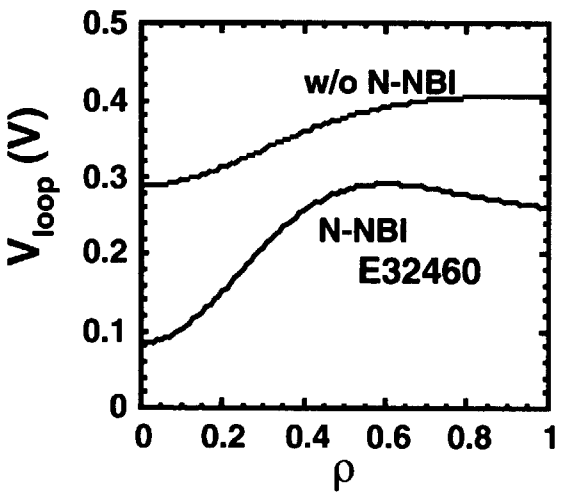

Figure 4.6: Profiles of loop voltage ($V_{\rm loop}$) for E32460 (N-NB injection) and a similar discharge without N-NB injection.

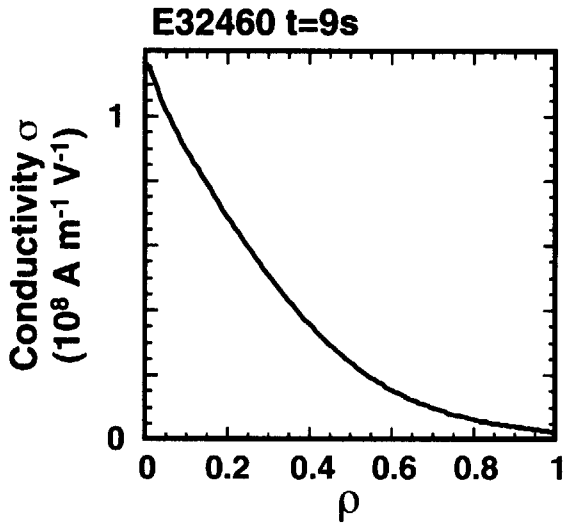

Figure 4.7: Profile of plasma conductivity $\sigma(\rho)$ at t = 9 s of E32460, calculated from $T_{\rm e}(\rho)$, $n_{\rm e}(\rho)$ and $Z_{\rm eff}(\rho)$ using the neoclassical transport theory.

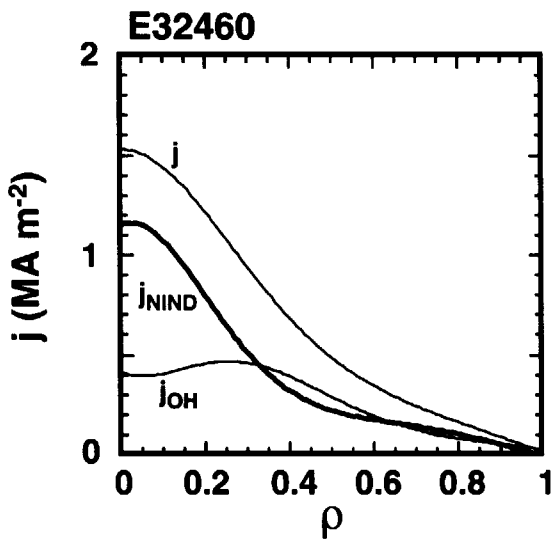

Figure 4.8: Profiles of total current density j_{total}, inductive (or ohmic) current density j_{OH} and non-inductive current density j_{nind} for E32460.

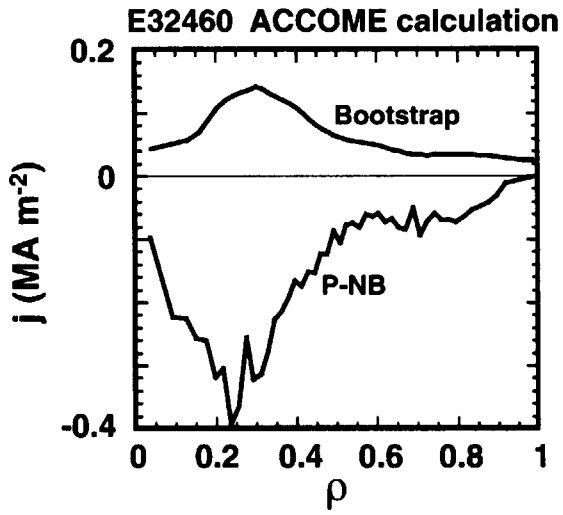

Figure 4.9: Profiles of bootstrap current density and P-NB driven current density, calculated by the ACCOME code.

NB particles, i.e., single-step model and multi-step model. The measured profile agrees well with the calculation using the multi-step model within the experimental error, due to uncertainties mainly in T_{e}, Z_{eff} and V_{loop}. The experimentally determined total N-NB driven current is 600 kA. ACCOME with the multi-step model predicted 580 kA, while ACCOME with the single-step model gave 430 kA. Validity of the multistep ionization cross-section model has also been confirmed by previous studies of the N-NB shinethrough power (power not absorbed by the plasma). Fast neutral particles of injected N-NB are ionized mainly inside the inner half minor radius for plasma parameters of E32460. Ionized particles carrying non-inductive current are well confined because tangentially injected fast particles hardly become trapped particles until they are slowed down by collisions. Thus, a centrally-peaked current density profile is expected from the on-axis trajectory of N-NB and plasma parameters of E32460. Fig. 4.11 shows the integrated N-NB driven and bootstrap currents inside each magnetic surface labelled by the normalized minor radius ρ. Due to the central deposition of N-NB, 70 % of the total N-NB driven current is within the inner half minor radius. The total bootstrap current is 140 kA, where the contribution of N-NB to the fast-ion component of bootstrap current is $\sim$ 50 kA.

4.2 Current Drive at High Electron Temperature

In the previous section, the non-inductive current density profile was determined experimentally for plasmas driven by a high energy neutral beam. The measured current density profile agreed well with theoretical prediction, using a multistep ionization model. However, the plasma temperature was relatively low ($T_{\mathrm{e}}(0) \sim 4$ keV). To increase confidence in predicting the driven current for next-step devices such as ITER and in developing a prospect for a fusion reactor, evaluation of the N-NB current

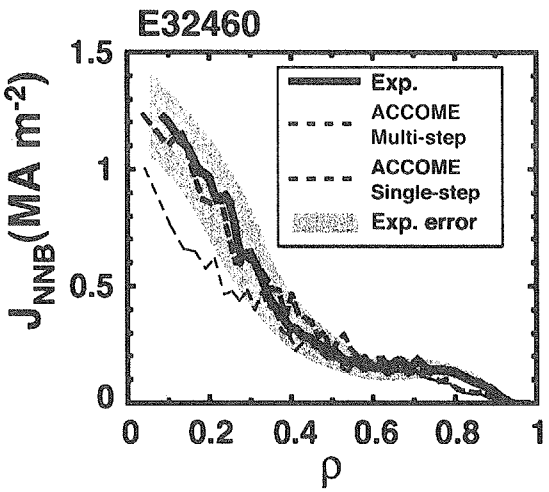

Figure 4.10: Measured (solid line) and calculated (dashed lines) N-NB driven current density profiles (j_{NNB}). Error due to uncertainties in the measurements is indicated by the shaded region. Thin and thick dashed lines correspond to theoretical calculation by ACCOME using the single-step and multi-step models for ionization cross-section for injected N-NB particles, respectively.

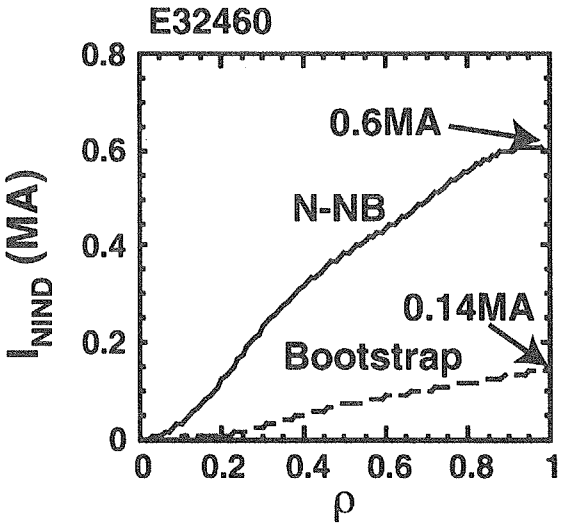

Figure 4.11: The integrated N-NB driven (solid line) and bootstrap (dashed line) currents within each flux surface as a function of normalized minor radius ρ.

drive capability in the high electron temperature regime is required.

4.2.1 Measurement of the N-NB current drive in EC heated plasmas

In order to evaluate the N-NB driven current in a high electron temperature regime with $T_{\mathrm{e}}(0) \sim$ 10 keV, ECRF (electron cyclotron range of frequencies) power has been applied to heat electrons [85]. A low density L mode plasma was employed for precise measurement of the N-NB driven current. Non-inductive current other than that driven by N-NB should be minimized because the N-NB driven current is evaluated by subtracting the bootstrap current and the driven currents by other methods (such as P-NB) from the total non-inductive current. The bootstrap current is small in low density L mode plasmas. As the P17 and P13 MSE systems view the counter-directional tangential P-NB (#7B) which drives negative current and the P3 MSE system views the co-directional tangential P-NB which drives positive current, the total P-NB driven current is nearly cancelled. The plasma configuration is shown in Fig. 4.12. The injection angle of ECRF was adjusted so as to make the rays pass through the plasma center. The toroidal magnetic field B_{T} was 3.73 T so the EC power deposition was centered near the magnetic axis. The EC resonance position for the vacuum B_{T} is shown in Fig. 4.12. The poloidal current in the plasma changes B_{T} in the plasma from the vacuum value. This is estimated about +0.015 T near the magnetic axis, corresponding to a 1.2 cm outward shift of the EC resonance. Absorption of the EC

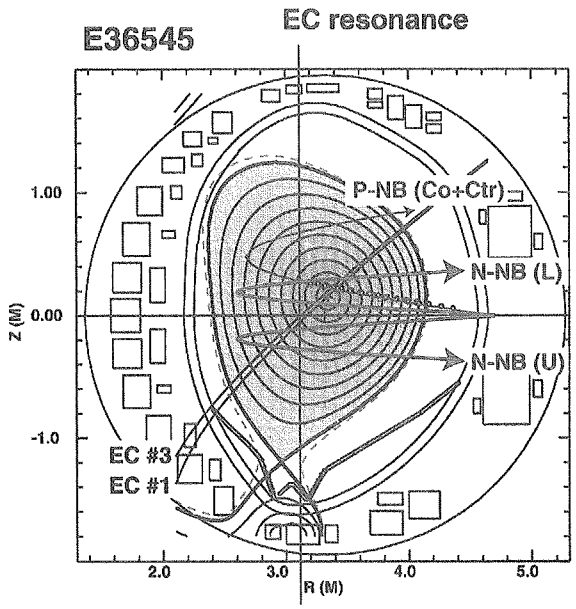

Figure 4.12: Plasma configuration (poloidal cross-section) of pulse E36545. Trajectories of N-NB (Upper and Lower units) and tangential P-NB injected for MSE spectroscopy are projected. Spatial points of MSE (open circles) are located along the P-NB orbit. Rays of two ECRF units (#1 and #3) and the resonance layer corresponding to the vacuum toroidal magnetic field are also shown.

wave occurs at a lower B_T (i.e., larger major radius R) due to the Doppler shift. Figure 4.13 shows the discharge waveforms of the EC heated plasma with N-NB injection (E36545). The plasma current was 1 MA. The line-averaged density through the central chord was kept at 0.84×10^{19} m^{-3}. Electron cyclotron wave injection (f_{EC} = 110 GHz, P_{EC} = 1.15 MW) started 0.4 s before N-NB injection (E_B = 354 keV, P_{INJ} = 3.4 MW). This is for increasing the N-NB current drive by building up more N-NB fast ions in a high T_e plasma obtained by EC heating. The central electron temperature $T_e(0)$ was raised to $\sim$ 5 keV rapidly by ECRF, and gradually increased to 6 keV with a time constant of slowing-down time of N-NB fast ions ($\sim$ 1.4 s) during N-NB injection (t = 7-8.4 s). The time evolution of the T_e profile is shown in Fig. 4.16. The T_e profile at t = 8.3 s (with N-NB and EC injection) is broader than at t = 6.95 s (EC injection only). This is because N-NB has a broader power deposition than ECRF.

After $T_e(0)$ has reached $\sim$ 5 keV at t = 6.8 s, $T_e(0)$ decreased slightly. There are two possible causes for this gradual decrease. One is as follows. As electron temperature is determined from the electron cyclotron emission (ECE), the ECE signal reflects the electron temperature in the direction perpendicular to the magnetic field line. The ECRF accelerates electrons in the perpendicular direction. Therefore, the energy diffusion in the velocity space is possible to cause the decrease in the electron temperature determined from ECE, although its time scale and decrease have not been evaluated quantitatively by solving the Fokker-Planck equation. Other possible cause is an appearance of an MHD instability in the central region where the EC wave power was deposited. Similar MHD activity occurred again at t = 7.6 s and 8 s, causing drops in T_e as shown in Fig. 4.13. Plasma discharge should be optimized to avoid such an instability in order to obtain a high T_e plasma. However, N-NB fast ions did not seem to be lost by this

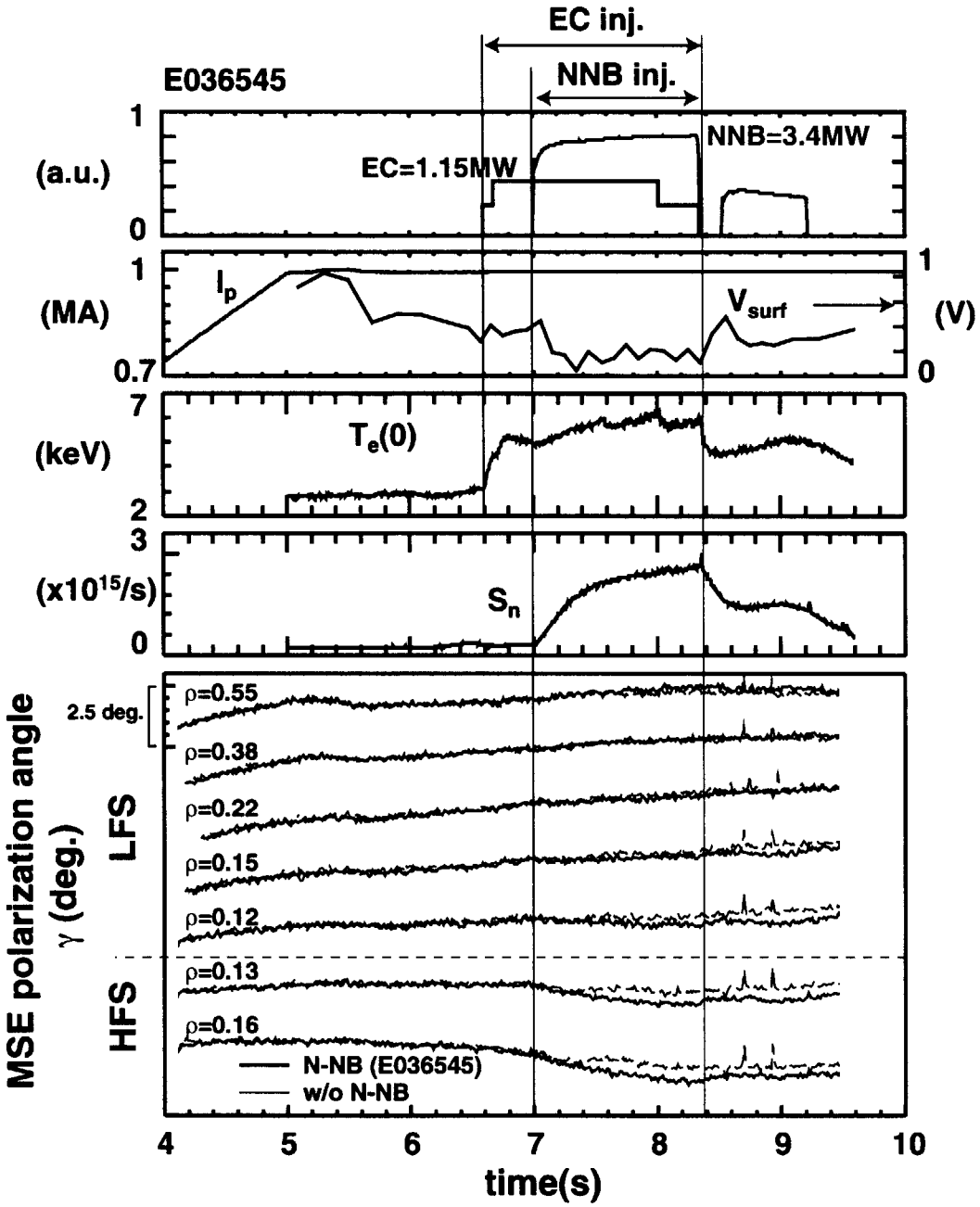

Figure 4.13: Discharge waveforms of pulse E36545. Time evolutions of the injected powers of N-NB and ECRF, the plasma current I_p, the surface loop voltage (V_{surf}), the central electron temperature $T_e(0)$, the neutron emission rate S_n , the MSE polarization angles at 7 locations from near the magnetic axis to half minor radius are shown. In the panel of MSE polarization angles, time-traces for a similar discharge without N-NB injection are shown for comparison. LFS and HFS mean lower and higher toroidal magnetic field sides of the plasma center, respectively.

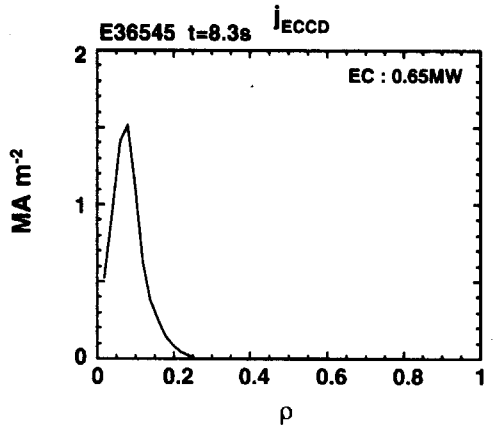

Figure 4.14: Profile of EC driven current calculated by a linear Fokker-Planck code.

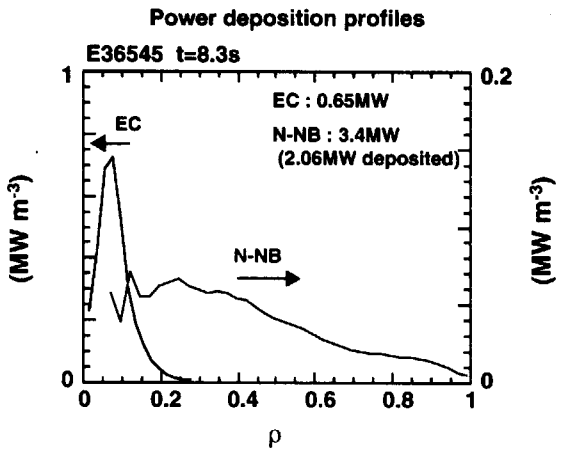

Figure 4.15: Power deposition profiles of the EC wave and N-NB injection at t = 8.3 s, calculated by a linear Fokker-Planck code and OFMC, respectively.

MHD instability because there was no clear drop in the neutron emission rate S_n which was produced mainly by reaction of the N-NB fast ions with thermal ions and P-NB fast ions. Since the EC heating and current drive are localized in a very narrow region near the magnetic axis as shown in Fig. 4.14 and 4.15, it is likely that only flux surfaces near the magnetic axis (r/a$\lesssim$ 0.1) are destroyed temporally or suffered reconnection of magnetic field lines. Therefore, we can continue analysis and discussion of E36545 except in the central region (r/a$\lesssim$ 0.1). Here, EC heating and current drive were calculation by a linear Fokker-Planck code [86], and the N-NB power deposition was calculated by OFMC. In Fig. 4.13, time-traces of polarization angles of 7 MSE channels located near the magnetic axis to half minor radius are shown. Approximate normalized minor radius of each channel is displayed. Waveforms for a similar discharge without N-NB injection are also shown for comparison. The difference between the two discharges becomes larger during N-NB injection, because of differences in current profile change due to N-NB current drive and in the Shafranov shift of the magnetic surfaces due to plasma pressure increase by N-NB injection. Time-evolutions of the poloidal magnetic flux Ψ obtained from plasma equilibrium reconstruction are shown in Fig. 4.17. The central safety factor $q(0)$ decreased with time. It was kept above one in order to avoid sawtooth activity. The time derivative of Ψ corresponds to the one-turn loop voltage at each location. During N-NB injection (t = 7-8.4 s), $d\Psi/dt$ decreased due to heating and current drive effects.

The result of non-inductive current density profile analysis for E36545 is shown in Fig. 4.18. Three periods during the discharge, i.e., before EC and N-NB injection (t = 6.38-6.6 s), during N-NB and EC injection (t = 8.1-8.34 s), and 3 s after the main N-NB pulse (very late phase of discharge, t = 11.06-11.26 s) are shown. Loop voltage profiles indicate that (a) plasma current has not penetrated fully at t = 6.38-6.6 s, (b) relatively broad profile of N-NB driven current density made the hollow region of V_{loop} wider and delayed current penetration at t = 8.1-8.34 s, and (c) plasma current profile reached a nearly

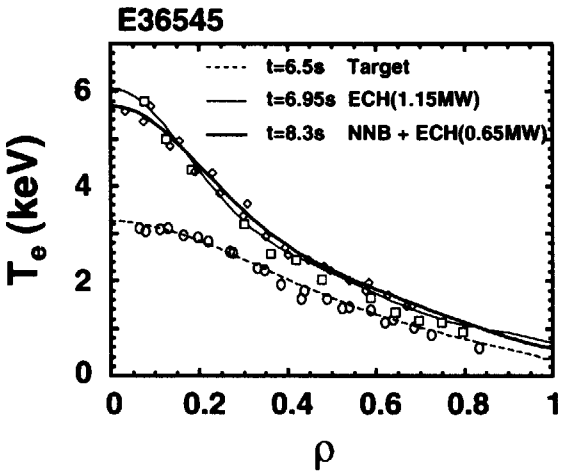

Figure 4.16: Electron temperature profiles at t = 6.5 s (target, without EC or N-NB), t = 6.95 s (EC of 1.15 MW) and t = 8.3 s (N-NB of 3.4 MW and EC of 0.65 MW).

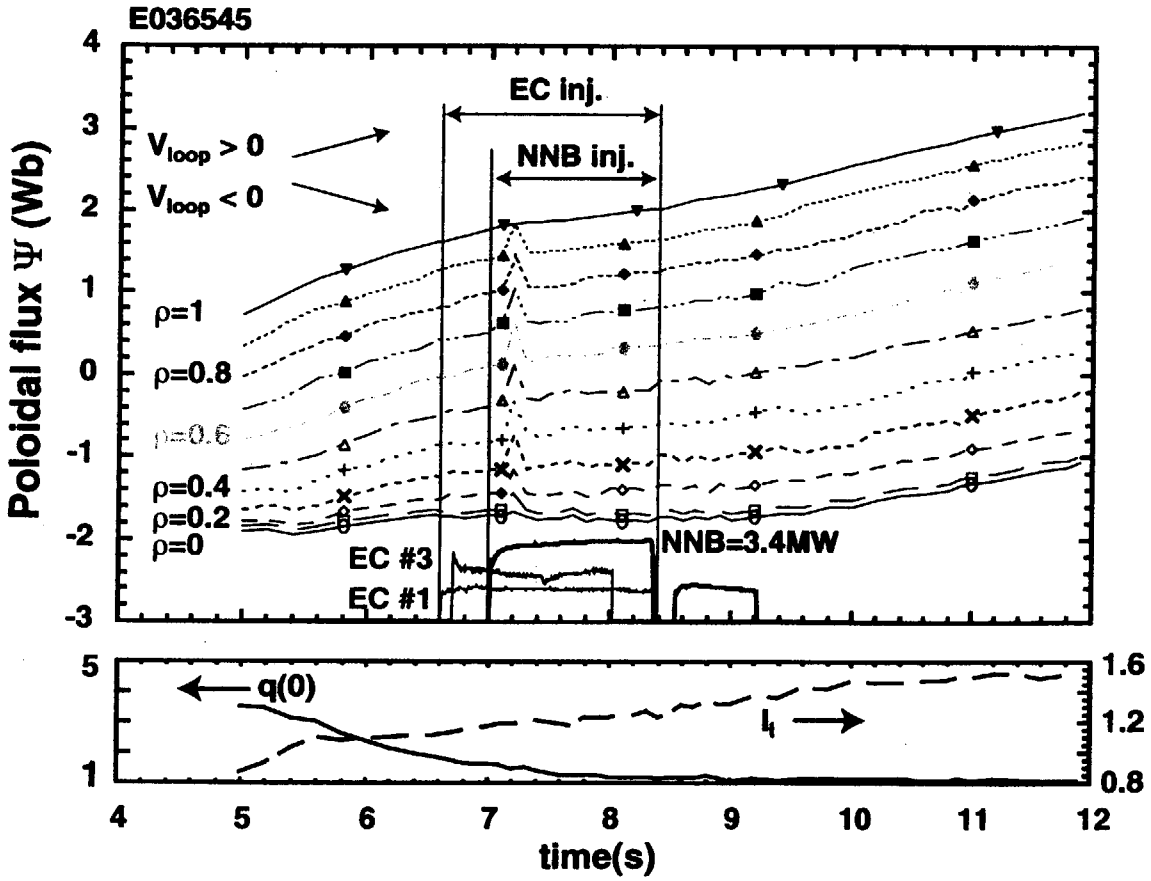

Figure 4.17: Time-evolutions of the poloidal magnetic flux Ψ for E36545 obtained from plasma equilibrium reconstruction. The central safety factor $q(0)$ and the internal inductance ℓ_i are also shown.

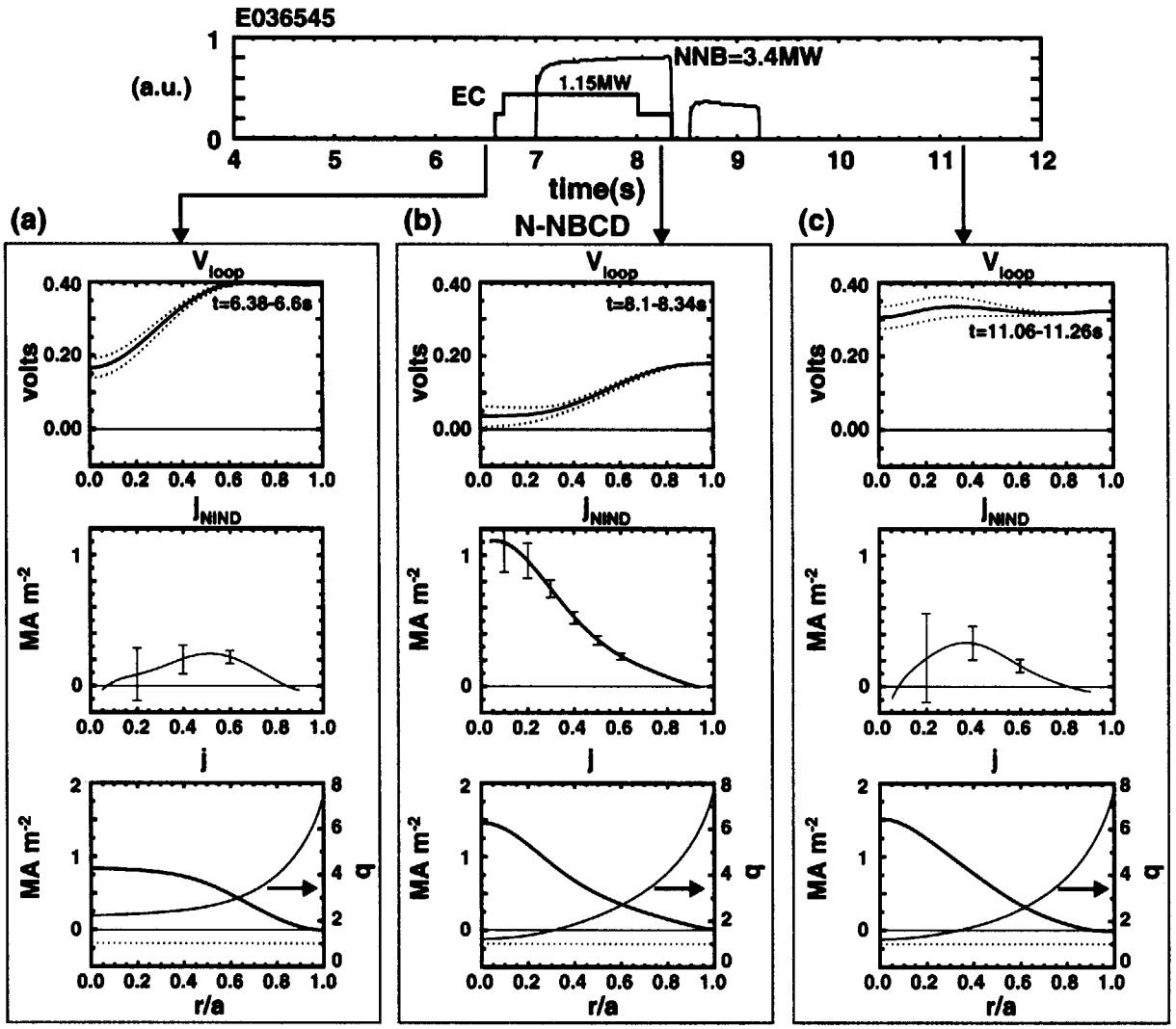

Figure 4.18: Non-inductive current density profile analyses at 3 time intervals in E36545, i.e., (a) before EC and N-NB injection (t = 6.38-6.6 s), (b) during N-NB and EC injection (t = 8.1-8.34 s) and (c) very late phase of discharge after N-NB and EC injection (t = 11.06-11.26 s). Profiles of the one turn loop voltage V_{loop}, the non-inductive current density j_{NIND}, the total current density j and the safety factor q are shown.

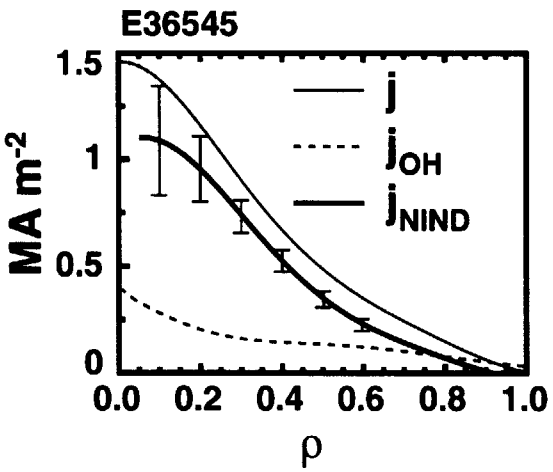

Figure 4.19: Profiles of the total current density j, the inductive component j_{OH} and the non-inductive component j_{NIND} during the time interval t = 8.1-8.34 s in E36545 are shown.

fully-relaxed state well after the N-NB pulse (t = 11.06-11.26 s). Current penetration can also be shown from time-evolutions of j and q. Non-inductive current density profile $j_{\mathrm{NIND}}(\rho)$ is very small at t = 6.38-6.6 s and 11.06-11.26 s because the bootstrap current is small due to low density and P-NB current drive is also very small due to balanced injection of co- and counter-directional beams (however, not zero due to unequal powers and difference in orbit losses of fast ions between co- and counter beams). During the time interval t = 8.1-8.34 s, non-inductive current dominates the plasma current (Fig. 4.19). The uncertainty in j_{NIND} specified in the figures mainly comes from the error in V_{loop} for the core region.

The neutron yield appears to be still increasing at the end of the N-NB pulse (t = 8.35 s) as indicated in Fig. 4.13. This means that N-NB fast ions have not been built up fully. To evaluate the fraction of the built-up N-NB fast ions compared to the steady-state value, a result of OFMC code calculation is compared with experiment in Fig. 4.20. The time-evolution of the plasma stored energy, which increases mostly due to the build-up of N-NB fast ions, is shown. Measured and calculated waveforms of plasma stored energy agree fairly well although there is a small difference which may be attributable to experimental errors in measured profiles of density and temperature. The OFMC calculation shows that N-NB fast ions build up and reach more than 95 % of the steady-state value at the end of the N-NB pulse (t = 8.35 s). Thus, calculated profiles assuming a steady-state (ACCOME, OFMC) can be compared with the measured profile. Time-evolution of the N-NB fast ion pressure profile is shown in Fig. 4.21. It takes ~1.5 s to reach a steady-state.

Measured N-NB driven current profile $j_{\mathrm{NNB}}(\rho)$ is compared with predictions of the ACCOME code and the OFMC code in Fig. 4.22. Here, j_{NNB} was evaluated by subtracting the calculated bootstrap current and the P-NB driven current from the measured non-inductive current j_{NIND} in Fig. 4.19. Although the ACCOME code assumes fast ions to stay on the magnetic surface where they are ionized, the result coincides with the OFMC result. The measured profile agrees fairly well with these calculations. There is a possibility that the EC driven current peaked in a narrow region near the magnetic axis (Fig.

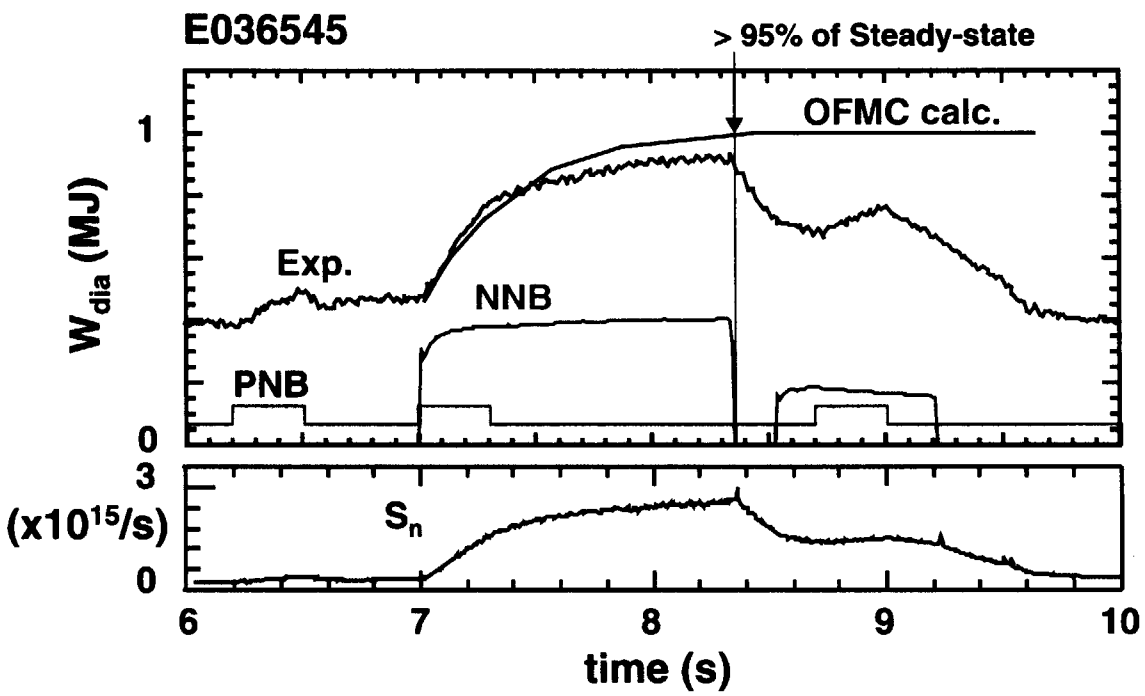

Figure 4.20: Time-evolution of the plasma stored energy is compared between measurement and OFMC calculation in E36545 to evaluate the fraction of N-NB fast ions compared to the steady-state value. Measured neutron yield S_n is also shown to compare the saturation time (slowing-down time).

4.14), which can not be resolved experimentally, affects equilibrium reconstruction and causes an error in $j_{\rm NNB}$ near the magnetic axis. The total EC driven current is calculated to be 60 kA, which is 10 % of the measured N-NB driven current.

4.2.2 Verification of NNB current drive capability at high electron temperature regime

The N-NB driven current density profile has been determined at an electron temperature of 10 keV obtained with three units of ECRF systems. Figure 4.23 shows discharge waveforms of pulse E36736. The plasma current and the toroidal magnetic field were 1.2 MA and 3.73 T, respectively. The line-averaged density through the central chord was kept at 0.74×10^{19} m^{-3}. The plasma configuration was the same as in E36545 (Fig. 4.12). Injection of N-NB ($E_{\rm B}$ = 360 keV, $P_{\rm INJ}$ = 3.75 MW) and EC wave ($P_{\rm EC}$ = 1.6 MW) started at t = 6.5 s. The central electron temperature $T_{\rm e}(0)$ increased rapidly to $\sim$ 8 keV by EC heating, and gradually increased up to 10 keV with a time constant of the slowing-down time of N-NB fast ions ($\sim$ 3 s). Figure 4.24 (a) shows the deposition profiles of the absorbed power by electrons for N-NB and ECRF calculated by the OFMC code and a linear Fokker-Planck code. Figure 4.24 (b) shows the electron temperature profiles just before N-NB and EC injection (t = 6.4 s), during the early phase of N-NB and EC injection (t = 6.8 s) and at the end of N-NB and EC injection (t = 7.9 s). At t = 6.8 s, a strongly peaked electron temperature was formed due to a narrow EC power deposition near the plasma center. At t = 7.9 s, higher and broader $T_{\rm e}$ profile with a central value of 10 keV was

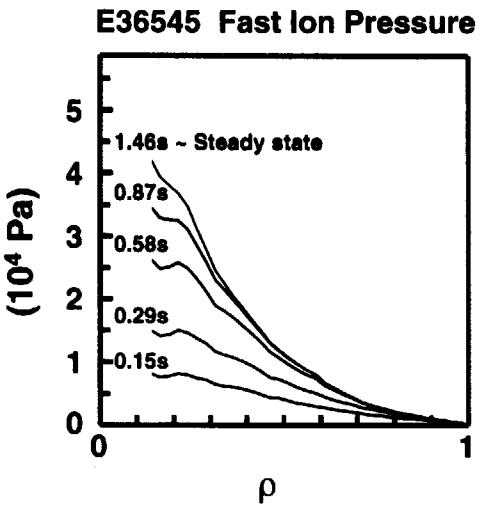

Figure 4.21: Time-evolution of the N-NB fast ion pressure profile calculated by the OFMC code.

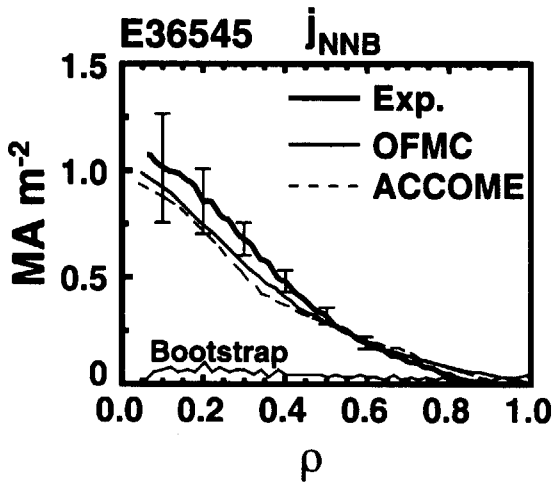

Figure 4.22: Measured and calculated N-NB driven current density profiles (j_{NNB}) are compared. Bootstrap current profile calculated by the ACCOME code is also shown.

obtained. The plasma stored energy W_{dia} and the neutron production rate S_{n} also increased over the time scale of slowing-down time of N-NB ions. For accurate determination of the N-NB driven current and comparison with theory, MHD instability should be avoided. By keeping the central safety factor $q(0)$ above 1 during N-NB injection, the sawtooth instability was avoided.

Time evolutions of the reconstructed poloidal flux from the magnetic axis to half minor radius are also shown in Fig. 4.23. Positive and negative slopes of each trace corresponds to positive and negative one-turn loop voltage at each location, respectively. During the interval t = 6.5-7.96 s, the loop voltage inside $\rho = 0.4$ became negative, which means the plasma current was overdriven by a large non-inductive current driven by N-NB and ECRF. At t = 7.96 s, 2 gyrotrons of the ECRF system faulted and the ECRF power decreased to 0.5 MW. The magnitude of the negative loop voltage became smaller due to the reduction of EC driven current and partially due to reduction of the N-NB current drive caused by a reduced T_{e}. The non-inductive current density profile was analyzed at the end of the first N-NB pulse (t = 7.9 s). The profile of the loop voltage V_{loop} shown in Fig. 4.25 indicates a strong overdrive in the central region. This was caused by N-NB current drive and a centrally localized profile of EC driven current ($\rho < 0.2$ in this discharge). Figure 4.26 shows the N-NB driven current profile J_{NNB} determined from the measurement (solid line) and theoretical prediction (dashed line). The measured J_{NNB} was determined by subtracting the thermal and P-NB fast ion components of the bootstrap current and the EC driven current from the non-inductive current density profile determined from the V_{loop} profile. The bootstrap current was calculated by the transport code TOPICS [80] and the EC driven current was evaluated from a measurement in a similar discharge with only EC injection. The bootstrap current density profile is also shown in Fig. 4.26. The shaded region indicates experimental error due to uncertainties in profiles of temperature, density and effective charge, V_{loop} and the estimation of the EC driven cur-

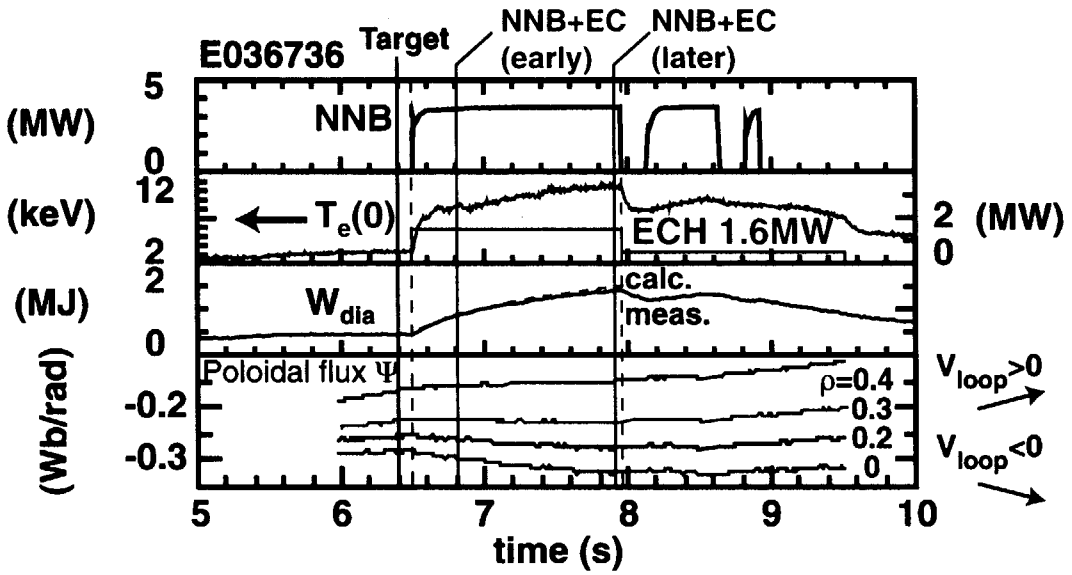

Figure 4.23: Discharge waveforms of pulse E36736. Shown are injection powers of N-NB and ECH, the neutron production rate S_n, the central electron temperature $T_e(0)$, the measured and simulated plasma stored energy W_{dia} and the poloidal flux at $\rho = 0 \sim 0.4$.

rent. The theoretical result calculated by OFMC is shown. The OFMC code is considered to be more precise in treating the beam ions than the current drive code ACCOME, because the OFMC code follows beam ion orbits which deviate from the equilibrium flux surfaces, while ACCOME assumes beam ions to stay on the flux surface. The N-NB fast ions have built up to 84 % of the steady-state value after 1.45 s of injection, based on comparison of time evolutions of the measured W_{dia} and calculated W_{dia} by OFMC, as shown in Fig. 4.23. Thus the OFMC j_{NNB} profile in Fig. 4.26 was adjusted to 84 % of the calculated steady-state value. The experimentally determined and theoretically calculated profiles of the N-NB driven current agrees within the experimental uncertainty. The experimentally measured N-NB driven current reached 1 MA, a record value of NB driven current in JT-60U. The corresponding current drive efficiency η_{CD} was 1×10^{19} $Am^{-2}W^{-1}$.

Figure 4.27 shows a comparison of the experimentally measured N-NB driven current with the calculated current in the range 0.1 - 1 MA. This confirmation of N-NB current drive capability with a high degree of accuracy over a wide range of electron temperatures up to ~10 keV and $\eta_{CD} \sim 1 \times 10^{19}$ $Am^{-2}W^{-1}$ proves the validity of theoretical prediction and gives greater confidence in predicting the performance of high energy neutral beam current drive in ITER and fusion reactors.

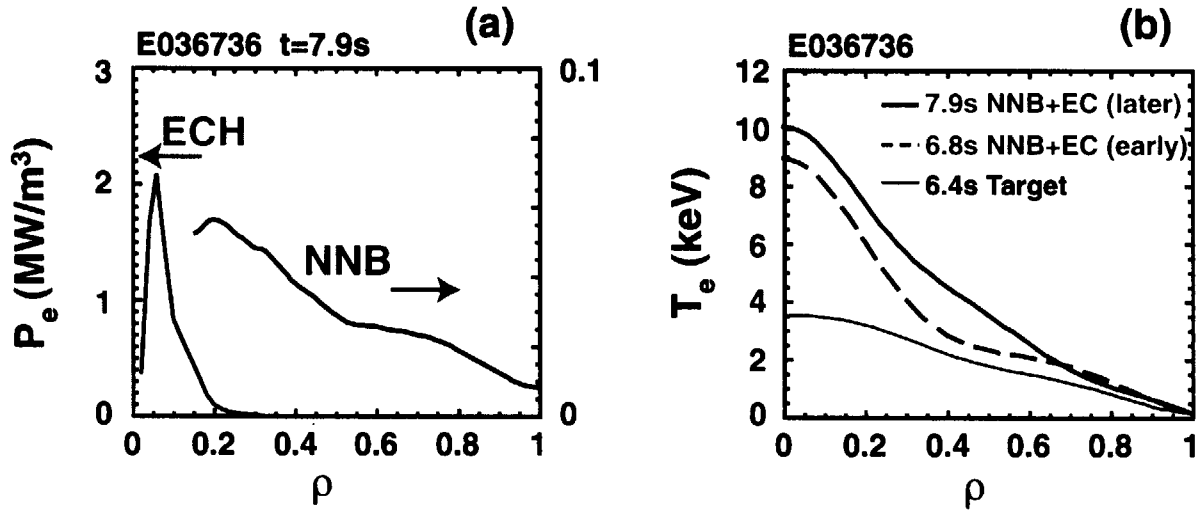

Figure 4.24: (a) Profiles of the absorbed powers of N-NB and ECRF by electrons at t = 7.9 s in E36736. (b) The electron temperature T_e profiles at t = 6.4 s (just before N-NB and EC injection, thin solid line), t = 6.8 s (0.3 s after the start of N-NB and EC injection, dashed line) and t = 7.9 s (the end of the first N-NB pulse, thick solid line).

4.3 Integration of N-NB Current Drive and High Beta High Confinement Plasma

4.3.1 Full current drive in ELMy H mode plasma

By using the ECRF system to obtain higher electron temperature and the newly developed plasma stored energy feedback control to ensure stability in the high beta regime, a full non-inductive current drive at $I_p = 1.5$ MA and an ITER relevant value of the N-NB current drive efficiency 1.55×10^{19} Am^{-2}W^{-1} were achieved. Discharge waveforms are shown in Fig. 4.28. N-NB (360 keV, 4 MW) was injected into a high β_p H mode [27] plasma formed by P-NB injection (80-85 keV, 20 MW). Time evolutions of the measured ion and electron temperature profiles are shown in Fig. 4.29. The evolution of the electron density profile is shown in Fig. 4.30. The profiles at the time-slices indicated by black solid lines in the surface plots are also shown. Here, the profiles of temperatures and density have some uncertainty in the edge region (ρ >0.8) because of restriction in time- and spatial resolutions of the diagnostics. An ITB in the ion channel was clearly formed before injection of EC and N-NB. The plasma stored energy was kept at around 5.5 MJ corresponding to $\beta_N \sim 2.5$ by plasma stored energy feedback control [50] to avoid a beta collapse and the neoclassical tearing instability which appear in high beta discharges. Prior to N-NB injection , 1.5 MW of EC power was injected in order to increase the electron temperature for effective N-NB current drive. After reaching a flattop of the plasma stored energy at t = 5.5 s, the electron temperature continued to increase due to N-NB electron heating over the timescale of the beam ion slowing-down time (~1.2 s). The central electron temperature reached around 14 keV at t = 5.8 s. On the other hand, the ion temperature remained almost constant after the formation of the high β_p mode at t = 5 s. The electron density profile evolved till t = 5.7 s as the confinement continued

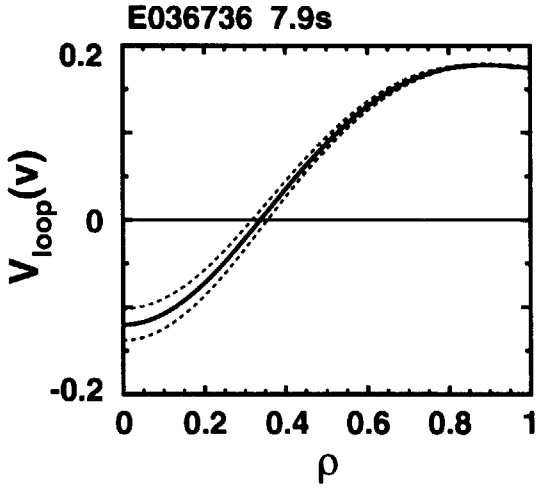

Figure 4.25: Measured loop voltage profile $V_{\rm loop}(\rho)$ for E36736.

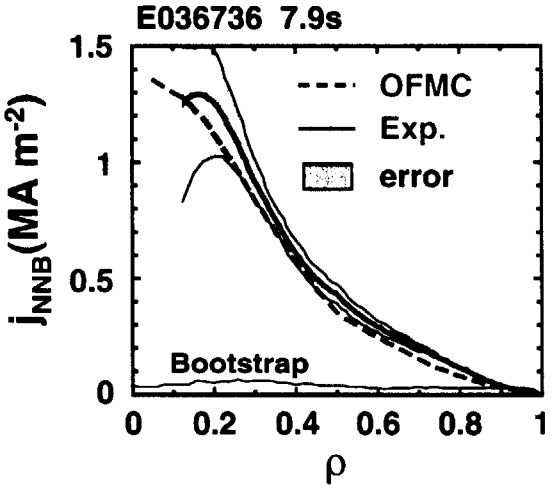

Figure 4.26: Comparison of $j_{\rm NNB}$(exp.) with $j_{\rm NNB}$(OFMC). They agree well within the experimental uncertainty indicated by the shaded region. The bootstrap current density profile is also shown.

to improve. The discharge was analyzed by the time-dependent transport code TOPICS [80] to evaluate non-inductive current drive. The TOPICS code calculates ionization of the injected NB and the velocity distribution function by solving the Fokker-Planck equation using the measured temperature, density and $Z_{\rm eff}$ profiles. The fast ion pressure profile and the NB driven current density profile can be calculated from the distribution function. The bootstrap current density profile is calculated from plasma equilibrium and profiles of temperature, density, $Z_{\rm eff}$ and the fast ion distribution function. Current diffusion is also calculated, and plasma equilibrium is solved, iteratively, to arrive at a solution consistent with current density and pressure profiles. Since the TOPICS code does not include an EC current drive module, the time evolution of the EC driven current density profile calculated by another code for EC heating and current drive that solves the linear Fokker-Planck equation is given as an input to the TOPICS code. Therefore, the TOPICS code can simulate a plasma discharge self-consistently. The measured temperature and density profiles are given at 100 ms intervals (Figs. 4.29 and 4.30). These profiles have 51 radial points. The toroidal and poloidal coil currents and the magnetic fluxes measured by flux loops are given at 1 ms intervals for equilibrium reconstruction in the TOPICS code. In a typical TOPICS simulation, plasma equilibrium is solved every 10 ms and the current diffusion is calculated every 1 ms. Starting from a reconstructed equilibrium at a certain time, current diffusion is calculated at specified time-steps (typically 1 ms). When the calculation reaches the next time-point for equilibrium reconstruction, TOPICS solves for equilibrium with the current density profile obtained by the current diffusion calculation and the pressure profile which is the summation of the input thermal pressures and the calculated fast ion pressure. All profiles calculated in TOPICS has 51 radial points.

Figure 4.31 shows time evolutions of the total current density j, the bootstrap current $j_{\rm BS}$, the NB

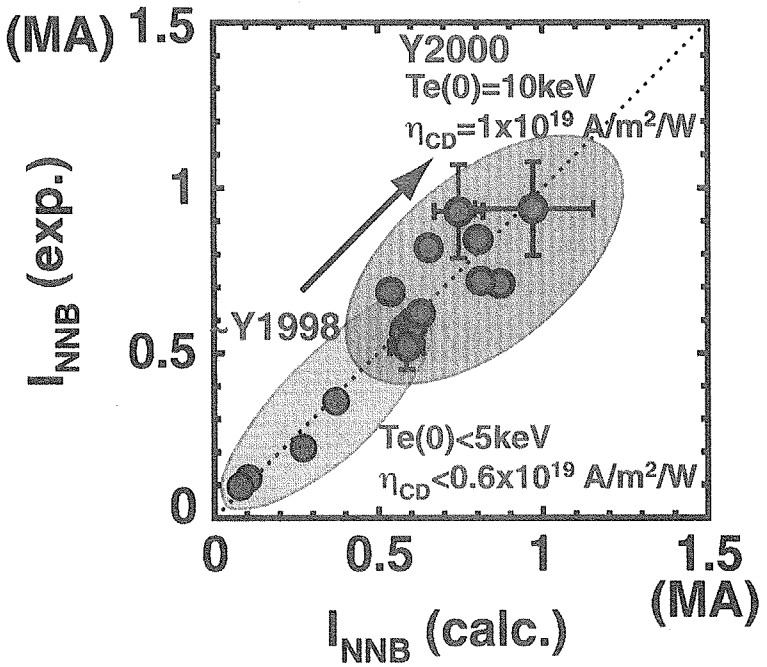

Figure 4.27: Comparison of the N-NB driven current I_{NNB}(exp.) with I_{NNB}(calc.) shows an agreement over a wide range from 0.1 MA to 1 MA.

driven current j_{NB} and the EC driven current j_{EC} profiles. Here, j_{NB} is the sum of the N-NB and P-NB driven currents. On the magnetic axis (r/a=0), j_{BS} and j_{NB} have large spikes due to numerical error because the area surrounded by a closed magnetic surface goes to zero on the magnetic axis. This causes a spike in the total current density j also. Although these spikes affect the total current density profile j not only on the magnetic axis but also in the region near the magnetic axis through current diffusion, its radial extent is narrow and discussion of non-inductive current drive is essentially not affected. Therefore, these spikes are ignored in the following discussion. The bootstrap current profile evolves till t = 5.7 s with confinement improvement and is maintained after that. The NB driven current profile starts to evolve with the N-NB injection and reaches a steady-state at t = 6.5 s.

In Fig. 4.32, radial profiles of the total current, the N-NB driven current, the P-NB driven current, the bootstrap current, the EC driven current and the ohmic current are shown for t = 4.95 s, 5.20 s, 5.80 s and 6.80 s indicated by solid lines in Fig. 4.31. The ohmic current density j_{OH} (light-blue line) dominates the total current density j (thick black line) at t = 4.95 s (only P-NB injection). After EC injection starts at t = 5.0 s, the structure of j_{EC} with a peak at r/a~0.1 appears in j. With increasing j_{BS} and j_{NNB}, the ohmic current density continues to decrease and finally becomes negative over the whole region at t = 6.8 s, which satisfies the "overdriven" state.

To validate TOPICS simulation, the measured total current density profile j is compared with the TOPICS result in Fig. 4.33. The measured j was obtained by the equilibrium reconstruction using the magnetic data and MSE measurements. Figure 4.34 shows the comparison of the safety factor profile.

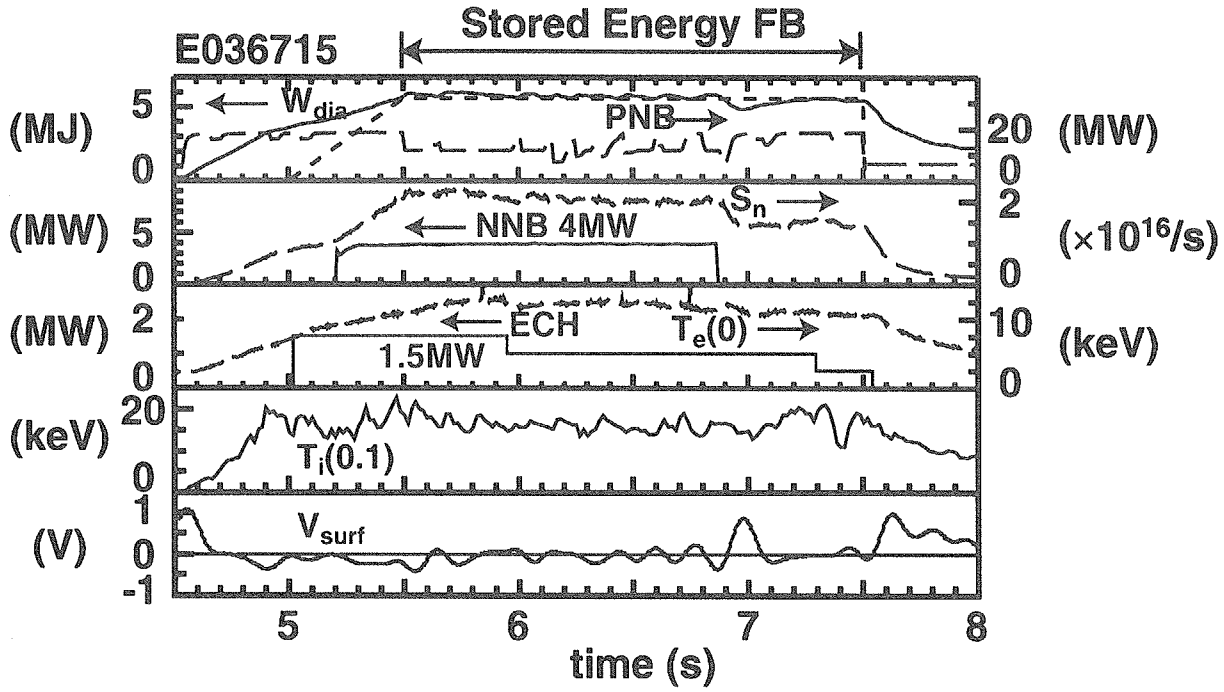

Figure 4.28: Waveforms of pulse E36715, in which the highest $\eta_{\rm CD}$ was achieved. Shown are the plasma stored energy $W_{\rm dia}$ and its reference value for plasma stored energy feedback control, N-NB, P-NB and ECRF injection powers, the neutron production rate $S_{\rm n}$, the central electron temperature $T_{\rm e}(0)$, the ion temperature near the axis (r/a=0.1) $T_{\rm i}(0.1)$, and the surface loop voltage $V_{\rm surf}$.

The MSE measurements does not cover the central region (ρ <0.15) and the edge region (ρ >0.9) in this discharge. TOPICS simulation also has uncertainties in the center (ρ <0.15) and at the edge (ρ >0.8), arising from the lack of profile measurements in these regions. Incomplete treatment of the bootstrap current near the magnetic axis in the TOPICS code ("potato" orbit of the trapped particles should be considered near the magnetic axis), the inconsistent $j_{\rm EC}$ profile and the numerical error at the magnetic axis mentioned above also cause uncertainties near the magnetic axis. Thus, the measured and simulated j profiles can not be determined in these regions. These region are light-colored in the figures. Figure 4.35 shows a comparison of the total pressure profile (red : measurement, blue : TOPICS). The thermal and fast ion pressures calculated by the TOPICS code are also shown. The sum of the thermal and fast ion pressures is the total pressure profile. Except in the central and peripheral regions where the uncertainty is large, the measurement agrees relatively well with the simulation at both t = 4.80 s (before N-NB and EC injection) and t = 6.80 s (N-NB and EC injection). The difference in j around $\rho = 0.6 - 0.8$ are considered to result mainly from uncertainties in the edge temperature and density profiles through the current diffusion process because profiles of the NB driven current, the bootstrap current and the conductivity can be affected. The error in the MSE diagnostic is another possible cause for discrepancy.

Figure 4.36 shows time evolutions of non-inductive current (integration of the profile) driven by N-NB, P-NB, EC and the bootstrap current. The N-NB driven current and the bootstrap current evolve in time, and a fully non-inductively current driven condition was reached at t = 5.6 s. This is also shown in

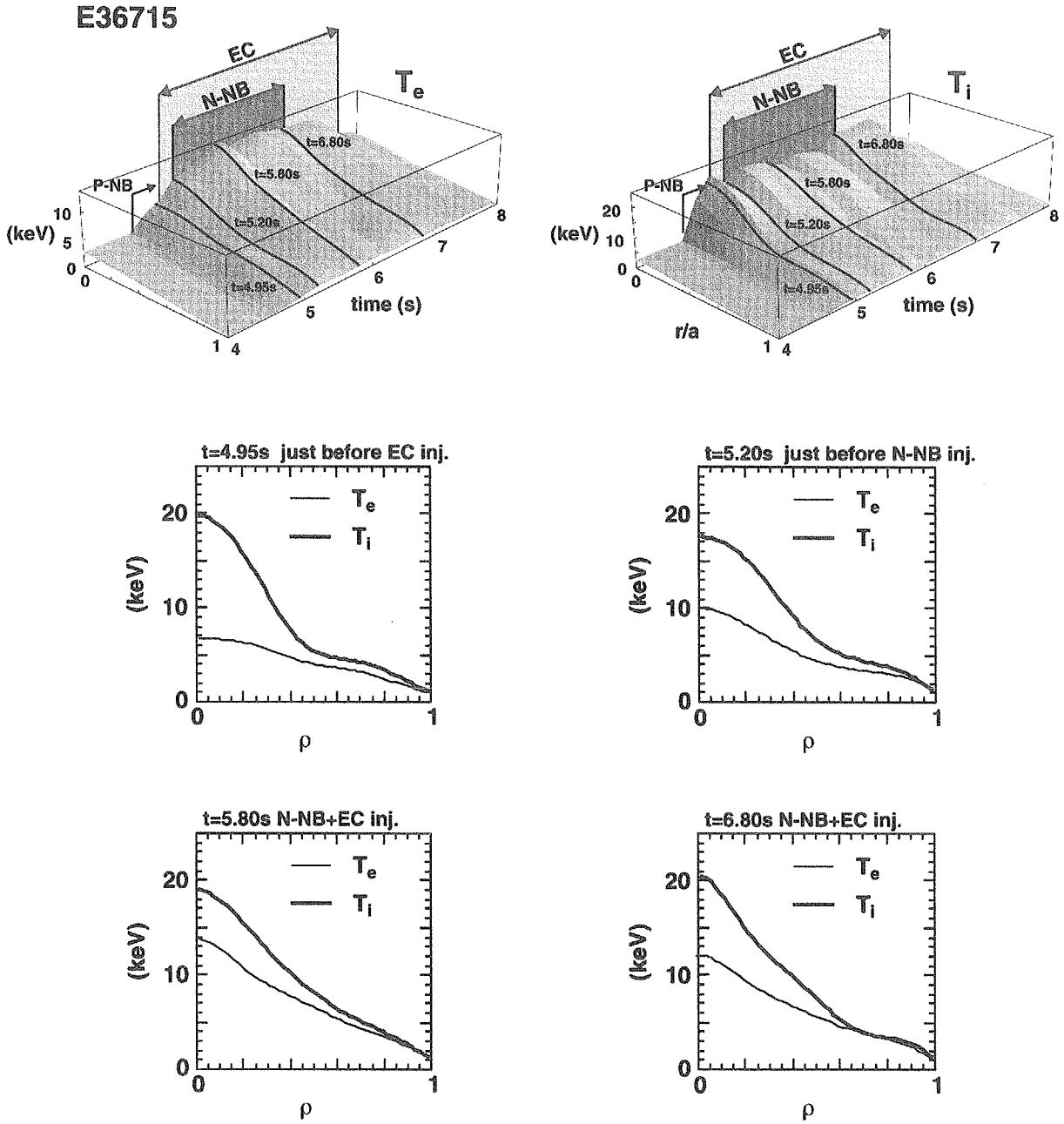

Figure 4.29: Time evolutions of the electron and ion temperature profiles for E36715. The electron temperature was measured by ECE (Electron Cyclotron Emission) and Thomson scattering. The ion temperature was measured by CXRS. The radial profiles at the time-slices indicated by black solid lines in the surface plots at t = 4.95 s(just before EC injection), 5.20 s (just before N-NB injection), 5.80 s (4 MW N-NB and 1.5 MW EC injection) and 6.80 s (4 MW N-NB and 1.1 MW EC injection) are also shown.

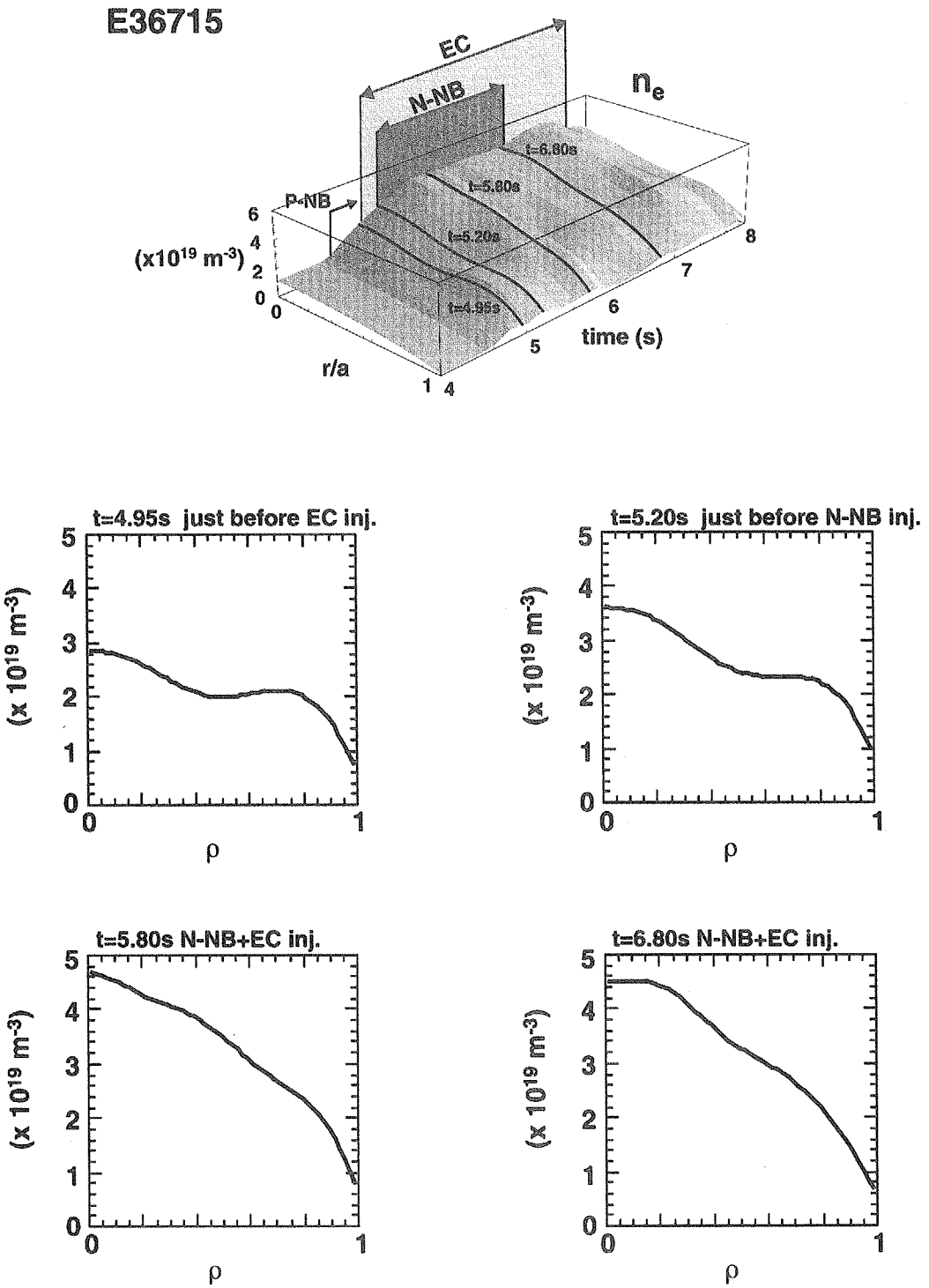

Figure 4.30: Time evolution of the electron density profile for E36715 measured by the YAG Thomson scattering. The radial profiles at the time-slices indicated by black solid lines in the surface plots at t = 4.95 s, 5.20 s, 5.80 s and 6.80 s are also shown.

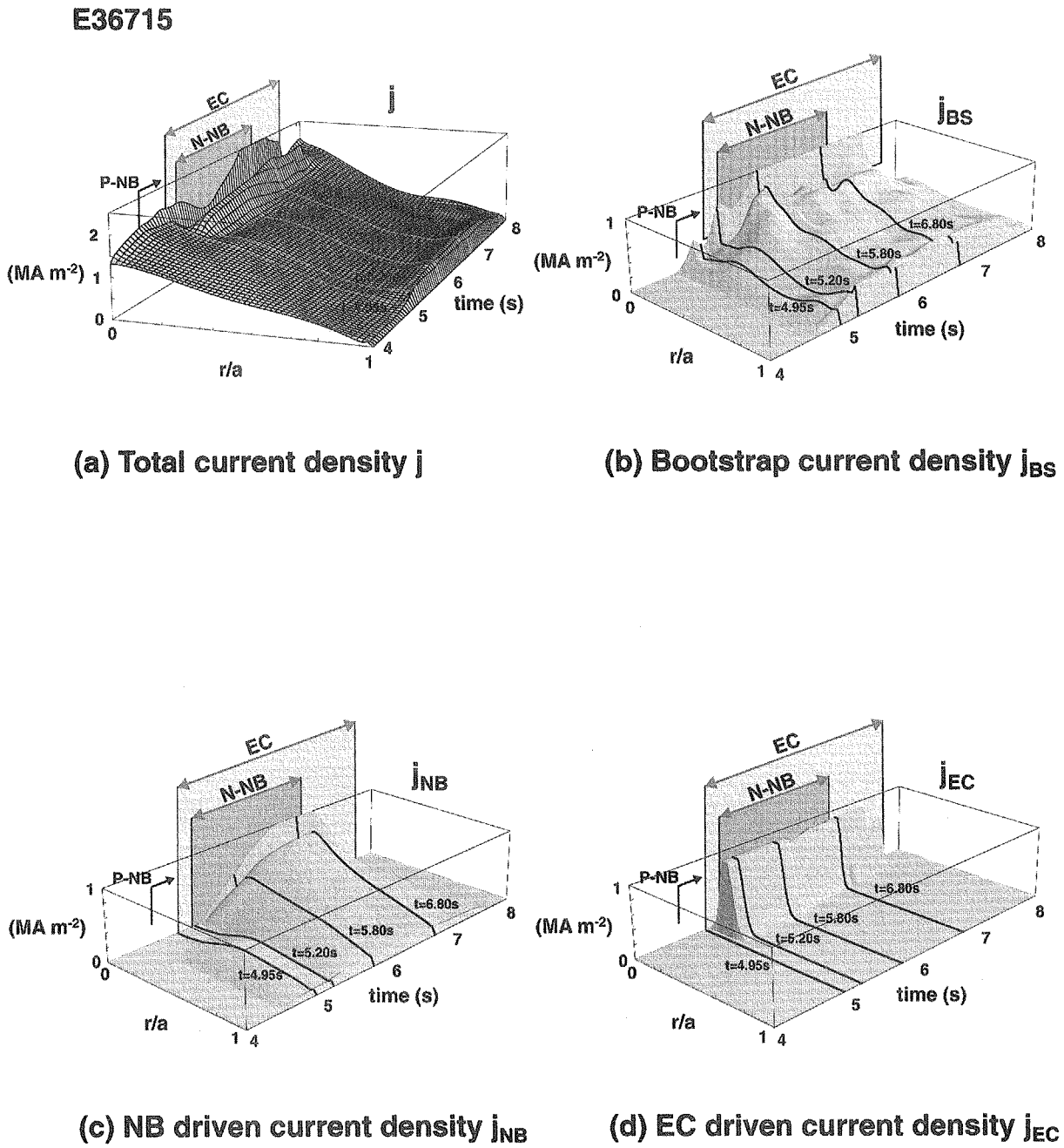

Figure 4.31: Simulation of E36715 by the TOPICS code. Time evolutions of the total current density j, the bootstrap current j_{BS}, the NB driven current j_{NB} and the EC driven current j_{EC} profiles are shown.

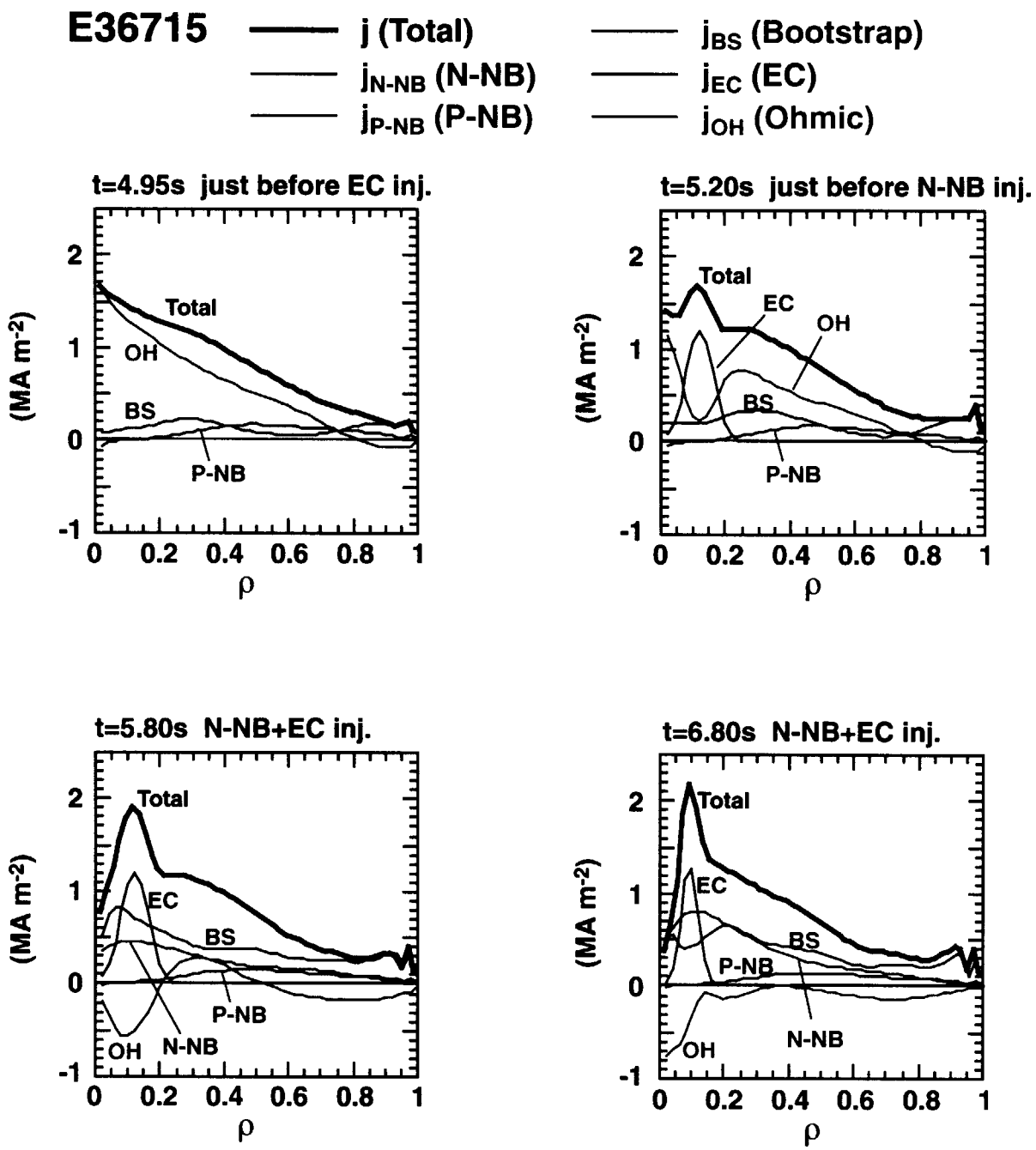

Figure 4.32: Simulation of E36715 by the TOPICS code. Shown are radial profiles of the total current density j, the N-NB current drive j_{NNB}, the P-NB driven current j_{PNB}, the bootstrap current j_{BS}, the EC drive current j_{EC} and the ohmic current j_{OH} at the time-slices indicated by solid lines in Fig. 4.31, t = 4.95 s, 5.20 s, 5.80 s and 6.80 s.

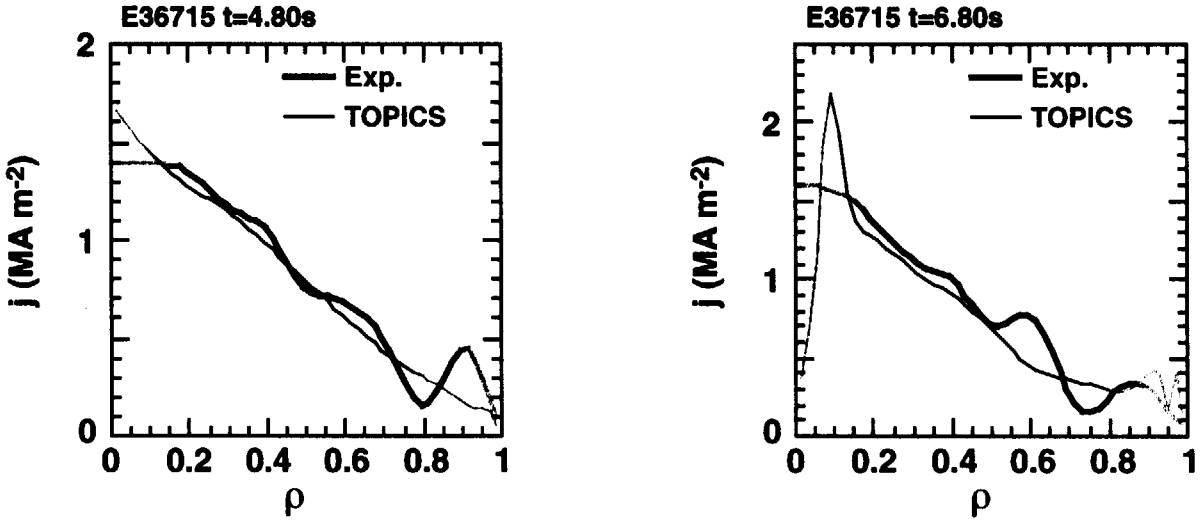

Figure 4.33: The measured total current density profile j is compared with the TOPICS result at t = 4.80 s (only P-NB injection) and 6.80 s (P-NB, N-NB and EC injection). Profiles have large errors in the light-colored regions.

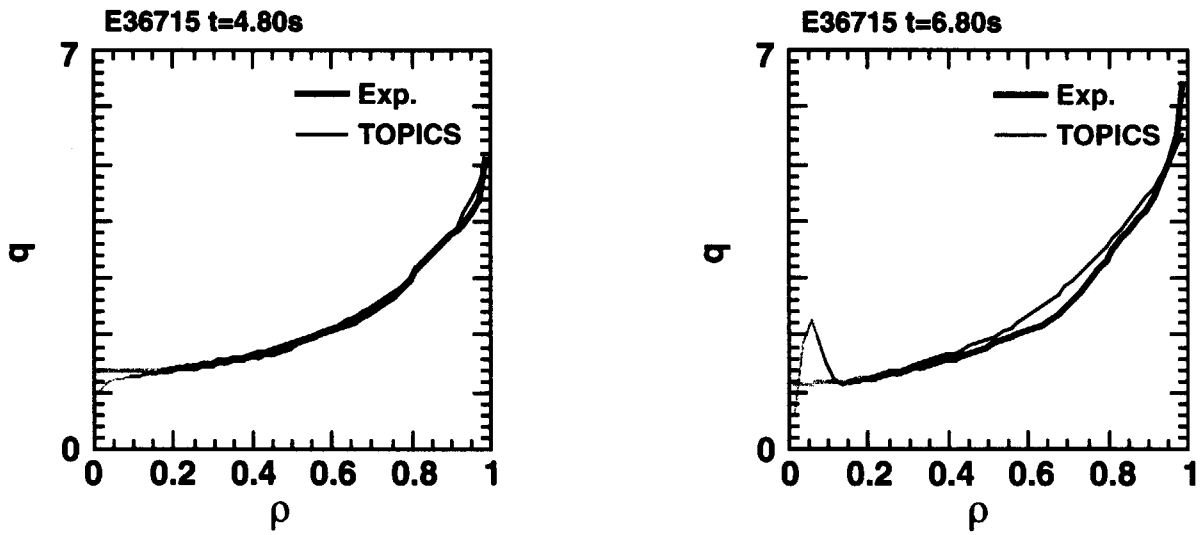

Figure 4.34: The measured safety factor profile q is compared with the TOPICS result at t = 4.80 s (only P-NB injection) and 6.80 s (P-NB, N-NB and EC injection). The measured profile is determined by the equilibrium reconstruction code SELENE with the magnetic data and MSE measurements. Profiles have large errors in the light-colored regions.

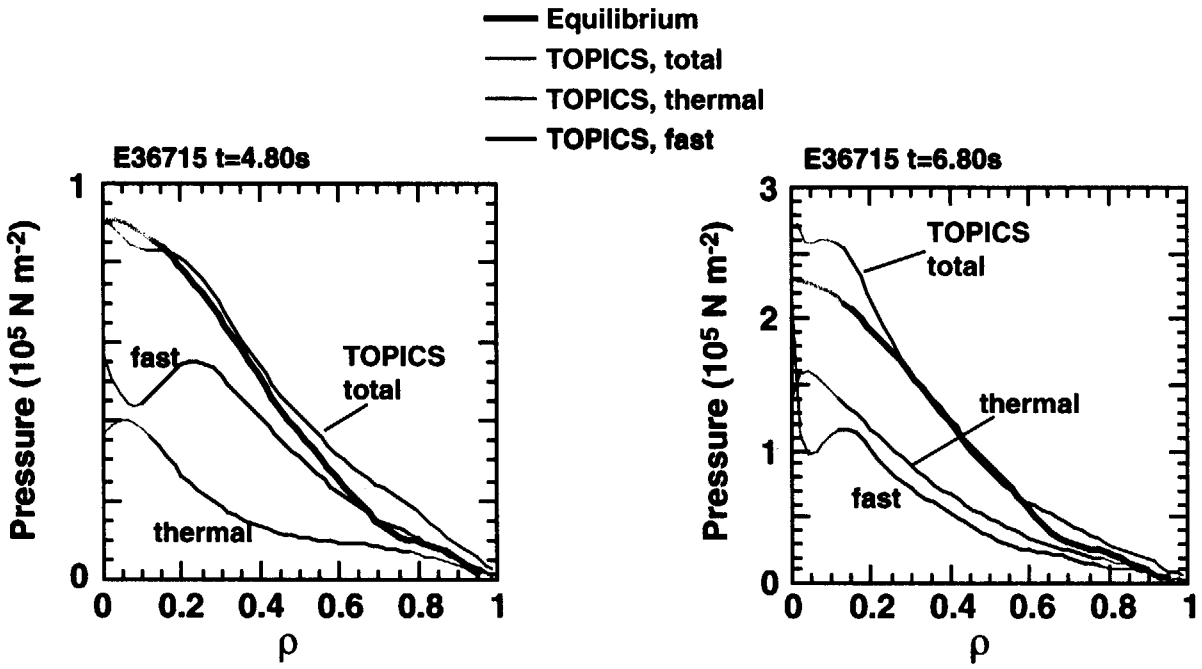

Figure 4.35: The pressure profile from equilibrium reconstruction by the SELENE code using the magnetic data and MSE measurements is compared with the TOPICS result at t = 4.80 s (only P-NB injection) and 6.80 s (P-NB, N-NB and EC injection). Profiles have large errors in the light-colored regions.

Fig. 4.32. Although there is a region ($\rho = 0.2 - 0.5$) of positive $j_{\rm OH}$, the total ohmic current became negative. Non-inductive current was fully built up by t = 6.5 s. Non-inductive currents calculated by the TOPICS code are 818 kA of NBCD (N-NB plus P-NB), 60 kA of ECCD and 861 kA of bootstrap current. In total, non-inductive current reaches 1.74 MA and exceeds the plasma current of 1.5 MA. The corresponding N-NB current drive efficiency is 1.55×10^{19} Am^{-2}W^{-1}. In Fig. 4.36, the calculated time evolutions (bold line) of the surface loop voltage $V_{\rm surf}$, the neutron production rate $S_{\rm n}$ and the plasma stored energy $W_{\rm dia}$ are compared to the measurements (thin line). The calculated time evolutions of these quantities are consistent with the experimental observation. Thus, together with the good agreement in the total current density j and pressure profiles between measurements and simulation mentioned above (Figs. 4.33 and 4.35), achievement of the highest current drive efficiency and the full non-inductive current-drive state can certainly be concluded.

4.3.2 Summary of the N-NB current drive capability

Figures 4.37 and 4.38 show the progress in the N-NB current drive capability. As shown in the $\eta_{\rm CD}$-$T_{\rm e}(0)$ plot (Fig. 4.37), $\eta_{\rm CD}$ was confirmed to increase with electron temperature to over 10 keV, approaching the ITER regime. High values of current drive efficiency, larger than 1×10^{19} Am^{-2}W^{-1} at $T_{\rm e}(0) > 8$ keV were achieved in a series of high driven current experiments described in 4.2.2 and high $\beta_{\rm p}$ H mode plasmas described in 4.3.1. Here, the range of N-NB beam energy was 330-370 keV, and $Z_{\rm eff}$ was from 2 to 4. In Fig. 4.38, $\eta_{\rm CD}$ is plotted against the driven current $I_{\rm NB}$. Simultaneous achievement

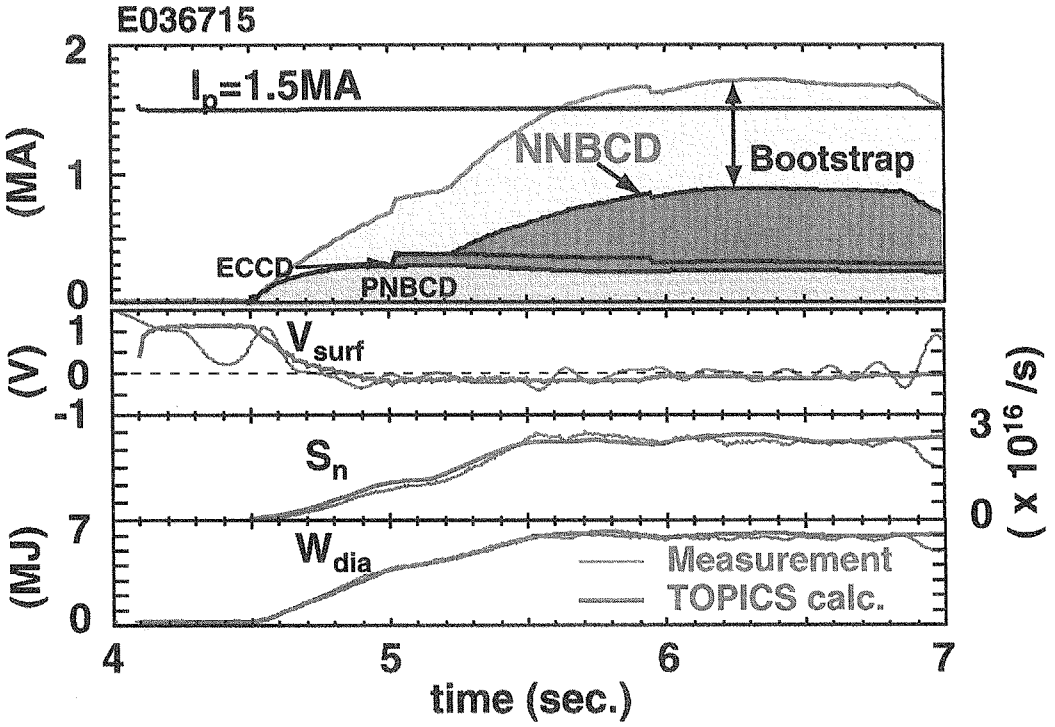

Figure 4.36: Time evolutions of non-inductive currents driven by N-NBCD, P-NBCD, ECCD and the bootstrap current calculated by the time-dependent transport code TOPICS for pulse E36715. Calculated time evolutions (bold line) of the surface loop voltage $V_{\rm surf}$, the neutron production rate $S_{\rm n}$ and the plasma stored energy $W_{\rm dia}$ are compared with measurements (thin line).

of $\eta_{\rm CD} = 1 \times 10^{19}\ {\rm Am^{-2}W^{-1}}$ and $I_{\rm NB} = 1$ MA indicates the advantage of high energy neutral beam for current drive. Further detailed discussion in relation to ITER regime is given in section 6.1.

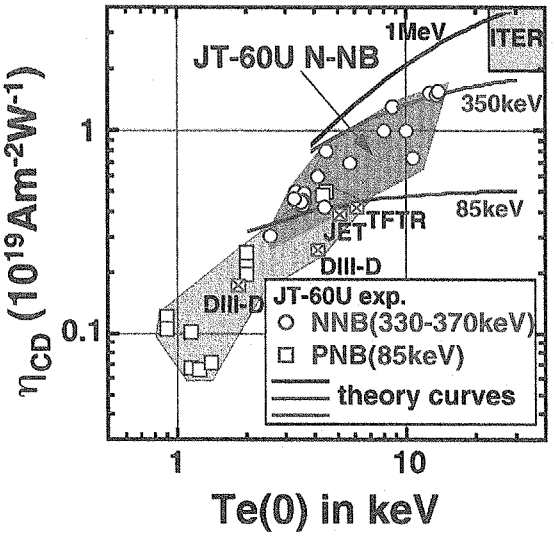

Figure 4.37: Electron temperature T_e dependence of the current drive efficiency η_{CD}. TFTR, JET and DIII-D data have been taken from Refs [87], [88] and [89].

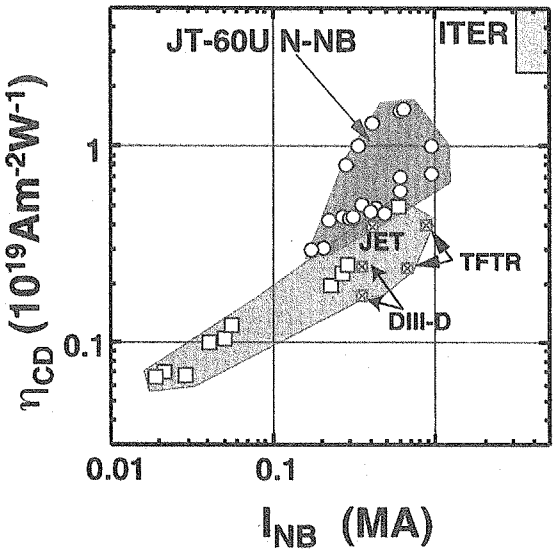

Figure 4.38: η_{CD} versus driven current I_{NB} for N-NB(330-370 keV) and P-NB(85 keV).

5. Influence of MHD Instabilities on Neutral Beam Current Drive

The conclusion of validity of theoretical prediction for N-NB current drive described in chapter 4 was for MHD-quiescent plasmas. However, various instabilities such as beam driven instabilities [90] and the neoclassical tearing mode [91] appear in tokamak plasmas. In this chapter, influence of such instabilities on N-NB current drive is discussed.

5.1 Beam-driven Instability

In low density plasmas where the beam ion pressure due to N-NB injection is comparable to the thermal pressure, a burst-like instability is sometimes observed. Figure 5.1 shows waveforms of a discharge in which such an instability appeared. The toroidal magnetic field was 3.73 T, and the line-averaged density through the central chord was 0.65×10^{19} m^{-3}. As shown in the time trace of S_n, N-NB ions built up gradually (to $\sim$ 90% of the steady state value during the 1 second injection according to the OFMC calculation). The frequency spectrum of magnetic fluctuation measured by Mirnov coils in the laboratory frame is also shown in Fig. 5.1. Small bursts with frequencies of 60-80 kHz were observed after N-NB injection started, and their range of frequency sweep became gradually wider as shown in the expanded time-traces of magnetic fluctuations (Fig. 5.2). Here, the rotation frequency ($1 - 1.5$ kHz) included in the observed frequency is negligible compared to the frequency of the burst instability. At t = 7.96 s when a large burst indicated as the 4th burst occurred, a reduction in S_n was observed. This indicates losses of thermal ions and/or fast ions of P-NB and/or N-NB. Time evolutions of the reconstructed poloidal flux inside $\rho < 0.4$ is also shown in Fig. 5.1. Time derivatives inside $\rho \leq 0.3$ increased from t = 7.96 s (the 4th burst). This indicates a loss of non-inductive current from the central region caused by this burst. In this discharge, the bootstrap current and the P-NB driven current were negligibly small because of low pressure and balanced injection of tangential P-NB. Reduction in T_e of $\sim$ 7 % was too small to explain the loop voltage increase. Thus, it can be concluded that the reduction in non-inductive current was caused by a loss of current carrying N-NB fast ions. In Fig. 5.3, T_e measured by the ECE (Electron Cyclotron Emission) diagnostic at $\rho = 0.3$ are shown for the time interval t = 7.9-8.2 s. Increase in T_e

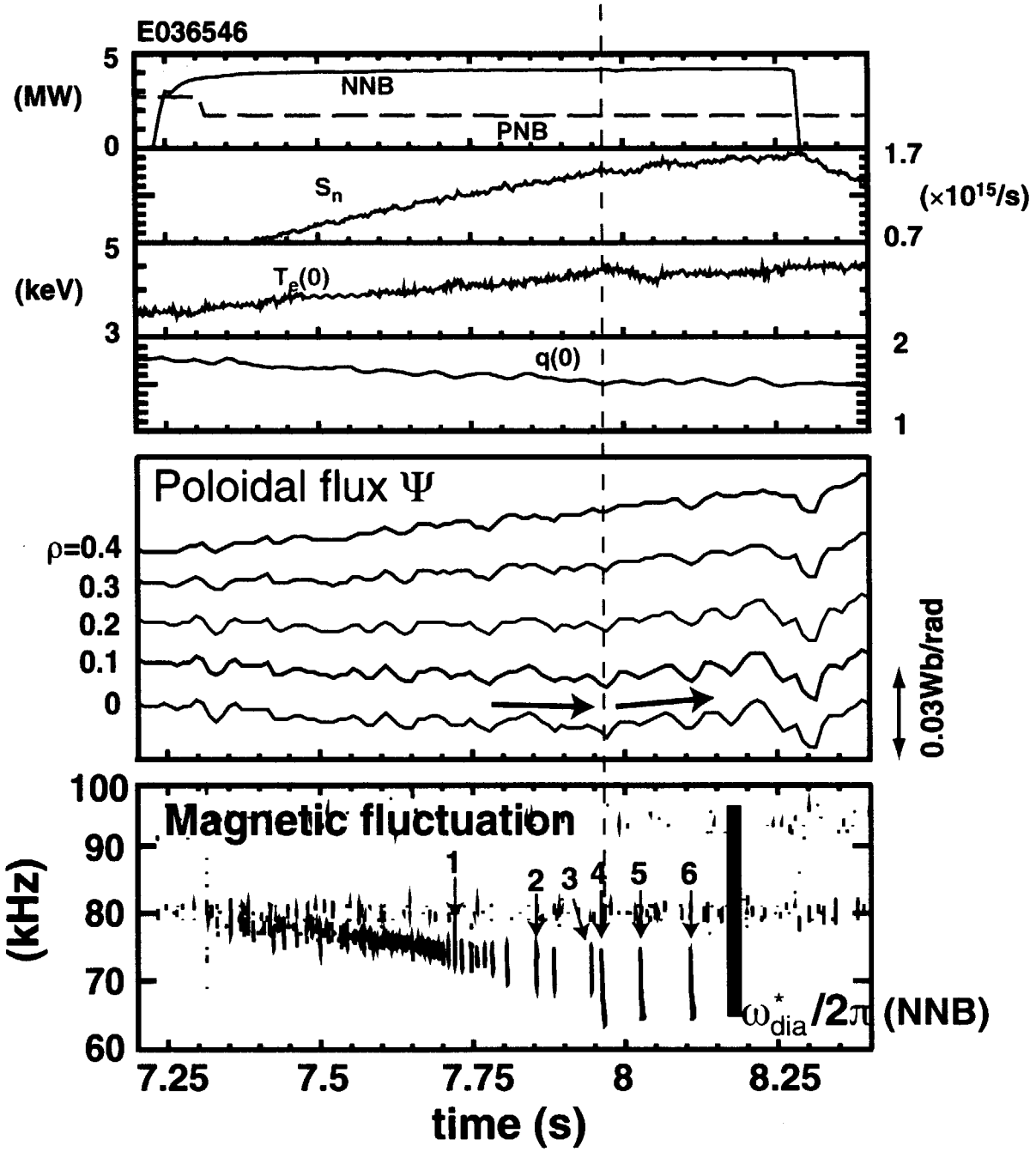

Figure 5.1: Waveforms of pulse E36546. N-NB and P-NB injection powers, S_n, $T_e(0)$ and $q(0)$ are shown in the top panel. Time evolutions of the reconstructed poloidal flux at $\rho = 0 - 0.4$ and the frequency spectrum of magnetic fluctuations are also shown. The range of diamagnetic drift frequency of N-NB fast ions ω^*_{dia} for the m=2 mode inside $\rho = 0.3$ is indicated in the bottom panel.

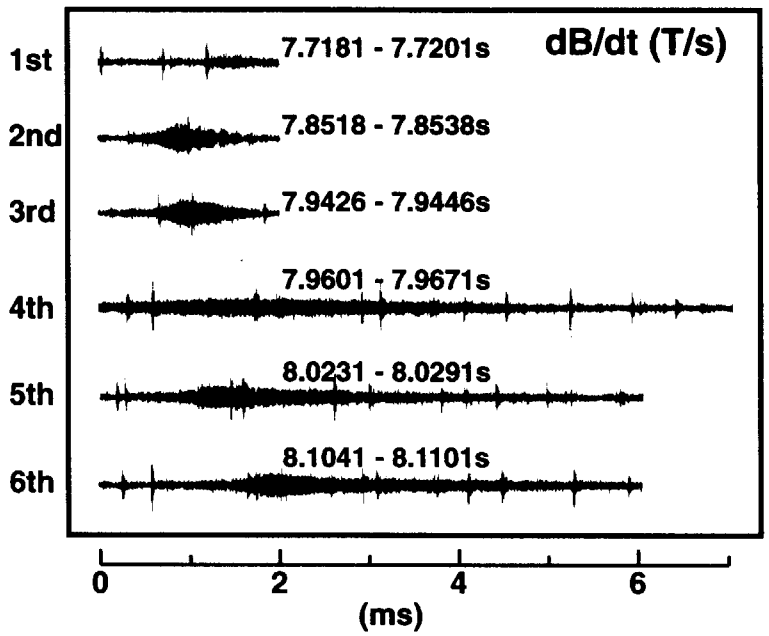

Figure 5.2: Expanded view of magnetic fluctuations shown in Fig. 5.1. Each (1st-6th) burst is plotted from a common origin. Horizontal axis corresponds to the duration of the frequency sweep.

corresponding to the 4th, 5th and 6th bursts were observed. This indicates that the instability occurred inside $\rho = 0.3$, which is consistent with the increase in loop voltage inside $\rho \sim 0.3$. No clear change

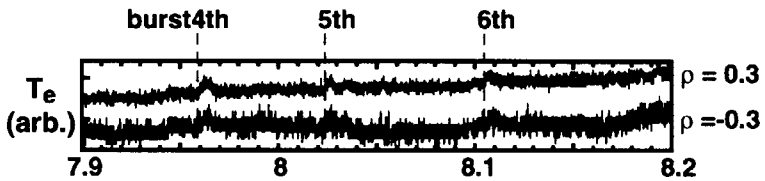

Figure 5.3: Crashes in T_e at r/a=0.3 measured by the ECE diagnostic corresponding to the three magnetic bursts (4th-6th) in Fig. 5.1.

in S_n and poloidal flux was observed for bursts before the 4th burst. The toroidal mode number of these bursts was $n = 1$. The central safety factor $q(0)$ was ~ 1.5, and safety factor at $\rho = 0.3$ was ~ 2. Thus, if this instability inside $\rho = 0.3$ were a TAE mode (Toroidal Alfvén Eigenmode), the poloidal mode number would be $m = 1$. However, the corresponding TAE frequency is 380 kHz, far larger than the observed frequency of $60 - 80$ kHz. In addition, the ratio of the N-NB ion velocity parallel to the magnetic field $v_{b//}$ to the Alfvén velocity v_A, $v_{b//}/v_A$, is 0.2, which is less than even the side-band resonant conditions of ~ 0.3 for the TAE mode and ~ 0.5 for the GAE mode (Global Alfvén Eigenmode). Thus, it is difficult to explain this instability by an AE mode, although a burst like behavior is similar to the frequency sweeping mode (considered to be a TAE mode) described in [92]. This burst instability cannot be explained by the fishbone instability with $m/n = 1/1$ because the 1/1 surface was absent. As shown in the frequency spectrum of magnetic fluctuations (Fig. 5.1), the diamagnetic drift frequency

of the N-NB fast ions $\omega^*_{\rm dia}/2\pi$ for the $m = 2$ mode inside $\rho = 0.3$ is estimated to be 64-96 kHz from the profile of the fast ion pressure calculated by the OFMC code, while the diamagnetic drift frequency of thermal ions is less than 3 kHz. Thus, the frequency of this burst-like instability (60 − 80 kHz as mentioned above) is possibly determined by the diamagnetic drift frequency of N-NB fast ions. Here, the diamagnetic drift frequency of the particle species i is defined by

$$\omega^*_{\rm dia} \equiv \frac{m_i}{r}\frac{1}{eZ_i n_i B}\frac{dp_i}{dr},$$

where r a minor radius, and n_i and p_i are the density and pressure of the species i, respectively. Classification of this instability is discussed again in section 6.2.1.

To evaluate the influence of this instability on N-NB current drive, profiles of the loop voltage and non-inductive current density just before and after the 4th burst were analyzed as shown in Fig. 5.4 (a) and (b), respectively. Non-inductive current density inside $\rho < 0.3$ decreased after the burst. Because the duration of analysis could not be taken long enough for accurate determination of the loop voltage profile, the maximum difference between non-inductive current density profiles before and after the burst has been estimated. The shaded regions indicate the errors for each profile. The upper bound for the lost N-NB driven current from $\rho < 0.3$ was estimated to be $\sim$ 40 kA, corresponding to 7 % of the total N-NB driven current. In most other discharges with similar instabilities, a clear influence on plasma as in this case was not observed. Thus, the loss of N-NB driven current was not serious in the present experimental regime. However, with a higher beam pressure and a different safety factor profile, there is a possibility that degradation of current drive caused by this type of instability is not negligible.

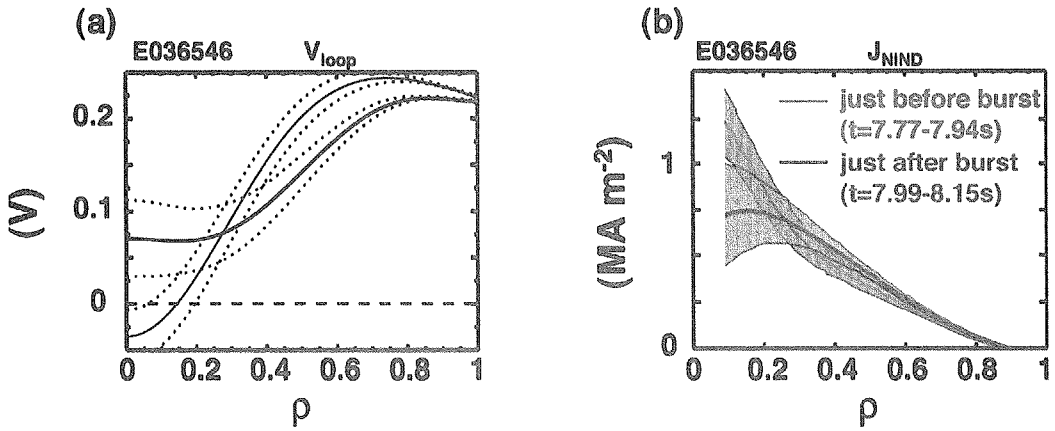

Figure 5.4: Measured profiles of (a) loop voltage and (b) non-inductive current density just before and just after the 4th magnetic burst in Fig. 5.1. Shaded regions indicate errors for each profile.

5.2 Neoclassical Tearing Instability in High Beta Plasmas

In high beta plasmas, the neoclassical tearing mode (NTM) appears when $\beta_{\rm N}$ (defined in 3.1.2) exceeds a threshold level [91, 93]. The critical value of $\beta_{\rm N}$ and the mode number of NTM depend

on profiles of the safety factor and the plasma pressure. A reduction in the neutron emission rate or saturation of its increase were observed during the instability. The neoclassical tearing mode not only enhances the transport of thermal energy but also seems to cause redistribution or loss of the neutral beam fast ions. The redistribution of fast ions can cause degradation in core heating and reduction of the neutral beam driven current.

5.2.1 Behavior of the magnetic island

The magnetic island behavior during the neoclassical tearing mode is presented in this section. Figure 5.5 shows the $n = 1$ component of magnetic fluctuations for discharge E36401 with the $m/n = 2/1$ NTM. A high time resolution measurement of the electron temperature by the ECE (Electron Cyclotron Emission) heterodyne radiometer with a sampling time of 20 μs showed the magnetic island structure as described below. Twelve channels of the fast ECE radiometer cover the frequency range of 177.5-187.5 GHz at 1 GHz interval. These frequencies correspond to $R = 3.55 - 3.77$ m ($\rho = 0.15 - 0.42$) and a spatial resolution of 2 cm in this discharge. The region of measurement in the plasma poloidal cross section is shown in Fig. 5.7. The frequency spectra of fluctuating T_e for 12 channels are shown in Fig. 5.6. Fluctuations in T_e appeared around t=3.4 s at f~3 kHz and disappeared around t=4.8 s. The peak frequency of the spectrum changed in the range of 2-5 kHz which corresponds to the plasma rotation frequency. The continuously existing peaks at f~2, 6 and 8 kHz for the 5th channel are considered to not reflect the fluctuating electron temperature $\tilde{T}_e$ at the observed location. In Fig. 5.7, the spatial profiles of the phase and the amplitude at the peak frequency of the spectrum are shown. The amplitude corresponds to the relative level of the T_e fluctuation, $\tilde{T}_e/T_e$. As explained in Fig. 5.8, the phase jumps by 180 degrees at the O-point of the island, and $\tilde{T}_e/T_e$ profile has two peaks at the edges of the island, where the separation of the two peaks indicates the width of the island. Because the low and high field sides of a magnetic island are connected along a field line, profiles of temperature and density become flat within a magnetic island as illustrated in Fig. 5.8. In fact, a flat region in the T_e profile is observed at the location of a magnetic island. At t = 3.5018 s shown in Fig. 5.7, the O-point is located around channels 8-9, and the $\tilde{T}_e/T_e$ profile has peaks at channels 4-5 and 11-12. Therefore, the island width is estimated to be 12-16 cm. The q=2 location determined by equilibrium reconstruction is indicated in the figure. This is consistent with the O-point location determined from the phase profile, considering the uncertainties in equilibrium reconstruction and the spatial mapping from frequencies of the ECE measurement.

The evolution of the relative fluctuation amplitude profile is shown as a contour plot in Fig. 5.9. Figure 5.10 shows the evolutions of the $\tilde{T}_e/T_e$ profile during the growing and shrinking periods of the island. The island started to grow around t = 3.4 s and saturated around t = 3.6-3.8 s. From t = 3.8 s, the island started to shrink gradually and disappeared around t = 4.7 s. A double peak structure is observed at t = 3.3994 s and t = 3.5018 s in Fig. 5.10. As the island grew, the peak on the high field side (larger channel number) shifted out of the measurement region. The phase inversion by 180 degrees, which corresponds to the O-point, can be seen clearly between channels 7-10 during the growing period in Fig.

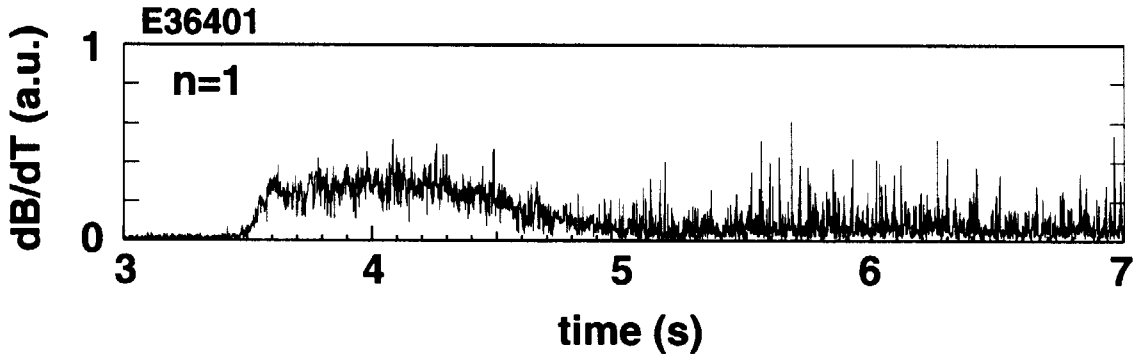

Figure 5.5: The n=1 component of magnetic fluctuations dB/dt for E36401.

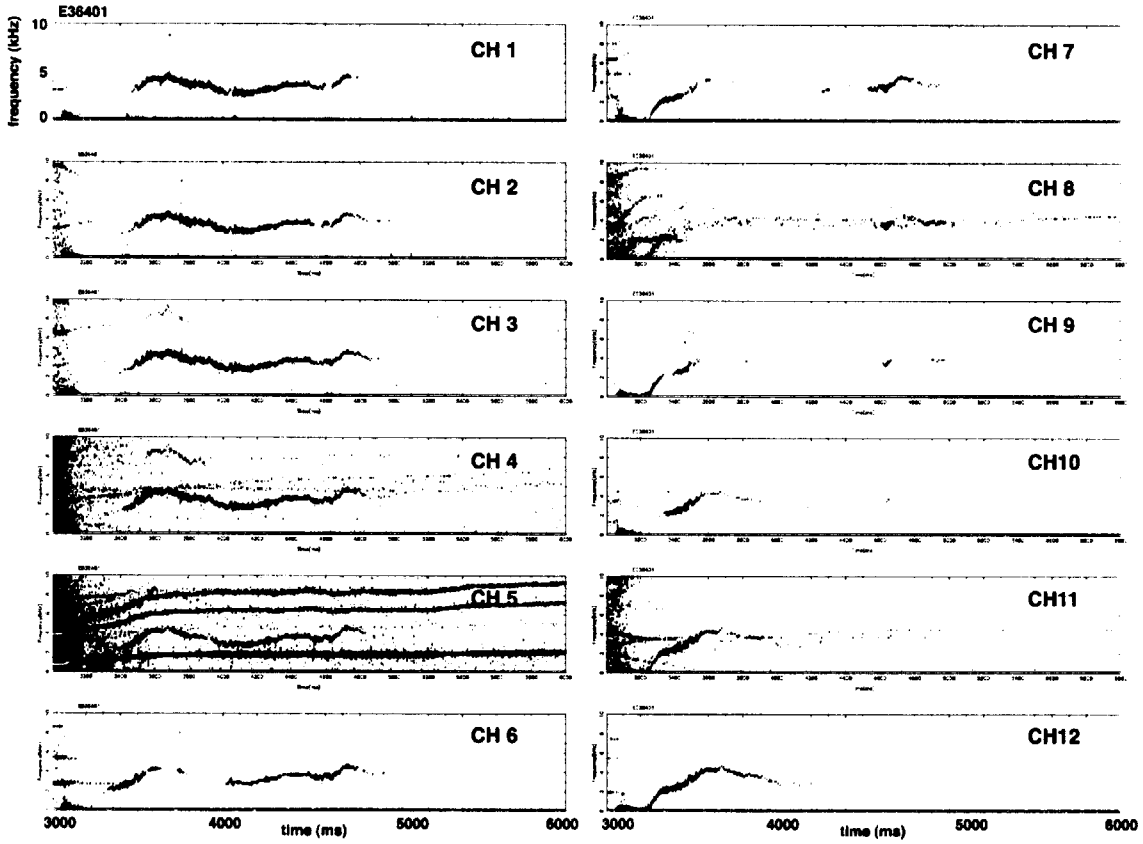

Figure 5.6: Time evolutions of the frequency spectrum of T_e fluctuations measured by the ECE heterodyne radiometer for E36401.

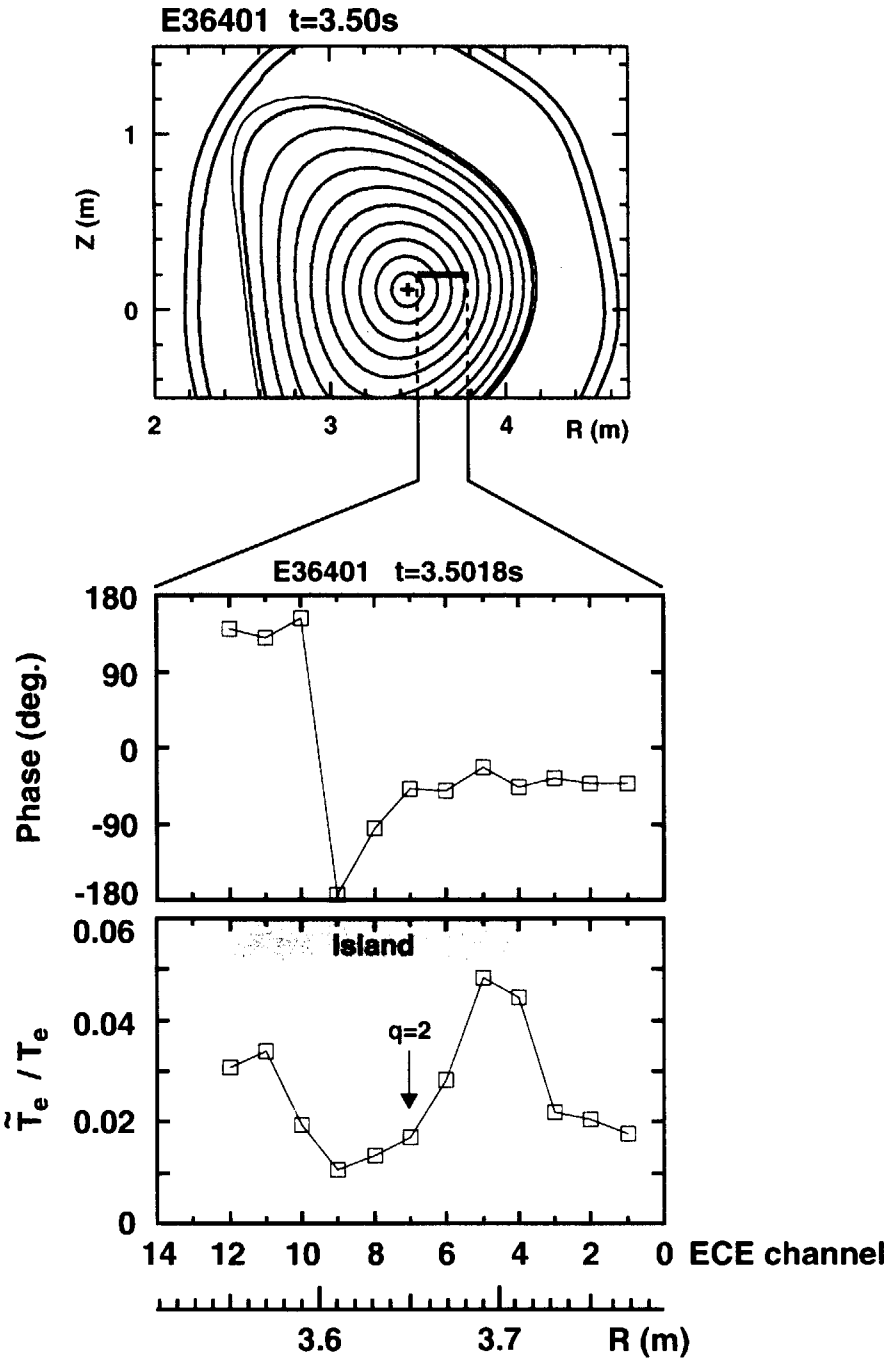

Figure 5.7: The region of measurement of the ECE heterodyne radiometer is shown in the plasma poloidal cross section for E36401. The spatial profiles of the phase and the relative fluctuation level of T_e at t = 3.5018 s in E36401 are also shown.

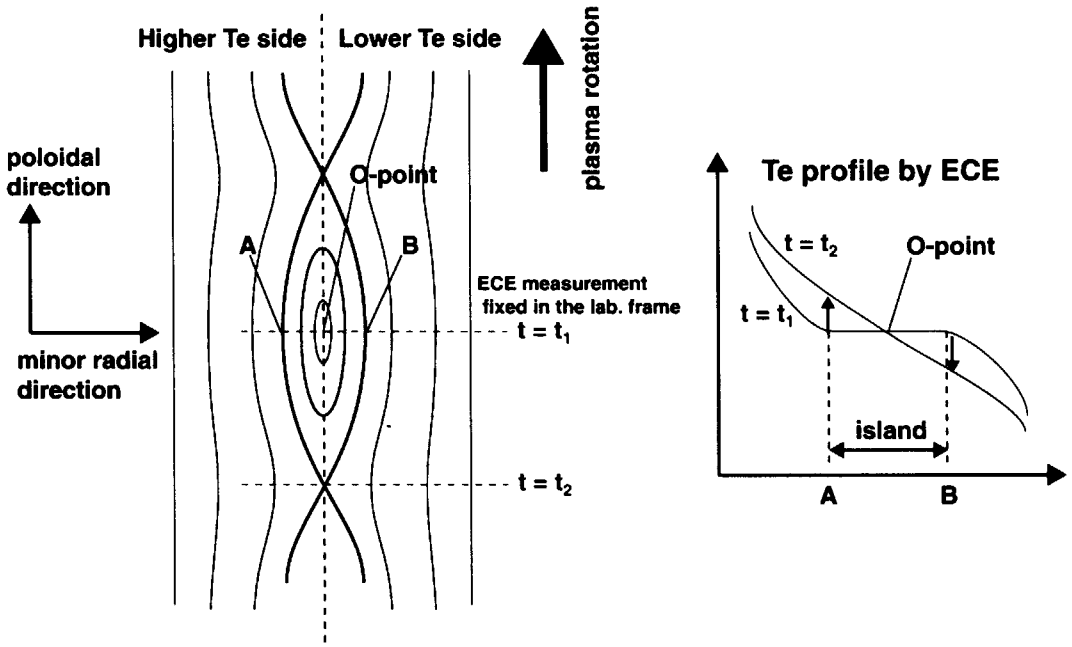

Figure 5.8: Schematic view of the T_e profile in the vicinity of a magnetic island The phase of the measured $\tilde{T}_e$ on the inboard side of the O-point is opposite to that on the outboard.

5.11. During the shrinking period of t = 3.8-4.7 s, the low field side peak of $\tilde{T}_e/T_e$ moved slightly inward. The lowest region of $\tilde{T}_e/T_e$ (dark blue) in Fig. 5.9 also seems to move slightly inward (towards the high field side). Figure 5.12 shows that the location of phase inversion also moves inward, although it is not so clear for t = 4.6026 s and 4.8022 s because of the reduced fluctuation level.

The profile flattening within a magnetic island causes a reduction or a disappearance of the bootstrap current, which is driven by the spatial gradients of temperature and density. The NTM theory states that the reduction of the bootstrap current becomes a driving term in the equation governing the magnetic island evolution. However, reduction of the bootstrap current itself has not been observed experimentally because of the difficulty in measuring a small change in j. The first observation of the reduction and the recovery of the bootstrap current during the growing and shrinking phases of the island is described in Sec. 5.2.3 in conjunction with the influence of NTM on beam fast ions.

5.2.2 Experimental observation of influence on neutral beam fast Ions

Figure 5.13 shows a P-NB heated plasma discharge in which the m/n=3/2 and 2/1 NTMs appeared. The plasma stored energy and the neutron emission rate decreased due to large NTMs as evidenced by large amplitude magnetic fluctuations. By injecting over 20 MW of P-NB, β_N was kept around 2.5 from t = 5.6 s. However, at t = 6.5 s, the m/n=3/2 NTM appeared and W_{dia} and S_n decreased. The m/n=2/1 NTM also appeared at t = 7.15 s . Further degradations of W_{dia} and S_n occurred. The plasma stored energy decreased to a half of the value just before the appearance of NTM, in spite of the same NB power injection. Figure 5.14 shows the ion temperature profiles at t = 6.5 s (just before the m/n=3/2 NTM onset), t = 7.15 s (large m/n=3/2 but small m/n=2/1 NTMs) and t = 7.7 s (large m/n=3/2 and m/n=2/1

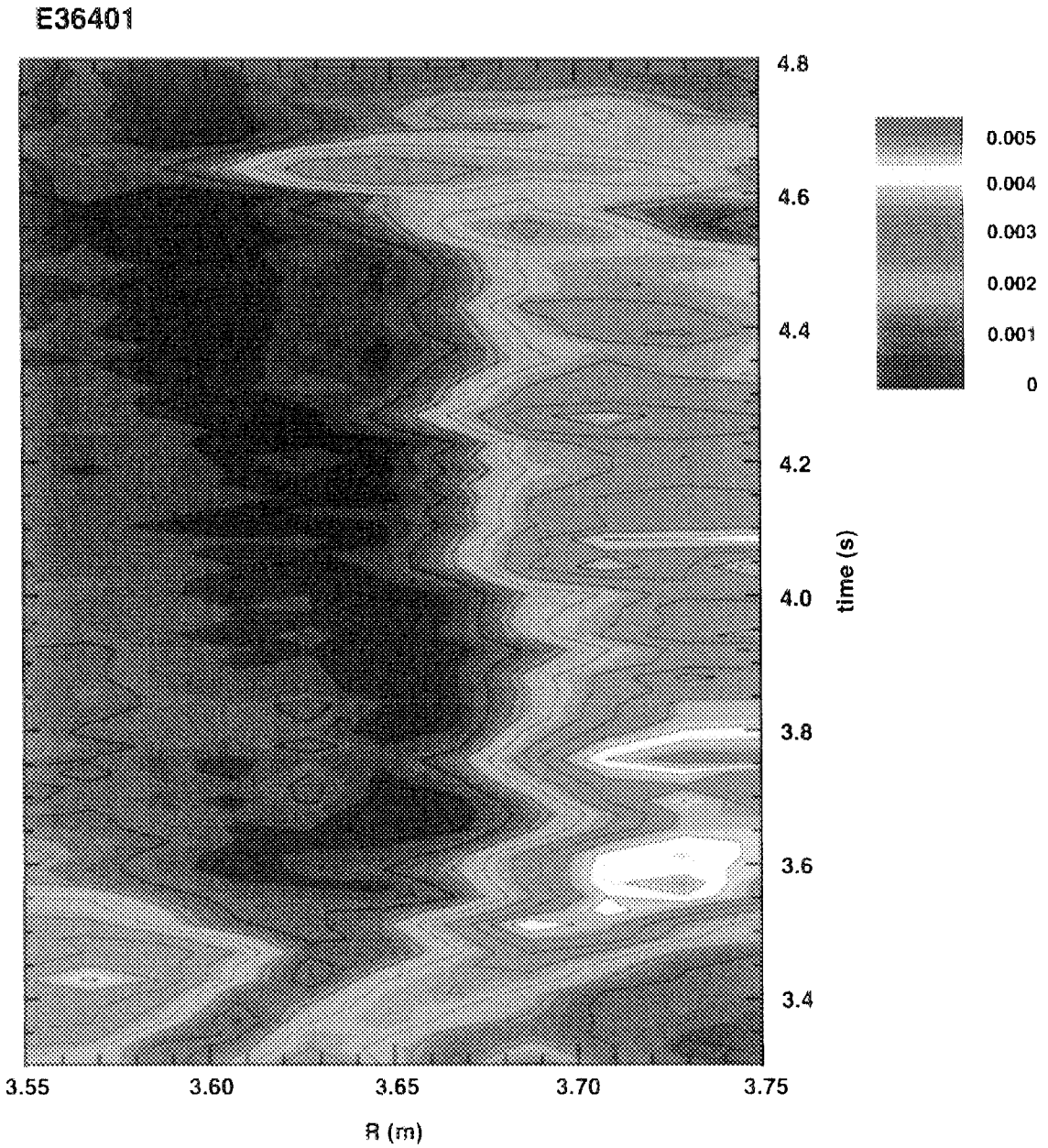

Figure 5.9: Contour plot of the $\tilde{T}_e/T_e$ profile evolution in E36401.

t]

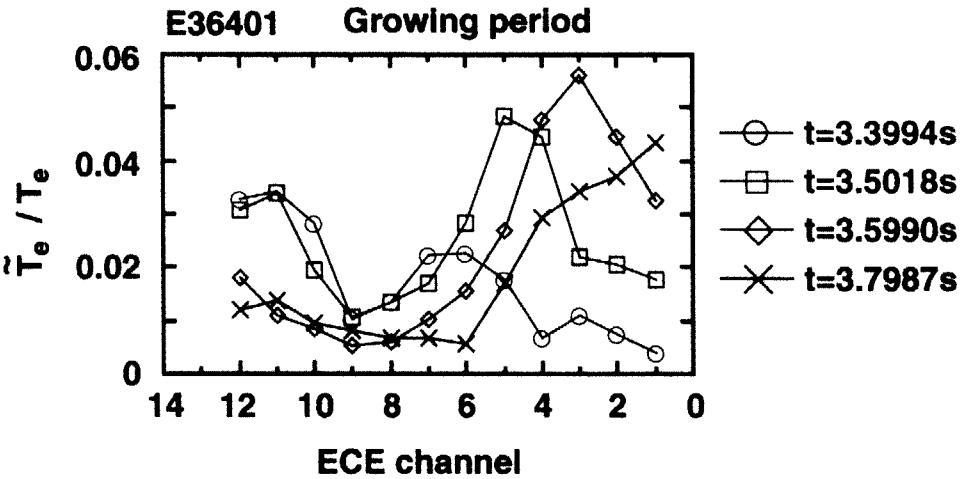

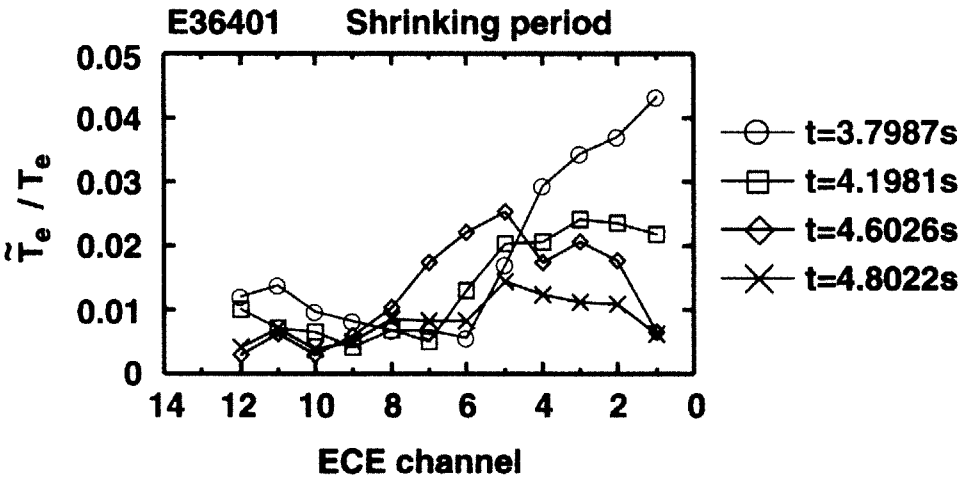

Figure 5.10: Evolutions of the $\tilde{T}_e/T_e$ profile for the growing and shrinking periods of the island in E36401.

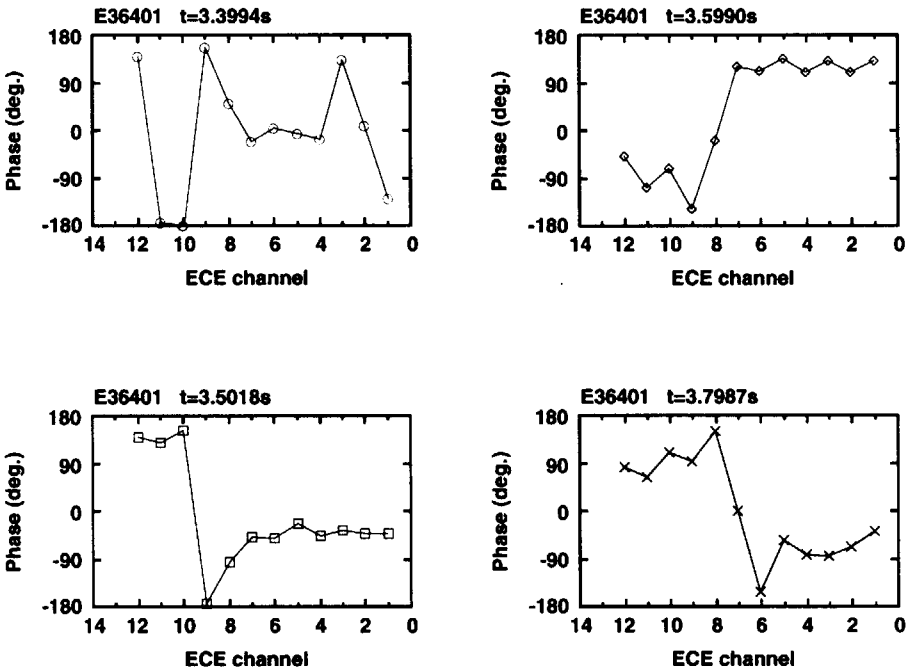

Figure 5.11: The evolution of the phase profile during the island growth phase in E36401.

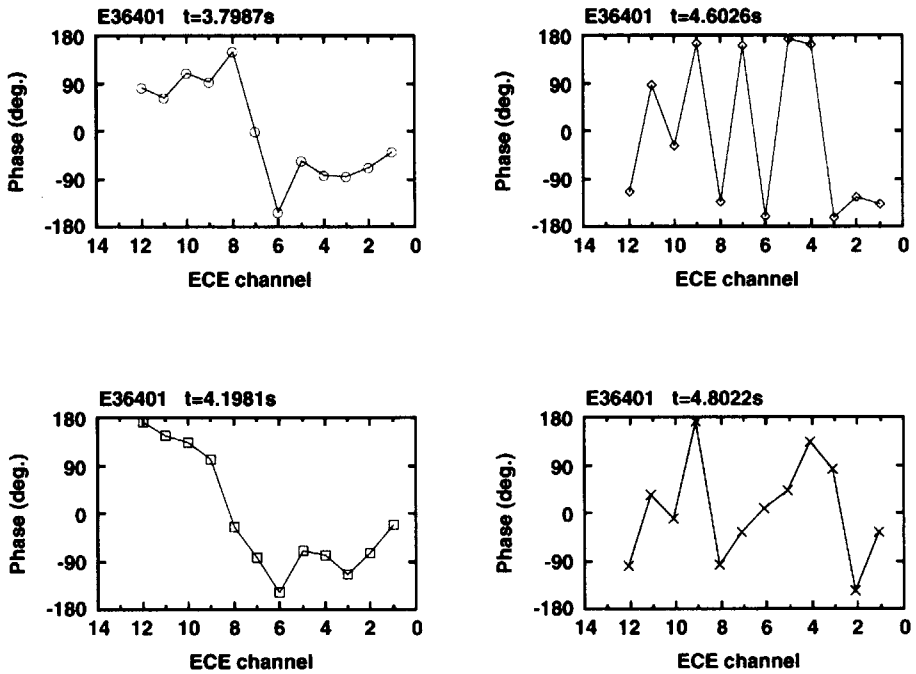

Figure 5.12: The evolution of the phase profile during the island shrinking phase in E36401.

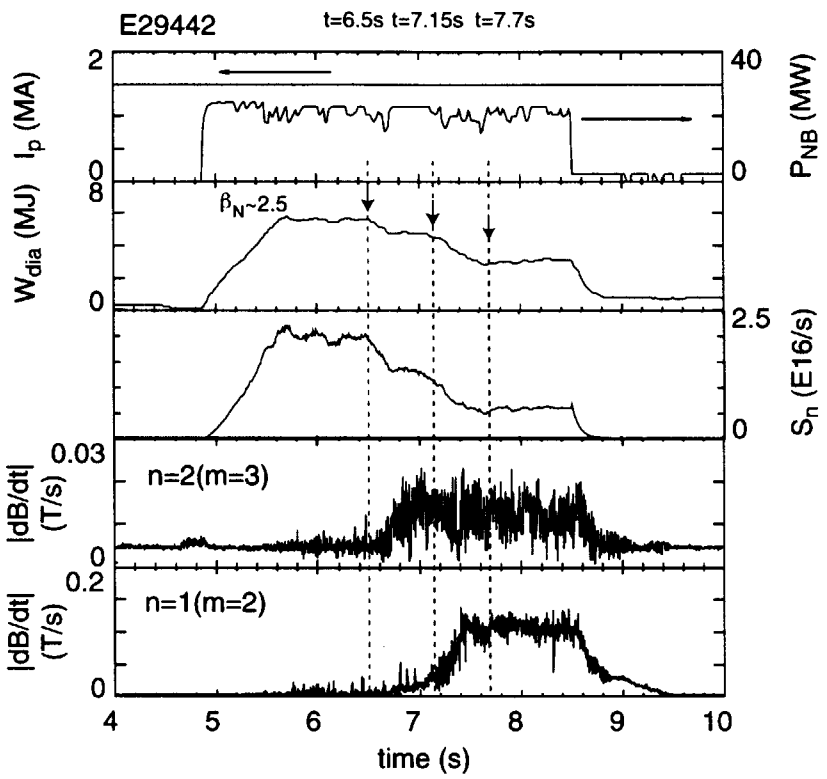

Figure 5.13: Waveforms of pulse E29442. Neoclassical tearing modes appeared in the P-NB injected H-mode plasma. The plasma stored energy W_{dia} and the neutron emission rate S_{n} degraded due to the appearance of NTMs with m/n=3/2 and 2/1. Magnetic fluctuations ($|dB/dt|$) for the two modes are shown.

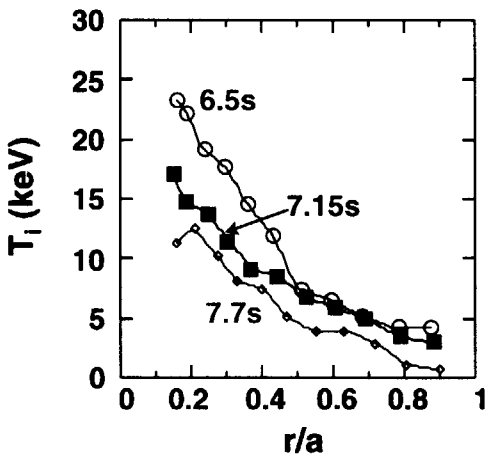

Figure 5.14: The ion temperature profiles at t = 6.5 s, 7.15 s and 7.7 s.

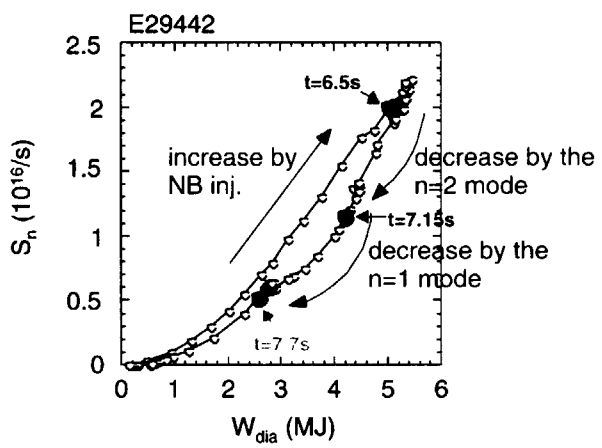

Figure 5.15: Time trajectory in the W_{dia} and S_{n} space in E29442.

NTMs). With the appearance of NTMs and their increased activity, a large decrease was observed in the T_i. A time trajectory in the W_{dia} and S_n space is plotted in Fig. 5.15. By NB injection, W_{dia} and S_n increase to the right-uppermost point. The red circle corresponds to t = 6.5 s (just before the m/n=3/2 NTM onset). Due to the m/n=3/2 and the m/n=2/1 NTMs, W_{dia} and S_n decreased as indicated by the blue point (t = 7.15 s) and the green point (t = 7.7 s). Comparing the blue and green points with the points at the same W_{dia} on the increasing path, S_n on the decreasing path is clearly below that on the increasing path. According to the transport code, the beam component of the plasma stored energy is 30 − 40 %, and the contribution from beam-thermal and beam-beam reactions to S_n is about 70 %. Therefore, there is a possibility that the neutral beam fast ions are lost or redistributed by the tearing mode. Here, the calculation uses the measured profiles and does not consider the loss mechanism of fast ion. Thus, the calculated values related to fast ion are the ones which are expected when there is no effect of NTMs on fast ions.

Figure 5.16 shows the N-NB injected case. 16 MW of P-NB was also injected. An NTM with poloidal and toroidal mode numbers m/n=2/1 appeared. At t = 3.4 s, a large m/n=2/1 mode appeared and was sustained till t = 4.8 s. A small n=2 mode also existed (not shown). The amplitude of magnetic fluctuations decreased gradually from t ~ 4.8 s and almost disappeared around t = 5.6 s. 4 MW of N-NB was injected during the large activity phase (t = 4-5 s), and after a short break, 2 MW was injected during the weak activity phase (t = 5.3-6 s). The ion temperature at $\rho = 0.2$, $T_i(0.2)$, started to increase gradually after the decrease in NTM activity. The central electron temperature $T_e(0)$ continued to increase after the decrease in NTM activity even with only half the N-NB injection power. The saturated value of S_n for the second N-NB pulse (2 MW), 6.3×10^{15} s^{-1}, was higher than for the first pulse (4 MW) with large NTM activity (5.8×10^{15} s^{-1}). This difference cannot be explained solely by differences in temperature and density. The neutron yield calculated by the transport code assuming no effect of NTM on fast ions using the measured profiles, are indicated by the closed circles in Fig. 5.16. At t = 4.9 s, S_n is calculated to be 1.24×10^{16} s^{-1} in which the beam-thermal and beam-beam fractions are 49 % and 50 %, respectively. At t = 5.85 s, the calculated S_n is 8.83×10^{15} s^{-1} (beam-thermal : 54 %, beam-beam :41 %).

In Fig. 5.17, the measured values of S_n are compared to the values calculated by the transport code with the orbit, ripple and charge exchange losses evaluated by the OFMC code. Data for P-NB and N-NB heated H mode discharges with no instability, and with m/n=3/2 and m/n=2/1 NTM are shown. The measured values agree with the calculated values for the cases with no NTM. For cases with only P-NB injection, the differences between the measurement and calculation are not large. The differences are larger for N-NB plus P-NB injections. This suggests that N-NB ions suffer larger transport than P-NB ions. Comparing the different phases (t = 4.9 s and t = 5.9 s) of pulse E37012 (m/n=2/1, N-NB plus P-NB injection) in Fig. 5.17, the difference between measured and calculated S_n is larger at t = 4.9 s with a larger magnetic fluctuation amplitude than at t = 5.9 s, as shown in Fig. 5.16. The larger amplitude of the perturbed magnetic field corresponds to the wider saturated island width, which has been confirmed by the fast T_e fluctuation measurement as mentioned in 5.2.3. Thus, the influence of NTM on the fast ion

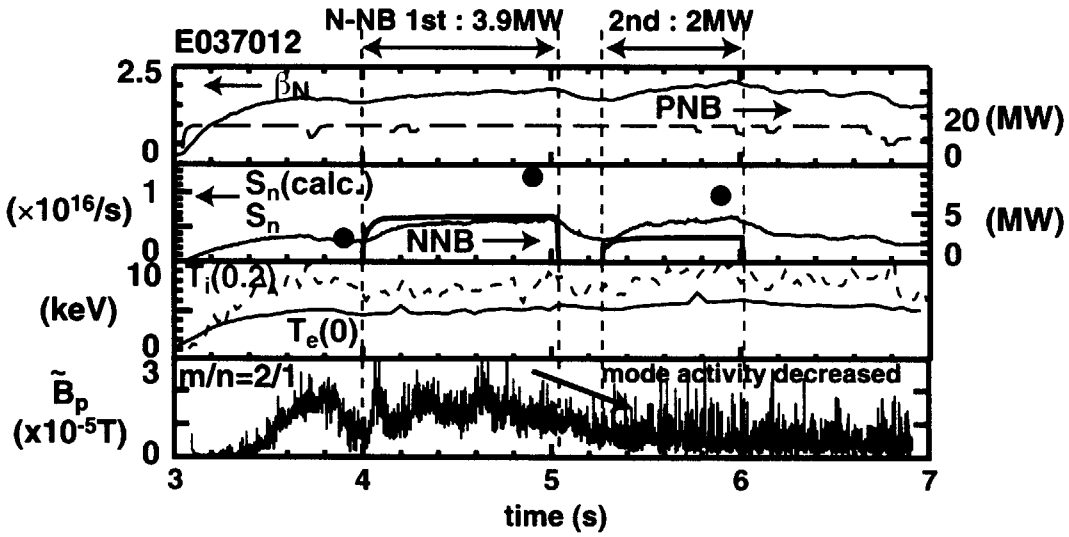

Figure 5.16: Waveforms of pulse E37012. A neoclassical tearing mode with m/n=2/1 appeared. β_N, N-NB and P-NB injection powers, S_n, $T_e(0)$, $T_i(0.2)$, and magnetic fluctuations (n=1) are shown. The values of S_n calculated by the transport code are also shown by the closed circles.

profile depends on the magnetic island size. Even for P-NB injection alone (E29442 in Fig. 5.13), the measured S_n became less than the calculated value clearly when two modes (n=2 and n=3) with large activity coexisted, as shown in Fig. 5.17. Figure 5.18 shows the dependence of $\Delta S_n/S_n^{CAL}$ on the relative level of magnetic fluctuations. Magnetic fluctuations were measured by magnetic field sensors located at the vessel wall. Data were obtained for plasmas with I_p=1 MA, P-NB injection power of 10-15 MW and N-NB injection. Here, S_n^{CAL} is the sum of beam-thermal and beam-beam components of S_n calculated by the transport code, and ΔS_n is defined as $S_n^{CAL} - (S_n^{MEAS} - S_n(\mathrm{thermal}))$ where S_n^{MEAS} is the measured value and $S_n(\mathrm{thermal})$ is the calculated thermal component of the neutron yield. Therefore, the quantity $\Delta S_n/S_n^{CAL}$ is a measure of the influence of NTM on the neutral beam fast ions (or the loss of fast ions). Since the NTM activity ($\tilde{B}_p/B_p$) is generally correlated with the NB injection power, a normalized value such as $\Delta S_n/S_n^{CAL}$ should be compared in order to investigate the dependence of NB fast ion losses on magnetic fluctuations. With increasing level of magnetic fluctuations, $\Delta S_n/S_n^{CAL}$ increases. These results on the neutron yield reduction suggest that NTM causes loss or redistribution of beam ions.

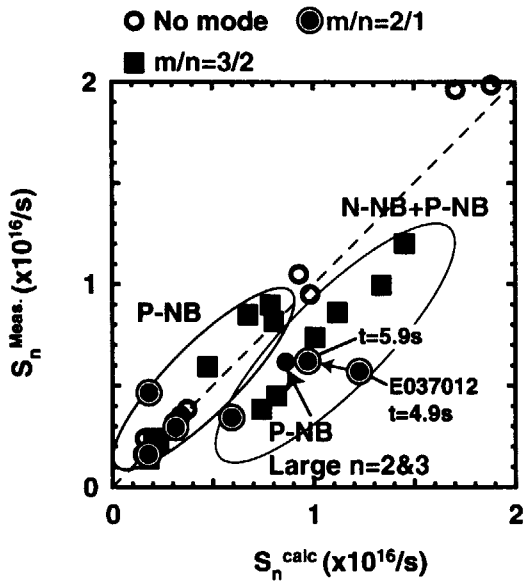

Figure 5.17: Comparison of the measured S_n to the calculated values. Data for discharges with no NTM, and with m/n=2/1, m/n=3/2 and n=3 modes are shown. Areas for cases with P-NB injection and with N-NB plus P-NB injections are also shown.

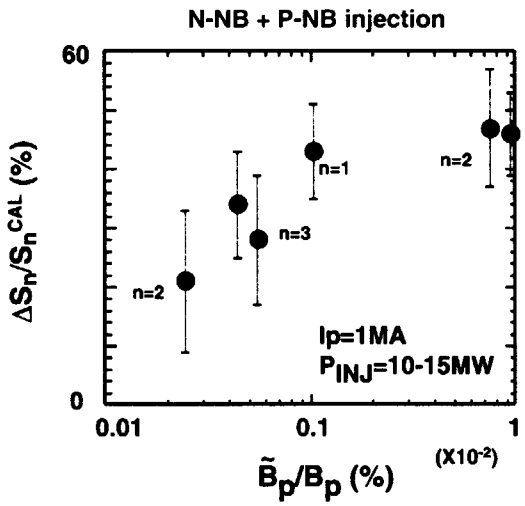

Figure 5.18: The dependence of $\Delta S_n/S_n^{CAL}$ on the relative level of magnetic fluctuations measured at the wall. The toroidal mode number for each data is shown aside.

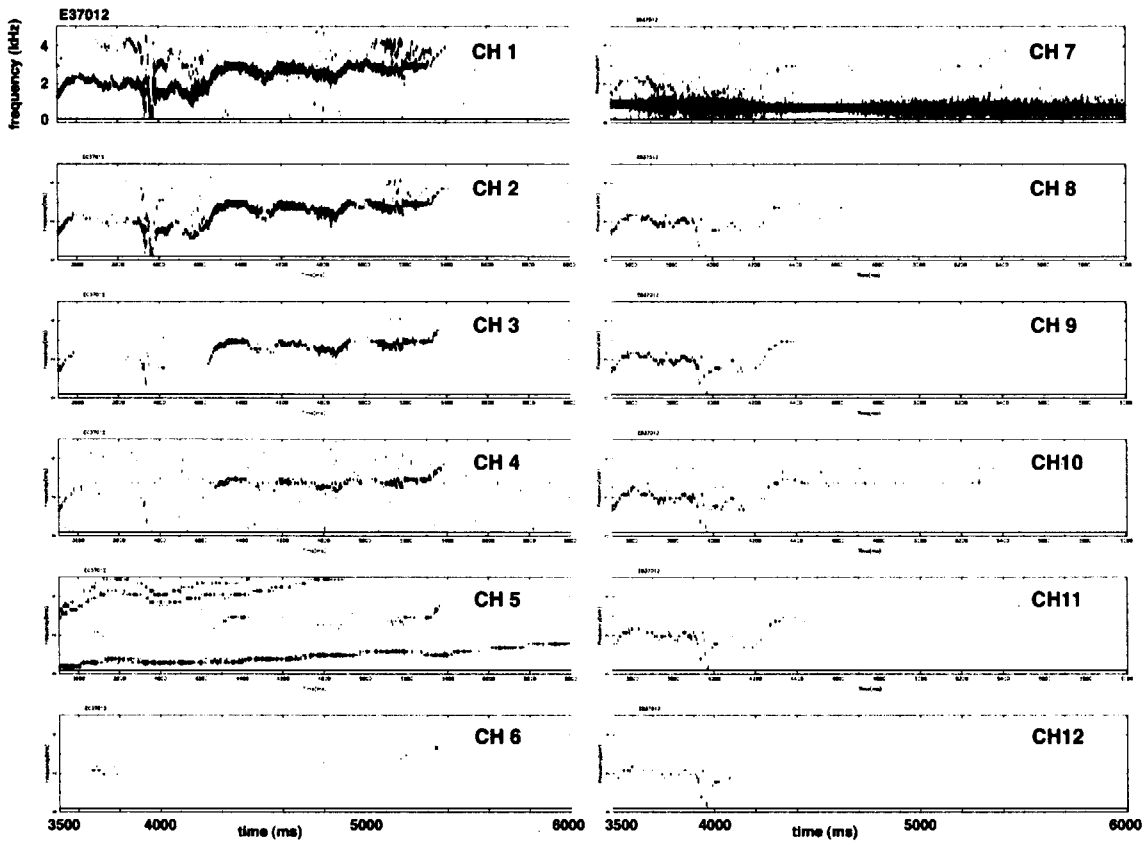

Figure 5.19: Time evolution of the frequency spectrum of T_e fluctuations measured by the ECE heterodyne radiometer for E37012.

5.2.3 Experimental evaluation of fast Ion profile modification

In the previous section, transport of the NB fast ions due to the NTM was discussed only from the macroscopic parameter (the integration over a whole plasma volume). However, transport of fast ions is considered to have some structure related to magnetic island. Therefore, detailed analysis of discharge E37012 with m/n=2/1 NTM described in the previous section is presented in this section. The plasma current and the toroidal magnetic field were 1.0 MA and 3.54 T, respectively. The frequency spectra of T_e fluctuations measured by the ECE heterodyne radiometer are shown in Fig. 5.19. The frequency range (177.5-187.5 GHz) of 12 detectors corresponds to $R = 3.44 - 3.66$ m ($\rho = 0.12 - 0.34$) in this discharge (Fig. 5.20). The peak frequency of the T_e fluctuation spectrum changed in the range of 1-3 kHz. The fluctuations disappeared around t = 5.4 s. The fluctuations below 1 kHz and above 3 kHz on channel 5 and the fluctuation around 1 kHz on channel 7 do not seem to relate to the m/n=2/1 NTM discussed here. In Fig. 5.20, the spatial profiles of the phase and $\tilde{T}_e/T_e$ for the peak frequency component at t = 3.8942 s are shown. All channels of the ECE heterodyne radiometer view the low field side (outside of the magnetic axis in the major radial direction) as indicated in the poloidal cross section shown in Fig. 5.20. The phase inversion occurs around channels 3-4. The q=2 surface determined from equilibrium reconstruction is located around channel 6. Therefore, the O-point of the m/n=2/1 magnetic island is lo-

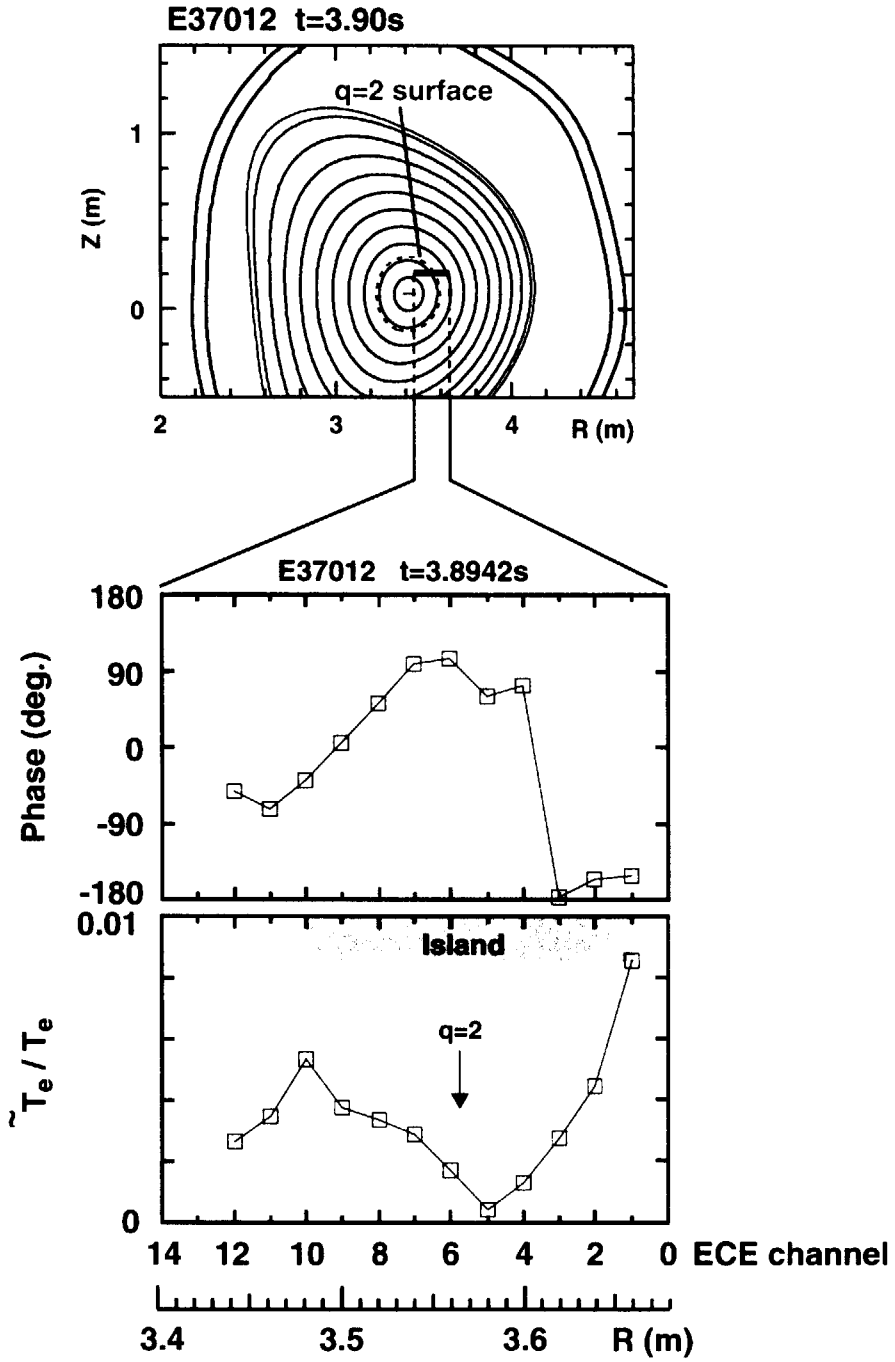

Figure 5.20: The range of measurement of the ECE heterodyne radiometer is shown in the plasma poloidal cross section for E37012. The spatial profiles of the phase and the relative fluctuation level $\tilde{T}_e/T_e$ at t = 3.8942 s in E37012 are also shown.

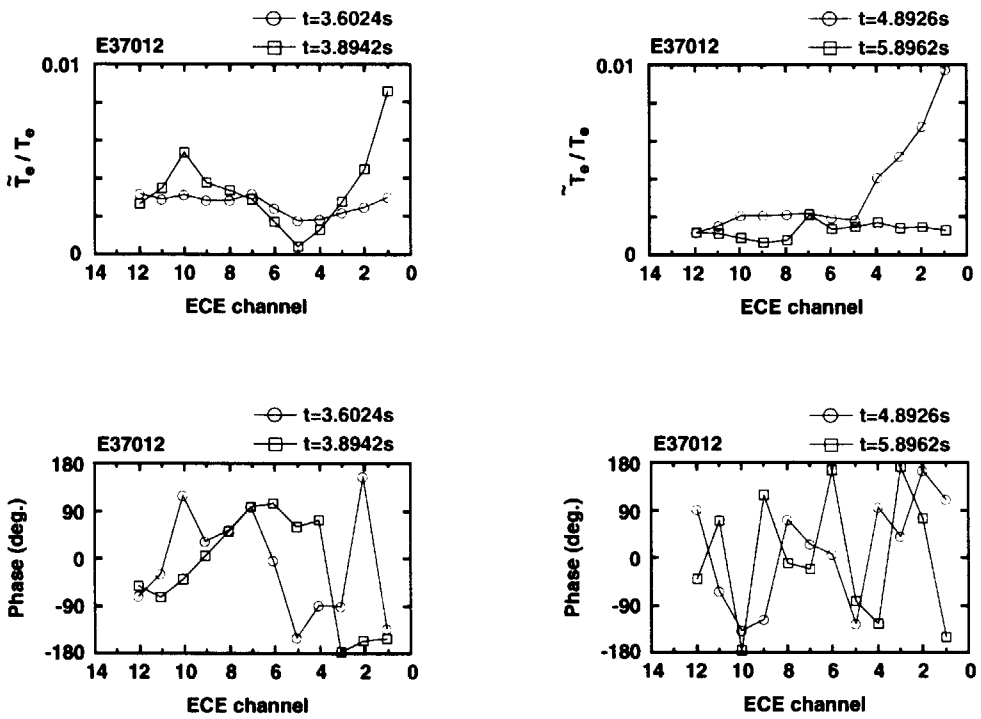

Figure 5.21: Evolutions of the phase and $\tilde{T}_e/T_e$ profiles for the growing and shrinking periods of the island in E37012.

cated between channels 3 and 6 with an uncertainty of 6 cm. The inboard (high field side) peak of $\tilde{T}_e/T_e$ corresponding to the inner edge of the island is located at channel 10 ($R = 3.48$ m, $\rho = 0.14$). The outboard (low field side) peak corresponding to the outer edge is at channel 1 ($R = 3.66$ m, $\rho = 0.34$) or possibly further outside. Therefore, the island width is estimated to be at least 18 cm (channels 1-10). Figure 5.21 shows the evolution of the phase and $\tilde{T}_e/T_e$ profiles during growing and shrinking periods of the island. At t = 4.8926 s, the high field side peak of $\tilde{T}_e/T_e$ has disappeared. If we assume that the high field side peak moved further inward beyond the ECE measurement range, the island width would have increased to 22 cm. The small inward shift of the q=2 surface shown in Fig. 5.22 may be responsible for this shift. The island structure disappeared at t = 5.8962 s, which is consistent with the time-trace of magnetic fluctuations shown in Fig. 5.16.

The time evolution of the plasma equilibrium is discussed next. Figure 5.22 shows the time-evolution of the current density profile as a contour plot and as radial profile plots at different times . During the interval t = 3.4-3.95 s, the current density decreased in the region $\rho = 0.2 - 0.4$ and became almost flat. This is considered to be caused by the reduced bootstrap current around the q=2 magnetic surface because of the flattening of the pressure profile inside the magnetic island, and this structure appeared in the total current density profile on the current diffusion time scale. The location of this structure in the j profile is consistent with the location of the magnetic island identified by the ECE heterodyne radiometer. Once the island growth saturated, current diffusion caused current density to increase on both sides of the region where the bootstrap current was lost, as shown in the j profile at t = 4.60 s. During

the shrinking period of the island t = 5.0-5.40 s, the width of the flat (or hollow) region in the j profile became narrower. After the island has disappeared, the flat (or hollow) structure disappeared from the current density profile. This is consistent with the explanation of NTM growth due to a reduction of the bootstrap current within the magnetic island. This is the first direct observation of the bootstrap current reduction in the magnetic island.

The fast ion pressure profile modified by NTM, deduced from equilibrium reconstruction, was compared to the fast ion pressure profile calculated by TOPICS. The fast ion pressure profile calculated by TOPICS corresponds to that expected in the absence of NTM. Discharge E37012 was analyzed using the measured temperature, density and effective charge profiles shown in Fig. 5.23. The electron temperature profile measurement, ECE FTS (Fourier Transform Spectroscopy), determines the profile by Fourier transform every 50 ms. The CXRS measurement averages the observed spectrum over 30-50 ms to obtain sufficient S/N ratio. Thus, the magnetic island structure rotating at several kHz could not be resolved clearly. TOPICS calculates the NB deposition profile for given temperature, density and effective charge profiles. Profiles of the calculated fast ion density $n_{\mathrm{D}}(\mathrm{fast})$, thermal ion density $n_{\mathrm{D}}(\mathrm{thermal})$ and impurity (carbon) density $n_{\mathrm{IMP}}(\mathrm{carbon})$ are also shown in Fig. 5.23. Here, $n_{\mathrm{D}}(\mathrm{fast})$ is the integral of the distribution function f_{b} over the velocity range for $v > v_{\mathrm{th}}$ (v_{th} : the bulk ion thermal velocity),

$$n_{\mathrm{D}}(\mathrm{fast}) \equiv \int_{v>v_{\mathrm{th}}} f_{\mathrm{b}}\, d\boldsymbol{v}.$$

The current density profile determined by equilibrium reconstruction and the calculated bootstrap current profile are shown in the top row of Fig. 5.24. The total pressure profile from equilibrium reconstruction ($P_{\mathrm{EQ}}(\mathrm{total})$) and the pressure profile calculated by TOPICS ($P_{\mathrm{TOPICS}}(\mathrm{total})$) are shown in the middle row. The thermal and fast ion components of pressure, $P_{\mathrm{TOPICS}}(\mathrm{thermal})$ and $P_{\mathrm{TOPICS}}(\mathrm{fast})$, calculated by TOPICS are also shown. In the bottom row, the measured fast ion pressure profile defined by $P_{\mathrm{EQ}}(\mathrm{fast}) \equiv P_{\mathrm{EQ}}(\mathrm{total}) - P_{\mathrm{TOPICS}}(\mathrm{thermal})$ is compared with $P_{\mathrm{TOPICS}}(\mathrm{fast})$. The difference is not large at t = 3.95 s (only P-NB was injected, and NTM existed) and t = 5.85 s (P-NB and N-NB were injected, and NTM has nearly disappeared), while a clear difference can be seen at t = 4.90 s (P-NB and N-NB were injected, and NTM existed). This difference is considered to be the lost portion due to NTM. These results indicate that the N-NB fast ions are transported from the core by NTM and that the lower energy P-NB ions were not affected as much as the N-NB ions. These are consistent with the behavior of the neutron yield described in 5.2.2. In Fig. 5.25 (a), the lost fast ion pressure profile defined by $P_{\mathrm{lost}}(\mathrm{fast}) \equiv P_{\mathrm{TOPICS}}(\mathrm{fast}) - P_{\mathrm{EQ}}(\mathrm{fast})$ is plotted together with $P_{\mathrm{EQ}}(\mathrm{fast})$ and $P_{\mathrm{TOPICS}}(\mathrm{fast})$ at t = 4.90 s and 5.85 s. The calculated N-NB fast ion pressure profile $P_{\mathrm{TOPICS}}(\mathrm{N-NB})$ and the P-NB fast ion pressure profile $P_{\mathrm{TOPICS}}(\mathrm{P-NB})$ are also shown. The N-NB driven current profile measured in the experiment $j_{\mathrm{NNB}}(\mathrm{exp.})$ could be lower than the profile calculated by OFMC $j_{\mathrm{NNB}}(\mathrm{OFMC})$.

In the following, $j_{\mathrm{NNB}}(\mathrm{exp.})$ is evaluated by comparing the measured and calculated fast ion pressure profiles $P_{\mathrm{EQ}}(\mathrm{fast})$ and $P_{\mathrm{TOPICS}}(\mathrm{fast})$. The N-NB fast ion pressure and the driven current density at minor radius ρ are given by

$$P_{\mathrm{NNB}}(\rho) \;=\; \left\langle \frac{m_{\mathrm{b}}}{2} \int f_{\mathrm{NNB}}(\boldsymbol{r},\boldsymbol{v}) v^2\, d\boldsymbol{v} \right\rangle_{\rho},$$

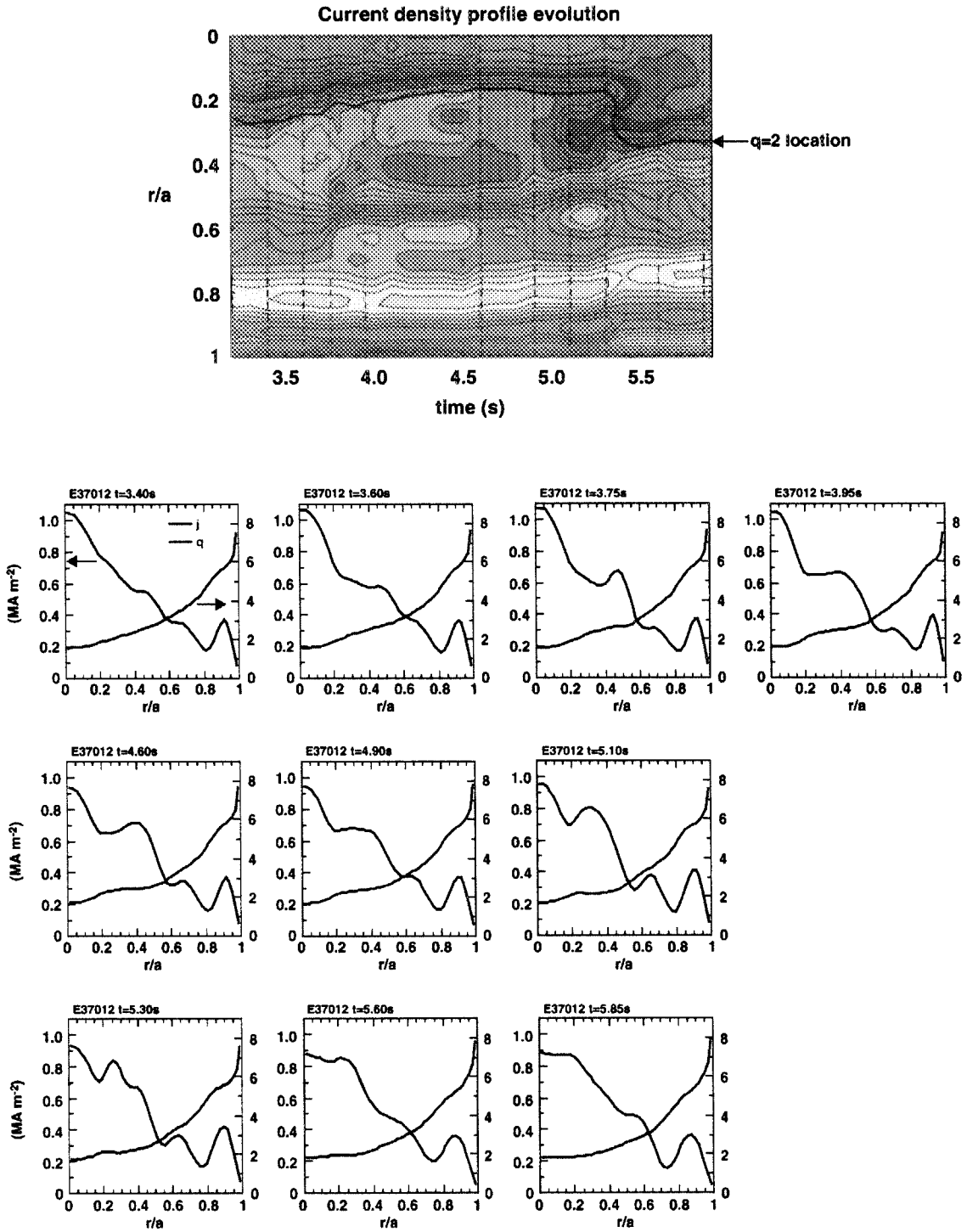

Figure 5.22: Contour plot of the total current density profile evolution from equilibrium reconstruction for E37012. The current density j and the safety factor q profiles are shown at different times.

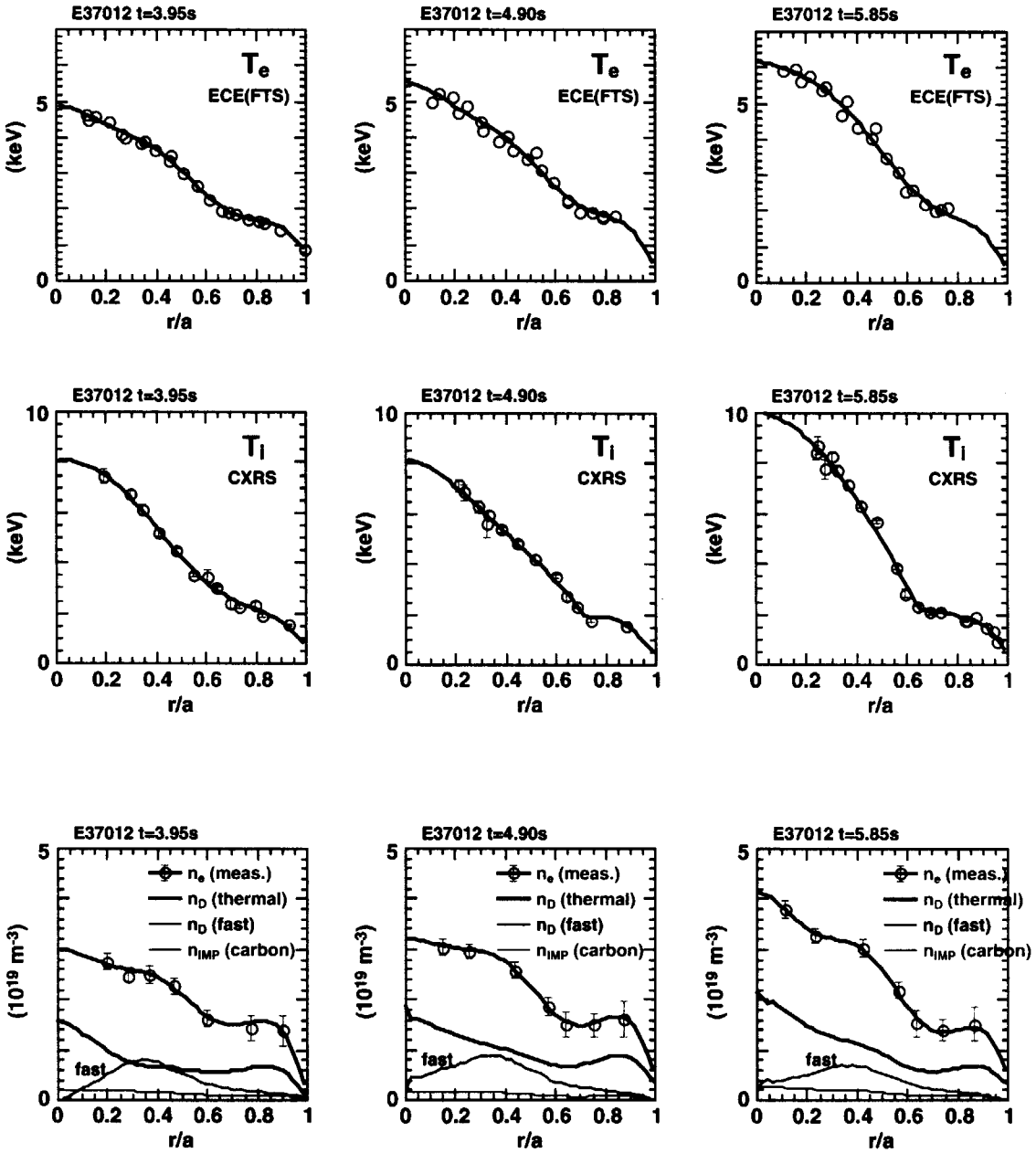

Figure 5.23: The measured electron and ion temperature profiles and the measured electron density profile are shown for E37012 t = 3.95 s, 4.90 s and 5.85 s. The density profiles of the thermal ion (deuterium), the fast ion and the impurity (carbon) calculated by the TOPICS code are also shown.

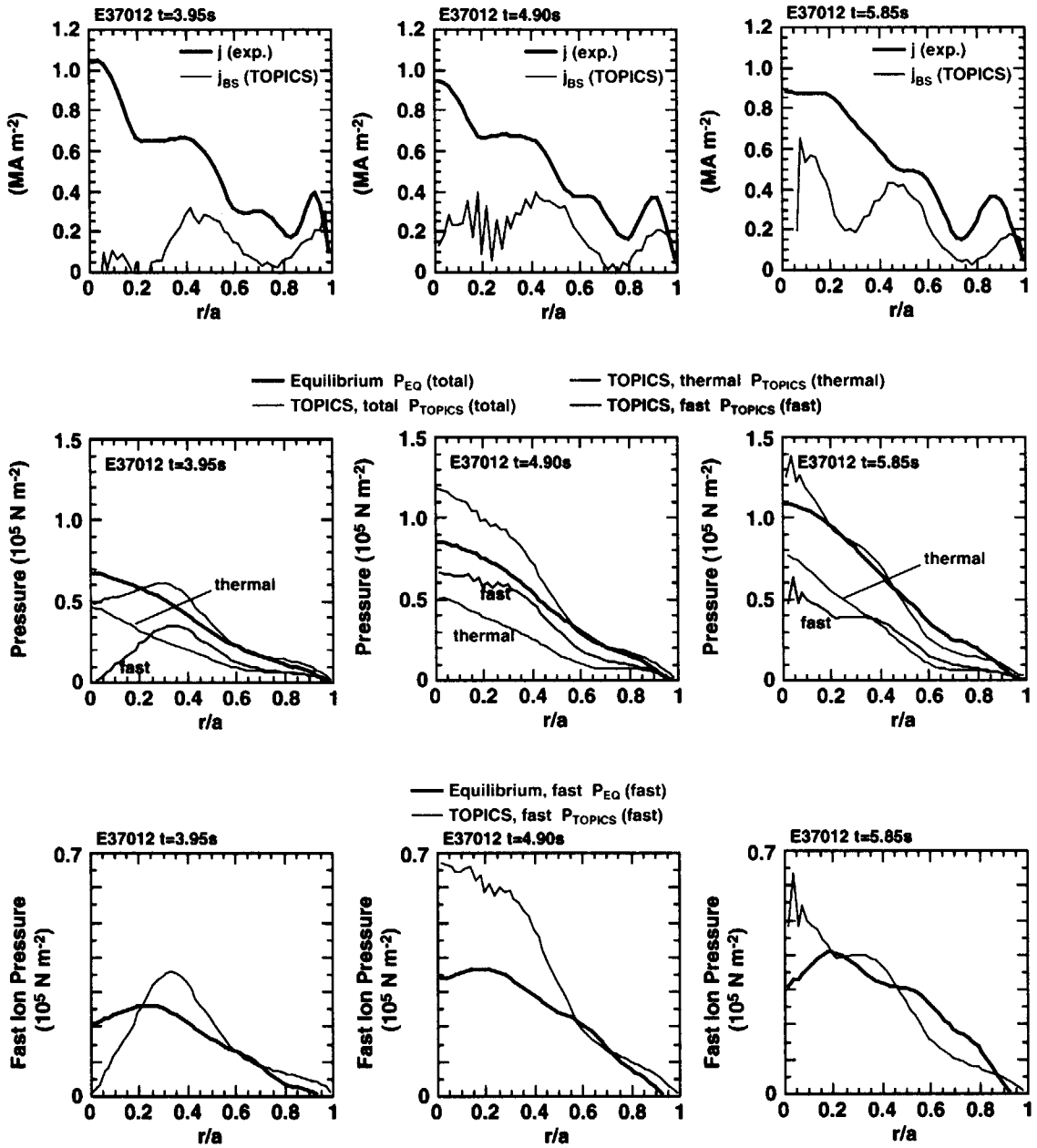

Figure 5.24: For E37012 at t = 3.95 s, 4.90 s and 5.85 s, shown are the measured current density and the calculated bootstrap current profiles in the top row. The total pressure profiles by equilibrium reconstruction and the TOPICS code are shown in the middle row. The thermal and fast ion pressure profiles calculated by TOPICS are also shown. In the bottom row, the fast ion pressure profiles calculated by equilibrium reconstruction and the TOPICS code are compared.

$$j_{\rm NNB}(\rho) \;=\; \left\langle eZ_{\rm b}\int f_{\rm NNB}(\boldsymbol{r},\boldsymbol{v})v_{//}\,d\boldsymbol{v}\right\rangle_{\rho},$$

where $Z_{\rm b}$ and $m_{\rm b}$ are the nuclear charge and mass of the N-NB ion, e is the electronic charge, $f_{\rm NNB}(\boldsymbol{r},\boldsymbol{v})$ is the N-NB fast ion distribution function, $v_{//}$ is the component of velocity $\boldsymbol{v}$ parallel to $\boldsymbol{B}$, and $\langle ...\rangle_{\phi}$ denotes flux surface average at minor radius ρ. Flux surface averages are taken in the equations above because $P_{\rm NNB}$ and $j_{\rm NNB}$ are not constant on a flux surface (the total pressure is constant on a flux surface). Here, we introduce the quantity α defined as the loss rate due to NTM (more precisely, $\alpha \equiv 1-(f'/f)$ where f' is the distribution function in the presence of NTM). Generally, α is a function of the velocity vector $\boldsymbol{v}$, and hence, depends on the ion energy and the pitch angle in velocity space. Thus, the lost fast ion pressure at minor radius ρ is

$$P^{\rm lost}_{\rm NNB}(\rho) = \left\langle \frac{m_{\rm b}}{2}\int \alpha(\boldsymbol{r},\boldsymbol{v})f_{\rm NNB}(\boldsymbol{r},\boldsymbol{v})v^2\,d\boldsymbol{v}\right\rangle_{\rho}. \tag{5.1}$$

For discharge E37012, this corresponds to $P_{\rm lost}$(fast) in Fig. 5.25 (a) if only N-NB ions were lost. The N-NB driven current profile in the presence of NTM $j^{\rm NTM}_{\rm NNB}$ can be also written using α,

$$j^{\rm NTM}_{\rm NNB}(\rho) = \left\langle eZ_{\rm b}\int (1-\alpha(\boldsymbol{r},\boldsymbol{v}))\,f_{\rm NNB}(\boldsymbol{r},\boldsymbol{v})v_{//}\,d\boldsymbol{v}\right\rangle_{\rho}.$$

To evaluate the N-NB driven current profile realized in the experiment $j_{\rm NNB}$(exp.) using the measured lost fast ion pressure profile $P_{\rm lost}$(fast) shown in Fig. 5.25, we adopt three assumptions. First, the lost fast ions originate only from N-NB, because the difference between the equilibrium (experimental) and calculated fast ion pressure profiles at t = 3.95 s is smaller than at t = 4.90 s (Fig. 5.24), and because the difference between the measured and calculated neutron yields (Fig. 5.17) for P-NB is small. Second, the loss rate α is independent of the velocity vector $\boldsymbol{v}$. Third, α is approximately constant on each flux surface. The second and third assumptions are necessary because we have no experimental information on the dependence of α on $\boldsymbol{v}$ or $\boldsymbol{r}$. The third assumption is considered to be appropriate as follows. The fluctuating radial magnetic field $\tilde{B}_r$, which produces the magnetic island structure, is far smaller than the equilibrium magnetic field (otherwise, equilibrium is destroyed). Thus, the radial excursion that a fast ion experiences while travelling near the O-point of the magnetic island where $\tilde{B}_r$ is maximum is much smaller than the magnetic island width. The magnetic island rotates at several kHz (~1 kHz for $m = 2$ in the present case), while an N-NB fast ion with an energy of 360 keV, which is produced as a passing particle, rotates at ~280 kHz toroidally, and hence, ~140 kHz poloidally near the $q = 2$ surface. Thus, a fast ion experiences the whole poloidal structure of the $m = 2$ island until the accumulated radial excursion exceeds the island half width. In this sense, it is appropriate that α is represented by an averaged value on a flux surface. The second assumption is reexamined in the discussion Sec. 6.2.2. Therefore, α can be evaluated from the equilibrium (experiment) fast ion pressure $P_{\rm EQ}$(fast) and the calculated fast ion pressure $P_{\rm TOPICS}$(fast),

$$\alpha = 1 - P_{\rm EQ}({\rm fast})/P_{\rm TOPICS}({\rm fast}) \;\; \text{(at each } \rho). \tag{5.2}$$

Figure 5.25 (b) shows $j_{\rm NNB}$(exp.) estimated by

$$j_{\rm NNB}({\rm exp.}) \equiv j^{\rm NTM}_{\rm NNB} = (1-\alpha)\,j_{\rm NNB}({\rm OFMC}). \tag{5.3}$$

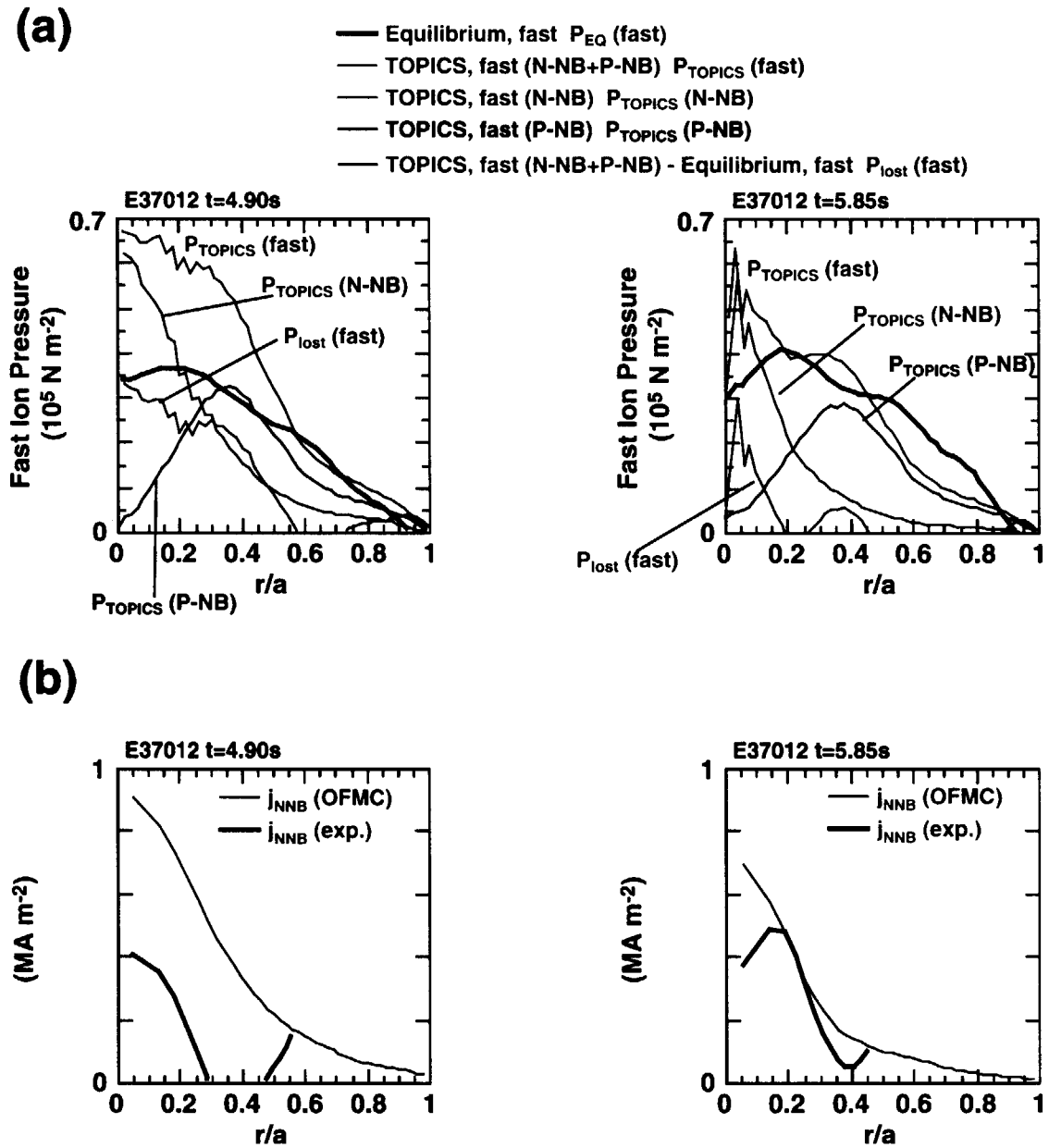

Figure 5.25: (a) Fast ion pressure profile deduced from equilibrium reconstruction and that calculated by TOPICS are shown. The equilibrium fast ion pressure is obtained by subtracting the measured thermal pressure from the equilibrium pressure. The fraction lost by NTM activity, defined by the difference between the fast ion pressure calculated by TOPICS and equilibrium fast ion pressure, is also shown. (b) The N-NB driven current density profile calculated by OFMC $j_{\mathrm{NNB}}(\mathrm{OFMC})$ and the experimentally determined profile $j_{\mathrm{NNB}}(\mathrm{exp.})$ evaluated using $j_{\mathrm{NNB}}(\mathrm{OFMC})$ and the fast ion pressure profile are shown.

In the presence of NTM (t = 4.90 s), $j_{\rm NNB}$(exp.) is greatly reduced from $j_{\rm NNB}$(OFMC), while both are nearly the same at t = 5.85 s (NTM has nearly disappeared). Here, α and $j_{\rm NNB}$(exp.) were evaluated within $\rho = 0.55$ at t = 4.90 s and $\rho = 0.45$ at t = 5.85 s, respectively. The total N-NB driven current calculated by OFMC is 450 kA at t = 4.90 s and 240 kA at t = 5.85 s. The lost driven current evaluated by integrating the difference between $j_{\rm NNB}$(OFMC) and $j_{\rm NNB}$(exp.) is 300 kA at t = 4.90 s and 40 kA at t = 5.85 s. Thus, the N-NB driven current was reduced by 67 % at t = 4.90 s (with NTM), while the reduction was 17 % at t = 5.85 s (with NTM nearly suppressed).

Next, the loss fraction of the N-NB fast ions is evaluated from the neutron yield. The neutron yield $S_{\rm n}$ is composed of thermal-thermal, beam-thermal and beam-beam components, denoted by $S_{\rm n}$(th-th), $S_{\rm n}$(b-th) and $S_{\rm n}$(b-b), respectively. In the present discussion, the beam contributions from N-NB and P-NB ions are treated separately. Thus, in the beam-thermal neutron yield, the NNB-thermal and PNB-thermal components, $S_{\rm n}$(N-th) and $S_{\rm n}$(P-th), are considered. The beam-beam neutron yield is divided into three components, i.e., the N-NB - N-NB, N-NB - P-NB and P-NB - P-NB components, denoted by $S_{\rm n}$(N-N), $S_{\rm n}$(N-P) and $S_{\rm n}$(P-P), respectively. Thus, the total neutron yield $S_{\rm n}$(total) is written as

$$\begin{aligned} S_{\rm n}(\text{total}) &\equiv S_{\rm n}(\text{th-th}) + S_{\rm n}(\text{b-th}) + S_{\rm n}(\text{b-b}) \\ &= S_{\rm n}(\text{th-th}) && \text{(thermal-thermal)} \\ &\quad + S_{\rm n}(\text{N-th}) + S_{\rm n}(\text{P-th}) && \text{(beam-thermal)} \\ &\quad + S_{\rm n}(\text{N-N}) + S_{\rm n}(\text{N-P}) + S_{\rm n}(\text{P-P}) && \text{(beam-beam).} \end{aligned}$$

The N-NB contribution to the neutron yield is defined by

$$\begin{aligned} S_{\rm n}(\text{N} - \text{NB}) &\equiv S_{\rm n}(\text{total}) - S_{\rm n}(\text{th-th}) - S_{\rm n}(\text{P-th}) - S_{\rm n}(\text{P-P}) \\ &= S_{\rm n}(\text{N-th}) + S_{\rm n}(\text{N-N}) + S_{\rm n}(\text{N-P}) \end{aligned} \tag{5.4}$$

The N-NB related components, $S_{\rm n}$(N-th), $S_{\rm n}$(N-N) and $S_{\rm n}$(N-P), are given by,

$$\begin{aligned} S_{\rm n}(\text{N-th}) &= \int d\boldsymbol{r} \left[\int_{\rm NNB} d\boldsymbol{v} \int_{\rm thermal} d\boldsymbol{v}' \, f_{\rm NNB}(\boldsymbol{r},\boldsymbol{v}) f_{\rm thermal}(\boldsymbol{r},\boldsymbol{v}') v_{\rm r}^{\rm N-th} \sigma(v_{\rm r}^{\rm N-th}) \right] , \\ S_{\rm n}(\text{N-N}) &= \int d\boldsymbol{r} \left[\int_{\rm NNB} d\boldsymbol{v} \int_{\rm NNB} d\boldsymbol{v}' \, f_{\rm NNB}(\boldsymbol{r},\boldsymbol{v}) f_{\rm NNB}(\boldsymbol{r},\boldsymbol{v}') v_{\rm r}^{\rm N-N} \sigma(v_{\rm r}^{\rm N-N}) \right] , \\ S_{\rm n}(\text{N-P}) &= \int d\boldsymbol{r} \left[\int_{\rm NNB} d\boldsymbol{v} \int_{\rm PNB} d\boldsymbol{v}' \, f_{\rm NNB}(\boldsymbol{r},\boldsymbol{v}) f_{\rm PNB}(\boldsymbol{r},\boldsymbol{v}') v_{\rm r}^{\rm N-P} \sigma(v_{\rm r}^{\rm N-P}) \right] , \end{aligned}$$

where $f_{\rm thermal}$, $f_{\rm NNB}$ and $f_{\rm PNB}$ are the distribution functions for the thermal, N-NB and P-NB ions, $v_{\rm r}^{\rm N-th}$, $v_{\rm r}^{\rm N-N}$ and $v_{\rm r}^{\rm N-P}$ are the relative velocities between N-NB and thermal ions, N-NB and N-NB ions, and N-NB and P-NB ions, and $\sigma(v_{\rm r})$ is the cross section for D-D fusion reaction at a kinetic energy of $m_{\rm D} v_{\rm r}^2/2$. Tables 5.1 and 5.2 show the breakdown into each $S_{\rm n}$ component for E37012 t = 4.90 s. According to table 5.2, $S_{\rm n}$(N-N) of $0.41 \times 10^{15}\,{\rm s}^{-1}$ is 10 times smaller than $S_{\rm n}$(N-th) of $4.24 \times 10^{15}\,{\rm s}^{-1}$ and $S_{\rm n}$(N-P) of $4.62 \times 10^{15}\,{\rm s}^{-1}$. Thus, ignoring $S_{\rm n}$(N-N) in eqn 5.4, $S_{\rm n}$(N − NB) is approximately given by

$$S_{\rm n}(\text{N} - \text{NB}) \approx S_{\rm n}(\text{N-th}) + S_{\rm n}(\text{N-P})$$

Table 5.1: Breakdown of the neutron yield for E37012 at t = 4.90 s (1)

	neutron yield (s^{-1})
thermal-thermal	0.17×10^{15}
beam-thermal	6.05×10^{15}
beam-beam	6.16×10^{15}
Total	1.24×10^{16}

Table 5.2: Breakdown of the neutron yield for E37012 at t = 4.90 s (2)

	thermal	N-NB	P-NB
thermal	0.17×10^{15}	4.24×10^{15}	1.81×10^{15}
N-NB	-	0.41×10^{15}	4.62×10^{15}
P-NB	-	-	1.12×10^{15}

$$= \int d\boldsymbol{r} \left[\int_{\mathrm{NNB}} d\boldsymbol{v} \int_{\mathrm{thermal}} d\boldsymbol{v}' \, f_{\mathrm{NNB}}(\boldsymbol{r}, \boldsymbol{v}) f_{\mathrm{thermal}}(\boldsymbol{r}, \boldsymbol{v}') v_{\mathrm{r}}^{\mathrm{N-th}} \sigma(v_{\mathrm{r}}^{\mathrm{N-th}}) \right] + \int d\boldsymbol{r} \left[\int_{\mathrm{NNB}} d\boldsymbol{v} \int_{\mathrm{PNB}} d\boldsymbol{v}' \, f_{\mathrm{NNB}}(\boldsymbol{r}, \boldsymbol{v}) f_{\mathrm{PNB}}(\boldsymbol{r}, \boldsymbol{v}') v_{\mathrm{r}}^{\mathrm{N-P}} \sigma(v_{\mathrm{r}}^{\mathrm{N-P}}) \right]. \quad (5.5)$$

Taking into consideration the NTM effect on the N-NB distribution function using α and assuming α to be spatially constant, the N-NB contribution to the neutron yield in the presence of NTM can be written from Eq. (5.5) as

$$S_{\mathrm{n}}^{\mathrm{EXP.}}(\mathrm{N-NB}) = (1-\alpha) S_{\mathrm{n}}^{\mathrm{CAL.}}(\mathrm{N-NB}).$$

Although the relationship between the measured and calculated $S_{\mathrm{n}}(\mathrm{N-NB})$ has the same form as that for N-NB driven current density described by Eq. (5.3), it should be noted that S_{n} is a quantity integrated both spatially and in velocity space. The experimental value $S_{\mathrm{n}}^{\mathrm{EXP.}}(\mathrm{N-NB})$ is derived from the measured S_{n} and the calculated values of S_{n}(th-th), S_{n}(P-th) and S_{n}(P-P) since we have assumed that NTM does not affect P-NB ions. The TOPICS calculation gives $S_{\mathrm{n}}^{\mathrm{CAL.}}(\mathrm{N-NB})$ as indicated in Table 5.2. For discharge E37012 at t = 4.90 s, $S_{\mathrm{n}}^{\mathrm{EXP.}}(\mathrm{N-NB})$ is 2.67×10^{15} s^{-1}, and $S_{\mathrm{n}}^{\mathrm{CAL.}}(\mathrm{N-NB})$ is 9.28×10^{15} s^{-1}. Thus, the loss rate α evaluated from S_{n} is 71 %.

6. Discussion

6.1 High Energy Neutral Beam Current Drive

Neutral beam current drive theory was examined by comparing with measurements of the NB driven current profile, and favorable dependence on beam energy E_b and electron temperature T_e was confirmed in the experimental condition of $E_b = 80 - 360$ keV, $T_e(0) \leq 10$ keV, $\overline{n}_e = (0.5 - 1.5) \times 10^{19}$ m^{-3} and $Z_{eff} = 2 - 4$. In order to increase the NB driven current for accurate measurements, $\overline{n}_e$ was limited in a relatively low range (typically $\overline{n}_e > 3 \times 10^{19}$ m^{-3} in the JT-60U high performance plasmas). However, a time decay of the neutron yield after turning off N-NB injection was confirmed to agree with the theoretical simulation in a wider range of $\overline{n}_e = (0.5 - 3) \times 10^{19}$ m^{-3} in Ref. [11]. As a temporal behavior of the neutron yield reflects a NB fast ion distribution function and its diffusion in velocity space due to collision, this result supports the NB current drive theory up to $\overline{n}_e = 3 \times 10^{19}$ m^{-3}.

From comparisons of the measured N-NB driven current profiles with theoretical predictions, neutral beam current drive theory was validated up to $E_B = 360$ keV. According to this theory, the NB fast ion current is proportional to the slowing down time of fast ions (section 3.3.1), and the slowing down time has T_e and E_B dependences as shown in section 1.4.4. Current drive efficiency is proportional to the beam velocity, i.e., square root of beam energy, and to the electron temperature. Thus, the 1 MeV N-NB in ITER, which has been designed based on NB current drive theory, is expected to satisfy the requirements in the ITER operation scenarios. Using the 360 keV N-NB, a largest NB driven current of 1 MA was obtained at $T_e(0) = 10$ keV, and a record value of NB current drive efficiency 1.55×10^{19} Am^{-2}W^{-1} was achieved at $T_e(0) = 14$ keV. The effective charge Z_{eff} was 2.5 and 3 in these experiments, respectively. Typical Z_{eff} is assumed to be $\lesssim 1.6$ in ITER or commercial fusion reactors which are operated at higher electron density to produce the fusion power more efficiently. As mentioned in Sec. 1.4.3, the directed flow of fast ions tends to drag electrons with it. Thus, the NB fast ion current is partially cancelled by the dragged electrons, and the net driven current is reduced. This tendency is weakened by collisions of electrons with background ions. According to Eq. (1.3) in Sec. 1.4.3, the net driven current obtained at $Z_{eff} = 3$ would be reduced to ~80 % at $Z_{eff} = 1$ (an ideal value for fusion reactor) for the beam ion charge $Z_b = 1$ (a general situation in fusion reactor based on fusion reactions of hydrogen and its isotopes). In ITER, the beam energy of N-NB is 1 MeV and the electron temperature is predicted to be 20-30 keV due to electron heating by the 3.5 MeV alpha particles produced by the D-T fusion reaction. Thus, based on the value achieved in JT-60U [1.55×10^{19} Am^{-2}W^{-1} at $T_e(0) = 14$ keV], current drive efficiency in ITER is predicted to be $(2.9 - 4.4) \times 10^{19}$ Am^{-2}W^{-1}. This value is sufficient for requirements of the proposed operation scenarios ($\geq 2.5 \times 10^{19}$ Am^{-2}W^{-1}).

There remains an uninvestigated theoretical prediction related to the NB current drive. Enhancement of beam ionization cross-section due to "beam-particle self-interaction (BPSI)"was predicted by Okano

[94, 95]. This is the ionization process of beam particles through interaction with fast ions. Although the fast ion density is much lower than the thermal ion density, the ionization cross-section by fast ions is larger than that by thermal ions because the relative velocities between beam neutrals and fast ions are smaller. Thus, the net contribution to beam ionization can be notable especially in case of relatively low n_e and high E_b. According to the calculation using the JT-60U parameters of plasma and N-NB (350 keV) in Ref. [95], enhancement due to the BPSI for $T_e = 3$ keV and $P_{NNB} = 3$ MW is comparable to that due to the multistep ionization process at $n_e \sim 3 \times 10^{18}\mathrm{m}^{-3}$. Although the BPSI is negligibly small in the experimental conditions discussed in this thesis, this effect is possible to become significant in some density regime of future reactors with higher E_b, P_{NNB} and T_e. If the existence of the BPSI is demonstrated, the NB current drive is expected to become larger in extremely low density plasmas than the present prediction using only the multistep ionization process. Therefore, the BPSI effect gives more flexibility in operational scenarios especially for the initial current ramp up without inductive current. Experimental validation of the BPSI is ongoing issue in JT-60U.

6.2 Influence of MHD Instabilities on Current Drive

6.2.1 Beam-driven instability

In a low density plasma in which the N-NB fast ion pressure is comparable to the thermal pressure, a intermittent beam-driven instability was observed. The range of rapid frequency change in several ms observed on magnetic fluctuations became larger with increasing beam pressure as time progressed. Reductions in the neutron yield S_n and N-NB driven current were observed clearly. However, such reduction did not occur after that and an intermittent instability disappeared even though the N-NB injection continued and the beam pressure was still increasing. Its possible cause is a small temporal change in the safety factor profile, which can affect the stability boundary and the resonance condition for beam driven instabilities. This argument may be applicable to the observation that no instability was observed after the 6th burst in spite of increasing N-NB fast ion pressure. As discussed in Sec. 5.1, the observed instability cannot be explained by the well-known AE modes (Alfvén eigen modes). Recently, the RTAE (resonant toroidal AE) mode, a branch of kinetic ballooning mode, has been reported both experimentally [92] and theoretically [96]. It is possible to explain the phenomena in this experiment by this mode. A relatively low frequency range of instability and a slow change of frequency during the buildup phase of the N-NB fast ions are consistent with RTAE mode. According to the RTAE theory, the observed frequency changes in very short timescales, which are called 'frequency chirping', are attributed to the change in fast ion distribution [96]. This is explained as follows. The RTAE occurs at a radial position satisfying a resonant condition and its frequency is sensitive to change of the velocity distribution function. Fast ions in certain velocity range are transported by the RTAE to different radial locations, at which the distribution function is modified in turn to satisfy the RTAE resonant condition and the RTAE frequency there is different from the one at the previous locations. This process continuously occurs till no resonant condition is satisfied. This is the mechanism of 'frequency chirping' in the RTAE

theory. Whether its stability boundary for this discharge exists around the observed safety factor profile with $q(0) \sim 1.5$ or not needs to be verified by a stability calculation code.

The evaluated lost N-NB driven current from the core region $\rho < 0.3$ ($\sim$ 40 kA) is not a large fraction of the total N-NB driven current ($\sim$ 600 kA). However, the lost driven current density within $\rho < 0.2$ was 15 - 40 %. Therefore, intolerable degradation of NB current drive may be possible with the combination of a higher beam ion pressure and a different safety factor profile. Whether the N-NB fast ions expelled from the central region were redistributed within the plasma or lost from the plasma is not clear presently. The measured non-inductive driven current profiles (dominated by the N-NB driven current) indicates that the profile in the region $0.3 < \rho < 0.6$ just after the burst is slightly larger than that just before the burst. This corresponds to a redistribution of fast ions. The charge exchange neutral particle measurement did not show a clear increase in the range of 100 - 360 keV in the energy spectrum when a burst occurred (the incident beam energy of N-NB is 360 keV). This diagnostic measures the neutral particles originating from the fast ions which are neutralized in the plasma peripheral region where the density of the low energy neutral particles is higher and charge exchange with fast ions occurs more frequently than in the central region. Thus, this measurement indicated that the N-NB fast ions expelled from the central region did not reach the peripheral region. On the other hand, in the experiments of large amplitude TAE modes accompanied with frequency change, which were conducted at lower toroidal magnetic fields than in this thesis for intentionally satisfying the TAE resonant condition, the transport of fast ions by each burst was observed in the charge exchange neutral particle measurement [92]. Recently, the change of radial profile of fast ion density due to large amplitude TAE was successfully measured by using the multi-chordal neutron emission measurement. The fast ion density decreased in the core and increased in the peripheral region after large TAE bursts [97].

6.2.2 Neoclassical tearing instability

The lost N-NB driven current was estimated to be 67 % from the loss rate α evaluated from the lost fast ion pressure profile. The loss rate evaluated from a comparison between the measured and calculated neutron yield, which gives a spatially averaged value, was 71 %. The v dependence of α was ignored in the estimation of α by the second assumption described in Sec. 5.2.3. However, α should have a positive dependence on energy, because the fast ion loss was observed to depend on the beam energy by comparing the lost $S_{\rm n}$ and $P_{\rm lost}$(fast) for P-NB and N-NB. The value of α evaluated using Eq. (5.2) is equivalent to an averaged α with a weight of $f_{\rm NNB}v^2$, i.e., $f_{\rm NNB}E^{3/2}$ in the energy (E) integral [Eq. (5.1)]. Figure 6.1 shows the time evolution of the distribution function for N-NB injection ($f_{\rm NNB}$) in the energy space at $\rho = 0.087$ and 0.287 which are close to the magnetic island, where the distribution function is calculated by OFMC without the NTM effect, and the origin of time (τ) is defined as the beginning of N-NB injection (t = 4.0 s in E37012). At τ =1.009, corresponding to t$\sim$5 s in E37012, $f_{\rm NNB}$ at ρ =0.287 can be approximated by $6.5 - 0.01E$(keV). Thus, α is evaluated with the weight of $6.5E^{3/2} - 0.01E^{5/2}$. The lost N-NB driven current density $j_{\rm NNB}^{\rm lost}$ was evaluated from this averaged α in Sec. 5.2.3. The integrand in $j_{\rm NNB}^{\rm lost}$ has a weaker E dependence by $E^{1/2}$ compared to $P_{\rm NNB}^{\rm lost}$. The weights

on α in the integrals for $P_{\rm NNB}^{\rm lost}$ and $j_{\rm NNB}^{\rm lost}$ are shown in Fig. 6.2. The one for $j_{\rm NNB}^{\rm lost}$ is broader. Thus, the combination of a positive dependence of α on energy and the use of α evaluated from pressure tends to overestimate $j_{\rm NNB}^{\rm lost}$. Here, $v_{//}$ is approximated by $v \propto \sqrt{E}$ as the tangentially injected N-NB fast ions are mostly produced as passing particles ($v_{//}$ component is dominant).

A transport mechanism for circulating fast ions due to low-frequency perturbations such as tearing modes was proposed in Ref. [98, 99] in relation to transport of MeV ions observed in TFTR. When a single helical magnetic field perturbation associated with a globally extended MHD mode exists, the $n = 0$ orbit shift of the fast particle motion couples to the added motion from the helical perturbation, resulting in multiple drift islands in the phase space of particle motion. That is, a single magnetic island structure with a poloidal mode number of m, creates multiple islands with $m \pm 1$, $m \pm 2$, $m \pm 3$, ... in the fast particle orbit if the corresponding rational surfaces exist in the plasma. The widths of these resonant islands increase with the magnitude of the magnetic perturbation and the particle energy. Therefore, adjacent drift islands can overlap and cause the the particle's motion to become stochastic. This 'orbit stochasticity' transport mechanism is consistent with our observation that the fast ion loss increases with the beam energy and the level of NTM activity. In E29442, the n=1 and n=2 NTMs appeared simultaneously and large transport of beam ions at low energy was observed as discussed in section 5.2.2. In such a situation, i.e., when multiple helical perturbation exist in a plasma, it is expected that the overlap of drift islands originating from multiple magnetic island structures occurs at narrower widths of the sideband drift islands and that the transport due to 'orbit stochasticity' is enhanced. In discharge E37012 with the m/n =2/1 magnetic island, the primary drift island is $m = 2$ at the $q = 2$ surface. The adjacent sideband islands are at $q = 1$ and $q = 3$ surfaces. Since $q > 1$ for this discharge, only the $q = 3$ island needs to be considered. For the primary and sideband islands to overlap, the sum of the drift island half-widths must become greater than the distance between the centers of the drift islands, so the Chirikov island overlap criterion can be written as

$$\frac{1}{2}\left(\delta\rho_2 + \delta\rho_3\right) \gtrsim \left|\rho_{q=2} - \rho_{q=3}\right| \ , \tag{6.1}$$

where $\delta\rho_2$ and $\delta\rho_3$ are the widths of the $m = 2$ and $m = 3$ drift islands, and $\rho_{q=2}$ and $\rho_{q=3}$ are the radial locations of the $q = 2$ and $q = 3$ surfaces. According to Ref. [98, 99], the drift island width $\delta\rho_l$ is related to the magnetic island width $\delta\rho$ by $\delta\rho_l \simeq \delta\rho\sqrt{|G_l(E)|}$, where l denotes the island harmonic number ($l = 0$ is the primary island, $l = \pm 1$, ± 2, ..., are sidebands) while G_l is the 'coupling coefficient' and is a function of energy E. Using the coupling coefficients calculated in Ref. [98, 99] and the magnetic island width of 0.2 measured by the ECE heterodyne radiometer (Sec. 5.2.3), $\delta\rho_2$ and $\delta\rho_3$ are estimated to be ~ 0.2 and ~ 0.1, respectively. Thus, the sum of the drift island half-widths is ~ 0.15. As $\rho_{q=2} = 0.18$ and $\rho_{q=3} = 0.58$, the right hand side of Eq. (6.1) is 0.4. Therefore, the Chirikov condition is not satisfied. The magnetic island width is possibly wider than 0.2 because the magnetic island structure extended beyond the spatial range of the ECE heterodyne radiometer as mentioned in Sec. 5.2.3. If this were the case, the left hand side of Eq. (6.1) becomes greater than the estimated value above. However, the magnetic island width should be 2.7 times larger in order to satisfy the condition (6.1). This may not

be possible.

The 'orbit stochasticity' model of fast ion transport due to a single magnetic island structure was proposed for interpretation of the experiments in TFTR with a circular poloidal cross-section [98, 99]. Derivation of the equation governing the sideband drift islands and overlap of the adjacent drift island structures was constructed upon the concentric magnetic surfaces with circular cross-sections and the radial perturbing magnetic field with a simple cosine dependence on poloidal angle. Such a cosine form of poloidal angle is exact for a straight cylinder configuration. In toroidal system with non-circular cross-sectional shapes, however, this form is just a zero-th order approximation. The distribution of magnetic islands is nonuniform along the poloidal angle coordinate due to nonuniform magnetic field strength. The magnetic island widths even on the same rational surface depend on the poloidal angle coordinate. In addition, higher order asymmetries of the poloidal magnetic field due to deformation of plasma shape such as elongation, triangularity and squareness can cause higher order coupling of fast particle motion to the added motion from the helical perturbation. Thus, the coupling coefficients derived in Refs. [98, 99] would be different from the ones for a non-circular plasma shape as in the JT-60U case. Future tokamak devices such as ITER are designed to have stronger shaping because of its favorable contribution to MHD stability. A low aspect ratio tokamak with further stronger toroidicity than the conventional tokamak such as JT-60U and ITER is also proposed as a next-step tokamak concept, expecting drastic improvement of plasma beta. Therefore, an improved treatment of non-circularity and toroidicity and the reproduction of fast ion behavior in simulation is a principal subject to be investigated.

There are two unresolved issues on NTM, i.e., its trigger and stability dependence on plasma parameters such as the normalized ion Larmor radius and normalized collisionality. According to the modified Rutherford equation governing a temporal evolution of magnetic island, growth of neoclassical tearing mode needs a 'seed' magnetic island with a critical island width as its trigger. As possible origins of seed islands, sawtooth instability and fishbone instability have been reported in DIII-D [100], ASDEX-U [101] and JET [102]. In JT-60U, NTM can appear in high β_p H mode discharges without MHD instability [103], and hence an origin of seed island can not be identified. In such cases, the seed island formation due to the initial destabilization of the classical tearing mode and/or edge localize mode (ELM) may be possible causes. On the other hand, in JT-60U, also reported was the case that NTM was not triggered even above the onset β_N level which NTM normally appeared [91], which is considered to be attributed to the decrease in the local pressure gradient at a rational surface and/or the stabilization effect due to toroidal rotation. The pulse E36715 discussed in section 4.3.1 is just the case. This gives a prospect of NTM avoidance by carefully tailoring the profiles of pressure, current density and rotation using neutral beam injection. Stability dependence on the normalized ion Larmor radius ρ^* and normalized collisionality ν^* has been anticipated from the driving (reduction of bootstrap current) and stabilizing (ion polarization current) terms in the modified Rutherford equation. However, experimental validation of each destabilizing/stabilizing term and its adjustable coefficients are still being studied intensively. In many tokamaks, reported has been the positive dependence of the NTM onset β_N on ρ^* and ν^*, although their exponents in power form are different. Thus, in future reactor with larger size and higher temper-

ature than the present experimental devices, ρ^* and ν^* become lower, and hence NTM is expected to be destabilized at lower β_N and degrade the confinements of thermal energy and fast ions as presented in this thesis. Thus, in ITER a possibility of further destabilization of NTM and higher beam energy of N-NB can cause the intolerable transport of NB fast ions and reduce heating and current drive by neutral beam. Understanding of fast ion transport due to the magnetic island structure is indispensable.

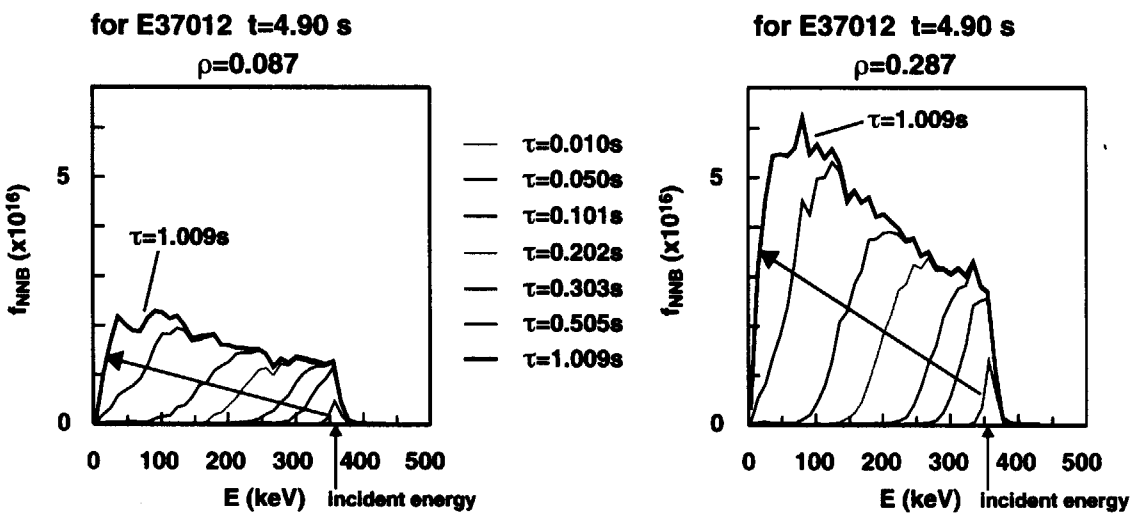

Figure 6.1: Time evolution of the N-NB fast ion distribution function in energy space at ρ =0.087 and 0.287, calculated by OFMC. The temperature and density profiles are taken from E37012 at t = 4.90 s.

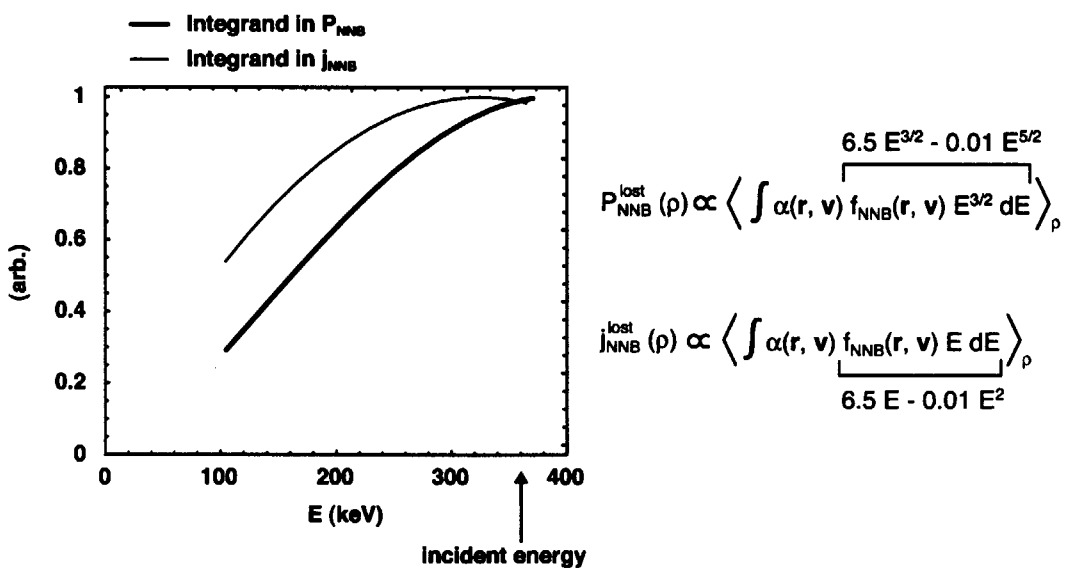

Figure 6.2: The energy (E) dependence of the integrands in $P^{\rm lost}_{\rm NNB}$ and $j^{\rm lost}_{\rm NNB}$ at ρ =0.287.

7. Conclusions

Characteristics of current drive by a high energy neutral beam has been studied experimentally using the 360 keV N-NB in the JT-60U tokamak. To determine the N-NB driven current density profile, a loop voltage profile analysis was used. This analysis method has become possible by an accurate equilibrium reconstruction using the MSE measurement. To improve the accuracy of equilibrium reconstruction, three MSE systems have been installed, and the optical components of the MSE systems have been modified to improve the calibration accuracy and to reduce the Faraday rotation in optical components

The N-NB driven current density was determined in a relatively low electron temperature plasma ($T_e(0)$ ~4 keV), . This was the first observation for high energy NB with a beam energy of several hundred keV. The measured profile was compared with theoretical predictions by ACCOME and OFMC codes. The measurement agreed well with theory.

The NB current drive theory predicts that the NB current drive efficiency increases with the electron temperature. Based on this favorable property, plasma performance is projected for future tokamak reactors such as ITER. Therefore, the electron temperature dependence of the N-NB current drive should be investigated experimentally. To obtain high electron temperature plasmas, EC heating was applied. The N-NB driven current density profile was measured at $T_e(0)$ =10 keV, and theoretical predictions were validated in this regime. At $T_e(0)$ =10 keV, the N-NB driven current reached 1 MA and the corresponding current drive efficiency was 1×10^{19} $\mathrm{Am^{-2}W^{-1}}$. The NB driven current of 1 MA is a record value for NB current drive among the results with direct driven current measurement.

A record value of NB current drive efficiency 1.55×10^{19} $\mathrm{Am^{-2}W^{-1}}$ was achieved at $T_e(0)$ =14 keV simultaneously with high confinement and high plasma pressure at a plasma current of I_p=1.5 MA. Combining a N-NB current drive with P-NB current drive, bootstrap current and EC current drive, a full non-inductively current driven state was also achieved. A simulation using the time-dependent transport code TOPICS has reproduced this discharge successfully. The measured time-evolutions of current density and pressure profiles agreed with the simulation.

The conclusion of validity of theoretical prediction for NB current drive is for MHD-quiescent plasmas. Effects of MHD instabilities such as the beam-driven mode and the neoclassical tearing mode on NB current drive was also investigated. In low density plasmas with the N-NB fast ion pressure comparable to the thermal pressure, a beam driven instability appears intermittently. This instability occurred within $r/a < 0.3$ and expelled the N-NB fast ions carrying non-inductive current from this region. The lost driven current within $r/a < 0.3$ was estimated to be ~40 kA, corresponding to 7% of the total N-NB driven current. This was the first measurement of the loss of NB driven current by a beam driven instability.

The neoclassical tearing mode (NTM) appears in high beta plasmas and degrades confinement. This instability must be avoided in long-sustained high beta plasmas. The influence of NTM on NB fast ions

was investigated. Comparison of the measured neutron yield with the calculated value by the TOPICS code reveals that the loss or redistribution of fast ions increases with the level of NTM activity and that fast ions at higher energy (N-NB) suffers larger transport than those at lower energy (P-NB). In addition, from a comparison of the fast ion pressure profile determined by equilibrium reconstruction with that by TOPICS, the following conclusions can be made. (1) When the NTM existed, the fast ion pressure profile within $r/a < 0.5$, which coincided with the region of N-NB fast ion deposition, was reduced to about a half during the N-NB and P-NB injection phase, while the fast ion pressure profile was not affected much during the P-NB injection phase. (2) After the NTM has disappeared, the fast ion pressure profile was not affected much during the N-NB and P-NB injection. Thus, fast ions at higher energies (N-NB) were affected more than lower energy beam ions (P-NB). This is consistent with the observation of neutron yield reduction. Dependence of the loss of NB fast ions on the beam energy has been made clear for the first time. From the lost fast ion pressure profile, the lost N-NB driven current profile was estimated. The loss of the total N-NB driven current was 67 % during the NTM. Assuming the loss rate of N-NB fast ions to be independent of their velocity, this result means that 67 % of the injected N-NB fast ions were lost. Under the same assumption, the loss rate was also evaluated from the neutron yield to be 71 %.

The results of N-NB current drive without an MHD instability validate theoretical prediction and gives greater confidence in predicting high energy neutral beam current drive in future reactors. However, it was also found that MHD instabilities can affect NB fast ions and degrade heating and current drive efficiencies. Especially, the neoclassical tearing mode not only degrades thermal energy confinement but also causes unacceptable loss of NB fast ions from the plasma core. A method of NTM suppression should be established for next step reactors such as ITER because they utilize N-NB with a beam energy larger than 1 MeV which would suffer larger transport due to the NTM compared to in the present experiment which used a 360 keV beam.

8. Prospect and Research Issues toward ITER Burning Plasmas

Prospected operational regime of ITER, a first burning plasma experiment, lies beyond the achievements in the present experimental devices. The mission in ITER, achievement of fusion amplification gain $Q = 10$ ($Q \equiv$ [fusion output power]/[externally input power]), plasma parameters, and machine parameters are set and designed based on the established theories and empirical laws. Principal MHD instabilities such as kink-ballooning modes related to disruptions are understood well from comparison between experiments and theories. Peeling-ballooning mode related to the edge localized mode (ELM), Alfvén eigen modes and neoclassical tearing mode are being established and nearly become predictable. Fast ion behavior in MHD quiescent plasmas related to current drive and heating by NBs can be understood with the present theory. As experimental efforts over several decades indicate that anomalous process dominates the transport, so confinement of energy and particle is predicted using the scaling laws which has been derived and is currently being updated from accumulation of the experimental data obtained in many tokamak devices.

Obviously, theoretical understanding of physical mechanisms in each area is essential to ensure the credibility of extrapolation in predicting plasmas. In ITER, a new regime of the normalized Larmor radius ρ^* and normalized collisionality ν^* is considered to alter the MHD stability and transport possibly to unfavorable side. The presence of self-generating energetic alpha particles can also affect their properties. In regard to the issues discussed in this thesis, transport mechanisms of fast ions give a great impact on both the heating and current drive by the 1 MeV N-NB and self-heating by the 3.5 MeV alpha particles produced from D-T fusion reactions. On a positive side, however, it is connected with a technique of removing intermediate energy alpha particles in a reactor through the external application of helical perturbations (The removal of this "helium ash" is necessary for a self-sustaining burn.). In references [98] and [99], illustrative perturbations are exhibited that are stochastic for low- but not for high-energy ions, for high- but not for low-energy ions, and for intermediate-energy ions, but not for low or high energy. These would lead to burn control and helium ash removal.

Predictive capability of transport simulation code was demonstrated in section 4.3.1, although it was limited to the current diffusion, neutral beam, and non-inductive currents. In recent years, some collaborative research activities have started around the world by taking into consideration anomalous transport models, MHD instabilities and burning plasmas (production of alpha particles) in transport simulation. Such time-dependent transport simulation codes enable a full simulation of burning plasma evolution. Validation of each theoretical packages for each physics process and their integration are the most important subjects for predicting and conducting actual experiments in the ITER burning plasmas.

Even when physics understanding progresses from the experimental validation of theories and the

control methods of MHD stabilities and transport are established in the present devices, ITER plasmas are still beyond the scope we can currently reach, and hence the predictions on ITER plasmas are extrapolations from our knowledge. However, that's what makes it worthy of challenge. The experimental, analytical and theoretical approaches we have taken hitherto are judged in the coming ITER project.

Acknowledgment

It is a great pleasure to acknowledge Prof. Y. Takase (University of Tokyo) for his support and guidance for completing this thesis. His advise from a viewpoint as a member of ITPA (International Tokamak Physics Activity) is a great help.

A routine operation of 500 keV NB in JT-60U was a first challenge in the world. I would like to acknowledge Dr. K. Ushigusa of JAERI for his support and effort as an organizer of the N-NB physics experiments since the beginning of the N-NB operation in 1996. I also would like to appreciate Dr. M. Kuriyama and the NBI group of JAERI for considerable effort for a long pulse and high power operation of N-NB injector.

I would like to acknowledge Drs. T. Fujita and T. Suzuki (JAERI) for cooperation in the equilibrium reconstruction code and the development and improvement of the MSE diagnostic which are crucial for the current drive study.

I also would like to appreciate Prof. C.B. Forest (University of Wisconsin) for introduction of the non-inductive current profile analysis, Dr. L.L. Lao (General Atomics, U.S.A) for the equilibrium code EFIT.

I would like to thank Drs. Y. Kamada and A. Isayama (JAERI) for collaboration on high performance plasma operation using N-NB and the NTM experiment. The world records of the NB current drive capability and its integration with high confinement plasma would not have been achieved without their extensive knowledge on plasma physics and the actual experience in the large tokamak operation.

The collaboration with Drs. Y. Kusama, K. Tobita, M. Nemoto, S. Suzuki, M. Takechi and K. Shinohara (JAERI) on high energy particle physics is greatly appreciated.

In this thesis, comparison of the measurement with the theoretical codes such as ACCOME, OFMC and TOPICS is essential. I would like to express my thanks Drs. M. Azumi, O. Naito, N. Hayashi and H. Shirai, and Messrs. M. Suzuki and I. Kamata.

The research in this thesis would not have been completed without assistance of the members of the JT-60 team. I would like to thank them for JT-60U operation, development and maintenance of high quality diagnostics and computational codes, and valuable discussion toward ITER and the steady-state fusion reactor in the future.

I must express my gratitude to Dr. M. Shimada, department of fusion plasma research and department of ITER project of JAERI for their support and giving me an opportunity of completing this thesis.

I wish to express my thanks to one-time Prof. H. Toyama (University of Tokyo) and Prof. Emeritus K. Miyamoto (University of Tokyo) for their encouragement and advice on fusion plasma research.

Finally, I am grateful to my parents.

Bibliography

[1] L. Artsimovitsh, Nucl. Fusion **12**, 215 (1972).

[2] I. P. B. Editors, Nucl. Fusion **39**, 2137 (1999).

[3] G. Miley, H. Towner, and N. Ivich, Fusion cross-sections and reactivities, University of Illinois Nuclear Engineering Report COO-2218-17, University of Illinois, Urbana, Illinois, 1974.

[4] J. Wesson, *Tokamak second edition*, Oxford Engineering Science Series 48, Oxford University Press, 1997.

[5] T. Ohkawa, Nucl. Fusion **10**, 185 (1970).

[6] N. Fisch, Phys. Rev. Lett. **41**, 873 (1978).

[7] M. Kikuchi, M. Azumi, K. Tsuji, H. Tani, and H. Kubo, Nucl. Fusion **29**, 343 (1990).

[8] M. Kikuchi and M. Azumi, Plasma Phys. Control. Fusion **37**, 1215 (1995).

[9] W. Clark et al., Phys. Rev. Lett. **45**, 1101 (1980).

[10] M. Kuriyama et al., Fusion Eng. Des. **26**, 445 (1995).

[11] K. Ushigusa and the JT-60 team, Fusion energy proc. 16th int. conf. (montreal, 1996), in *Fusion Energy Proc. 16th Int. Conf. (Montreal, 1996)*, volume 1, page 37, IAEA, 1997.

[12] *ORNL-6086 V1*.

[13] M. Kuriyama et al., Fusion Eng. Des. **39-40**, 115 (1998).

[14] R. Janev et al., Nucl. Fusion **12**, 2125 (1989).

[15] K. Tani et al., Journal of Phys. Soc. Jpn. **50**, 1726 (1981).

[16] K. Tobita et al., Plasma Phys. Control. Fusion **32**, 429 (1990).

[17] M. Nemoto et al., J. Plasma and Fusion Research **73**, 1374 (1997).

[18] S. Suzuki et al., Plasma Phys. Control. Fusion **40**, 2097 (1998).

[19] D. Start and J. Cordey, Phys. Fluids **23**, 1477 (1980).

[20] D. Start and J. Cordey, Nucl. Technology/Fusion **4**, 237 (1983).

[21] K. Tani, M. Azumi, and R. Devote, Journal of Computational Physics **98**, 332 (1992).

[22] F. Hinton and R. Hazeltine, Reviews of Modern Physics **48**, 239 (1976).

[23] S. Hirshman and D. Sigmar, Nucl. Fusion **21**, 1079 (1981).

[24] S. Hirshman, R. Hawryluk, and B. Birge, Nucl. Fusion **17**, 3 (1977).

[25] F. Wagner et al., Phys. Rev. Lett. **49**, 1408 (1982).

[26] F. Söldner et al., Phys. Rev. Lett. **61**, 1105 (1988).

[27] Y. Koide et al., Phys. Rev. Lett. **72**, 3662 (1994).

[28] Y. Kamada et al., in *Fusion Energy Proc. 15th Int. Conf. (Seville, 1994)*, volume 1, page 651, IAEA, 1995.

[29] Y. Kamada et al., in *Fusion Energy Proc. 16th Int. Conf. (Montreal, 1996)*, volume 1, page 247, IAEA, 1997.

[30] Y. Kamada et al., volume 39, page 1845, 1999.

[31] G. Jackson et al., Phys. Rev. Lett. **67**, 3098 (1991).

[32] T. Fujita et al., Phys. Rev. Lett. **78**, 2377 (1997).

[33] S. Ishida, T. Fujita, and the JT-60 team, Phys. Rev. Lett. **79**, 3917 (1997).

[34] T. Fujita et al., Nucl. Fusion **39**, 1627 (1999).

[35] T. Fujita et al., Phys. Rev. Lett. **87**, 245001 (2001).

[36] J. Callen et al., page : *Plasma Physics and Controlled Nuclear Fusion Research 1986* (Proc. 11th Int. Conf. Plasma Phys Control. Nucl. Fusion Res., Kyoto, 1986), Vol. 2, p. 157.

[37] P. Rutherford, Phys. Fluids **16**, 1903 (1973).

[38] A. Glasser et al., Phys. Fluids **18**, 875 (1975).

[39] R. Carrera, R. Hazeltine, and M. Kotschenreuther, Phys. Fluids **29**, 899 (1986).

[40] C. Hegna and J. Callen, Phys. Fluids B **4**, 1855 (1992).

[41] F. Levinton et al., Phys. Rev. Lett. **63**, 2060 (1989).

[42] T. Fujita, H. Kubo, T. Sugie, N. Isei, and K. Ushigusa, Fusion Eng. Des. **34-35**, 282 (1995).

[43] J.-. TEAM, Nucl. Fusion, Suppl. **1**, 11 (1987).

[44] A. Kitsunezaki et al., Fusion Science and Tech. **42**, 179 (2002).

[45] N. Hosogane et al., Fusion Science and Tech. **42**, 368 (2002).

[46] K. Kurihara et al., Fusion Eng. Des **11**, 441 (1990).

[47] K. Kurihara et al., IEEE Transactions on Nuclear Science **47**, 205 (2000).

[48] T. Fukuda et al., Fusion Science and Technology **42**, 357 (2002).

[49] Y. Neyatani et al., Fusion Eng. Des. **36**, 429 (1997).

[50] T. Oikawa, JAERI Research **99-048**, 15 (1999).

[51] T. Oikawa and the JT-60 team, Nucl. Fusion **40**, 1125 (2000).

[52] T. Sugie et al., Fusion Science and Tech. **42**, 512 (2002).

[53] H. Yoshida et al., Rev. Sci. Instrum. **70**, 751 (1999).

[54] T. Hatae et al., Rev. Sci. Instrum. **70**, 772 (1999).

[55] S. Ide et al., Nucl. Fusion **40**, 445 (2000).

[56] M. Sato, H. Yokomizo, and A. Nagashima, Kakuyugo Kenkyu Supplement [in Japanese] **59**, 47 (1988).

[57] S. Ishida, A. Nagashima, M. Sato, N. Isei, and T. Matoba, Rev. Sci. Instrum. **61**, 2834 (1990).

[58] A. Isayama, N. Isei, S. Ishida, and M. Sato, Rev. Sci. Instrum. **73**, 1165 (2002).

[59] N. Isei et al., Rev. Sci. Instrum. **66**, 413 (1995).

[60] Y. Koide, A. Sakasai, Y. Sakamoto, H. Kubo, and T. Sugie, Rev. Sci. Instrum. **72**, 119 (2001).

[61] T. Fujita, H. Kubo, T. Sugie, N. Isei, and K. Ushigusa, Fusion Eng. Des. **34-35**, 282 (1995).

[62] T. Oikawa, L. Lao, and T. Fujita, JAERI Research **99-048**, 122 (1999).

[63] M. Kuriyama et al., Fusion Science and Tech. **42**, 424 (2002).

[64] M. Kuriyama et al., Fusion Science and Tech. **42**, 410 (2002).

[65] M. Seki et al., Fusion Science and Tech. **42**, 452 (2002).

[66] S. Moriyama et al., Fusion Science and Tech. **42**, 467 (2002).

[67] Y. Ikeda et al., Fusion Eng. Des **53**, 351 (2001).

[68] Y. Ikeda et al., in *Proc. 18th Fusion Energy Conf.(Sorrento, 2000), EXP4/03*, IAEA, 2000.

[69] Y. Ikeda et al., Fusion Science and Tech. **42**, 435 (2002).

[70] D. Wròblewski and L. Lao, Rev. Sci. Instrum. **63**, 5140 (1992).

[71] B. Rice, D. Nilson, and D. Wròblewski, Rev. Sci. Instrum. **66**, 373 (1995).

[72] F. Levinton et al., Phys. Fluids B **5**, 2554 (1993).

[73] R. Wolf et al., Nucl. Fusion **33**, 1835 (1993).

[74] N. Hawkes et al., Rev. Sci. Instrum. **70**, 894 (1999).

[75] F. Troyon et al., Plasma Phys. Control. Fusion **26**, 209 (1984).

[76] J. Christiansen and J. Taylor, Nucl. Fusion **22**, 111 (1982).

[77] S. Tsuji et al., JAERI-M **86-006** (1986).

[78] C. Forest et al., Phys. Rev. Lett. **73**, 2444 (1994).

[79] L. Lao et al., Nucl. Fusion **30**, 1035 (1990).

[80] H. Shirai et al., J. Phys. Soc. Jpn. **64**, 4209 (1995).

[81] J. Cordey, Nucl. Fusion **16**, 449 (1976).

[82] T. Oikawa et al., Nucl. Fusion **40**, 435 (2000).

[83] C. Forest et al., Phys. Plasmas **3**, 2846 (1996).

[84] T. Fujita et al., Phys. Rev. Lett. **87**, 085001 (2001).

[85] T. Oikawa et al., Nucl. Fusion **41**, 1575 (2001).

[86] K. Hamamatsu et al., Fusion Eng. Des. **53**, 53 (2001).

[87] S. Scott et al., in *Proc. 12th Int. Conf.(Nice,1988)*, volume 1, page 655, Vienna, 1989, IAEA.

[88] C. Challis et al., Nucl. Fusion **29**, 563 (1989).

[89] R. Prater et al., Plasma Phys. Control Fusion **35**, A53 (1993).

[90] W. Heidbrink and G. Sadler, Nucl. Fusion **34**, 535 (1994).

[91] A. Isayama et al., Nucl. Fusion **41**, 761 (2001).

[92] K. Shinohara et al., in *18th Fusion Energy Conf.(Sorrento, 2000), EXP2/05*, IAEA, 2000.

[93] A. Isayama et al., Achievement of a high fusion triple product. steady state sustainment in high β_p elmy h-mode discharges in jt-60u, in *19th Fusion Energy Conf. IAEA-CN-94/EX/C2-2*, IAEA, 2002.

[94] K. Okano, Nucl. Fusion **31**, 1349 (1991).

[95] K. Okano et al., in *Proc. 28th EPS Conference on Contr. FUsion and Plasma Phys.*, volume 25A, page 809, 2001.

[96] N. Gorelenkov et al., Nucl. Fusion **40**, 1311 (2000).

[97] M. Ishikawa, *Study of fast ion transport using neutron emission profile measurement on JT-60U*, PhD thesis, Univ of Tsukuba, 2003.

[98] H. Mynick, Phys. Fluids B **5**, 1471 (1993).

[99] H. Mynick, Phys. Fluids B **5**, 2460 (1993).

[100] R. L. Haye et al., Nucl. Fusion **37**, 397 (1997).

[101] H. Zohm et al., Plasma Phys. Control. Fusion **39**, B237 (1997).

[102] R. Battery et al., in *Proc. 26th EPS Conference on Contr. FUsion and Plasma Phys.*, volume 23J, page 121, 1999.

[103] A. Isayama et al., Plasma Phys. Control. Fusion **41**, 35 (1999).

Appendix A

Glossary

The quantities which have radial profiles in minor radius direction are followed by (ρ), e.g., $q(\rho)$.

R	:	major radius
R_0, R_{maj}, R_{p}	:	major radius of the last closed flux surface (plasma surface)
r	:	minor radius
a	:	minor radius of the last closed flux surface (plasma surface)
ρ	:	normalized minor radius ($\equiv r/a$)
ϕ	:	toroidal angle
θ	:	poloidal angle
I_{p}	:	toroidal plasma current
B_{T}, B_ϕ	:	toroidal magnetic field
B_{p}, B_θ	:	poloidal magnetic field
W_{dia}	:	plasma stored energy
S_{n}	:	neutron emission rate (neutron production rate, neutron yield)
E_{b}	:	Beam energy
P_{NNB}, P_{PNB}	:	N-NB (P-NB) injection power
η_{CD}	:	current drive efficiency $\equiv \bar{n}_{\mathrm{e}} R_{\mathrm{p}} I_{\mathrm{CD}} / P_{\mathrm{abs.}}$
I_{CD}	:	non-inductive driven current
$P_{\mathrm{abs.}}$	:	heating power absorbed in a plasma
V_{surf}	:	toroidal one-turn loop voltage at plasma surface
$V_{\mathrm{loop}}(\rho)$	:	toroidal one-turn loop voltage
$j(\rho)$	:	total (equilibrium) current density
$j_{\mathrm{OH}}(\rho)$	:	inductive (ohmic) current density
$j_{\mathrm{NIND}}(\rho)$	:	non-inductive current density
$j_{\mathrm{NB}}(\rho)$	:	Neutral Beam driven current density
$j_{\mathrm{BS}}(\rho)$	:	bootstrap current density
$j_{\mathrm{RF}}(\rho)$	:	RF driven current density
$q(\rho)$	:	safety factor
$T_{\mathrm{e}}(\rho)$	:	electron temperature
$T_{\mathrm{i}}(\rho)$	:	ion temperature
$n_{\mathrm{e}}(\rho)$	:	electron density
$V_{\mathrm{T}}(\rho)$, $V_\phi(\rho)$	:	toroidal rotation velocity
$Z_{\mathrm{eff}}(\rho)$	:	effective plasma ion charge
$\eta(\rho)$	:	plasma resistivity ($= 1/\sigma$)
$\sigma(\rho)$	:	plasma conductivity ($= 1/\eta$)

国際単位系 (SI) と換算表

表 1　SI 基本単位および補助単位

量	名称	記号
長さ	メートル	m
質量	キログラム	kg
時間	秒	s
電流	アンペア	A
熱力学温度	ケルビン	K
物質量	モル	mol
光度	カンデラ	cd
平面角	ラジアン	rad
立体角	ステラジアン	sr

表 2　SI と併用される単位

名称	記号
分，時，日	min，h，d
度，分，秒	°，′，″
リットル	l，L
トン	t
電子ボルト	eV
原子質量単位	u

$1\ \mathrm{eV} = 1.60218 \times 10^{-19}\ \mathrm{J}$

$1\ \mathrm{u} = 1.66054 \times 10^{-27}\ \mathrm{kg}$

表 5　SI 接頭語

倍数	接頭語	記号
10^{18}	エクサ	E
10^{15}	ペタ	P
10^{12}	テラ	T
10^{9}	ギガ	G
10^{6}	メガ	M
10^{3}	キロ	k
10^{2}	ヘクト	h
10^{1}	デカ	da
10^{-1}	デシ	d
10^{-2}	センチ	c
10^{-3}	ミリ	m
10^{-6}	マイクロ	μ
10^{-9}	ナノ	n
10^{-12}	ピコ	p
10^{-15}	フェムト	f
10^{-18}	アト	a

表 3　固有の名称をもつ SI 組立単位

量	名称	記号	他の SI 単位による表現
周波数	ヘルツ	Hz	s^{-1}
力	ニュートン	N	$m \cdot kg/s^2$
圧力，応力	パスカル	Pa	N/m^2
エネルギー，仕事，熱量	ジュール	J	N·m
工率，放射束	ワット	W	J/s
電気量，電荷	クーロン	C	A·s
電位，電圧，起電力	ボルト	V	W/A
静電容量	ファラド	F	C/V
電気抵抗	オーム	Ω	V/A
コンダクタンス	ジーメンス	S	A/V
磁束	ウェーバ	Wb	V·s
磁束密度	テスラ	T	Wb/m^2
インダクタンス	ヘンリー	H	Wb/A
セルシウス温度	セルシウス度	℃	
光束	ルーメン	lm	cd·sr
照度	ルクス	lx	lm/m^2
放射能	ベクレル	Bq	s^{-1}
吸収線量	グレイ	Gy	J/kg
線量当量	シーベルト	Sv	J/kg

表 4　SI と共に暫定的に維持される単位

名称	記号
オングストローム	Å
バーン	b
バール	bar
ガル	Gal
キュリー	Ci
レントゲン	R
ラド	rad
レム	rem

$1\ \text{Å} = 0.1\ \mathrm{nm} = 10^{-10}\ \mathrm{m}$

$1\ \mathrm{b} = 100\ \mathrm{fm}^2 = 10^{-28}\ \mathrm{m}^2$

$1\ \mathrm{bar} = 0.1\ \mathrm{MPa} = 10^5\ \mathrm{Pa}$

$1\ \mathrm{Gal} = 1\ \mathrm{cm/s}^2 = 10^{-2}\ \mathrm{m/s}^2$

$1\ \mathrm{Ci} = 3.7 \times 10^{10}\ \mathrm{Bq}$

$1\ \mathrm{R} = 2.58 \times 10^{-4}\ \mathrm{C/kg}$

$1\ \mathrm{rad} = 1\ \mathrm{cGy} = 10^{-2}\ \mathrm{Gy}$

$1\ \mathrm{rem} = 1\ \mathrm{cSv} = 10^{-2}\ \mathrm{Sv}$

（注）

1. 表 1 ― 5 は「国際単位系」第 5 版，国際度量衡局 1985 年刊行による。ただし，1 eV および 1 u の値は CODATA の 1986 年推奨値によった。
2. 表 4 には海里，ノット，アール，ヘクタールも含まれているが日常の単位なのでここでは省略した。
3. bar は，JIS では流体の圧力を表わす場合に限り表 2 のカテゴリーに分類されている。
4. EC 閣僚理事会指令では bar，barn および「血圧の単位」mmHg を表 2 のカテゴリーに入れている。

換　算　表

力	N(=10^5dyn)	kgf	lbf
	1	0.101972	0.224809
	9.80665	1	2.20462
	4.44822	0.453592	1

粘　度　1 Pa·s(N·s/m^2)=10 P(ポアズ)(g/(cm·s))

動粘度　1 m^2/s=10^4St(ストークス)(cm^2/s)

圧力	MPa(=10 bar)	kgf/cm^2	atm	mmHg(Torr)	lbf/in^2(psi)
	1	10.1972	9.86923	7.50062×10^3	145.038
	0.0980665	1	0.967841	735.559	14.2233
	0.101325	1.03323	1	760	14.6959
	1.33322×10^{-4}	1.35951×10^{-3}	1.31579×10^{-3}	1	1.93368×10^{-2}
	6.89476×10^{-3}	7.03070×10^{-2}	6.80460×10^{-2}	51.7149	1

エネルギー・仕事・熱量	J(=10^7erg)	kgf·m	kW·h	cal(計量法)	Btu	ft·lbf	eV
	1	0.101972	2.77778×10^{-7}	0.238889	9.47813×10^{-4}	0.737562	6.24150×10^{18}
	9.80665	1	2.72407×10^{-6}	2.34270	9.29487×10^{-3}	7.23301	6.12082×10^{19}
	3.6×10^6	3.67098×10^5	1	8.59999×10^5	3412.13	2.65522×10^6	2.24694×10^{25}
	4.18605	0.426858	1.16279×10^{-6}	1	3.96759×10^{-3}	3.08747	2.61272×10^{19}
	1055.06	107.586	2.93072×10^{-4}	252.042	1	778.172	6.58515×10^{21}
	1.35582	0.138255	3.76616×10^{-7}	0.323890	1.28506×10^{-3}	1	8.46233×10^{18}
	1.60218×10^{-19}	1.63377×10^{-20}	4.45050×10^{-26}	3.82743×10^{-20}	1.51857×10^{-22}	1.18171×10^{-19}	1

1 cal = 4.18605 J（計量法）

= 4.184 J　（熱化学）

= 4.1855 J　（15 °C）

= 4.1868 J（国際蒸気表）

仕事率　1 PS（仏馬力）

= 75 kgf·m/s

= 735.499 W

放射能	Bq	Ci
	1	2.70270×10^{-11}
	3.7×10^{10}	1

吸収線量	Gy	rad
	1	100
	0.01	1

照射線量	C/kg	R
	1	3876
	2.58×10^{-4}	1

線量当量	Sv	rem
	1	100
	0.01	1

（86 年 12 月 26 日現在）

Study of Non-inductive Current Drive Using High Energy Neutral Beam Injection on JT-60U

R100
古紙配合率100%
白色度70%再生紙を使用しています